



ΠΑΝΕΠΙΣΤΗΜΙΟ ΔΥΤΙΚΗΣ ΑΤΤΙΚΗΣ

ΣΧΟΛΗ ΜΗΧΑΝΙΚΩΝ

ΤΜΗΜΑ ΗΛΕΚΤΡΟΛΟΓΩΝ & ΗΛΕΚΤΡΟΝΙΚΩΝ ΜΗΧΑΝΙΚΩΝ

Διπλωματική Εργασία

Ανάπτυξη Βιοϊατρικής Διάταξης με Τεχνολογία Τυπωμένων Ηλεκτρονικών



Φοιτήτρια: Σκεντάι Φρισέλα

ΑΜ: 18387137

Επιβλέπων Καθηγητής

Καλτσάς Γρηγόριος

Καθηγητής

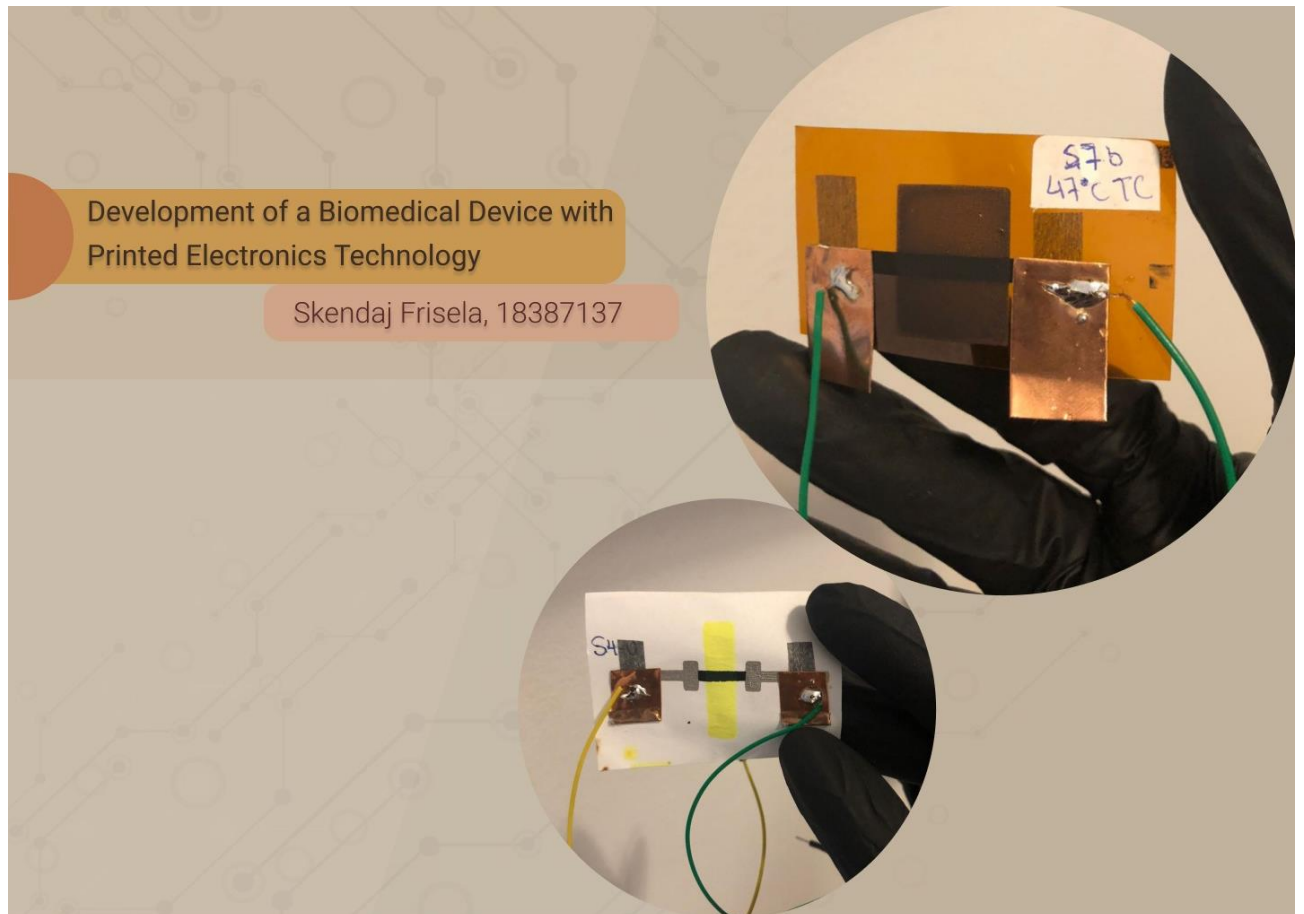
ΑΘΗΝΑ-ΑΙΓΑΛΕΩ, ΣΕΠΤΕΜΒΡΙΟΣ 2023



UNIVERSITY OF WEST ATTICA
FACULTY OF ENGINEERING
DEPARTMENT OF ELECTRICAL & ELECTRONICS ENGINEERING

Diploma Thesis

Development of a Biomedical Device with Printed Electronics Technology



Student: Skendaj Frisela
Registration Number: 18387137

Supervisor

Kaltsas Grigorios
Professor

ATHENS-EGALEO, SEPTEMBER 2023

Η Διπλωματική Εργασία έγινε αποδεκτή και βαθμολογήθηκε από την εξής τριμελή επιτροπή:

Γρηγόρης Καλτσάς Καθηγητής	Ιωάννης Φαμέλης Καθηγητής	Δημήτριος Γουστουρίδης Καθηγητής
(Υπογραφή)	(Υπογραφή)	(Υπογραφή)

Copyright © Με επιφύλαξη παντός δικαιώματος. All rights reserved.

ΠΑΝΕΠΙΣΤΗΜΙΟ ΔΥΤΙΚΗΣ ΑΤΤΙΚΗΣ

και ΣΚΕΝΤΑΪ ΦΡΙΣΕΛΑ, ΣΕΠΤΕΜΒΡΙΟΣ, 2023

Απαγορεύεται η αντιγραφή, αποθήκευση και διανομή της παρούσας εργασίας, εξ ολοκλήρου ή τμήματος αυτής, για εμπορικό σκοπό. Επιτρέπεται η ανατύπωση, αποθήκευση και διανομή για σκοπό μη κερδοσκοπικό, εκπαιδευτικής ή ερευνητικής φύσης, υπό την προϋπόθεση να αναφέρεται η πηγή προέλευσης και να διατηρείται το παρόν μήνυμα. Ερωτήματα που αφορούν τη χρήση της εργασίας για κερδοσκοπικό σκοπό πρέπει να απευθύνονται προς τους συγγραφείς.

Οι απόψεις και τα συμπεράσματα που περιέχονται σε αυτό το έγγραφο εκφράζουν τον/την συγγραφέα του και δεν πρέπει να ερμηνευθεί ότι αντιπροσωπεύουν τις θέσεις του επιβλέποντος, της επιτροπής εξέτασης ή τις επίσημες θέσεις του Τμήματος και του Ιδρύματος.

ΔΗΛΩΣΗ ΣΥΓΓΡΑΦΕΑ ΔΙΠΛΩΜΑΤΙΚΗΣ ΕΡΓΑΣΙΑΣ

Η κάτωθι υπογεγραμμένη ΣΚΕΝΤΑΪ ΦΡΙΣΕΛΑ του ΑΛΦΡΕΝΤ, με αριθμό μητρώου 18387137 φοιτήτρια του Πανεπιστημίου Δυτικής Αττικής της Σχολής ΜΗΧΑΝΙΚΩΝ του Τμήματος ΗΛΕΚΤΡΟΛΟΓΩΝ ΚΑΙ ΗΛΕΚΤΡΟΝΙΚΩΝ ΜΗΧΑΝΙΚΩΝ,

δηλώνω υπεύθυνα ότι:

«Είμαι συγγραφέας αυτής της διπλωματικής εργασίας και ότι κάθε βοήθεια την οποία είχα για την προετοιμασία της είναι πλήρως αναγνωρισμένη και αναφέρεται στην εργασία. Επίσης, οι όποιες πηγές από τις οποίες έκανα χρήση δεδομένων, ιδεών ή λέξεων, είτε ακριβώς είτε παραφρασμένες, αναφέρονται στο σύνολό τους, με πλήρη αναφορά στους συγγραφείς, τον εκδοτικό οίκο ή το περιοδικό, συμπεριλαμβανομένων και των πηγών που ενδεχομένως χρησιμοποιήθηκαν από το διαδίκτυο. Επίσης, βεβαιώνω ότι αυτή η εργασία έχει συγγραφεί από μένα αποκλειστικά και αποτελεί προϊόν πνευματικής ιδιοκτησίας τόσο δικής μου, όσο και του Ιδρύματος.

Παράβαση της ανωτέρω ακαδημαϊκής μου ευθύνης αποτελεί ουσιώδη λόγο για την ανάκληση του διπλώματός μου.

Η Δηλούσα
ΣΚΕΝΤΑΪ ΦΡΙΣΕΛΑ



Ευχαριστίες

Η διπλωματική αυτή εργασία συνιστά έργο μιας συνολικής προσπάθειας αποτελούμενη από τη συλλογή πειραματικών μετρήσεων, καταγραφή των δεδομένων και χρόνο μελέτης.

Αρχικά, θα ήθελα να ευχαριστήσω τον καθηγητή κ. Γρηγόριο Καλτσά, για την αποδοχή στην εργαστηριακή του ομάδα, την σωστή επίβλεψη, καθοδήγηση και εμπιστοσύνη του, συμβάλλοντας να φέρω εις πέρας την συγκεκριμένη εργασία. Θα ήθελα επίσης, να ευχαριστήσω τα μέλη της εργαστηριακής ομάδας του *microSENSES Laboratory*, για τις πολύτιμες συμβουλές και την συνεργασία τους, καθ' όλη τη διάρκεια εκπόνησης της διπλωματικής μου εργασίας.

Τέλος, θα ήθελα να εκφράσω τις ευχαριστίες μου στους γονείς και φίλους μου, που πίστεψαν σε εμένα, προσφέροντας μου κουράγιο και στήριξη τα τελευταία χρόνια.

Σας ευχαριστώ θερμά όλους.

Με εκτίμηση,
Φρισέλα.

Περίληψη

Η ανάπτυξη των εύκαμπτων ηλεκτρονικών διατάξεων με τεχνολογία τυπωμένων ηλεκτρονικών, έχει λάβει τα τελευταία χρόνια ένα ευρύ ενδιαφέρον από επιστήμονες και ερευνητές. Η συγκεκριμένη εργασία επικεντρώνεται στους εύκαμπτους αισθητήρες, οι οποίοι κατασκευάζονται με τεχνολογίες εκτύπωσης, με εφαρμογές στο τομέα της βιοϊατρικής. Οι εύκαμπτοι αισθητήρες με εφαρμογές στη βιοϊατρική, είναι ιδανικοί για χρήση σε φορητές διατάξεις (wearables) και άλλες εφαρμογές, όπου η χρήση ενός παραδοσιακού αισθητήρα θα ήταν μη εφικτή. Ειδικότερα, στα πλαίσια της συγκεκριμένης εργασίας αναλύεται ο σχεδιασμός, η κατασκευή και ο χαρακτηρισμός, ενός εύκαμπτου αισθητήρα μέτρησης της θερμοκρασίας, για βιοϊατρικούς σκοπούς. Ο αισθητήρας αυτός κατασκευάστηκε με screen-printing τεχνολογία και βασικό του στοιχείο είναι τα θερμοχρωμικά (Thermochromic – TC) μελάνια, τα οποία μεταβάλλουν το χρώμα τους αναλόγως τη μεταβολή της θερμοκρασίας. Η δομή, το υλικό του υποστρώματος, οι ηλεκτρικές ιδιότητες συναρτήσει της θερμοκρασίας και η απόδοση, είναι οι παράγοντες που αναλύονται για την ανάπτυξη και αξιολόγηση του αισθητήρα. Αρχικός στόχος είναι η λήψη πειραματικών μετρήσεων για την συσχέτιση της αντίστασης με τη θερμοκρασία που αναπτύσσεται στη δομή. Η ευαισθησία του αισθητήρα, εξαρτάται κυρίως από τον θερμοκρασιακό συντελεστή (TCR), ο οποίος βρέθηκε πειραματικά ότι έχει αρνητική τιμή, γεγονός που συνεπάγεται μείωση της αντίστασης με την αύξηση της θερμοκρασίας (NTC). Στη συνέχεια, ακολούθησε η συσχέτιση του θερμικού πεδίου του αισθητήρα μέσω θερμικής (IR) κάμερας, με το οπτικό πεδίο μέσω φωτογραφίας. Η χρήση του εύκαμπτου αισθητήρα θερμοκρασίας επαληθεύεται με την ενσωμάτωσή του σε μια ηλεκτρονική διάταξη, βασιζόμενη στον ESP32-WROOM-32D, έναν διαιρέτη τάσης και μια γέφυρα Wheatstone. Ειδικότερα, ο μικροελεγκτής διαβάσει την αντίσταση του αισθητήρα, και χρησιμοποιεί τον θερμοκρασιακό συντελεστή του για να υπολογίσει τη θερμοκρασία, την οποία και καταγράφει. Ύστερα, τα καταγεγραμμένα δεδομένα εμφανίζονται στον χρήστη σε πραγματικό χρόνο, μέσω εφαρμογής στο διαδίκτυο, στο Arduino IoT, ή Bluetooth εφαρμογής στο κινητό. Με το τρόπο αυτό, διασφαλίζεται η διαρκής επικοινωνία του αισθητήρα με τον έξω κόσμο. Η διάταξη αυτή αποτελεί ένα ουσιαστικό βήμα για νέους τύπους εύκαμπτων αισθητήρων μέτρησης της θερμοκρασίας με εφαρμογές στην ιατρική και τις βιοϊατρικές επιστήμες.

Λέξεις – κλειδιά

βιοϊατρικές διατάξεις, εύκαμπτος αισθητήρας θερμοκρασίας, θερμοχρωμικά μελάνια, screen-printing, θερμοκρασιακός συντελεστής, ESP32 μικροελεγκτής, IoT, web server, Bluetooth

Abstract

The development of flexible electronic devices with printed electronics technology has recently attracted significant interest from scientists and researchers. This project focuses on the fabrication of flexible sensors, via printing technologies, with applications in medicine and biomedical engineering. Flexible biomedical sensors, make ideal use in wearable devices and other applications, where a traditional sensor would not be feasible. Specifically, in the context of this work, the primary focus lies in the design, fabrication and characterization of a flexible temperature sensor, implemented for biomedical applications. This sensor is fabricated with screen-printing technology and its main element is Thermochromic (TC) inks, which alter their color in response to temperature. Several critical parameters, including, the sensor's structure, the substrate material, the electrical, thermal-optical properties and overall performance, are evaluated to ensure the successful development of the sensor. The initial objective is to obtain experimental measurements to correlate the resistance with the temperature developed in the device. The sensitivity of the sensor mainly depends on the temperature coefficient of resistance (TCR), which was experimentally found to have a negative temperature coefficient (NTC), which implies a decrease in resistance in response to the increasing temperature. The analysis is followed by the correlation of the thermal field of the sensor through a thermal (IR) camera, with the optical field via photography. In combination with the fabricated sensor, an electronic setup based on the ESP32-WROOM-32D microcontroller, a voltage divider and a Wheatstone bridge, is also developed. In this setup, the microcontroller reads the resistance of the sensor and uses its temperature coefficient of resistance to calculate the detected temperature which then, logs it. The recorded data is then displayed in real-time to the user via a web server, IoT, or Bluetooth application. This device provides a solid foundation for the development of new types of flexible temperature sensors, holding significant promise both in the medical field and patient care.

Keywords

Biomedical devices, flexible sensor, thermochromic inks, temperature patch, screen-printing, temperature coefficient, ESP32 microcontroller, IoT, web server, Bluetooth

CONTENTS

List of Figures	10
List of Tables.....	21
List of Graphs	21
Alphabetic Index.....	23
INTRODUCTION	25
Diploma Thesis Subject.....	25
Methodology.....	25
Innovation	26
Structure.....	26
CHAPTER 1: Flexible Temperature Sensors in Biomedical Engineering	27
1.1 Introduction to Flexible Biomedical Sensors	27
1.1.1 Working Principles & Advances	28
1.1.2 Materials, Substrates, Printing Technologies, Curing & Sintering.....	33
1.2 Wearables & Wireless Biosensor Networks (WBSNs).....	51
1.2.1 Classification of Wearable Sensors &Types of Wearable Devices	53
1.2.2 Wireless Biosensor Networks (WBSNs)	60
1.2.3 Internet of Things (IoT), Apps for Data Representation & ESP32 Module	67
1.3 Flexible Temperature Sensors.....	72
1.3.1 Skin Temperature.....	74
1.3.2 Temperature & Resistance Correlation.....	76
1.3.3 Thermochromics	79
2 CHAPTER 2: Development of a Screen – Print Thermochromic Device for Temperature Sensing	82
2.1 Design of the Layout Masks	82
2.2 Implementation of the Screen – Printed Device and Materials	86
2.2.1 Materials and Equipment used for the Temperature Sensing Device	86
2.2.2 Screen – Printing Process & Optical Characterization	87
2.2.3 Optical Characterization of the Screen-Print Configurations	94
2.3 Electrical – Thermal Measurements	101
2.3.1 Temperature – Power/Area and Resistance – Temperature Graphs	101
2.3.2 Temperature Coefficient of Resistance.....	109
3 CHAPTER 3: Optical Temperature detection of the TC Device.....	111
3.1 Temperature Determination – Correlation of the Thermal and Optical Field	111
3.1.1 Measurements of the TC Device with the Thermal (IR) and a High-Resolution Camera.....	112
3.1.2 Data Processing & Correlation Graph of the Thermal and Optical Field of the TC device	113
4 CHAPTER 4: Final Printed Electronic Temperature Sensing Device – Wireless Communication	125
4.1 Electronic Setup of the Temperature Sensing Device.....	125
4.1.1 Electronic Setup Circuit Prototype Explanation	126
4.1.2 C++ Code Explanation for Skin-Temperature Detection	128
4.2 Wireless Communication.....	132
4.2.1 Web Server App.....	132
4.2.2 IoT App.....	135
4.2.3 Bluetooth App.....	137
4.3 Comparison of the Three Technologies (Web Server, IoT and Bluetooth App)	143
5 CONCLUSIONS – Future Work.....	145

6	FINAL REMARKS – Learning Outcomes	148
	References	149

List of Figures

CHAPTER 1: Flexible Temperature Sensors in Biomedical Engineering

Figure 1.1: Noninvasive continuous monitoring of health data with biomedical sensors [3].

Figure 1.2: A schematic overview of flexible biosensors including their: (a) benefits, (b) detection mechanisms, (c) detection targets, (d) potential areas of application [4].

Figure 1.3: Illustrative depiction of colorimetric sensors designed for smartphone integration [5].

Figure 1.4: Visual representation of a photoelectric colorimetric sensor integrated into a μ PAD for sweat assessment [6].

Figure 1.5: (a) Diagram illustrating a semi-transparent wearable pressure sensor (PLS) device, utilizing ECL as a light-emitting response to external triggers, (b) Captured photographs from the operational camera portraying the ECL-based PLS emitting red light, serving as: a tactile sensor integrated into wearables, (c) a sensor for human movements detection, and (d) a tool for pattern visualization generated by consistent external stimulations. The sensor works by emitting light in response to the stimulus, which can then be detected by a camera. This type of sensor is wearable and semitransparent, making it ideal for use in applications where a discreet sensor is required [8].

Figure 1.6: This platform consists of a flexible electrochemical sensing patch that is powered by a smartphone and detects Ca^{2+} and Cl^{-} ions in real time, and it is suitable for wearable and implantable applications [12].

Figure 1.7: A schematic and structural diagram of a conventional flexible electrochemical glucose sensor, with the schematic showing the sensor's overall design, and the structural diagram displaying the design of the working electrode (WE) [13].

Figure 1.8: A thorough evaluation of the capabilities and applications of flexible electrochemical sensing systems. The systems are a promising new technology for biomedical applications, in monitoring treat diseases. These adaptable and extensible electrochemical sensing setups encompass (a) sensor components, (b) power supplies, (c) electronic elements [14].

Figure 1.9: (a) Fluorescent sensor applications [15], (b) Explanation of the fluorescence mechanism through the Jablonski diagram [17].

Figure 1.10: The fundamental concept behind the implantable glucose-sensing system based on the CMOS principle, that involves the utilization of a responsive fluorescent hydrogel in reaction to glucose levels [16].

Figure 1.11: Structural designs and formations of Nanoparticle Network hydrogels (NNHs) [9].

Figure 1.12: (a) Basic schematic representations of the initial pH device employing WO_3 NPs as a sensing layer. This device switches between ON state ($I_D > 0$) and OFF state ($I_D = 0$) based on the oxidation-reduction states of the WO_3 , (b) a visual guide to the sensor's fabrication process, (c) the sensor's architecture, (d) a picture of the completed sensor [18].

Figure 1.13: (Left) A visual representation of the fabrication procedure of the Cu/CuNi flexible temperature sensor, including the substrate preparation, Aerosol Jet printing, and sintering steps,

(Right) A comprehensive overview of the printed flexible temperature sensor, with the schematic providing a technical overview and the photos providing a visual representation of the sensors [19].

Figure 1.14: Solid-State Nanomaterials utilized as sensing electrodes in biomedical sensors [1].

Figure 1.15: Schematic representation of carbon nanomaterials for 0D, 1D, 2D, or 3D structures [20].

Figure 1.16: Categorization of the Carbon Nanomaterials, explanation and industrial use [21].

Figure 1.17: Single – Walled CNT and Multi – Walled CNT Structures [21][24].

Figure 1.18: Carbon Dots (CDs) **(a)** Categories of CDs, GQDs, CNDs and Polymer Dots (PDs) [25], **(b)** CDs properties [26].

Figure 1.19: GO and rGO Structure, Properties, Functionality and Applications Schematic Representation [28][29].

Figure 1.20: **(a)** Visual optical characterization of metal nanoparticles, carbon-based nanomaterials, and hybrid nanocomposites, **(b)** Flowchart of the process for nano(bio)sensor fabrication that entails the integration of screen-print carbon-based nanomaterials, metal NPs, and, optionally, biological elements, followed by subsequent electrochemical analysis [23].

Figure 1.21: Schematic representation of: **(a)** Ionic Liquids, **(b)** Metal Liquids Applications [30][31].

Figure 1.22: A visual classification of the flexible substrates used in flexible biomedical sensors [32].

Figure 1.23: Correlation of the polyimide substrates durability in various temperatures [97].

Figure 1.24: Molecular Structure of (a) PET, (b) PEN [35].

Figure 1.25: A cohesive integration of temperature and capacitive gas sensors onto a bendable polyimide (PI) film [36].

Figure 1.26: Development of a flexible pH sensing platform utilizing a conductive PANI membrane for pH tracking **(a)** Schematic Representation, **(b)** Visual representation of a collection of the manufactured sensors, **(c)** Demonstrating the sensor's flexibility through bending at an angle of approximately 135° [37].

Figure 1.27: Introduction of an electrochemical impedimetric biosensor incorporating a nanostructured polycarbonate (PC) substrate: **(a)** Graphic representation **(b)** Visual representation various PC based biosensor samples [38].

Figure 1.28: An adaptable PDMS-based three-electrode sensor is introduced, where the WE is gold, the RE is silver, and the CE is gold [39].

Figure 1.29: Paper-based biomedical sensors sensing categories and functionalities for PoC Testing [40][42].

Figure 1.30: **(Left)** Visual representation of a biomedical sensor whose electrodes are printed onto glossy paper, **(Right)** Schematic of the glossy paper-based biosensor [43].

Figure 1.31: Electronic textiles (e-textiles) designed to facilitate wearable sensing and display applications [44].

Figure 1.32: Printing Technologies – Contact Printing & Non-Contact Printing Techniques [50].

Figure 1.33: (a) Schematic representation of the screen-printing technology, (b) Parameters that influence the resolution and outcome of the final screen-print structure [51].

Figure 1.34: A schematic flow and a step-by-step sequence detailing the production of flexible sensors through inkjet printing technology [45].

Figure 1.35: A comprehensive schematic illustration of flexible sensors fabrication through inkjet printing techniques [45].

Figure 1.36: Schematic Representation of the Coffee Ring Effect [56].

Figure 1.37: Sintering Techniques. (a) Thermal (b) Selective Laser (c) Electrical (d) Plasma (e) Chemical [45].

Figure 1.38: Visual representation flow of the Thermal Inkjet Printing process [58].

Figure 1.39: Piezoelectric Inkjet Printing Mechanism [45].

Figure 1.40: Visual Representation of the Electrostatic Inkjet Printing Mechanism [49].

Figure 1.41: Visual Representation of the Acoustic Inkjet Printing Mechanism [59].

Figure 1.42: Continuous Inkjet (CIJ) and Drop-on-Demand (DOD) modes [60].

Figure 1.43: Continuous Inkjet (CIJ) Mode Mechanism [61].

Figure 1.44: a) Drop-on-Demand (DoD) Mode Mechanism [63], b) High-Resolution Images of Inkjet Droplets in various stages of formation, expelled from a Drop-of-Demand Inkjet Mode [62].

Figure 1.45: Visual Representation of the Roll-to-Roll (R2R) Printing Technique [64].

Figure 1.46: Gravure and Flexographic R2R Printing Techniques [49].

Figure 1.47: (A-C) Graphical representations of the flexographic printing mechanism, (D) Inks used for flexographic printing, (E-F) Flexible device fabrication through flexographic printing [66].

Figure 1.48: Graphical representation of the Gravure Printing Mechanism [67].

Figure 1.49: Graphical representation of the Aerosol Jet Printing Mechanism [68].

Figure 1.50: Schematic illustration of the elements of a flexible wearable system [62].

Figure 1.51: a) Applications in wearable systems for continuous healthcare monitoring [72], b) Architecture of a flexible sensing system [77].

Figure 1.52: a) Illustration of an ECG patch onto the skin for continuous heart-rate monitoring [78], b) A visual representation of a screen-print flexible ECG sensor attached onto the chest for real-time ECG-related data analysis for arrhythmia management [79].

Figure 1.53: Visual representation of the surface EMG (sEMG) and invasive EMG [74].

Figure 1.54: Schematic representation of the applications and configurations of flexible wearable sensors in cardiovascular healthcare [80].

Figure 1.55: (a) Design and architecture of a flexible silicone elastomer heart beat wearable sensor (b) Visual representation of the set-up for heart beat monitoring [81].

Figure 1.56: Flexible wearable device on 0.125mm Kapton substrate for human respiration tracking [72].

Figure 1.57: Thermometer Flexible Patch System attached onto the body [82].

Figure 1.58: Schematic Diagram about glucose detection by non-invasive, minimal invasive and invasive means [83].

Figure 1.59: a) Sweat Collection Techniques [86], b) Visual representation of a skin patch electrochemical glucose sensor applied on wet skin [47].

Figure 1.60: a) Development of a home-testing glucose colorimetric sensor for saliva analysis, b) The shift from blue to pink on the membrane surface is an indication of hyperglycemia - The Ctrl represents plain human saliva, the S1 contains 15 mg/dL of 0.8 mM glucose concentration, and the S2 contains 30 mg/dL of 1.6 mM glucose concentration [87].

Figure 1.61: Schematic representation of a Tear Glucose Monitoring Sensor, via a 2D Photonic Crystal Hydrogel. The sensor efficiently exploits light diffraction, causing its structural color to shift progressively from red to green. This shift correlates with changes in glucose concentration spanning 0 to 20 mM, covering the physiological ranges observed in both tears and blood [88].

Figure 1.62: Schematic and visual representation of various of electrochemical sensors designed to analyze the levels of glucose, lactate, potassium, and sodium in sweat. This system is affixed to the wrist and integrates battery-operated electronics to capture digital signals and transmit them wirelessly via Bluetooth [90].

Figure 1.63: a) Presentation of a wearable sensor designed to detect wound-related biomarkers for wound healing monitoring process, b) Mapping of pH values during the wound healing process [91].

Figure 1.64: a) Visual representation of a completely wireless, battery-free biomedical e-tattoo with wireless energy harvesting techniques, securely attached onto the human body [95], b) Visual representation of a multi-purpose flexible wearable patch-type sensor (e-skin) on a PDMS substrate, attached around the wrist for visual reference [96].

Figure 1.65: Smart Clothing for remote monitoring biomedical applications [97].

Figure 1.66: a) Visual representation of an integrated microneedles sensor attached to the arm, b) Schematic Illustration and Assessment of the Microneedle-based Sensor for Multi-biomarkers [100].

Figure 1.67: Broad representation of a wearable biosensor patch for point-of-care (PoC) systems within the mIoT field [107].

Figure 1.68: Image representation of a smartphone-driven, battery-independent flexible electrochemical patch, equipped with NFC technology [12].

Figure 1.69: MCU function diagram [112].

Figure 1.70: Real-time data monitoring wearable sensors, incorporating microcontrollers: **a)** Visual Representation of a Heat-Patch System on the arm [203], **b)** Flexible oxygen monitoring sensor incorporated with an LMP91000 electronic setup [113], **c)** Electrochemical real-time blood monitoring with an integrated MCU platform [114], **d)** Hand gesture recognition device with an incorporated ARM Cortex M4 MCU for real-time data management [115].

Figure 1.71: Schematic Representation of Self-Powered Medical Sensors [119].

Figure 1.72: Wearable Biosensors capable of remote real-time health data monitoring [70].

Figure 1.73: **a)** Schematic representation of the interaction between the sensing device and the outside world via wireless communication technologies [104], **b)** Graphic representations comparing the wireless communication technologies [99].

Figure 1.74: Schematic Representation of the IoT-Cloud in remote healthcare monitoring [128].

Figure 1.75: IoT Components [121].

Figure 1.76: Schematic Illustration of an mIoT System [130].

Figure 1.77: Architecture of the ESP32 MCU [112].

Figure 1.78: **a)** Schematic Illustration and electronics components used for the development of the client-server model for vital body signs tracking [124], **b)** Diagram Flow of the iMedBox and visual representation of the prototype circuit [133].

Figure 1.79: ESP32-WROOM-32D Pinout [137][138].

Figure 1.80: Flexible Patch for Temperature Monitoring through the IoT, developed by NAMI [144].

Figure 1.81: **a)** Representation of the suggested structure for a Wireless Body Sensor Network (WBSN) based on FPGA technology, **b)** Diagram Flow of the overall FPGA-based system [101].

Figure 1.82: Wireless Detection Patch System for real-time Heart Rate (HR) and Body Temperature monitoring via BT communication: **a)** Flowchart of the Sensor Patch, **b)** Visual representation of the Detection Patch, **c)** Visual image of the sensor patch on the body, for real-time data display on the mobile phone [145].

Figure 1.83: Body Temperature variations across various body parts and different ambient conditions [150].

Figure 1.84: **a)** Circuit Diagram and visual representation of the wearable wireless sensor patch system, for real-time monitoring of the skin's temperature, pressure and humidity, powered by a polymer battery [158], **b)** Schematic and visual display of the wearable wrist device with BLE wireless communication capabilities for continuous identification gradual skin temperature changes, for infection identification [151], **c)** Visual representation of the flexible wireless sensor sheet that examines how the finger responds to thermoregulation and moisture changes [152].

Figure 1.85: Wheatstone Bridge [161].

Figure 1.86: NTC vs PTC vs RTDs Graph in response to temperature variations [163].

Figure 1.87: **a)** Schematic displaying the alterations in the synthesis of polydiacetylene (PDA) and **(b)** Visual representation of the shift in color of the PDA compounds, upon temperature fluctuations [164].

Figure 1.88: Photos A1 and B1 display the TLC probes (black arrows) at peak temperature, whereas A2 and B2 illustrate the corresponding skin burns. In particular, there are three distinct zones that correspond to specific areas on the TLC layer. Severe burns at temperatures >58 °C appear as black. Burns at TLC temperatures of 52 to 58°C exhibit blue tones, indicating hyperemia and edema. Skin areas at 50–52°C display light blue discoloration [167].

Figure 1.89: **a)** The design and choice of materials for the bio-inspired colorimetric sensor, **b)** Thermal and visual image analysis that captures the varying temperature and color alterations in the colorimetric sensor, and visual images showcasing the sensor's responses under different pressures, voltages, and temperatures [168].

Figure 1.90: **a)** Schematic representation of the thermotherapeutic device that merges stretchable strain sensors of three thermochromic dyes on micro-patterned PDMS surfaces, **b)** Visual and thermal image of the changes in temperature and color of the device that is attached onto the finger, while it is moving [169].

CHAPTER 2: Development of a Screen – Print Thermochromic Device for Temperature Sensing

Figure 2.1: **a)** L1 mask layout (first approach for designing the TC temperature sensor), **b)** L2 mask layout (second approach for designing the TC temperature sensor) **c)** L3 mask layout (third and final design of the TC temperature sensor).

Figure 2.2: **a)** Laser engraved gelatin mask for the carbon layer of the L1 layout, **b)** Laser engraved gelatin mask for the Ag layer of the L1 layout.

Figure 2.3: L2 layout Laser engraved gelatin mask for **a)** the Ag layer, **b)** the Carbon layer, **c)** the TC layer.

Figure 2.4: Mesh mask layout designs of the Carbon and TC structure: **a)** Carbon design, **b)** TC design, of the L2 layout.

Figure 2.5: Screen- printing inks: **a)** Metalon HPR-059, Novacentrix [176], **b)** Metalon HPS-FG77, Novacentrix [177] **c)** Thermochromic Screen Printing Ink Black 31°C, SFXC [171], **d)** Thermochromic Screen Printing Ink Black 47°C, SFXC [172], **e)** Thermochromic Screen Printing Ink Orange 28°C, SFXC [173].

Figure 2.6: Substrates: **a)** Polyethylene Terephthalate/PET, Goodfellow [178], **b)** Kapton® HN Film, Goodfellow [179], **c)** A4 paper.

Figure 2.7: Equipment: **a)** Heating & Dry Heat Sterilization Oven (NUVE FN400) [180], **b)** Screen Printing Semi-Automatic Machine (Ever-bright, S-200HFC) [181].

Figure 2.8: 1st and 2nd Layer (Carbon and Ag layer) of the L1 layout temperature sensor prototype, for the S1, S2, and S3 samples.

Figure 2.9: **a)** Laser-Engraved Gelatin Mask paper taped onto an 80T portrait mesh, for screen-printing the desired pattern of the L1 layout, **b)** Paper substrate secured onto the screen-printer's bed.

Figure 2.10: 1st, 2nd, and 3rd Layer (Carbon, Ag, TC layers) of the L2 layout temperature sensor prototype, for samples S1, S2, S3, S4, S5.

Figure 2.11: **a)** Laser-Engraved Gelatin Mask paper taped onto an 80T portrait mesh, for screen-printing the desired pattern of the L2 layout, **b)** Paper substrate secured onto the screen-printer's bed.

Figure 2.12: **a)** Screen-printing on paper substrate the 1st and 2nd Layer (Carbon and Ag inks) of the L2 layout configuration, **b)** Screen-printing on paper substrate the 3rd Layer (Black TC ink – 31 °C) of the L2 layout configuration.

Figure 2.13: **a)** Screen-printing on PET substrate the 1st and 2nd Layer (Carbon and Ag inks) of the L2 layout configuration, **b)** Screen-printing on PET substrate the 3rd Layer (Black TC ink – 31 °C) of the L2 layout configuration.

Figure 2.14: New Screen-Print Setup after the printing procedure (mesh mask, red squeegee, print on PET substrate).

Figure 2.15: Flexible Screen-Print black TC Structures with 31 °C activation temperatures on PET and Kapton substrates, based on the L3 mesh mask layout: **a)** S1a & S1b samples on PET substrate, **b)** S2a & S2b samples on Kapton substrate.

Figure 2.16: Flexible Screen-Print black TC Structures with 47 °C activation temperatures on PET and Kapton substrates, based on the L3 mesh mask layout: **a)** S3a & S3b samples on PET substrate, **b)** S4a & S4b samples on Kapton substrate.

Figure 2.17: OLYMPUS | MX Semiconductors – MX51 Microscope.

Figure 2.18: Visual representation of the: **a)** S1 sample, **b)** S2 sample, with the L1 layout configuration.

Figure 2.19: Optical Characterization of the S1 sample – L1 layout configuration, with detailed description.

Figure 2.20: Optical Characterization of the S2 sample – L1 layout configuration, with detailed description.

Figure 2.21: Visual representation of the: **a)** S2 sample utilizing the Black TC (47 °C), **b)** S3 sample, utilizing the Orange TC (28 °C) with the L2 layout configuration.

Figure 2.22: Optical Characterization of the S1 sample utilizing the Black TC (47 °C) – L2 layout configuration, with detailed description.

Figure 2.23: Optical Characterization of the S2 sample utilizing the Orange TC (28 °C) – L2 layout configuration, with detailed description.

Figure 2.24: Visual representation of the: **a)** S1 sample utilizing the Black TC (31 °C) on PET substrate, **b)** S2 sample, utilizing the Black TC (31 °C) on Kapton substrate, with the L3 layout configuration.

Figure 2.25: Visual representation of the: **a)** S3 sample utilizing the Black TC (47 °C) on PET substrate, **b)** S2 sample, utilizing the Black TC (47 °C) on Kapton substrate, with the L3 layout configuration.

Figure 2.26: Optical Characterization of the S1a and S1b samples utilizing the Black TC (31 °C), on PET surface – L3 layout configuration, with detailed description.

Figure 2.27: Optical Characterization of the S2a and S2b samples utilizing the Black TC (31 °C), on Kapton surface – L3 layout configuration, with detailed description.

Figure 2.28: Optical Characterization of the S3a and S3b samples utilizing the Black TC (47 °C), on PET surface – L3 layout configuration, with detailed description.

Figure 2.29: Optical Characterization of the S4a and S4b samples utilizing the Black TC (47 °C), on PET surface – L3 layout configuration, with detailed description.

Figure 2.30: Errors on S1b and S2a samples: **a)** Scratch within the black TC ink in the middle of the S1b sample, **b)** Hole on the left side of the S2a sample.

Figure 2.31: Errors on S3b and S4b samples, **a)** Deformity in the screen-printing outcome on the left upper corner of the Black TC ink of S3b sample, **b)** Voids on the right upper corner of the carbon ink structure of S4b sample.

Figure 2.32: Equipment used for the internal heating of the TC flexible structures: **a)** Keithley source-meter [174] and LabView Software, **b)** probe station with integrated hot-plate.

Figure 2.33: IR thermal cameras for thermal measurements: **a)** UNI-T PRO - UTI690B / Professional Thermal Imager [183], **b)** High precision Thermal IR Camera (FLIR SC655) [184].

Figure 2.34: Visual representation of the: **a)** S1 sample, **b)** S2 sample, **c)** S3 sample with the L1 layout configuration, onto the hot-plate for internal heating.

Figure 2.35: L1 layout configuration. This design is inappropriate for the heating of the TC element, as only a specific area of the carbon resistance is heated, when power is applied.

Figure 2.36: Visual representation of the: **a)** S1 sample (Black TC 31 °C), **b)** S2 sample (Black TC 47 °C), **c)** S3 sample (Orange TC 28 °C), with the L2 layout configuration, onto the hot-plate for internal heating.

Figure 2.37: Discoloration process of the S1 sample (Black TC 31 °C), with the application of various power rates.

Figure 2.38: Discoloration process of the S2 sample (Black TC 47 °C), with the application of various power rates.

Figure 2.39: Discoloration process of the S3 sample (Orange TC 28 °C), with the application of various power rates.

CHAPTER 3: Temperature Recognition via Photography of the TC Device

Figure 3.1: **a)** S3a Sample: Black TC with 47 °C activation temperature on PET Substrate, **b)** S4a Sample: Black TC with 47 °C activation temperature on Kapton Substrate.

Figure 3.2: Internal Heating phases of the S3a and S4a samples, on PET and Kapton substrates respectively: **a)** 50 °C, **b)** 60 °C, **c)** 70 °C.

Figure 3.3: Thermal & Optical Field Correlation Graph of the S3a sample with Gaussian Fittings for 50 °C temperature.

Figure 3.4: Thermal & Optical Field Correlation Graph of the S3a sample with Gaussian Fittings for 60 °C temperature.

Figure 3.5: Thermal & Optical Field Correlation Graph of the S3a sample with Gaussian Fittings for 70 °C temperature.

Figure 3.6: Thermal & Optical Field Correlation Graph of the S4a sample with Gaussian Fittings for 50 °C temperature.

Figure 3.7: Thermal & Optical Field Correlation Graph of the S3a sample with Gaussian Fittings for 60 °C temperature.

Figure 3.8: Thermal & Optical Field Correlation Graph of the S3a sample with Gaussian Fittings for 70 °C temperature.

Figure 3.9: Grayscale graph of the optical image for a sample with intermediate black ink layer between the Carbon resistance and TC element, to mitigate the exposure of the underlying carbon resistance.

Figure 3.10: Internal Heating phases of the S3a and S4a samples, on PET and Kapton substrates respectively: **a)** 40 °C, **b)** 43 °C, **c)** 46 °C, **d)** 49 °C, **e)** 52 °C.

Figure 3.11: Thermal & Optical Field Correlation Graph of the S3a sample with Gaussian Fittings for 40 °C temperature.

Figure 3.12: Thermal & Optical Field Correlation Graph of the S3a sample with Gaussian Fittings for 43 °C temperature.

Figure 3.13: Thermal & Optical Field Correlation Graph of the S3a sample with Gaussian Fittings for 46 °C temperature.

Figure 3.14: Thermal & Optical Field Correlation Graph of the S3a sample with Gaussian Fittings for 49 °C temperature.

Figure 3.15: Thermal & Optical Field Correlation Graph of the S3a sample with Gaussian Fittings for 40 °C temperature.

Figure 3.16: Thermal & Optical Field Correlation Graph of the S4a sample with Gaussian Fittings for 40 °C temperature.

Figure 3.17: Thermal & Optical Field Correlation Graph of the S4a sample with Gaussian Fittings for 43 °C temperature.

Figure 3.18: Thermal & Optical Field Correlation Graph of the S4a sample with Gaussian Fittings for 46 °C temperature.

Figure 3.19: Thermal & Optical Field Correlation Graph of the S4a sample with Gaussian Fittings for 49 °C temperature.

Figure 3.20: Thermal & Optical Field Correlation Graph of the S4a sample with Gaussian Fittings for 52 °C temperature.

CHAPTER 4: Final Printed Electronic Temperature Sensing Device – Wireless Communication

Figure 4.1: Electronic Components for Electronic Setup Prototype of the Temperature Sensing Device.

Figure 4.2: Electronic Setup Circuit prototype for accurately measuring the temperature acquired from the flexible TC-based temperature sensor.

Figure 4.3: Voltage Divider for the accurate measurement of the thermistor's resistance (R_{th}) [196].

Figure 4.4: Wheatstone Bridge used for accurately measuring the resistance of the flexible temperature sensor [198].

Figure 4.5: Global Variable Initialization and Explanation.

Figure 4.6: Variable Initialization and Explanation, in 'void setup()' function.

Figure 4.7: Ambient Temperature Estimation and Explanation, in 'void loop()' function.

Figure 4.8: Estimation and Explanation of the temperature by the flexible temperature sensor, in 'void loop()' function.

Figure 4.9: ESP32 ADC Non-Linear Graph [201].

Figure 4.10: Electronic setup with the flexible temperature sensor at an ambient temperature of 25 °C (Black TC 47 °C on Kapton substrate – L3 layout design).

Figure 4.11: Data displayed via a Web Server user interface: **a)** $a = 0.02755 + 0.00751 (k\Omega/^\circ C)$, **b)** $a = 0.02755 + 0.00101 (k\Omega/^\circ C)$.

Figure 4.12: Ambient temperature of 41 °C: **a)** Electronic setup with the flexible temperature sensor – transparency of the black TC element, **b)** Corresponding data displayed via a Web Server user interface.

Figure 4.13: Initial variables required for setting up the Wi-Fi connection and Web Server.

Figure 4.14: **a)** Wi-Fi network of the ESP32, with a protected password, **b)** Web server user interface, via the web browser.

Figure 4.15: HTML Content, the structure of the web content that gets retrieved from the HTTP response.

Figure 4.16: CSS Styling of the web content that gets retrieved from the HTTP response.

Figure 4.17: JavaScript code, for the logic of the web content that gets retrieved from the HTTP response.

Figure 4.18: Handlers for the routing of the web server.

Figure 4.19: Subscribe the SSID and Password the Wi-Fi library and set the handlers to valid paths for the web server.

Figure 4.20: a) IoT Desktop dashboard that displays live data of the ESP32, b) IoT mobile application dashboard that displays live data of the ESP32.

Figure 4.21: a) Cloud variables created in the Arduino Cloud Platform, b) Generated code comment ensuring developers that variables are automatically generated.

Figure 4.22: Arduino Cloud Platform – Connect to a Wi-Fi Network window.

Figure 4.23: Assigning the measurement values to the IoT variables initialized on the platform.

Figure 4.24: Bluetooth mobile application, first look and Bluetooth/Location permissions.

Figure 4.25: a) Bluetooth mobile application: a) list of discovered and connectable ESP32 devices, b) display of live data after successful Bluetooth pairing.

Figure 4.26: Required imports for the ESP32 code with Bluetooth.

Figure 4.27: Defined UUIDs for Service and Characteristics.

Figure 4.28: Defined pointers for the characteristics, which will later hold data values to be transmitted.

Figure 4.29: Initializing all the defined variables and enabling the device to work with BLE.

Figure 4.30: Passing the measurements into the initialized variables for the Characteristics pointers.

Figure 4.31: Defined UUIDs for the mobile application, in order to communicate with the ESP32.

Figure 4.32: Regulating permissions for the mobile application (Bluetooth & Location/GPS) .

Figure 4.33: Method for scanning BLE (ESP32) devices for the mobile application.

Figure 4.34: Method for ensuring no duplicate devices get added to the results of discovered devices in the mobile application.

Figure 4.35: Method for connecting and pairing with the selected BLE (ESP32) device.

Figure 4.36: Method for allowing transmission of the data from the BLE device (ESP32) to the mobile application via Characteristics.

Figure 4.37: Method for updating the mobile application values every time the BLE (ESP32) device's data changes.

Figure 4.38: Method for decoding the transmitted data into readable numeric (float) values.

List of Tables

CHAPTER 2: Development of a Screen – Print Thermo-chromic Device for Temperature Sensing

Table 2.1: Dimensions for each of the layout masks, correspondingly.

Table 2.2: Design Measurements vs Printed Measurements on the laser engraver of the L2 layout.

Table 2.3: Inks and Substrates and Equipment for TC structures' fabrication.

Table 2.4: Carbon – Ag – Paper L1 Layout Structure Information about the Screen-Printing Process.

Table 2.5: Carbon – Ag – TC – Paper L2 Layout Structure Information about the Screen-Printing Process.

Table 2.6: Flexible Screen-Print TC Structures with various activation temperatures.

Table 2.7: Data gained from the Internal Heating of S1, S2 and S3 Sample, respectively.

Table 2.8: Data gained from the Internal Heating of S1 Sample.

Table 2.9: Data gained from the Internal Heating of S2 Sample.

Table 2.10: Data gained from the Internal Heating of S3 Sample.

CHAPTER 3: Temperature Recognition via Photography of the TC Device

Table 3.1: Power applied to get the desired temperatures, for each of the two temperature range scenarios, respectively.

Table 3.2: Data gained from the Internal Heating of S3a and S4a Samples.

CHAPTER 4: Final Printed Electronic Temperature Sensing Device – Wireless Communication

Table 4.1: Electronic Components for Electronic Setup Prototype of the Temperature Sensing Device.

Table 4.2: Temperature-Resistance data of the NTC 10K B3950 thermistor, provided by the manufacturer [\[202\]](#).

List of Graphs

CHAPTER 2: Development of a Screen – Print Thermo-chromic Device for Temperature Sensing

Graph 2.1: Temperature – Power/Area (T-P/A) Graph for S1, S2 S3, samples - L2 Layout.

Graph 2.2: Resistance – Temperature (R-T) Graph for S1, S2 S3, samples - L2 Layout.

Graph 2.3: R-T Graph of the S2 sample, showing non-linearity and an unusual pattern.

Graph 2.4: Temperature – Power/Area (T-P/A) for the S1 (Black TC 31 °C), S2 (Black TC 47 °C) and S3 Samples (Orange TC 28 °C).

Graph 2.5: Resistance – Temperature (R-T) Graph for the S1 (Black TC 31 °C) and S3 Samples (Orange TC 28 °C).

Graph 2.6: Temperature – Power/Area (T-P/A) Graph for the S1 (Black TC 31 °C), S2 (Black TC 47 °C) and S3 Samples (Orange TC 28 °C) – Representation of the double resistance values of the S2 sample, in comparison to the S1 and S3 samples.

Graph 2.7: TCR ($\Delta R/R_0 - T$) Graph for samples S1 and S3 with the L1 layout configuration.

Graph 2.8: TCR ($\Delta R/R_0 - T$) Graph for samples S1 and S3 with the L2 layout configuration.

CHAPTER 3: Temperature Recognition via Photography of the TC Device

Graph 3.1: TCR ($\Delta R/R_0 - T$) Graphs: **a)** PTC behavior of S4a sample (Kapton substrate), **b)** NTC behavior of S3a sample (PET substrate).

Alphabetic Index

ADC: Analog-to-Digital Converter
AI: Artificial Intelligence
ANNs: Artificial Neural Networks
APs4: Access Points for 4G (or 4th Generation) Wireless Networks
BLE: Bluetooth Low Energy
BR/EDR: Basic Rate/Enhanced Data Rate (Bluetooth communication modes)
BT: Bluetooth (can also refer to Body Temperature, context-dependent)
CBTM: Continuous body Temperature Measurement
CDs: Carbon Dots
CE: Counter Electrode
CIJ: Continuous Inkjet Printing
CL: Chemiluminescence
CMOS: Complementary Metal-Oxide-Semiconductor
CNTs: Carbon Nanotubes
CPU: Central Processing Unit
CSS: Cascading Style Sheets
CTS: Compatibility Test Suit
DAC: Digital-to-Analog Converter
DoD: Drop-on-Demand
ECL: Electrochemiluminescence
ECG: Electrocardiography
EEG: Electroencephalography
EES: Epidermal Electronic Systems
EM: Electromagnetic
EMG: Electromyography
FE: Flexible Electronics
FPGAs: Field-Programmable Gate Arrays
GQDs: Graphene Quantum Dots
GPIO: General Purpose Input/Output
GNRs: Graphene Nanoribbons
GO: Graphene Oxide
HAL: Hardware Abstraction Layer
HFID: High-Frequency Identification
HTML: Hypertext Markup Language
HTTP: Hypertext Markup Language
IDE: Integrated Development Environment
IEEE: Institute of Electrical and Electronics Engineers
I2C: Inter-Integrated Circuit (communication protocol)
I2S: Inter-IC Sound (audio communication protocol)
IP: Internet Protocol
IPV4: Internet Protocol Version 4
IPV6: Internet Protocol Version 6
IPX: Internetwork Packet Exchange
IR: Infrared
ISM: Industrial, Scientific, and Medical (radio frequency bands)

JSON: JavaScript Object Notation (data interchange format)

LFID: JavaScript Object Notation (data interchange format)

MCU: Microcontroller Unit

MEMS: Micro-Electro-Mechanical Systems

MWCNTs: Multi-Walled Carbon Nanotubes

mIoT: Medical Internet of Things

NFC: Near Field Communication

NPs: Nanoparticles

OS: Operating System

PAN: Personal Area Network

PANI: Polyaniline

PDA: Polydiacetylene

PDMS: Polydimethylsiloxane

PET: Polyethylene Terephthalate

PEN: Polyethylene Naphthalate

PI: polyimide

PoC: Point-of-Care

PFCs: Printed Flexible Circuits

PTC: Positive Temperature Coefficient

PU: Polyurethane

PWM: Pulse Width Modulation

R2R: Roll-to-Roll Printing

RF: Radio Frequency

RFID: Radio Frequency

RPM: Remote Patient Monitoring

RTC: Real-Time Clock

RTDs: Resistance Temperature Detectors

rGO: Reduced Graphene Oxide

SD: Secure Digital

sEMG: Surface Electromyography

SPI: Serial Peripheral Interface

SRAM: Static Random-Access Memory

SSID: Service Set Identifier

STA: Station (in wireless networking)

TFTs: Thin-Film Transistors

TC: Thermochromic

TCR: Temperature Coefficient of Resistance

TLC: Thermochromic Liquid Crystal

UART: Universal Asynchronous Receiver/Transmitter

URL: Uniform Resource Locator

UUID: Universally Unique Identifier

WBSNs: Wireless Body Sensor Networks

WE: Working Electrode

WMMMS: Wearable Mobile Medical Monitoring Systems

WSNs: Wireless Sensor Networks

XML: Extensible Markup Language

INTRODUCTION

Flexible printed electronics are a rapidly growing field of technology with the potential to revolutionize the biomedical industry. They consist of printing electronic components, onto flexible substrates. Their fabrication is achieved through printing technologies including screen-printing and inkjet printing. These technologies, are ideal candidates for mass production, due to their cost-effectiveness and scalable characteristics. The combination of printed biomedical devices, with the field of IoT and wireless communication protocols including Wi-Fi or Bluetooth apps, can be used for real-time monitoring and display of health-related data, providing both doctors and patients, valuable insights into the patient's health. One of the most promising applications of flexible printed electronics for biomedical applications, is in skin temperature measurement, encompassing areas like fever, inflammation, skin cancer, and heat stroke. This convergence of technologies holds significant promise for flexible wearable bio-devices, advancing both in the medical field and patient care.

Diploma Thesis Subject

This project presents the development of a thermochromic-based flexible screen-print device for biomedical applications. Thermochromic (TC) inks are inks that change color in response to temperature, making them suitable for implementing flexible printed electronic devices, that can visualize skin temperature. The layout design, substrate material, and electrical properties of the sensor are analyzed to ensure its correct functionality, along with the Temperature Coefficient of Resistance (TCR), determined from the resistance-temperature graphs. Additionally, the temperature recognition of the flexible sensor, via photography is also analyzed. Furthermore, the implementation of an electronic setup with an ESP32 microcontroller, a voltage divider and a Wheatstone bridge, is achieved. This configuration calculates the temperature data obtained from the sensor and then logs it and displays it to the user via a web server, IoT, or Bluetooth application.

The device has the potential to be used for a variety of biomedical applications, such as skin temperature monitoring or heat stroke estimation, useful for athletes or people who work in warm environments. It can also be used as a wearable sensor, that tracks a person's exposure to the sun and alerts them for any sunburn indications and sun-related injuries. Further development of the sensor can be accomplished by adding skin conductivity measurements via hydrochromic inks, which alter their color in response to moisture. This would make the device even more versatile and useful for a variety of biomedical applications.

Methodology

The thermochromic-based flexible device for temperature detection, involves a two-step screen-printing process. Initially, the carbon ink is screen-print onto a flexible substrate, with the carbon element serving as a resistance for the internal heating of the TC element. In the second step, the TC element is printed on top of the carbon layer. The aim of this project is to assess the device's temperature response. This evaluation is achieved through:

- a LabView program, used to control the power input to the thermochromic device and log the output data,
- the Keithley 2612 source-meter to provide the power input to the thermochromic device,
- and an IR thermal camera to estimate the temperature of the thermochromic device.

The graphs generated from these data, give an estimation of the device's temperature coefficient of resistance (TCR).

The temperature recognition via photography, of the TC flexible temperature sensor, is achieved by capturing pictures with a thermal (IR) camera and a high-resolution camera, at different temperatures. These pictures are converted into matrixes, through the OriginPro and ImageJ software and are processed accordingly to create the correlation graphs of the thermal and optical fields.

The electronic circuit setup relies on the ESP32-WROOM-32D as its central component. This microcontroller unit (MCU), along with a Wheatstone bridge, and a voltage divider, serve as the foundation of the system, for precise temperature calculations obtained from the flexible temperature sensor. This MCU also incorporates wireless communication protocols, allowing the design and implementation of Wi-Fi, IoT, and Bluetooth applications. Through these applications, the temperature data can be continuously monitored and wirelessly displayed onto a screen.

Innovation

This sensor can be used for skin temperature monitoring, which can be a sign of a variety of health conditions, including skin cancer, heat stroke and sunburns. Additionally, it can be used as a smart-label for food products, indicating their temperature reading. The screen-printing technology provides a low-cost, environmentally friendly and scalable manufacturing process, for flexible devices.

The correlation of the thermal field obtained by an IR camera and the optical field gained from a high-resolution camera, builds a more accurate and comprehensive picture of the patient's thermal profile. In particular, the data from these two sources can be combined to establish a thermal map of the skin, and identify the areas that are warmer or cooler than normal, indicating a sign of a variety of health conditions.

Due to the device's small size and connectivity with mobile gadgets, it can be considered as a temperature patch that allows patients to track their temperature over time and remotely share the data with their doctors, avoiding prolonged hospital stays.

Structure

This project consists of four (4) chapters. Chapter 1 provides a literature review on flexible sensors, their applications in biomedical engineering, relevant printing technologies, commonly employed inks and substrates, the wireless communication technologies of a wearable device or sensor with the outside world, and concludes with a review on body and skin temperature, flexible temperature sensors, the correlation between the resistance and temperature, and thermochromic inks. Chapter 2 delves into the fabrication of the thermochromic temperature sensing system, providing insights on the materials and equipment used, as well as an in-depth assessment of the collected data and graphs. Chapter 3 explores the correlation between the thermal and optical field of the developed device, in order to achieve its temperature recognition, via photography. Chapter 4 focuses on the electronic setup of the temperature sensing device that tags and logs the temperature data. It also explains the programming behind the accurate determination of the detected temperature, as well as the programming of the web server, IoT, and Bluetooth applications, all designed for displaying the temperature data on both mobile and desktop devices. A comparison of these three technologies, is also provided in this chapter.

1 CHAPTER 1:

Flexible Temperature Sensors in Biomedical Engineering

This chapter centers around the advancements of innovative flexible biomedical sensors and their potential impact on future healthcare applications. Flexible biosensors offer various benefits, including miniature size, portability, real-time monitoring, and high performance. The printing technologies, as well as the materials used for the construction of these devices, are also analyzed. Furthermore, the chapter discusses about wearable flexible biosensors that result from the incorporation of electronics, microcontrollers, the Internet of Things (IoT), the Wi-Fi and Bluetooth wireless communication applications. This integration constitutes to the development of low-energy and environmentally-friendly flexible wearable devices, such as smart sensor tags, that enable real-time monitoring and display of various health parameters including blood flow, heart rate, oxygen level, skin temperature and skin conductivity. Moreover, a significant portion of this chapter is dedicated to flexible self-powered skin temperature sensors that incorporate thermochromic (TC) materials. The integration of TC materials, which alter their color in response to temperature, simplifies the fabrication of temperature sensing skin-patch wearable sensors, by eliminating the need for external detection systems. Overall, this exploration of flexible wearable biosensors along with diverse applications, demonstrates their promising role in advancing healthcare and biotechnology.

1.1 Introduction to Flexible Biomedical Sensors

The development of flexible biomedical sensors is a rapidly growing domain with the potential to further advance modern science and technology, revolutionizing both high-performance electronics and medical devices [1]. Flexible biosensors can obtain the shape of any (curved) surface to be sensed, within the human skin and body, without major alterations in their characteristics (Fig. 1.1). Consequently, their non-invasive nature eliminates the need for expensive painful procedures, constituting health monitoring more comfortable and accessible for individuals. Flexible biomedical sensors are made from organic materials, which offer a set of advantages over traditional sensors, including flexibility, simple fabrication, low cost, quick response, adaptability and accurate data. To enhance the accuracy of these sensors, a powerful approach is to enhance the sensing area and resolution, through miniaturization. At the micro- and nanoscale, the sensor's surface area is maximized, implementing more sites for analyte molecules to bind and produce measurable signals. Especially in medical diagnostics and applications – where detecting minute quantities of analytes is crucial – this increased sensitivity is especially beneficial [2].



Figure 1.1: Non-intrusive continuous monitoring of health data with biomedical sensors [3].

A biosensor consists of a detection device and a biocatalyst, working together to convert biological events into measurable parameters [1]. In flexible biomedical sensors, physical entities are detected, and their electrical behavior undergoes changes, converting them into readable data [3].

Despite the significant progress made in flexible sensors and devices, as well as their promising advances, there are still constraints and ongoing progress, to be discussed in this relatively new field.

- One of the key areas requiring attention is the flexible sensors' fabrication, and incorporation, that constitute an enhanced and specific sensing efficiency.
- Additionally, most studies have focused on detectors with a solo operation, making them capable of detecting only specific functions, such as pressure, temperature, conductivity, etc. Therefore, researchers and engineers need to explore novel design concepts and fabrication techniques to implement flexible sensors that offer diverse sensing operations. The integration of various sensing principles into a single flexible sensing platform could enhance its adaptability and applicability across different scenarios.
- The collaboration between experts in different fields, such as material technology, electronics, and biology, is essential to drive innovation and design truly versatile and high-performance flexible sensors. By addressing these challenges, flexible biomedical sensors can revolutionize in the healthcare industry.

1.1.1 Working Principles & Advances

Flexible sensors operate based on various working principles, and among the mainstream sensing strategies for flexible biosensors, several have been extensively explored and proven effective. These strategies include colorimetric detection, fluorescence, (electro)chemiluminescence, nanoparticle (NP) sensing, and electrochemical sensing (Fig. 1.2).

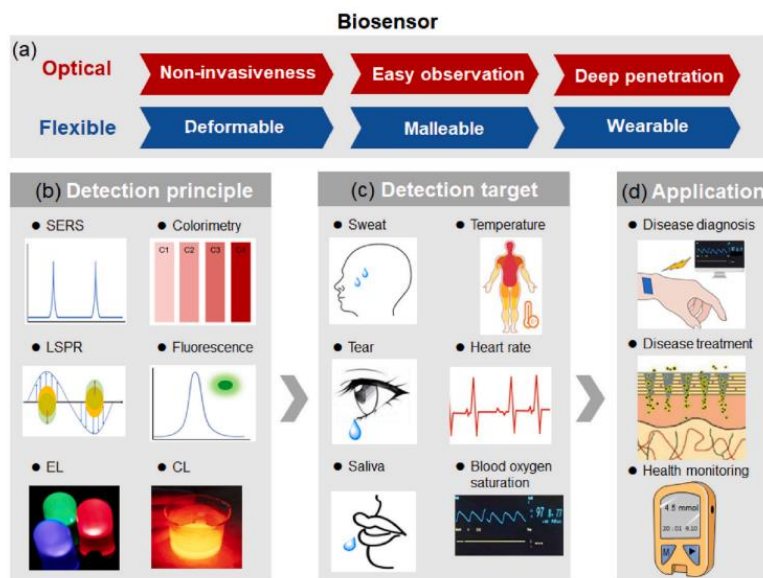


Figure 1.2: A schematic overview of flexible biosensors including their: (a) benefits, (b) detection mechanisms, (c) detection targets, (d) potential areas of application [4].

▪ **Colorimetric Detection**

Colorimetric biosensors, function according to the chromogenic reaction of colored elements and are widely utilized for detecting analytes. The process involves the implementation of hydrophilic channels on a flexible substrate, separated by hydrophobic lines, to direct the flow of the sample. As the sample travels through the channels and interacts with the reagents, a color change occurs, which corresponds to the analyte’s concentration [2]. This straightforward and visually accessible method finds applications in diverse fields, such as biomedicine, environmental monitoring, among others. Recently, wearable flexible colorimetric biosensors, have gained traction for detecting biological fluids like blood, sweat, saliva, and tears (Fig. 1.3), as well as physiological parameters like skin or body temperature and pressure. [5].

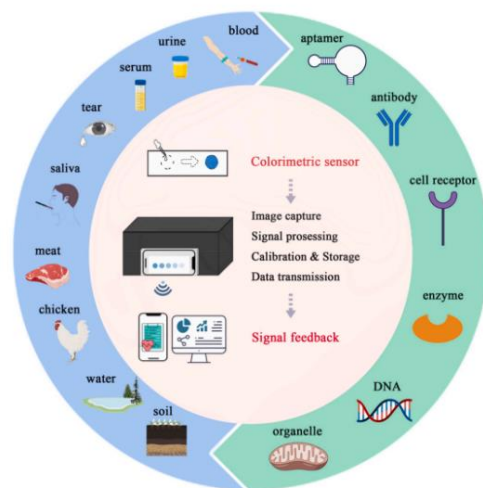


Figure 1.3: Illustrative depiction of colorimetric sensors designed for smartphone integration [5].

Nonetheless, traditional colorimetric methods may lack precision, necessitating the exploration of more advanced data extraction techniques [4]. To enhance precision in colorimetric measurements, researchers are turning to advanced techniques, including machine learning algorithms and smartphone-assisted calibration, especially in paper-based analytical devices (μ Pads) [6] (Fig. 1.4). As technology continues to progress, colorimetric flexible biosensors have the potential to transform the landscape of personalized healthcare, facilitating continuous monitoring and early detection of various health conditions. Moreover, the ease of use and portability of smartphone-based colorimetric biosensors, offers a promising pathway towards accessible and cost-effective medical diagnostics, benefiting individuals and communities worldwide.

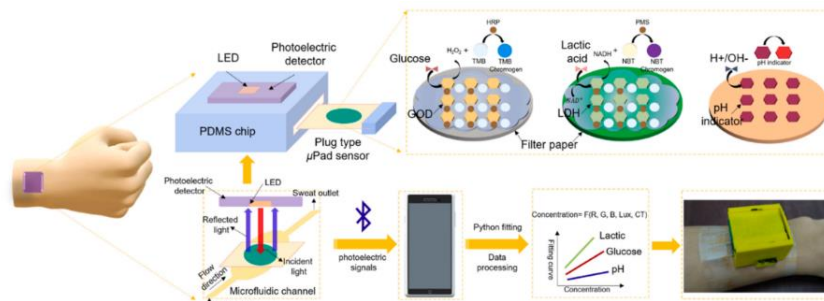


Figure 1.4: Visual representation of a photoelectric colorimetric sensor integrated into a μ PAD for sweat assessment [6]

▪ Chemiluminescence & Electrochemiluminescence Detection

Chemiluminescence (CL), as a detection principle, involves observing radiation during a chemical reaction and quantify biological targets, without the need for bulky or expensive equipment [2]. This approach, basically implicates a light-emitting chemical reaction, that does not require an external energy source. Microfluidics technology is used for improving the function of CL sensors, by providing a controlled environment for the reaction, while increasing the surface area for the reaction to occur. This novel concept has initiated the evolution of CL sensors used for biological targets detection, in very small volumes of sample, such as sweat, saliva and tears, for glucose and blood levels non-invasive continuous monitoring [7].

Electrochemiluminescence (ECL), is a fascinating technique that incorporates the emission of light through a chemical reaction, driven by an exergonic electron transfer reaction, making it an ideal candidate for next-generation wearable tactile sensors, due to its low operation voltage requirements and the ability to use electrodes, without any limitations. [8]. This technology's exceptional sensitivity and accuracy in detecting specific substances or analytes, has paved the way for research and practical applications [1]. For example, Kwon and Myoung, developed a semi-transparent wearable ECL pressure sensor (PLS), integrating visual alarm functions to prevent harm from external stimuli (Fig. 1.5) [8].

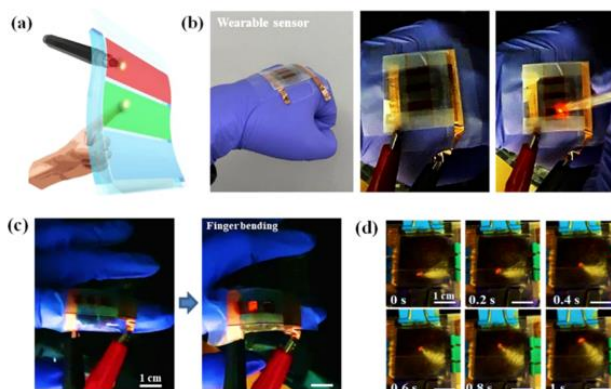


Figure 1.5: (a) Diagram illustrating a semi-transparent wearable pressure sensor (PLS) device, utilizing ECL as a light-emitting response to external triggers. (b) Captured photographs from the operational camera portraying the ECL-based PLS emitting red light, serving as: a tactile sensor integrated into wearables, (c) a sensor for human movements detection, and (d) a tool for pattern visualization generated by consistent external stimulations. The sensor works by emitting light in response to the stimulus, which can then be detected by a camera. This type of sensor is wearable and semitransparent, making it ideal for use in applications where a discreet sensor is required [8].

▪ Electrochemical Sensing

Electrochemical sensors are specialized devices that detect specific chemical substances, by converting binding reactions into measurable electrical signals [9]. These sensors have gained popularity for their ease of use, rapid response, and potential to provide crucial information about the human body [10]. Noble metal nanoparticles (NPs), including Au, Ag, Pt, Pd, and Cu, have gained significant attention in the field of electrochemical glucose sensing, offering advantages such as rapid charge transfer, great electrocatalysis, low toxicity, and excellent biocompatibility [11]. Furthermore, the integration of the electrochemical sensing into smartphones has emerged as a convenient and accessible platform for point-of-care (PoC) diagnostics (Fig. 1.6) [12].

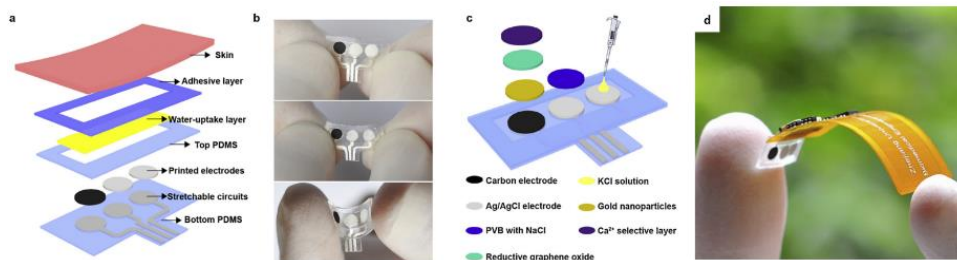


Figure 1.6: This platform consists of a flexible electrochemical sensing patch that is powered by a smartphone and detects Ca^{2+} and Cl^{-} ions in real time, and it is suitable for wearable and implantable applications [12].

Electrochemical sensors consist of three electrodes: (Fig. 1.7) [2].

1. Working Electrode (WE); catalyzes the reaction with the analyte of interest
2. Reference Electrode (RE); maintains a stable potential during the process
3. Counter Electrode (CE); determines the concentration of the analyte, through the current flow between the WE and CE.

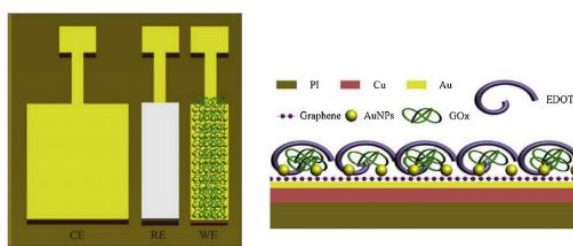


Figure 1.7: A schematic and structural diagram of a conventional flexible electrochemical glucose sensor, with the schematic showing the sensor's overall design, and the structural diagram displaying the design of the working electrode (WE) [13].

Overall, flexible electrochemical sensors are nowadays a considerable advancement with applications in numerous fields, including wearable health monitoring devices and human-machine interfaces, due to their better interfacing capabilities with the human skin, and its biological tissues (Fig. 1.8) [14].

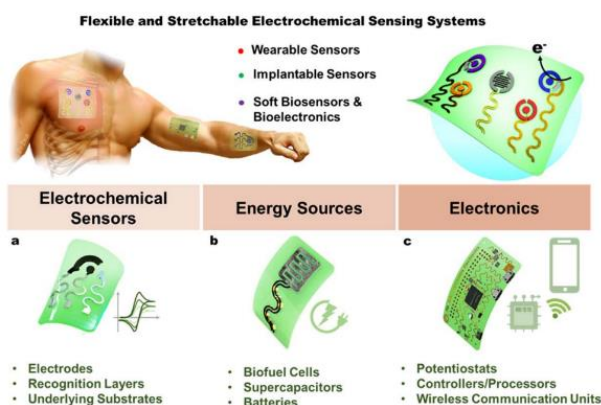


Figure 1.8: A thorough evaluation of the capabilities and applications of flexible electrochemical sensing systems. The systems are a promising new technology for biomedical applications, in monitoring treat diseases. These adaptable and extensible electrochemical sensing setups encompass (a) sensor components, (b) power supplies, (c) electronic elements [14].

▪ **Fluorescence Sensing**

Fluorescent sensors have gained remarkable interest across various fields, such as analytical, environmental and pharmaceutical analysis. Its sensing operation, is based on radiative emission from a fluorophore, after excitation at a specific shorter wavelength, offering a safe and cost-effective alternative to radioactive tracers. This mechanism and its applications can be better understood via

the Jablonski diagram (Fig. 1.9b) [2][15]. In addition to their analytical applications, fluorescent sensors have found extensive use in biology and medicine, through their high analytical sensitivity and selectivity to identify organic and inorganic materials (Fig. 1.9a) [15]. One notable application involves a glucose monitoring device implanted to the body, incorporating a Complementary Metal-Oxide-Semiconductor (CMOS) image sensor onto the skin, that utilizes a fluorescent hydrogel, as a mediator (Fig. 1.10) [16]. Through continuous research and advancements, fluorescent sensors are expected to play a vital role in various scientific and medical fields, further enhancing their importance in modern technology and diagnostics.

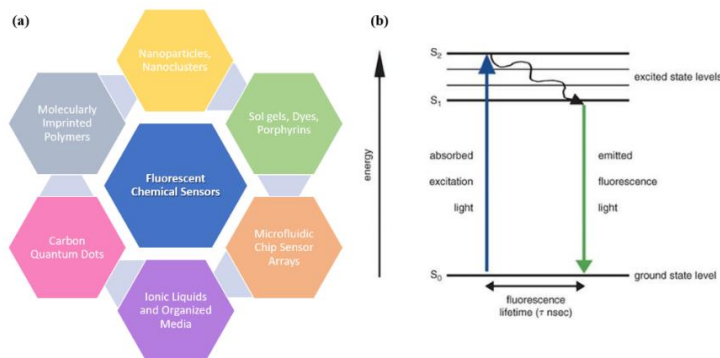


Figure 1.9: (a) Fluorescent sensor applications [15], (b) Explanation of the fluorescence mechanism through the Jablonski diagram [17].

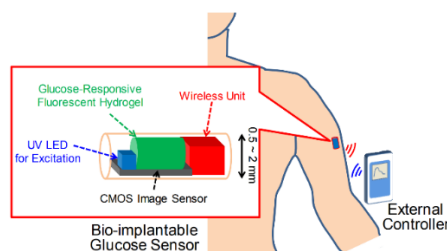


Figure 1.10: The fundamental concept behind the implantable glucose-sensing system based on the CMOS principle, that involves the utilization of a responsive fluorescent hydrogel in reaction to glucose levels [16].

▪ Nanoparticle (NP) Sensing

Recently, the adoption of nanoparticles (NPs) in biosensing has grown exponentially, owing to their compact size, chemistry and wide surface for detection. NPs, such as nanowires, and nanotubes, reveal excellent electrical, chemical, and physical properties, making them ideal candidates for various sensing applications. Furthermore, surface adjustments, doping, and nanoparticle-infused composites, strengthen their binding capabilities, enhancing their effectiveness in detecting specific biomolecules. When these biomolecules interact with target analytes, changes in the properties of the sensor occur, allowing for the detection of the analyte of interest [2]. For example, Nanoparticle network hydrogels (NNHs) offer exciting potential as new functional materials, leveraging the favorable properties of hydrogels and nanoparticles (Fig. 1.11) [9].

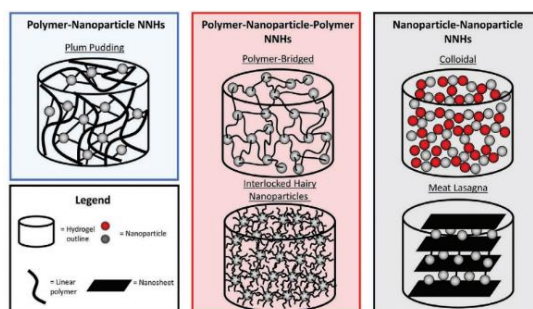


Figure 1.11: Structural designs and formations of Nanoparticle Network hydrogels (NNHs) [9].

Certain developments have been explored, regarding NP-based biomedical sensors. Among these, is the metal/metal oxide-based pH sensors, crucial for monitoring physiological parameters in disease diagnosis, treatment, and other biological processes, particularly those using WO_3 NPs (Fig. 1.12). [18]. Additionally, flexible and deformable Cu–CuNi temperature sensors and 3D cellular sensor arrays (Fig. 1.13), demonstrate high performance and can withstand bending and twisting without compromising functionality [19], opening up new possibilities for soft robotics, and biometric sensing.

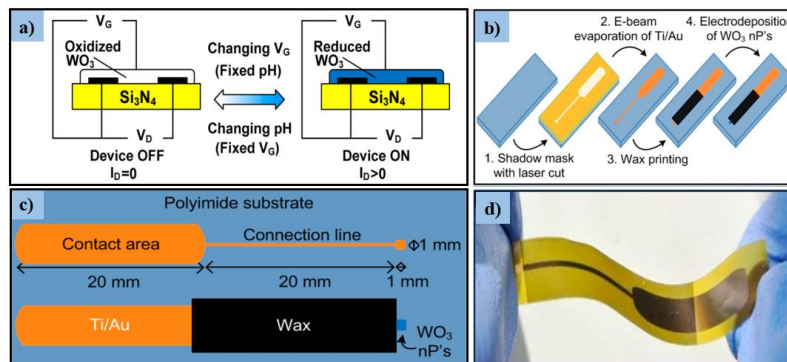


Figure 1.12: (a) Basic schematic representations of the initial pH device employing WO_3 NPs as a sensing layer. This device switches between ON state ($I_D > 0$) and OFF state ($I_D = 0$) based on the oxidation-reduction states of the WO_3 , (b) a visual guide to the sensor's fabrication process, (c) the sensor's architecture, (d) a picture of the completed sensor [18].

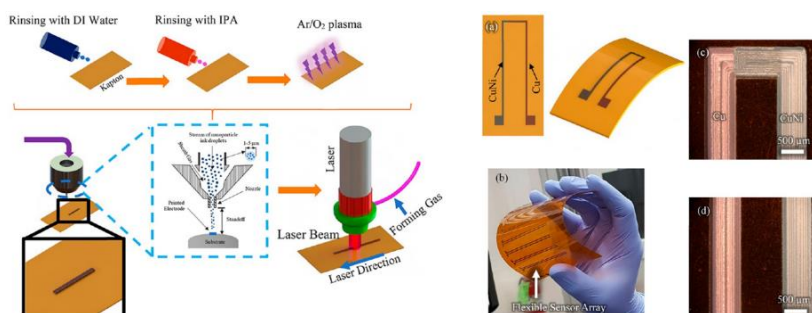


Figure 1.13: (Left) A visual representation of the fabrication procedure of the Cu/CuNi flexible temperature sensor, including the substrate preparation, Aerosol Jet printing, and sintering steps, (Right) A comprehensive overview of the printed flexible temperature sensor, with the schematic providing a technical overview and the photos providing a visual representation of the sensors [19].

1.1.2 Materials, Substrates, Printing Technologies, Curing & Sintering

The rapid development of flexible and wearable sensors, necessitates advancements in the exploration of new materials and fabrication techniques. The conventional photolithography fabrication, leads to alternative manufacturing methods. In particular, printed electronics, have emerged as a prominent manufacturing technique for flexible sensing platforms. This approach utilizes printing techniques with conductive inks, enabling their uniform deposition on polymeric substrates, and subsequent curing at high temperatures and/or sintering.

1.1.2.1 Materials

In biosensors, electrodes are a crucial parameter, as they must meet specific criteria for optimal performance, like compact size and heightened sensitivity to particular substances. Essentially, they act as a bridge between the biological recognition element (enzymes or antibodies) and the electronic system, by converting biological responses into measurable electrical signals [1]. Consequently, researchers have explored various materials for biosensor electrode fabrication, each with its own set

of advantages and limitations. The sensing material stands out as one of the most critical components of any sensor, intricately imprinted on flexible templates with electrical connections, facilitated by the electrodes. Based on the changes that the sensing material may face; flexible sensors are divided into solid-state and liquid-state sensing devices [3].

a) Solid-State Materials

In recent years, significant strides have been noted in engineering flexible and wearable solid-state sensors, capable of high mechanical distortion and convenience. Solid-state sensors employ solid active sensing elements from highly conductive, stretchable, and fine nanomaterials including polymers, carbon, semiconductors, and metals [3]. In particular, nanomaterials like polymer nanofibers, silver and gold NPs, carbon nanotubes (CNTs), and graphene, have been widely employed in designing flexible conductors (Fig. 1.14), due to their distinct physical quality.

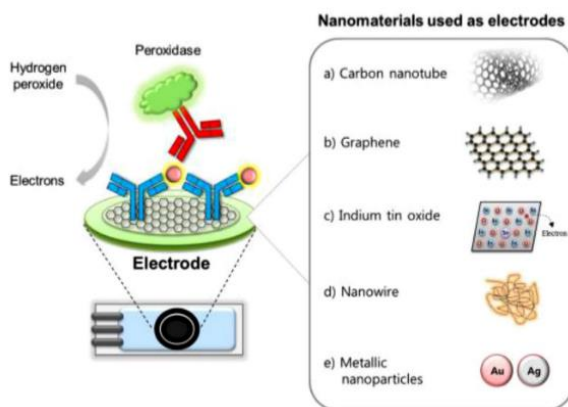


Figure 1.14: Solid-State Nanomaterials utilized as sensing electrodes in biomedical sensors [1].

Carbon Nanomaterials and Carbon Nanotubes

Carbon nanomaterials, carbon nanotubes (CNTs), carbon dots, and graphene have gathered significant attention as sensing electrodes in flexible biomedical sensors, for their remarkable properties, including outstanding electrical conductivity, and sturdy thermal and electrochemical stability [1]. They offer great advantages by enhancing the available surface area, leading to a substantial improvement in sensitivity and resolution. Additionally, as versatile tools in various scientific domains, carbon nanomaterials can act as a multi-functional platform (Fig. 1.15), or as highly active chemical reaction sites, promoting catalysis, and facilitating complex chemical transformations with remarkable efficiency and selectivity [2]. Their controllable and biocompatible attributes, make them suitable for enzyme sensors, offering significant potential in the domain of medicine (Fig. 1.16).

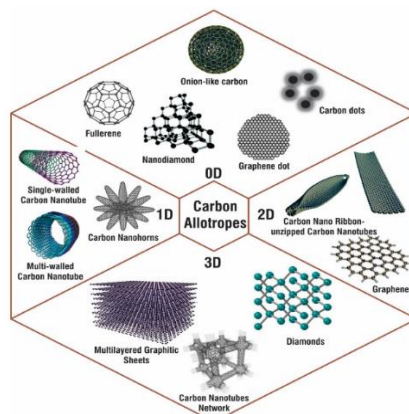


Figure 1.15: Schematic representation of carbon nanomaterials for 0D, 1D, 2D, or 3D structures [20].

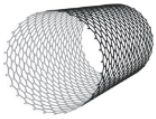
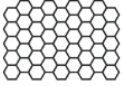
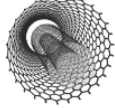
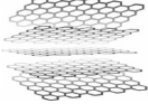

Single-walled carbon nanotubes (SWCNTs), also called graphene nanotubes (GNTs)	Graphene	Multi-walled carbon nanotubes (MWCNTs)	Nanographite structures (incl. few-layer "graphene", graphene flakes (graphene nanoplatelets), graphene oxide (GO), reduced graphene oxide (RGO) and others)	Graphite structures (incl. carbon black)
				
A graphene layer seamlessly rolled into a tube	A single sheet or monolayer of carbon atoms tightly bound in a hexagonal honeycomb lattice	A concentric arrangement of SWCNTs, i.e. multiple layers of graphene seamlessly rolled into a concentric tubular structure	Graphene flakes are small platelets of graphite; GO/RGO are few-layer nanoscale graphites, have oxygen groups or have undergone additional reduction	A large set of multiple graphene sheets
Industrial-scale production (hundreds of tonnes)	Not designed as an additive to materials (production in kgs)	Industrial-scale production (thousands of tonnes)	Industrial-scale production (thousands of tonnes)	Industrial-scale production (millions of tonnes)

Figure 1.16: Categorization of the Carbon Nanomaterials, explanation and industrial use [21].

CNTs can be divided into single-walled CNTs (SWCNTs) and multi-walled CNTs (MWCNTs), according to the amount of graphene layers they consist of (Fig. 1.17) [22]. Carbon dots (CDs) and graphene quantum dots (GQDs), possess unique structures with diameters less than 10 nm (Fig. 1.18). Specifically, carbon dots and graphene quantum dots find applications in flexible biomedical sensors, including electrochemical sensing and electrocatalysis. GQDs, in particular, are often preferred for (bio)sensing applications due to their quantum confinement and superior electrical and thermal conductivity [23].

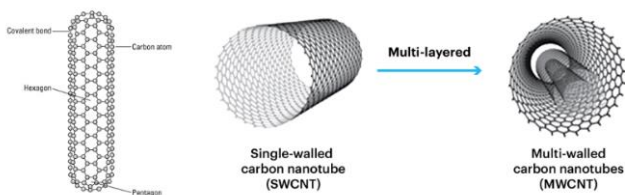


Figure 1.17: Single – Walled CNT and Multi – Walled CNT Structures [21][24].

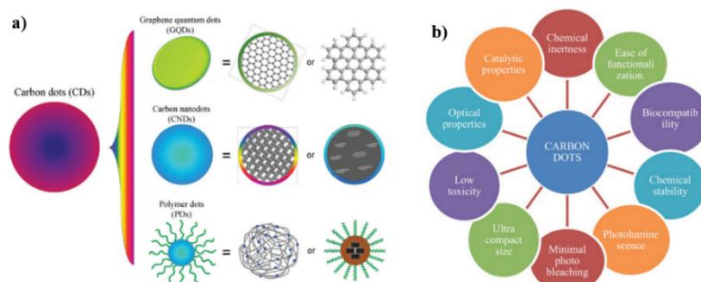


Figure 1.18: Carbon Dots (CDs) (a) Categories of CDs, GQDs, CNDs and Polymer Dots (PDs) [25], (b) CDs properties [26].

Graphene

Researchers have been actively exploring the potential of 2D nanomaterials, with graphene being a prominent candidate. Graphene, exhibits a plethora of fascinating properties, such as high sensitivity and conductivity, significant selectivity, fair stability and strength, and excellent electrocatalytic events, making it the most strong and thin material known to date [22]. Its outstanding performance is proved in various bio-related applications, including pH, humidity and biochemical sensing. Its versatility allows it to adopt different forms, including graphene oxide (GO), reduced graphene oxide (rGO) (Fig. 1.19), and graphene nanoribbons (GNRs), each serving specific purposes in sensing and biosensing applications [23].

- Derived from graphene, Graphene Oxide (GO), emerges as a crucial material, which can be produced cost-effectively, via high performing chemical methods. Its high hydrophilic character, and great conductivity (both electrical and thermal), allow for easy exfoliation in the water, at decent ultrasounds.
- Reduced Graphene Oxide (rGO), possesses a plethora of electroactive exposure and groups, enhancing its suitability for chemical operation [27].

Despite the remarkable advancements in graphene-based materials, certain challenges still persist. Basic mechanical characteristics, relatively high production costs, and non-biocompatibility, are among the limitations that researchers must address, to fully exploit their potential in various applications. Finding solutions to these challenges, will be crucial to unlock the full range of benefits offered by graphene and its derivatives, in diverse industries and fields.

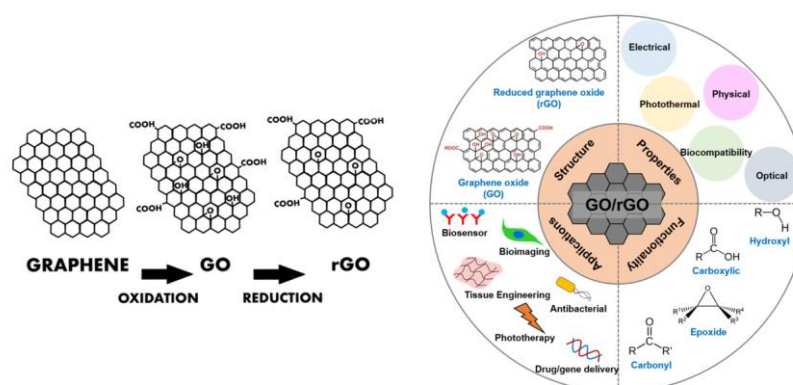


Figure 1.19: GO and rGO Structure, Properties, Functionality and Applications Schematic Representation [28][29].

Metal Nanomaterials

Noble metal nanoparticles (e.g., Au, Ag, Pt, Pd, and derivatives), significantly boost bio-analysis in electrochemistry and medical sensing. Their size, large surface-to-volume ratio, atoms and shape-based attributes enhance sensitivity and selectivity of vital molecules in bio-related fields, especially in applications related to signal amplification (Fig. 1.20) [22]. Metal nanoparticles (NPs) can also be used with other NPs, in order to enhance their sensing characteristics, for an improved biomolecule detection and quantification [23]. Furthermore, metal oxide nanomaterials, such as copper oxide (CuO), and metallic materials, like gold (Au) nanoparticles (NPs), silver NPs, and platinum NPs, have made significant contributions to electrochemical sensor and biosensor devices for infection detection and other threats, due to their efficient analyte sensing, electron-transport properties, large surface area, good conductivity, and high chemical strength [22]. In addition to individual solid-state elements, hybrid elements are also gaining popularity as sensing materials in flexible sensors. One

example, is the elastomeric compounds with conductive nanofillers, forming highly filtering networks to facilitate conduction paths. Even though solid-state materials are commonly used for commercial sensors, their conventional electronic technology's rigidity limits their flexibility and stretchability, leading to ongoing exploration and development of more advanced materials suitable for flexible sensors.

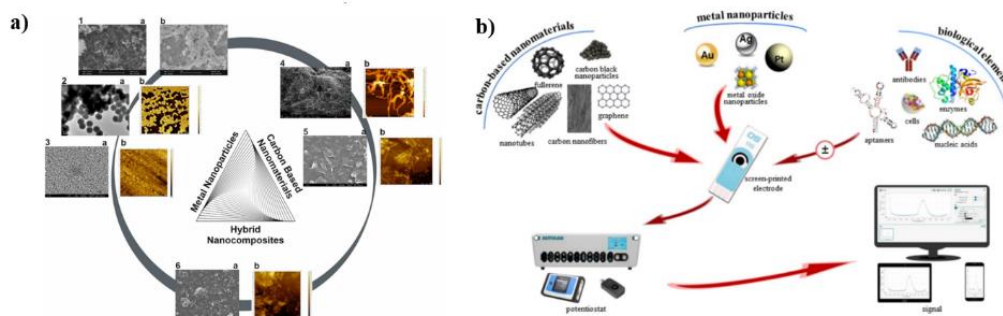


Figure 1.20: (a) Visual optical characterization of metal nanoparticles, carbon-based nanomaterials, and hybrid nanocomposites, (b) Flowchart of the process for nano(bio)sensor fabrication that entails the integration of screen-print carbon-based nanomaterials, metal NPs, and, optionally, biological elements, followed by subsequent electrochemical analysis [23].

b) Liquid-State Materials

Flexible sensing platforms have witnessed remarkable advancements in recent years, giving rise to liquid-state flexible sensing devices, as a notable group of sensors. Due to their inherent nature, unlike traditional solid-state sensors, they utilize conductive liquids as the active sensing element, confined within soft flexible substrate structures, via microfluidics-based configurations [3]. Their minimal requirements result in ease of fabrication, cost-effectiveness and time-saving process, to exhibit a highly sensitive device. Ionic and metal fluids are particularly advantageous as working fluids for liquid-state sensors, because of their greater conductivity and excellent physical, chemical and environmental strength (Fig. 1.21). Additionally, the encapsulation of conductive liquids onto flexible substrates, allows for the development of elaborate-shaped functional sensors.

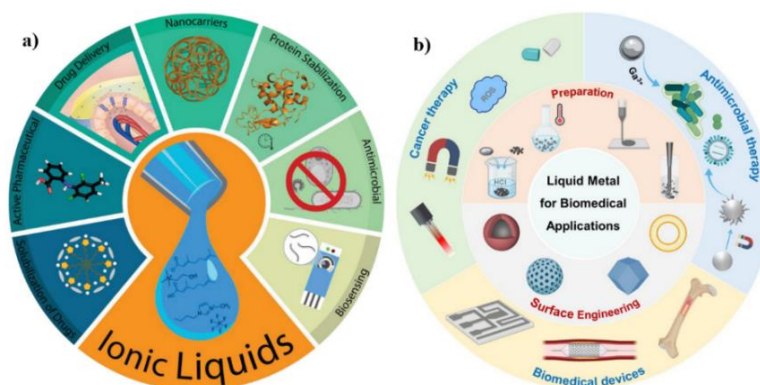


Figure 1.21: Schematic representation of: (a) Ionic Liquids [30], (b) Metal Liquids Applications [31].

1.1.2.2 Substrates

Flexible substrates are highly desirable for flexible biomedical sensors, due to their excellent bendability, conductivity and ability to durably conform to various surfaces, with different shapes and topologies. The performance of these sensors greatly depends on the material's careful selection and fabrication, especially in the context of biomedically and biochemically oriented devices [3]. Apart from the substrate's bendability rate, its adhesiveness that bonds it with the sensing material,

also plays a crucial role in the overall stability of the sensor system. To address any challenges posed by the adhesive-substrate relationship, researchers are exploring various approaches, such as surface modifications, as well as the utilization of novel adhesive materials [14]. These innovations aim to achieve better compatibility and bonding between the sensing material and the substrate, ultimately enhancing the sensor's performance and reliability.

Flexible sensors commonly utilize a variety of substrates known for their ease of deformity, fabrication, and high transparency. The choice of substrate material depends on the specific demands of the sensor, including the intended application, sensitivity, and environmental conditions. These substrates include polyethylene terephthalate (PET), polyethylene naphthalate (PEN), polycarbonate (PC), polyurethane (PU), polyethersulphone (PES), and polyimide (PI), as well as conductive polymers like polyaniline (PANI) (Fig. 1.22). Another category of flexible substrates gaining significant attention, is soft silicone stretchable elastomers, including polydimethylsiloxane (PDMS) and silicone rubbers. These are ideal candidates for specialized applications, that require sensors to conform to irregular or curved surfaces. In addition to traditional flexible substrate materials, emerging research has shown promising potential in using paper and textiles, as flexible sensor platforms. Both paper and textiles offer their own set of advantages, such as cost-effectiveness, lightweight nature, and biocompatibility, making them suitable for various sensor applications, especially in the field of wearable and environmental monitoring devices.



Figure 1.22: A visual classification of the flexible substrates used in flexible biomedical sensors [32].

a) Polymer Substrates

In modern medical surgical practices, the utilization of biodegrading polymers has become increasingly common. These polymers are designed to gradually break down, and be absorbed by the body, eliminating the need for their removal after the healing process. Among the various types of polymers used, thermoplastic polymers such as PET, PEN, and PI are often preferred, due to their low thermal coefficient, cost-effectiveness and high transparency. Although PET, PI, and PEN are inherently less flexible, they gain a certain level of flexibility by reducing their thickness [33]. These properties make them suitable for sensitive medical applications, where precise measurements and clarity are essential. However, most thermoplastic polymers, are not well-suited for high temperature exposure, as their properties can be compromised under such conditions (Fig. 1.23). Furthermore, their surface smoothness may not meet the stringent requirements of certain medical devices or surgical procedures. The following paragraphs provide an overview of the widely used polymers that serve as flexible substrates for various biomedical sensing applications.

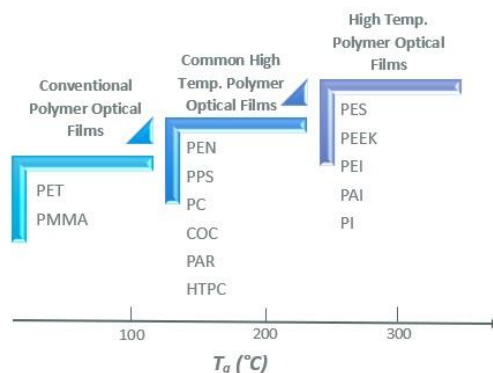


Figure 1.23: Correlation of the polyimide substrates durability in various temperatures [97].

1. Polyethylene Terephthalate (PET)

One of the most prominent plastic flexible substrates used in biomedical sensing, is polyethylene terephthalate (PET), due to its remarkable mechanical strength and outstanding electrical insulating characteristics. Through thermal processing, PET offers the option to be processed in a transparent state, or as a thermoplastic semi-crystalline polymer, and thanks to its non-polar molecular composition, it acts as a water-resistant structure [2]. Its transparency and cost-efficiency make it a favorable choice for sensor fabrication, as well as its thin nature and recyclability, add to its appeal. Moreover, PET emerges as an attractive substrate material for conductors and optical sensors, boasting colorless attributes, chemical inertness, stability and stretchability. With its ability to withstand high temperatures up to 200 °C, PET offers a promising avenue for the development of transparent conductors in the biomedical sensing domain [34].

2. Polyethylene Naphthalene (PEN)

Polyethylene Naphthalene (PEN), stands out as a notable plastic flexible substrate. In many ways, it resembles polyethylene terephthalate (PET), but possesses higher temperature resistance, making it more suitable for applications with higher operating temperatures. Compared to PET, PEN demonstrates enhanced chemical stability against water vapor and oxygen. This is because of the presence of two aromatic rings in PEN's molecular structure, contributing to its stiffer nature, setting it apart from PET fibers (Fig. 1.24) [2]. This material offers a light, transparent, and cost-effective option for various electronic components [33]. The exceptional performance of PEN in maintaining its properties under challenging conditions makes it a valuable candidate for a range of applications in the electronics industry.

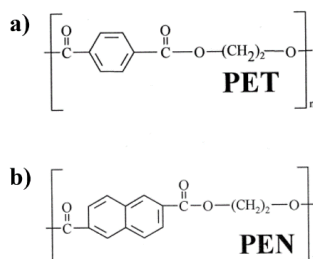


Figure 1.24: Molecular Structure of (a) PET, (b) PEN [35].

3. Polyimide (PI)

Polyimide (PI) has recently emerged as a highly promising flexible substrate. This polymer, offers numerous advantageous properties, including outstanding heat resistance, high transparency, remarkable mechanical characteristics, and a low dielectric constant, all uninfluenced by temperature fluctuations or humidity. Kapton, a specific type of polyimide, is ideal for applications requiring

higher temperatures, as well as its thin, flexible, and chemical-resistant nature further add to its appeal [2]. In comparison to PET materials, polyimide (PI) holds several advantages, with its greatest strength lying in its outstanding heat resistance. Due to these characteristics, PI is an excellent candidate as a protective layer for sensors, shielding them from any undetectable external influences that could impact the device's performance (Fig. 1.25) [33].

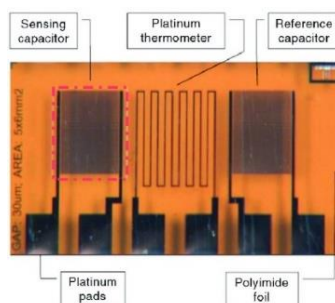


Figure 1.25: A cohesive integration of temperature and capacitive gas sensors onto a bendable polyimide (PI) film [36].

4. Polyaniline (PANI)

One of the primary advantages of utilizing PANI in various sensing applications, lies in its exceptional properties such as high conductivity, good electrochemical reactions, and satisfying porosity, leading to enhanced sensitivity, selectivity, and performance of the device (Fig. 1.26). Whether it is detecting hazardous gases by protecting metals from corrosion, or improving the efficiency of energy storage, PANI's versatility proves invaluable, across different industries. Additionally, PANI's widespread use, is also attributed to its straightforward electrode deposition process, simplifying the manufacturing and assembly of sensor devices [2]. This user-friendly feature, reduces the production time and costs of the fabricated device. As a result, PANI continues to gather attention in research and industrial domains, where the pursuit of cutting-edge sensor technologies is always ongoing.

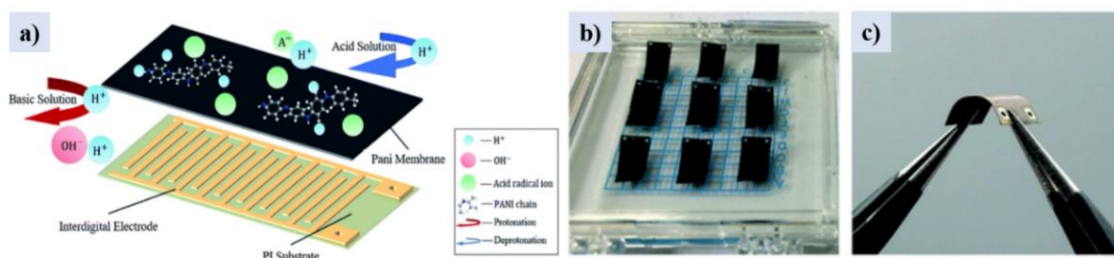


Figure 1.26: Development of a flexible pH sensing platform utilizing a conductive PANI membrane for pH tracking (a) Schematic Representation, (b) Visual representation of a collection of the manufactured sensors, (c) Demonstrating the sensor's flexibility through bending at an angle of approximately 135° [37].

5. Polycarbonate

Polycarbonate (PC) is an extensively studied polymer that finds widespread use in numerous optical applications, due to its chemical strength and remarkable optical, and mechanical characteristics (Fig. 1.27). Despite its advantages, its surface properties pose certain challenges, such as low durability, deficient abrasion resistance, and poor surface energy. Consequently, these disadvantages contribute to the substrate's poor compatibility with liquid materials, leading to difficulties in achieving strong adhesion of the sensing films [2].

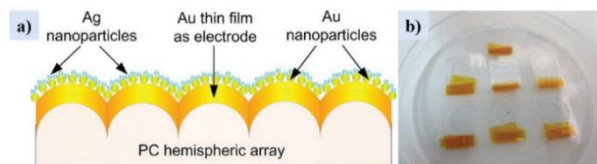


Figure 1.27: Introduction of an electrochemical impedimetric biosensor incorporating a nanostructured polycarbonate (PC) substrate: (a) Graphic representation (b) Visual representation various PC based biosensor samples [38].

b) Silicone Elastomers

Silicone elastomers, known for their exceptional flexibility and deformability, are frequently employed as soft substrates in various applications. They offer unique properties that make them ideal substrates in flexible sensors, wearable devices, and other technologies that require conformability to irregular surfaces. Their ability to stretch and bend without losing their structural integrity, allows them to serve as an excellent foundation, for sensitive and reliable sensor systems. These materials can be engineered to exhibit different levels of elasticity, enabling precise control over the degree of flexibility required for specific applications. Additionally, their biocompatibility, makes them suitable for biomedical devices and wearable health monitors [3], with polydimethylsiloxane (PDMS) being the most common silicon elastomer used.

PDMS

Polydimethylsiloxane (PDMS), is a highly versatile elastic polymer, commonly employed in microfluidic platforms and wearable sensors (Fig. 1.28). Its initial liquid shape can be altered into any desired form, through thermo-chemical processes. PDMS is particularly popular in soft lithography, due to being a thermally and chemically stable transparent element, in both high and low temperatures. [2]. Nonetheless, its weak adhesion poses a constraint in the direct utilization of normal patterning conductive inks. To address this, coupling or gluey layers are used to enhance the bonding reaction between the PDMS surface and the material ink. Another approach involves a film transfer procedure, from an imprinted template, onto the PDMS, using materials like Si or glass as the release substrate [14]. Overall, PDMS remains a top choice for flexible sensors and microfluidic chips. Its ability to be shaped into various forms, combined with its excellent performance in different sensing applications, makes it a highly sought-after material in the field of flexible and wearable electronics.

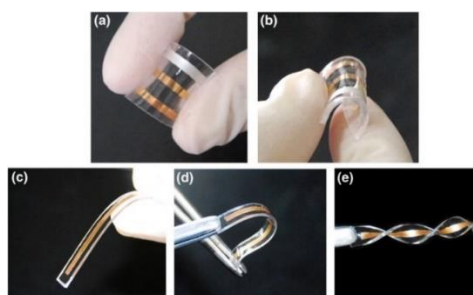


Figure 1.28: An adaptable PDMS-based three-electrode sensor is introduced, where the WE is gold, the RE is silver, and the CE is gold [39].

c) Paper

Paper, with its abundant availability on the market and versatility, has emerged as a viable material for the fabrication of flexible biomedical devices. Its numerous advantages include great stretchability, sensitivity, cost-efficiency compared to polymer-based materials, and hydrophilicity, making it ideal for microfluidic systems and Point-of-Care (PoC) devices, each providing different

functionalities, considering the application (Fig. 1.29) [40]. While filter paper is widely used due to its absorption capacity, other variations of paper have been investigated, to meet specific requirements. For example, the glossy paper's smooth surface and non-degradable nature, render it a preferable choice over filter papers, when modifications with nanomaterials are needed (Fig. 1.30) [41]. The inclusion of nanomaterials or biomolecules enables swift adaptations of paper, facilitating the implementation of paper-based nano-biosensors, which are designed to monitor signals arising from immunoreactions or DNA/RNA hybridization [27]. Moreover, the incorporation of metal NPs, carbon NPs, and metal-organic frameworks (MOFs), attributes significant enhancements, in terms of the optical signal, strength and affinity, towards target analytes. Such modifications, address crucial technical-related challenges, leading to the superior performance of paper-based medical optical devices [14].

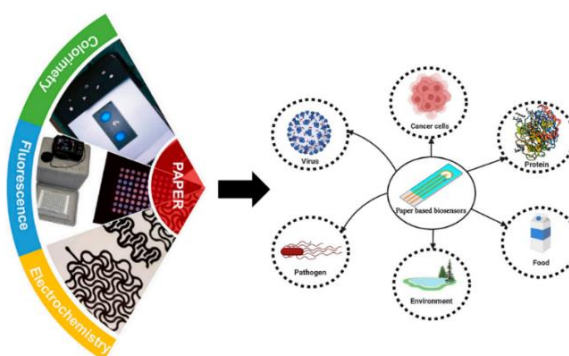


Figure 1.29: Paper-based biomedical sensors sensing categories and functionalities for PoC Testing [40][42].

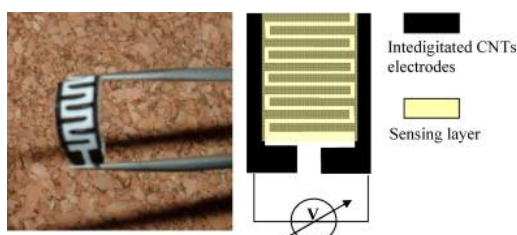


Figure 1.30: (Left) Visual representation of a biomedical sensor whose electrodes are printed onto glossy paper, (Right) Schematic of the glossy paper-based biosensor [43].

d) Textiles

Textiles emerge as highly attractive substrates, allowing the seamless integration of electrodes into casual clothing, to support a wide array of wearable applications. Notably, high-performance textiles such as carbon fabric and aramid, as well as smart textiles (GORE-TEX) [27], have proven their exceptional capabilities and overall effectiveness in military, air force, and marine applications [40]. This success has sparked interest in exploring advanced textiles for the development of portable wearable sensors (Fig. 1.31). Beyond their applications in the military, the incorporation of conductive materials as electrodes on textile surfaces, leads to textile-based electrochemical biosensors. Furthermore, for accurate data assurance and biocompatibility, the selected textiles should possess inert properties, without interfering with the analyte signals. Despite the advantages, the conventional curing methods of textiles, involve high temperatures, potentially compromising their mechanical integrity. Addressing this issue, calls for the deployment of conductive inks that cure at lower temperature rates, but offer limited large-scale production. Textiles on uneven surfaces, pose an additional challenge, for ink patterning and electrode adhesion, which can be enhanced with techniques like laminating polymeric sheets and applying vapor-phase organic chemistry [14]. Overcoming the challenges related to the curing conditions, ink patterning, and the electrode's adhesion, will further unlock the capabilities of textiles in the field of wearable sensing.



Figure 1.31: Electronic textiles (e-textiles) designed to facilitate wearable sensing and display applications [44].

1.1.2.3 Printing Technologies

Printing technology is experiencing rapid growth in sensor fabrication, due to its low-cost production process, for an extensive spectrum of electronic devices on various substrates [45]. This approach stands as an alternative, to the commonly employed photolithography processes for conventional sensor fabrication [3]. Printing fabrication of flexible devices brings numerous advantages, such as enhanced flexibility, increased comfort, eco-friendliness, and cost-effectiveness [46], offering a promising pathway for developing advanced wearable flexible electronics, for personal healthcare applications. This approach, enables efficient deposition of functional materials on both flat and irregular surfaces, reducing any manufacturing costs and the increasing accessibility of flexible sensors to the public [47][48]. Various printing techniques, including screen, inkjet, roll-to-roll, gravure, flexography, and (photo)lithography printing, offer precise control over the placement and arrangement of biological molecules, and the functional materials, onto flexible substrates. These technologies, utilize screen masks, nozzles, or patterned cylinders to deposit conductive ink at desired positions, unlocking a wide range of potential applications in various industries [49].

The field of flexible sensor fabrication utilizes two main categories of printing technology: contact printing and non-contact printing (Fig. 1.32).

- a. Contact printing involves the direct contact between the designed medium and the substrate’s surface, during the ink deposition and includes techniques mainly like screen printing, gravure printing, and flexography printing [45][47]. Out of these methods, screen printing stands out for the development flexible biomedical sensors. Despite its popularity, contact printing poses excessive material loss, and limitations in resolution and material range [50].
- b. In non-contact printing technique, only the deposition material comes into contact with the substrate. Specifically, the ink is discharged by the printer and onto the substrate, through stencils or nozzles. Various non-contact printing technologies include laser printing, aerosol printing, and inkjet printing. This method is conformable with an array of substrates, which need low curing temperatures to prevent damage [50]. Its simple operation, less material waste, adaptability, high printing resolution, adjustable printing parameters, and no mask requirement, distinguish it from contact printing techniques [45].

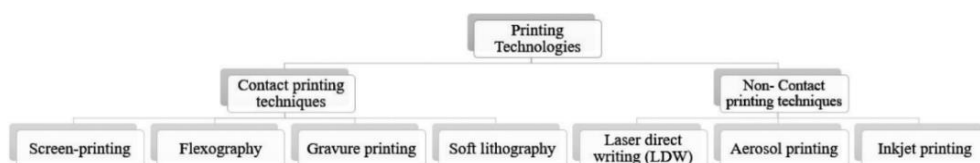


Figure 1.32: Printing Technologies – Contact Printing & Non-Contact Printing Techniques [50].

Selecting the right printing technique for wearable flexible electronics (FE) requires several factors for consideration, including minimum line width and thickness, printing speed and resolution, and mask or nozzle requirements. The characteristics of the substrate and conductive material also hold substantial importance in the decision-making process [47]. Outlined below are some of the most widely recognized and extensively employed printing technologies, specifically catered for flexible biomedical sensors. These innovative printing techniques have played a pivotal role in advancing the field of wearable healthcare monitoring devices and have gained significant attention from researchers and industry professionals alike.

▪ Screen Printing

Screen printing, a well-established, cost-effective and simple printing technique, holds great promise in the realm of flexible biomedical sensors. The process involves depositing ink onto a framed mesh, which is then moved back and forth via a flat object; typically, a squeegee [49]. Through this motion, the ink is transferred onto the substrate's surface, creating diverse patterns that determine the thickness and mechanical properties, of the fabricated device (Fig. 1.33). This precise and controlled printing method, enables the production of intricate designs for flexible biomedical sensors, making it a valuable technology for various medical devices [51]. The resolution of the screen-printed device is influenced by several factors, including the characteristics of the mesh, the parameters of the squeegee, and the properties of the ink. Therefore, addressing concerns related to resolution, film thickness, printing velocity, squeegee pressure, and spacing between the mesh and the substrate, are among the primary objectives in enhancing the capabilities of the screen-printing technique for diverse applications [51]. By fine-tuning these parameters, precise and efficient printing of any electronic device can be succeeded, catering to the specific needs of various industries. Although widely used and promising for flexible sensor fabrication, screen-printing is not without its limitations. One of the drawbacks is the requirement for pattern-specific screens, which can be a tedious, expensive and material-wasteful process [52]. With the enhanced control over the printing process, the right choice of materials and improved viscosity properties, finer and more precise patterns can be achieved. It is also important to note that the screen-printing technique's ability to achieve temporal resolutions, is confined to the milli-scale range. This restriction, limits its application in high-precision micro patterns production. [53]. Despite these challenges, ongoing improvements and optimizations in screen-printing techniques, enhance the resolution and performance of the resulting sensors, giving further growth and innovation in the field of flexible electronics. With its remarkable capabilities and potential for customization, screen-printing remains a vital process for the development of advanced, and practical healthcare devices.

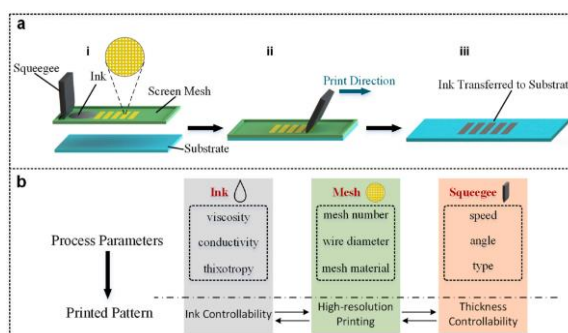


Figure 1.33: (a) Schematic representation of the screen-printing technology, (b) Parameters that influence the resolution and outcome of the final screen-print structure [51].

▪ Inkjet Printing

Flexible sensors with inkjet-printing technology, are gaining major interest due to their cost-effectiveness, swift manufacturing process, superior resolution, adaptability and lightweight attributes, holding significant importance in the development of flexible biomedical devices [45]. Inkjet printing, is a non-contact, maskless technique, that enables patterning through drop-on-demand (DoD) mechanisms, on diverse flexible substrates [54]. Its digitally controlled drop-on-demand variant, minimizes ink consumption and increases the accuracy of the ink drop, proving advantageous for applications involving costly biomolecular deposition, in biosensor manufacturing [55]. Fig. 1.34 illustrates the manufacturing procedure of flexible sensors using inkjet printing technology, while a more comprehensive description can be found in Fig. 1.35.

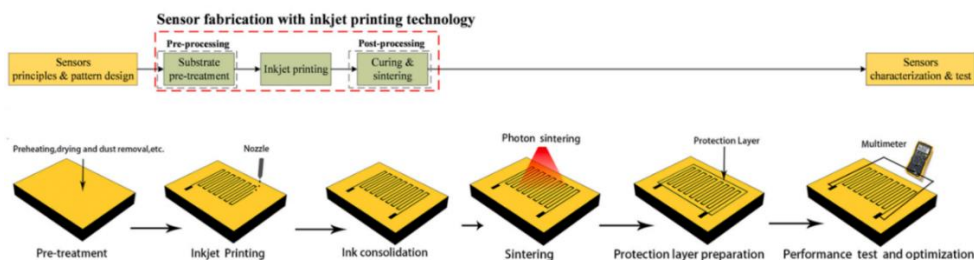


Figure 1.34: A schematic flow and a step-by-step sequence detailing the production of flexible sensors through inkjet printing technology [45].

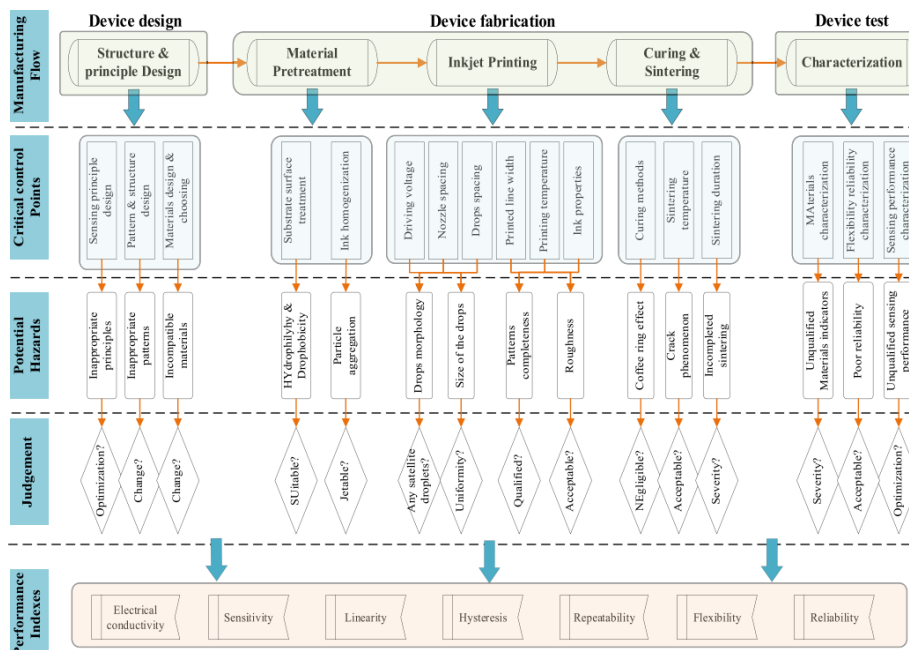


Figure 1.35: A comprehensive schematic illustration of flexible sensors fabrication through inkjet printing techniques [45].

During the curing process, ink droplets disperse and expand over the substrate, along with the evaporation of the organic solvent contained within, at ambient temperature [45]. This progressive transformation from liquid to solid state, is marked by the emergence of the ‘coffee ring effect’; an undesirable event that leads to an uneven distribution of ink material, adversely impacting the clarity and conductive properties, of the printed designs (Fig. 1.36). This phenomenon, has a pronounced influence on the functionality of flexible sensors, leading to their lower performance. Therefore, several approaches have been explored, including techniques like the substrate’s heating throughout the curing process, the utilization of porous substrates with increased hydrophobic properties, and the

augmentation of the printing layers quantity, which aim to alleviate the impact of the coffee ring effect and promote a more even ink dispersion.

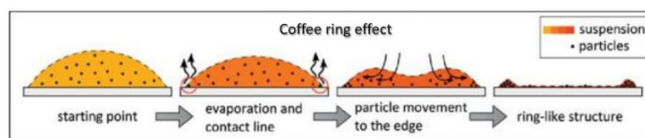


Figure 1.36: Schematic Representation of the Coffee Ring Effect [56].

Upon completion of the curing process, sintering becomes a pivotal step, particularly for metal NP-based materials. Its primary role is to eradicate any remnants of organic solvent within the droplets [45]. Diverse sintering methods are employed, including thermal, selective laser, electrical, plasma and chemical sintering techniques (Fig. 1.37).

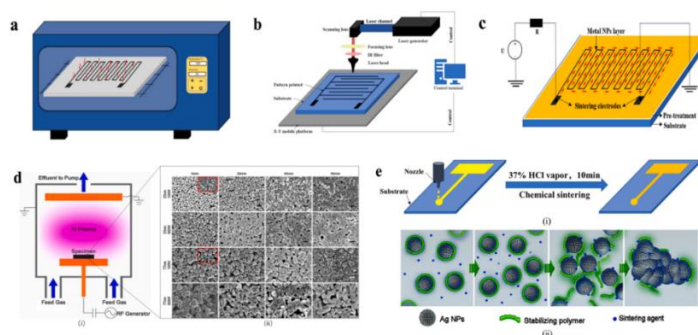


Figure 1.37: Sintering Techniques. (a) Thermal (b) Selective Laser (c) Electrical (d) Plasma (e) Chemical [45].

Despite its great potential, inkjet printing technology faces various limitations like nozzle blocking, and ink viscosity constraints [57]. These factors intricately influence the printing outcome, necessitating material and process optimizations, for superior performance and clear patterns. Despite its limitations, further advancements and optimizations in inkjet printing technology hold the promise of enhancing its capabilities and broadening its scope in various industries, especially in healthcare.

❖ Inkjet Printing: Print-Head Categories

In inkjet printing technology, a diverse array of print-head categories exists, each harnessing distinct principles for droplet ejection. These include thermal, piezoelectric, electrostatic, and acoustic inkjet printing techniques, each offering unique advantages and addressing specific challenges [50]. While these methods offer novel avenues for droplet ejection, their widespread implementation in research and development is still evolving. It is essential to point out that the selection of inkjet printing technology hinges on factors such as ink viscosity, surface tension, and material compatibility [45].

a) Thermal Inkjet Printing

Thermal inkjet printing, operates on the principle of rapid ink vaporization, induced by localized resistive heating. The ink within the chamber is swiftly heated to temperatures around 300 – 400 °C, prompting the formation of vapor bubbles [57]. The ensuing pressure fluctuations, expel the ink droplets through the nozzle (Fig. 1.38). While efficient, this method is limited by the necessity of ink materials that are both evaporative and thermally steady, potentially restricting its application to specific scenarios. Nevertheless, researchers have investigated suitable ink formulations and printing methods to alleviate these constraints. Despite its limitations, thermal inkjet printing is characterized by a more straightforward operational process and solvents that are less detrimental to the environment.

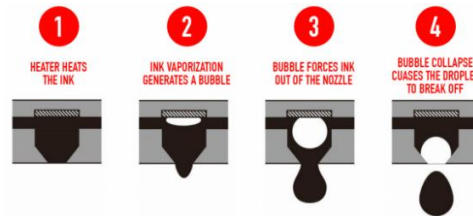


Figure 1.38: Visual representation flow of the Thermal Inkjet Printing process [58].

b) Piezoelectric Inkjet Printing

Piezoelectric inkjet printing presents an alternative mechanism by utilizing piezoelectric elements that deform, upon the application of voltage [45]. This deformation generates pressure waves that eject ink droplets. Notably, piezoelectric inkjet printing enables a broader range of ink compositions, avoiding the high temperatures associated with thermal inkjet printing, while generating higher-quality droplets (Fig. 1.39) [49]. Despite its advantages, the cost of piezoelectric inkjet printing technology, including the print head and associated software, remains a consideration [59].

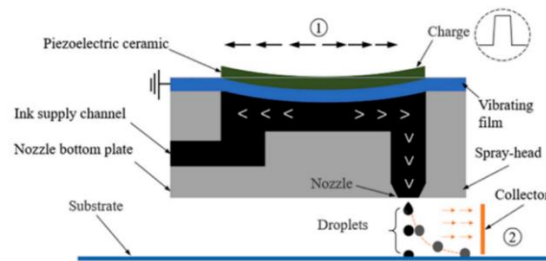


Figure 1.39: Piezoelectric Inkjet Printing Mechanism [45].

c) Electrostatic Inkjet printing

Electrostatic inkjet printing is based on the manipulation of charged plates, to direct the droplets and tune their fine size, through electrical potential variation (Fig. 1.40). Its main asset resides in its ability to precisely eject fine droplets, as well as in its inherent simplicity at the printhead design [49]. This technique showcases exceptional advantages that differentiate it from the abovementioned inkjet printing technologies, which dispense droplets smaller than the nozzle's size and face any highly-viscous fluids related challenges [54].

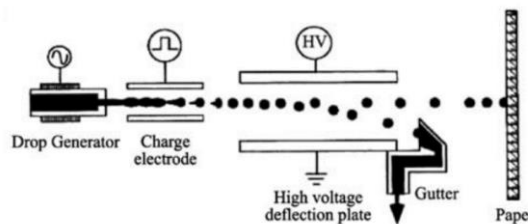


Figure 1.40: Visual Representation of the Electrostatic Inkjet Printing Mechanism [49].

d) Acoustic Inkjet printing

The utilization of concentrated acoustic frequencies in acoustic inkjet printing, effectively conquers surface tension, enabling the accurate expulsion of minute droplets [49]. This type of inkjet printing mechanism is the only one without a nozzle (Fig. 1.41) [59]. This innovative technology not only offers meticulous management of the droplet dimensions, but also serves as a safeguard for printheads, averting any potential blockages [54].

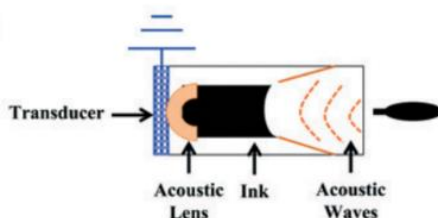


Figure 1.41: Visual Representation of the Acoustic Inkjet Printing Mechanism [59]

❖ Inkjet Printing: Mechanisms

There are two primary operational mechanisms that take place in the inkjet printing process: continuous inkjet (CIJ) and drop-on-demand (DOD) mode (Fig. 1.42).

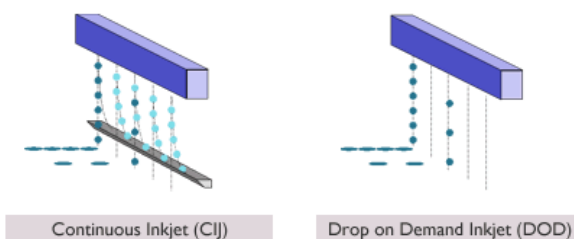


Figure 1.42: Continuous Inkjet (CIJ) and Drop-on-Demand (DOD) modes [60].

1. Continuous Inkjet (CIJ) Mode

Continuous inkjet (CIJ), functions by maintaining a continuous discharge of ink droplets controlled by a vibrating nozzle, via a piezoelectric crystal (Fig. 1.43) [59]. Considering the input signals, these droplets are charged and directed, allowing their selective deposition onto the substrate. While its continuous operation enables rapid printing, this approach leads to ink wastage, and diminished resolution, in contrast to the Drop-On-Demand (DoD) mode [50].

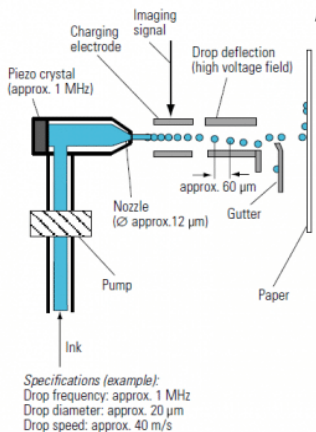


Figure 1.43: Continuous Inkjet (CIJ) Mode Mechanism [61].

2. Drop-on-Demand (DoD) Inkjet Mode

In the Drop-On-Demand (DoD) mode, ink droplets are expelled from a nozzle by inducing an acoustic or electrostatic pulse, through thermal or piezoelectric means (Fig. 1.44a) [62]. The former relies on heated ink, while the latter involves the deformation of piezoelectric materials. Particularly in contexts such as electronic device manufacturing, the DoD technique gains major preference, due to its selective ink ejection, leading to smaller droplets, with enhanced precision (Fig. 1.44b) [50].

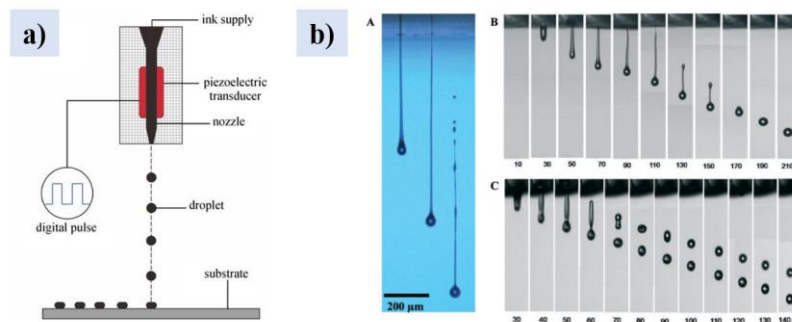


Figure 1.44 a) Drop-on-Demand (DoD) Mode Mechanism [63], b) High-Resolution Images of Inkjet Droplets in various stages of formation, expelled from a Drop-of-Demand Inkjet Mode [62].

▪ **Roll-to-Roll (R2R) Printing**

Roll-to-roll (R2R) methodologies find significant utility in large-scale, and cost-efficient biosensor production [49]. This method employs two rolls, being the anilox and printing roll. The anilox roll keeps the conductive inks, and through roll pressure, it transfers them to the printing patterned roll, that is placed above the substrate (Fig. 1.45). Notwithstanding its benefits, roll-to-roll printing poses certain difficulties. Particularly, in unfavorable printing scenarios, the continuous nature of the process presents certain challenges in effectively transferring the material inks to the substrate, necessitating a precise fine-tuning of the operating parameters, and the adoption of suitable materials [64]. In the field of flexible biomedical sensors, roll-to-roll printing has showcased its efficiency in surface treatment, the implementation of glucose biosensors, and patterning of various antibodies.

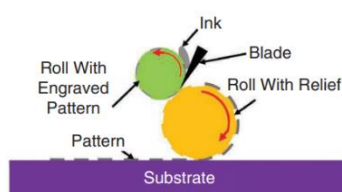


Figure 1.45: Visual Representation of the Roll-to-Roll (R2R) Printing Technique [64].

Roll-to-roll printing, encompasses diverse techniques such as flexographic and gravure printing (Fig. 1.46) [49].

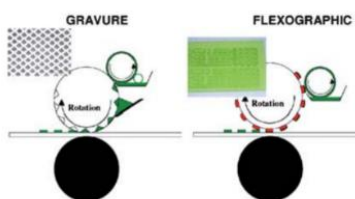


Figure 1.46: Gravure and Flexographic R2R Printing Techniques [49].

a) Flexography

Flexography stands as a roll-to-roll (R2R) printing method, where the resulting pattern is distinct from the ink transfer process. In this procedure, the ink is transferred to an anilox roll containing numerous micro-cavities especially designed to gather skillfully the ink, and establish their interaction with the printing plate cylinder, whose continuous rotation, guarantees a fast, smooth and low-pressure printing procedure of the flexible substrate (Fig. 1.47) [65]. The swift rotary capabilities of flexographic printing, make it an advantageous selection for extensive electrode production, while the incorporation of UV curing and annealing procedures, significantly enhances production speed. Additionally, its versatile characteristics enable the seamless formation of arbitrarily oriented lines, a

trait frequently favored in continuous manufacturing. [52]. This printing technology is frequently used in the fabrication of e-labels, skin patches, flexible batteries, among others. Nevertheless, despite the minimal pressure application, specific issues may emerge, such as excessive ink patterns (Halo effect), due to the compression amount amidst the printing plate and the substrate, reducing the stability and the resolution of the final device [50].

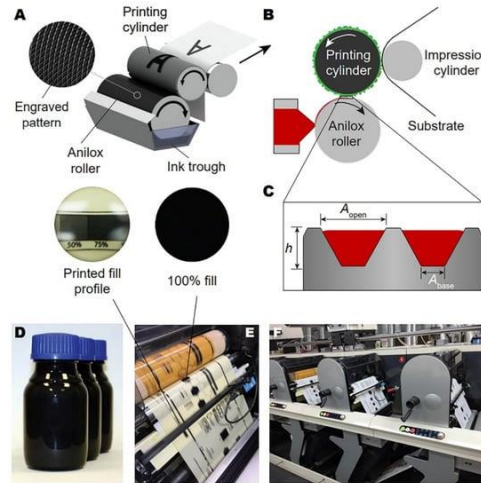


Figure 1.47: (A-C) Graphical representations of the flexographic printing mechanism, (D) Inks used for flexographic printing, (E-F) Flexible device fabrication through flexographic printing [66].

b) Gravure Printing

The process of gravure printing includes the engraved pattern of the intended design onto a cylindrical printing surface. When the ink is pressed on the printing cylinder, its etched cells are filled with it, while the excessive ink is effectively cleared with a flexible doctor blade. Therefore, as illustrated in Fig. 1.48, when the printing roll interacts with the substrate, it transfers the ink onto its surface [49][65].

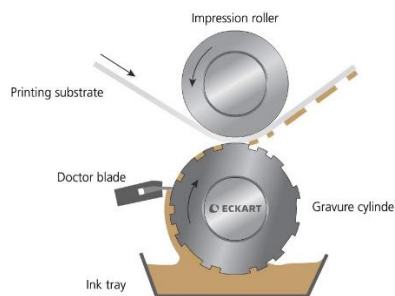


Figure 1.48: Graphical representation of the Gravure Printing Mechanism [67].

▪ **Aerosol Jet Printing**

Aerosol jet printing represents an innovative approach for depositing materials, for printed electronics. In this process, the ink's aerosolization is comprised of numerous droplets, with diameters ranging from 2 to 5 μm . Following this, the aerosolized ink is transferred to the material deposition head via nitrogen (N_2) gas. Once there, a controlled jet stream guides the ink onto the substrate, ensuring its accurate placement (Fig. 1.49) [48]. Similarly, to inkjet technology, the nozzle does not touch the substrate, enabling the printing of diverse materials onto stretchable substrates, such as thin-film transistors (TFTs) and flexible displays. Furthermore, this capability extends to the precise positioning of nanoscale biological components on intricate three-dimensional structures [50].

Despite its advantages, a common challenge faced with aerosol jet printing is the potential overspray of material from the nozzle, resulting in its unintended deposition, beyond the desired printed patterns.

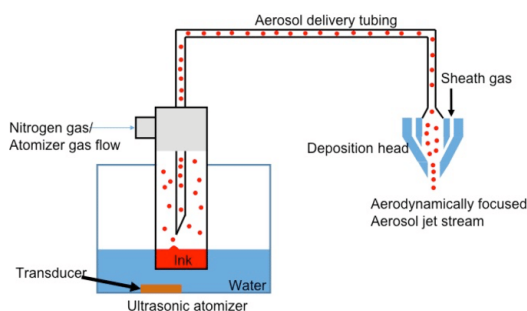


Figure 1.49: Graphical representation of the Aerosol Jet Printing Mechanism [68].

1.2 Wearables & Wireless Biosensor Networks (WBSNs)

In the context of biomedical applications, recent strides in incredibly thin, pliable, flexible, and adaptable sensors, have unlocked exciting possibilities for designing personalized medical diagnostic and therapeutic platforms. Wearable devices are intricate structures that combine multiple components, including:

- ✓ flexible substrates
- ✓ sensors
- ✓ circuits for reporting signals
- ✓ materials for encapsulation
- ✓ and effective fabrication methods

The design of wearable biosensors that can stretch and bend as needed, requires careful consideration of certain key elements, including the thickness of the substrate and the appropriate selection of functional inks [69].

Within the domain of remote monitoring, flexible wearable systems consist of three fundamental elements (Fig. 1.50) [70]:

- a. the hardware responsible, for collecting both biometric and kinetic data
- b. a communication system, designed to transmit this data to a remote location
- c. intricate data analysis methods, for clinical data extraction from the collected information

The convergence of flexible bioelectronic devices and wireless communication has opened up possibilities for the ongoing real-time monitoring of an individual's physiological parameters, including heart and respiratory rates, and body temperature, empowering individuals to actively manage their health, while potentially reducing the need for extended hospital stays [71][72].

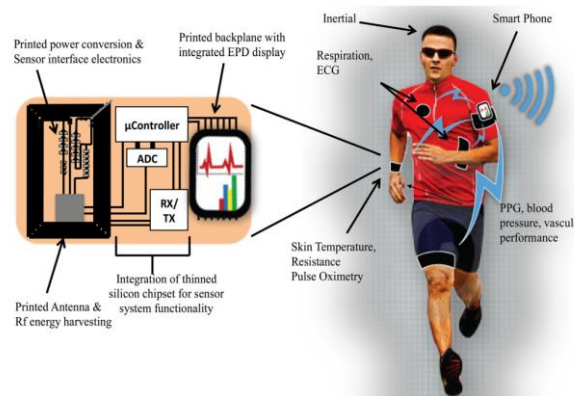


Figure 1.50: Schematic illustration of the elements of a flexible wearable system [62].

Fueled by progress in smart technology and continuous wireless monitoring, the integration of biosensors into common devices [73], has heightened a new phase of data-centric healthcare wearable sensors, that offer improved reliability and great promise, in medical diagnostics and health tracking [70][74]. This progress extends beyond wearable technology, and is paramount influencing the growth of the Internet of Things (IoT), through innovations like intelligent sensor labels and tags [75], paving the way for groundbreaking, user-centric, and lightweight bio-integrated health monitoring solutions, with significant advantages to the society. With the increasing sophistication and affordability of wearable devices, their adoption within clinical environments is expected to expand significantly [73]. Through ongoing research and innovation in flexible biomedical sensor technology, the future holds even more promising developments, capable of transforming medical diagnostics and preventive healthcare, ultimately revolutionizing the way an individual manages and prioritizes his welfare.

Although wearable health monitoring systems have witnessed substantial recent advancement, they do not come without their challenges. One notable drawback, is their insufficient attachment to the body, which entails the choice of the appropriate materials and printing principles [73], leading to compromised compatibility and durability [62]. Other challenges extend to various domains, encompassing technological barriers, such as power supply for continuous home-based clinical monitoring [70]. As a result, the development of innovative solutions for energy generation and storage, becomes a critical factor in unlocking the complete capabilities of wearable devices [76]. An additional limitation regards to the current prototype stage of flexible wearable devices, which leads to their slow progress rate within the market. Furthermore, the limited exploration of highly integrated multi-functional health monitoring devices, that seamlessly integrate both physical and biochemical sensing units, is a subject that requires further development, to ensure their flawless functionality [62]. Moreover, given that non-intrusive body signals often appear weak and disruptive, techniques involving the noise reduction and the signal amplification, are commonly employed to counteract any undesirable interference [72]. Notwithstanding these challenges, the mass customization along with the cost-effective packaging, are pivotal for the flexible healthcare sensing systems' commercialization, although, the performance, fabrication efficiency, and cost considerations, have been barriers to achieving the desired large-scale production.

Despite the challenges, the integration of intelligent wearable systems with signal processing units, feedback mechanisms, and computer or/and smartphone communication, represent a substantial step towards setting wearable health monitoring more accessible to the market. Additionally, as technology progresses, it is conceivable that display modules might also become seamlessly integrated within wearable systems, enhancing their flexibility, and user-friendly interaction [76].

Therefore, with ongoing advancements in material science, fabrication techniques, and integrated circuitry, wearable healthcare systems are poised to transform the landscape of disease detection, treatment, and preventive measures, paving the way for predictive health management.

1.2.1 Classification of Wearable Sensors & Types of Wearable Devices

The rapid evolution of wearable technology has led to a novel and sophisticated classification of flexible wearable sensors. This classification is based on the diverse range of physical, biochemical, and electrochemical signals, inherent to the human body. Such signals are harnessed to fabricate flexible wearable sensors, capable of continuously detecting and monitoring various physiological parameters. These sensors, find their integration into an array of wearable devices, that is applied onto the human body. From the ingenious application of temporary skin tattoos, to the adaptability of flexible bandages, their primary purpose is to enable continuous health monitoring, facilitated by wireless systems and display interfaces. This aspect highlights the practical application and significance of flexible wearable sensors, as they contribute to the implementation of devices that offer real-time health data tracking.

1.2.1.1 Classification of Wearable Sensors

An exceptional advancement in wearable biosensors revolves around flexible electrodes, which enable non-invasive and immediate capture of human physiological and physical data (Fig. 1.51). This encompasses a diverse array of signals, spanning from facial expressions and movements, to crucial metrics, such as body temperature, pulse rate, blood pressure, and even electrophysiological impulses like ECG, EEG, and EMG. Furthermore, by converting the biological responses into electrical signals, wearable detectors expand their capabilities to the electrochemical analysis of bio-fluids like blood, sweat, pH, saliva, tears, and even urine. The fabrication of wearable biochemical sensors, incorporating receptors and transducers via printing technology, demands both mechanical resilience and comfort when placed on delicate tissues. When worn, these sensors need to possess mechanical durability, while providing comfort on delicate tissues [52].

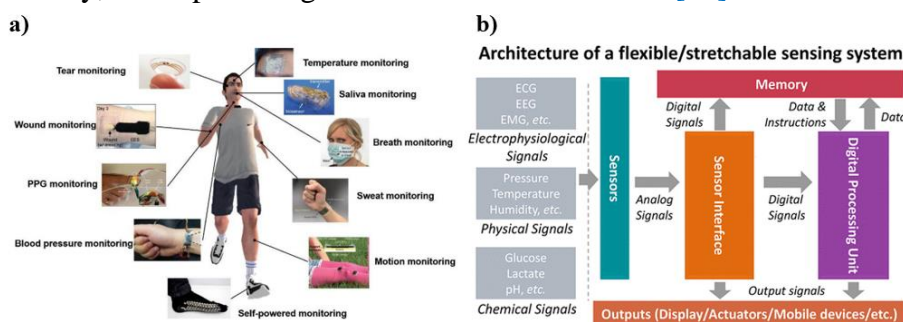


Figure 1.51: a) Applications in wearable systems for continuous healthcare monitoring [72], b) Architecture of a flexible sensing system [77].

Therefore, determined by the body's functionality, as well as the physical and chemical signals gained, non-invasive wearable sensors are categorized into two main groups:

A. Physiological & Physical Wearable Sensors

- **Motion Detection**

The basis of human motion detection relies on strain sensors, which convert the resistance caused by physical deformations, into motion-related electrical signals [47]. There is a wide spectrum of body motions, including limb and spine movements, as well as subtler gestures like those seen in the neck,

sternum, hands and face, during emotional and speech interactions. These movements may serve as early warnings of serious conditions like Parkinson's, Alzheimer's, and diabetes, prompting for timely diagnosis and treatment. Therefore, recent research endeavors have resulted in the emergence of non-invasive flexible wearable systems, capable of real-time and ongoing tracking of human motion [72].

▪ **Electrophysiological Detection**

Electrophysiology involves the measurement of voltage and current alterations, through medical techniques like, electrocardiography (ECG), electromyography (EMG), and electroencephalography (EEG), which are crucial for the diagnosis, treatment and prevention of cardiovascular conditions following surgery [72].

Electrocardiography (ECG) for instance, deciphers the heart's electrical behavior in a defined period. This technique involves electrodes placed on the skin which capture voltage shifts, arising from the heartbeat's myocardial depolarization (Fig 1.52a) [74]. The distinctive peaks within the ECG electrode's signal, offer critical health-related insights, facilitating in the early identification of medical issues, such as arrhythmia, hypertension and hypotension [72]. The recent advancement of screen-print ECG electrodes onto diverse wearable surfaces (Fig. 1.52b), has opened doors to their scalable production, along with their potential use as a biometric tool for assessing the cardiovascular well-being [51][74].

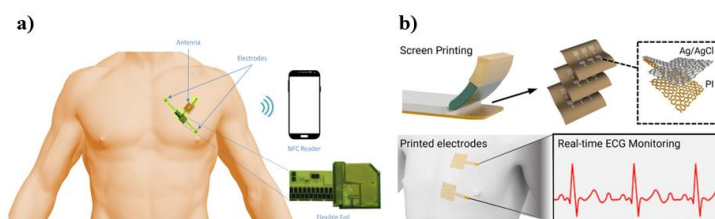


Figure 1.52: a) Illustration of an ECG patch onto the skin for continuous heart-rate monitoring [78], b) A visual representation of a screen-print flexible ECG sensor attached onto the chest for real-time ECG-related data analysis for arrhythmia management [79].

Electromyography (EMG) focuses on the detection of bioelectrical signals discharged by skeletal muscles, providing valuable data about the muscle's performance and the contraction dynamics. The muscle contraction relies on electrical signals initiated by nerves, which in turn stimulate the muscle cells, to either contract or relax; a process known as excitation-contraction coupling. Overall, EMG sensors available in surface (sEMG) and invasive (needle) forms, hold great promise for wearable applications (Fig. 1.53) [74].

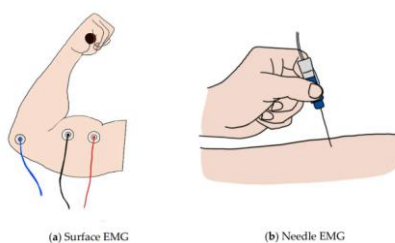


Figure 1.53: Visual representation of the surface EMG (sEMG) and invasive EMG [74].

▪ **Heart Rate & Blood Pressure**

The heart functions as the central hub of the body's blood circulation system, constituting in the maintenance of optimal cardiac performance, crucial for the overall well-being. The most recognizable non-invasive device in this context, is the oximeter [76]. Recent studies have highlighted the significance of monitoring pulse/heart rate, as a fundamental aspect of real-time health

assessment, achievable via flexible wearable sensing technology [47]. These sensors exhibit exceptional flexibility and sensitivity, providing non-invasive alternatives for assessing cardiovascular signs (Fig. 1.54). The integration of strain, optical, and electronic components, has led to improved precision in measuring heart rate and blood pressure [72].

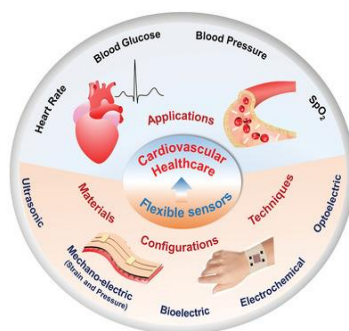


Figure 1.54: Schematic representation of the applications and configurations of flexible wearable sensors in cardiovascular healthcare [80].

Heart-rate monitoring relies on a range of mechanisms, including pressure sensors and optoelectronic devices, notably valuable for respiratory conditions management. Abnormal respiratory rates can indicate a range of health issues, underscoring the importance of continuous monitoring. The exploration of flexible pressure and strain sensors, is a dynamic field, characterized by the use of diverse materials and geometric configurations, to optimize the conversion of pressure and strain into measurable signals [47]. Rapid advancements are also continuously evolved in respiration monitoring sensors, often coupled with other physiological sensors – like strain sensors – contributing to a comprehensive approach to health assessment, aiding in the early detection of irregularities (Fig. 1.55) [47]. Among these mechanisms, the adoption of flexible pressure sensors, integrated into skin-attachable patches, has gained traction, owing to their cost-effectiveness, and user-friendly design (Fig. 1.56). However, the challenge of achieving a balance between the sensitivity and pressure range, still persists. Beyond heart rate, respiration, and blood pressure assessment, the surging interest in wearable flexible pressure and strain sensors, reflects their wide-ranging applications to provide a comprehensive dataset for comprehensive evaluation in physiological monitoring, such as emotion detection, touch recognition, and disease diagnosis [51].

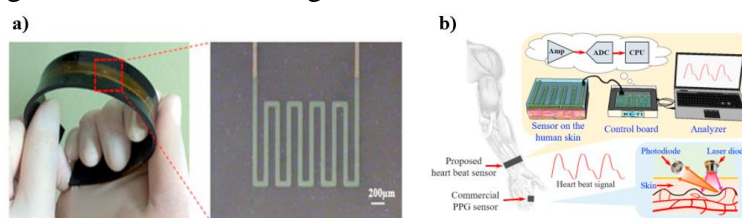


Figure 1.55: (a) Design and architecture of a flexible silicone elastomer heart beat wearable sensor (b) Visual representation of the set-up for heart beat monitoring [81].

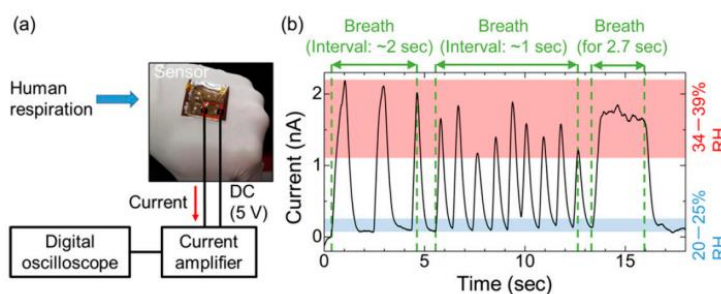


Figure 1.56: Flexible wearable device on 0.125mm Kapton substrate for human respiration tracking [72].

▪ **Temperature Detection**

In the domain of medical and clinical evaluation, the continuous and real-time tracking of skin and body temperature, emerges as a pivotal tool for assessing an individual's health status. The human body maintains a meticulously controlled temperature range, typically spanning from 36.5 to 37.5 degrees Celsius (°C). This regulation ensures the proper functioning of several essential bodily processes, including the metabolism, blood circulation, and the immune system's condition. Notably, the detection of temperature fluctuations is of critical importance, as any deviations from the typical temperature range, serve as noteworthy indicators that provide valuable insights into diverse aspects, including wound healing, and the potential presence of various contagious or allergy symptoms [72]. While conventional methods of temperature monitoring often involve uncomfortable, and potentially infection-prone procedures – like the insertion of clinical thermometers into a patient's body – cutting-edge wearable and flexible temperature monitoring skin-attachable devices, have been engineered via advanced printing techniques and wireless communication protocols (Fig. 1.57). Given the centrality of this topic as core of the present thesis, both their underlying mechanisms and the latest technological advancements are comprehensively examined in the subsequent sections and chapters.

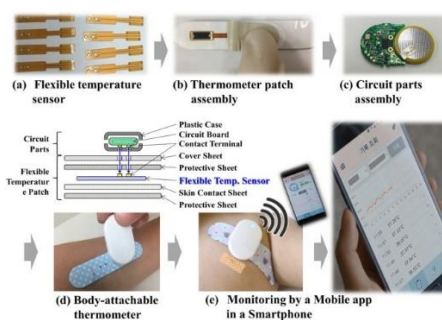


Figure 1.57: Thermometer Flexible Patch System attached onto the body [82].

B. Biochemical & Electrochemical Wearable Sensors

▪ **Glucose Detection**

Non-invasive glucose sensing with flexible wearable devices, stands as a significant technological advancement with profound implications for healthcare and wellness management. Traditionally, glucose monitoring has heavily relied on invasive techniques, often leading to discomfort, and pain. Flexible wearable devices, with integrated sensors and microelectronic components, offer an alternative solution for glucose detection, by providing non-intrusive means to monitor glucose levels, while analyzing various biofluids like sweat, saliva, and tears. Fig. 1.58 illustrates a schematic diagram about glucose monitoring by non-invasive, minimal invasive and invasive means.

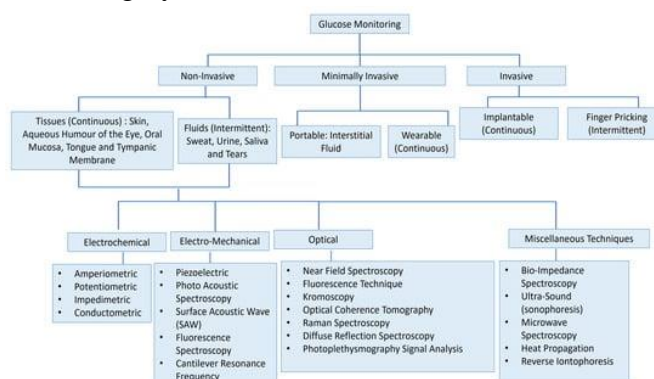


Figure 1.58: Schematic Diagram about glucose detection by non-invasive, minimal invasive and invasive means [83].

Sweat, a vital biological fluid, contains a plethora of biomarkers and analytes, often found in concentrations lower than those present in blood, designating it as an ideal means for pioneering research, in wearable glucose sensing technologies [47][57]. Consequently, recent technological advancements are focused in the implementation of versatile wearable point-of-care (POC) biomarker patches, designed exclusively for sweat collection and the continuous monitoring of glucose concentrations (Fig. 1.59). Significantly, smartphone applications interface, empowers users with real-time glucose and cortisol biomarkers data [57]. Additionally, saliva analysis, also stands as an attractive alternative to conventional blood analysis, thanks to its non-invasive nature and user-friendly collection methods [84]. One notable example, is the evolution of wearable saliva biosensors from traditional paper-based test strips, which analyze the saliva components, via visual colorimetry or electrochemistry (Fig. 1.60), proving their effectiveness in glucose detection [85]. Further research attention has also been directed towards tear biosensors, which manifest in flexible, strip-like configurations and other inventive formats, for glucose detection while offering health-related information (Fig. 1.61) [85].

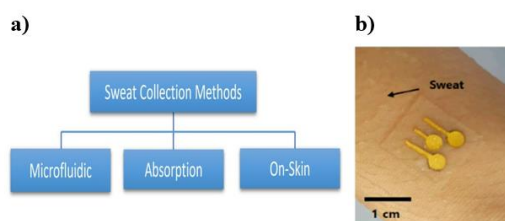


Figure 1.59: a) Sweat Collection Techniques [86], b) Visual representation of a skin patch electrochemical glucose sensor applied on wet skin [47].

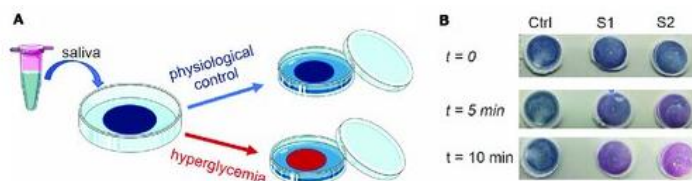


Figure 1.60: a) Development of a home-testing glucose colorimetric sensor for saliva analysis, b) The shift from blue to pink on the membrane surface is an indication of hyperglycemia - The Ctrl represents plain human saliva, the S1 contains 15 mg/dL of 0.8 mM glucose concentration, and the S2 contains 30 mg/dL of 1.6 mM glucose concentration [87]

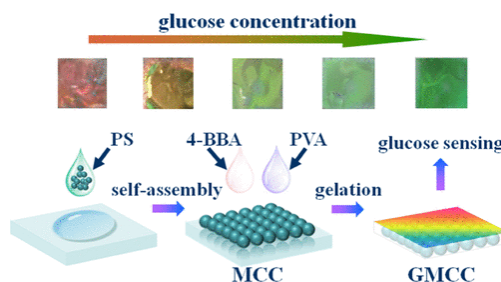


Figure 1.61: Schematic representation of a Tear Glucose Monitoring Sensor, via a 2D Photonic Crystal Hydrogel. The sensor efficiently exploits light diffraction, causing its structural color to shift progressively from red to green. This shift correlates with changes in glucose concentration spanning 0 to 20 mM, covering the physiological ranges observed in both tears and blood [88].

▪ **Lactate Detection**

Lactate, a vital metabolite formed in muscles, is present in varying quantities within diverse liquid biomarkers fluids inside or outside the body, that can effectively mirror the changes in blood concentration, via a range of metabolites, including lactic acid (Fig. 1.62) [76][85]. A particularly noteworthy stride in this domain, is the development of a versatile, cost-effective, and adaptable

wearable point-of-care biomarker patch. This innovation employs wax-printed channels on filter paper, to guide sweat towards the collection and biomarker detection zones, respectively [89]. Beyond this, the emergence of wearable electrochemiluminescence (ECL) devices is generating substantial excitement. A flexible and wearable ECL platform has been successfully engineered by Chen et al., to identify lactate and urea in human sweat, further propelling the potential of wearable technology within the domain of health monitoring devices [10].

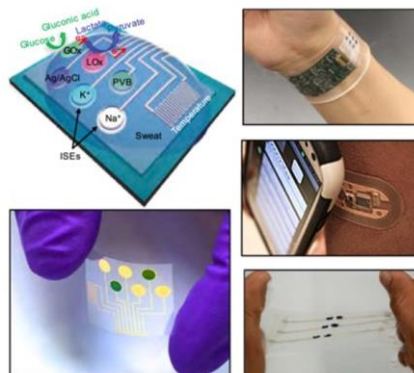


Figure 1.62: Schematic and visual representation of various of electrochemical sensors designed to analyze the levels of glucose, lactate, potassium, and sodium in sweat. This system is affixed to the wrist and integrates battery-operated electronics to capture digital signals and transmit them wirelessly via Bluetooth [90].

▪ pH Detection

Flexible wearable biomedical sensors with pH detection capabilities, represent a remarkable advancement in healthcare technology. These sensors, provide continuous and non-invasive monitoring of pH levels of acidity or alkalinity in various body fluids, holding significant diagnostic potential. For instance, in sweat detection, pH monitoring offers vital insights into an individual's hydration status. Furthermore, in saliva, it provides diverse indications of digestive health and metabolic disorders. In wound care, pH fluctuations may detect infection or impaired healing (Fig. 1.63) [72]. Consequently, the ability to harness pH information through wearable sensors, enables timely interventions and personalized healthcare strategies, ultimately improving the patients' quality of life.

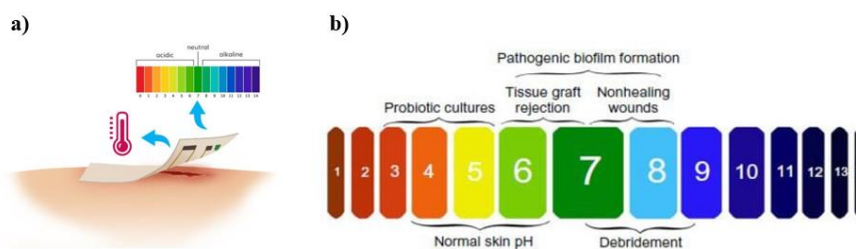


Figure 1.63: a) Presentation of a wearable sensor designed to detect wound-related biomarkers for wound healing monitoring process, b) Mapping of pH values during the wound healing process [91].

1.2.1.2 Types of Wearable Devices

A significant benefit that lies in the versatility of flexible sensors, is their optimal attachment across the body, seamlessly integrating into a variety of wearable platforms, including temporary tattoos, flexible bandages, gloves, contact lenses, and even smart textiles [92]. In pursuit of non-invasive continuous monitoring of health metrics, wearable systems connect to electronic modules, signal processing units, power sources, and display interfaces, via wired or wireless techniques [72].

Wearable systems provide essential insights into a person's health condition, by facilitating real-time health monitoring, and wireless transmission of the physicochemical signals, related to his well-being [76]. Recently, substantial strides have been made in developing wearable, non-invasive, health monitoring sensor designs, that prioritize comfort and data accuracy. This has been achieved through the integration of wearable platforms like patches, tattoos, bandages, microneedles, contact lenses, and watches, aiming to seamlessly blend the medical, electronic and material technology with the human experience [71].

▪ *Patches, Tattoos, Electronic Skin*

Recent strides in wearable sensor technology have led to innovative solutions, like epidermal patches and tattoos, which enable direct and non-invasive measurement of health parameters across different body regions [93]. These skin-integrated devices, fabricated with conductive materials and flexible substrates, through techniques like inkjet and screen printing, offer a dynamic approach to health monitoring [85]. Their flexibility allows them to adapt to the skin's surface, offering a comprehensive way to monitor various biomarkers, without any interference [94]. This technological progress aligns with the concept of skin-mounted epidermal electronics systems (EES), revolutionizing the way electronics interact with the human body. Embracing these sensors will significantly improve the quality of life, exceeding traditional systems in both comfort and functionality [94]. Among the latest innovations are the electronic tattoos (e-tattoos) and the electronic skin (e-skin), both characterized by their ultra-thin, flexible architecture, that adheres seamlessly to the skin, via van der Waals forces (Fig. 1.64) [84]. A recent breakthrough, includes the development of a bioinspired color-changing stretchable electronic skin, capable of multi-mode sensing. This technology, responsive to external stimuli, finds applications in diverse fields, ranging from interactive wearables, to health monitoring and beyond [94]. Moreover, temporary electronic tattoos designed for alcohol level detection, highlight the versatility of this approach. By transporting specific compounds to the skin, to induce sweat and trigger biochemical reactions, these tattoos offer a novel and efficient method for monitoring various markers [85].

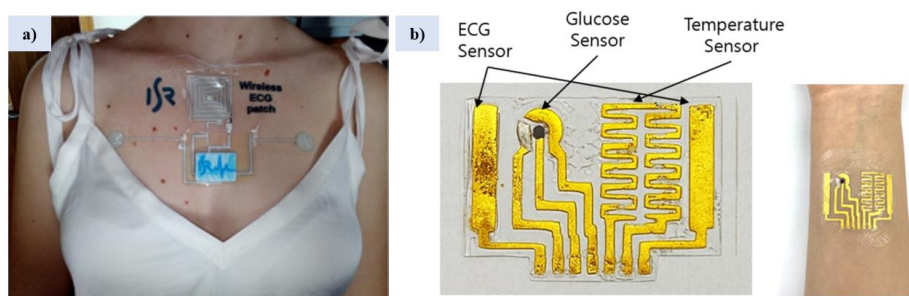


Figure 1.64: a) Visual representation of a completely wireless, battery-free biomedical e-tattoo with wireless energy harvesting techniques, securely attached onto the human body [95], b) Visual representation of a multi-purpose flexible wearable patch-type sensor (e-skin) on a PDMS substrate, attached around the wrist for visual reference [96].

▪ *Textiles & Smart Clothing*

Continuous health monitoring, has witnessed a significant boost with the rise of textile-based wearable sensors, which offer an array of advantages, including excellent air permeability, comfort, cost-effectiveness, and adaptability [52]. By utilizing common materials like cotton and polyester, these sensors may incorporate functional components capable of vital health biomarker detection [84]. Their integration with embedded microsystems and low-power wireless communication technologies has led to the realization of a personalized healthcare (Fig. 1.65) [52]. Notably, the convergence of nanotechnology and textiles, exemplified by conducting polymers, has established

the foundation "smart clothing" seamlessly integrating technology into our daily routines (Fig. 1.31). A prime illustration of this progress, is the implementation of a smart bandage designed for continuous monitoring of wound through pH levels sensing [52]. This evolution aligns with the emergence of body sensor networks, granting individuals the ability to continually track personal health metrics and environmental factors, while also facilitating the sharing of this valuable information, through online platforms and the cloud [97].

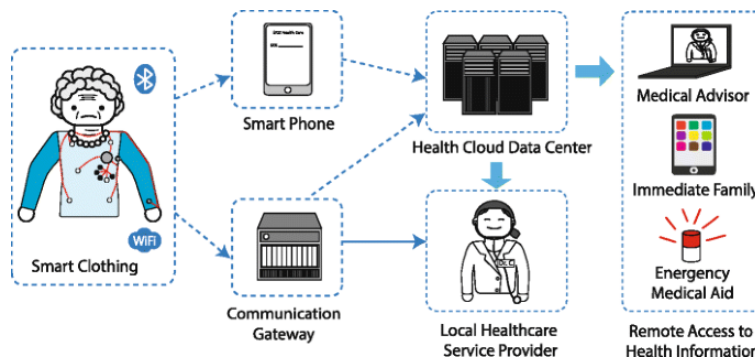


Figure 1.65: Smart Clothing for remote monitoring biomedical applications [97].

▪ Microneedles

The emergence of microneedles, stands as an alternative over conventional needles, notorious for their discomfort and invasive nature, which may lead to sensor detachment and unreliable muscle analysis, during the body's movements. Microneedles, with their minute punctures, facilitate painless application, and automatic healing in just a few hours, leaving no wounds (Fig. 1.66). Their main asset lies in the detection of biomarkers within interstitial fluid, a critical aspect of health monitoring. When coupled with shapeshifting capabilities, microneedles unlock heightened measurement accuracy and sensitivity, as well as a sense of comfort, particularly in unfavorable environmental conditions [99].

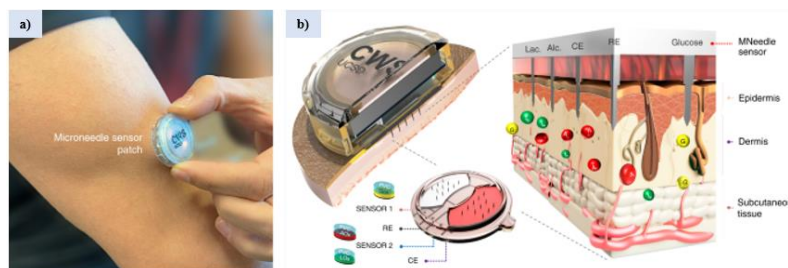


Figure 1.66: a) Visual representation of an integrated microneedles sensor attached to the arm, b) Schematic Illustration and Assessment of the Microneedle-based Sensor for Multi-biomarkers [100].

1.2.2 Wireless Biosensor Networks (WBSNs)

Healthcare is valuing extensively the development of early health threat detection platforms such as Wireless Sensor Networks (WSNs) and Wireless Biomedical Sensor Networks (WBSNs) for continuous physiological signal monitoring [101] in remote areas [102]. The objective is to develop micro/nano-scale systems for medical applications, capable of detecting and treating diverse diseases, by interacting with the body's tissues and organs [48]. This is exemplified by the emergence of compact wearable devices, integrated with wireless modules (wireless nodes) that connect the biosensors and the monitoring systems [71][103]. Integrated biosensors, wireless communication, and power harvesting, have led to advanced point-of-care (PoC) diagnostic devices (Fig. 1.67). These devices, equipped with micro-sensors and battery-less operation, constitute of the wearable mobile

medical monitoring systems (WMMMS) [99], which reshape the healthcare industry, via continuous real-time health monitoring, in secluded areas. Despite the considerable efforts made in advancing Wireless Biomedical Sensor Networks (WBSNs), challenges persist. Researchers aim to improve sensor sensitivity and sustainability, while addressing data management complexities, security issues, power and memory constraints, and real-time data transmission [104]. Consequently, strong security measures and wireless power supply systems are needed to prevent data mishandling and enhance the life-span of the WBSNs and WMMMS, for remote continuous health monitoring [105][106].

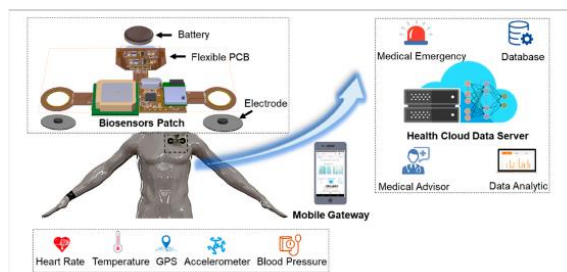


Figure 1.67: Broad representation of a wearable biosensor patch for point-of-care (PoC) systems within the mIoT field [107].

1.2.2.1 Electronics & Microcontrollers

The commercial and academic interest of wireless wearable electronics, propelled by the need for continuous health tracking, serves various roles, spanning from converting signals to wirelessly transmitting them (Fig. 1.68). [12][108]. Wireless body sensors revolutionize patient care, by measuring vital signs like heart rate and skin temperature, in a non-intrusive manner [109]. These compact devices, are the result of miniaturized circuits and imprinted bioelectronic patterns onto flexible surfaces [110]. The precision in measuring vital metrics, is achieved through their incorporation with microcontrollers and communication units, supported by a protocol management software, OS services, signal visualization systems, and wireless interfaces [70][71]. These devices, enhanced by the A.I, the embedded processing, and signal interpretation, pave the way for sophisticated wearables harmonizing with human life.

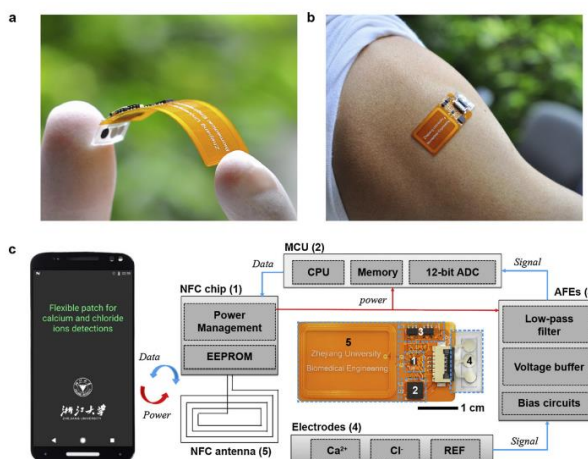


Figure 1.68: Image representation of a smartphone-driven, battery-independent flexible electrochemical patch, equipped with NFC technology [12].

In the domain of wearable electronics, the correlation between the flexible sensor’s materials and electronic circuit design in healthcare applications, remain unexplored. Therefore, a comprehensive analysis of the Printed Circuit Boards (PCBs), electronic components, and microcontrollers employed within Wireless Body Sensor Networks (WBSNs) is presented below:

▪ **PCBs**

The primary technologies employed in PCBs, are ‘through-hole’, and ‘surface-mount’. Through-hole technology was utilized initially, to establish connections by inserting metal leads into holes, followed by soldering. However, the prominence of surface-mount technology, emerged due to its compatibility with soft electronics, offering the comfort of connecting smaller components through pads on the PCB surfaces, and mounting them on both sides of the board [111]. Traditional rigid printed circuit boards (PCBs) consist of conductive pathways on insulating substrates. The direct attachment of electronic components to these substrates, necessitates the incorporation of printed electrical pathways. Yet, the constraints arising from the rigidity and form of the conventional rigid boards, introduce a range of complexities, during the design of flexible circuits. In response to these challenges, current research trends, lean towards the construction of flexible PCBs or printed flexible circuits (PFCs), which make use of thin films substrates, such as Kapton or polydimethylsiloxane (PDMS). In this domain, copper emerges as the preferred material for interconnections, manufactured through layer-by-layer processes, involving photolithography.

▪ **Electronic Components**

Wireless Body Sensor Networks (WBSNs) require electronic components with compact dimensions and efficient power consumption, to ensure their prolonged functionality. This array of components is embedded within flexible electronic systems, including sensors, signal conditioning hardware, filters, ADCs/DACs, MCUs, microprocessors, RF transceivers, batteries, and voltage regulators. Notably, their selection necessitates a delicate equilibrium between the energy efficiency, device size, and performance trade-offs [111]. For example, in scenarios where a single resource, like an ADC, must be shared among multiple data sources, a multiplexer proves invaluable. This mechanism enables the resource's connection to toggle between various data sources, proving its functionality in multiple analog sensors, that necessitate sequential ADC readings. A common practice in microcontroller design, is to incorporate multiplexers with internal ADCs. Furthermore, a common mechanism for mitigating noise, is by encompassing both thermal and RF interference. Within this context, the deployment of filters can also play a significant role for optimal noise elimination.

▪ **Microcontroller Units (MCUs)**

The progression of wearable technology results from the microfabrication of sensors and electronic systems, facilitated by microelectronics. Notably, the field of biomedical sensors has witnessed significant progress, through the manufacturing of microelectromechanical systems (MEMS), effectively integrated with elements like microprocessors and radio communication circuits. Microcontroller Units (MCUs) serve as the fundamental core of embedded systems, in flexible electronics. Their role encompasses an array of functions, such as data collection and management, signal conditioning and processing, and power supplies (Fig. 1.69). Their designs range from basic configurations, to those equipped with embedded peripherals, including ADCs/DACs and RF transceivers. While internal ADCs and DAC options exist in modern MCUs, their sampling rates and bit resolution might not align with high-resolution applications. In such scenarios, where the sensor's signal-to-noise ratio output is low, external ADCs present an advantageous option, offering higher bit precision [111]. The selection of the proper microprocessor involves a consideration of various factors such as physical dimensions, power consumption, clock speed, and an array of available peripherals (UART, I2C, SPI, and external I/O pins). Datasheets provide valuable assistance in determining the compatibility of a microcontroller with the intended tasks.

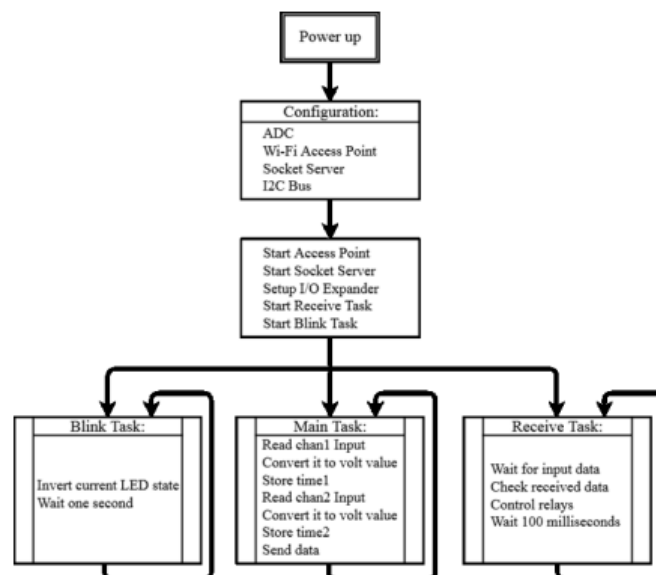


Figure 1.69: MCU function diagram [112].

Although in most cases, contemporary microprocessors effectively fulfill the requisites of flexible electronic systems, their integration into a Wireless Body Sensor Network (WBSN) device and Wearable Mobile Medical Monitoring Systems (WMMMS), requires vital attention and evaluation of the RAM and flash memory capacity, to prevent potential data loss. Moreover, ensuring data accuracy and reliability, is critical in healthcare integrity maintenance. Therefore, the incorporation of Field Programmable Gate Arrays (FPGAs), characterized by power-efficient configurations and optimized hardcore blocks, offers various attributes encompassing adaptability, high performance, processor support, and cost-effectiveness, collectively enhancing the device's architectural optimization for cryptographic algorithm execution [101].

Within the realm real-time data monitoring in wearable sensor technology, numerous advancements have been conducted, involving the integration of microcontrollers. For example, Jang et al., researched into the convergence of a heat-patch with a microcontroller unit (MCU), that possesses wireless capabilities for data transmission and reception (Fig. 1.70a) [203]. Additionally, a flexible oxygen sensor with precise sensitivity and linear current output was successfully developed by Mustafalu et al. The amplified signal originating from the oxygen sensor establishes a connection with the readout electronics (Fig. 1.70b). [113] Fu and Guo introduced an innovative medical smartphone, with a built-in electrochemical analyzer for real-time blood monitoring (Fig. 1.70c). Through its seamless integration with the analyzer, the smartphone measured enzymatic reaction currents, using disposable test strips that convert biochemical signals into electrical ones. An ADC captured the resulting electrochemical current, which was then analyzed by the MCU within the platform. The collected data is then stored and seamlessly transmitted wirelessly to a dedicated personal health management center [114]. Moreover, Benatti et al., presented an embedded system with an ARM Cortex M4 MCU integration, designed to recognize hand gestures in real-time, through EMG signals (Fig. 1.70d) [115]. Consequently, the advancements witnessed in Wireless Body Sensor Networks (WBSNs) exhibit significant potential for transforming real-time health monitoring, revolutionizing the medical care hospitalization, and eliminating the need for prolonged hospital stays.

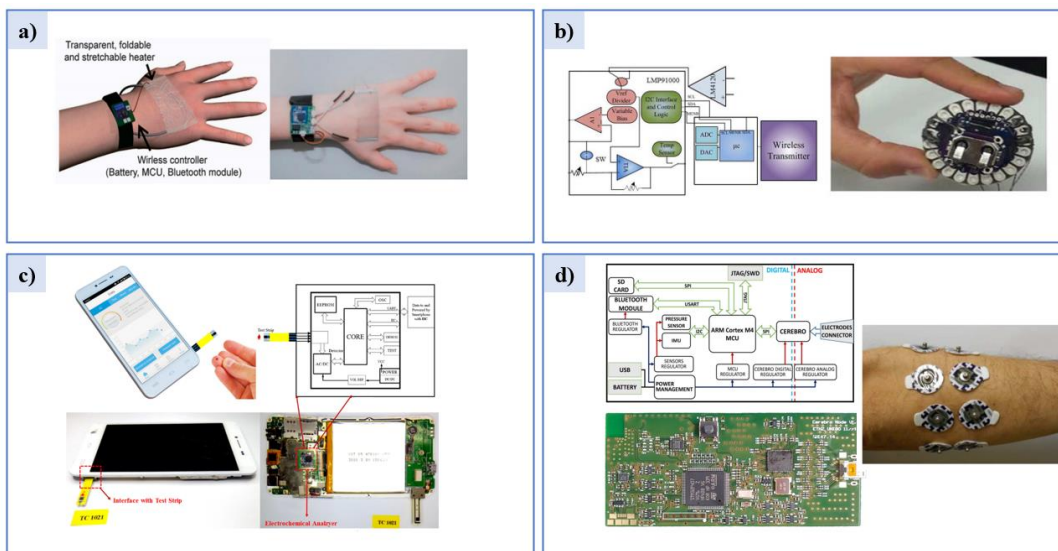


Figure 1.70: Real-time data monitoring wearable sensors, incorporating microcontrollers: **a)** Visual Representation of a Heat-Patch System on the arm [203], **b)** Flexible oxygen monitoring sensor incorporated with an LMP91000 electronic setup [113], **c)** Electrochemical real-time blood monitoring with an integrated MCU platform [114], **d)** Hand gesture recognition device with an incorporated ARM Cortex M4 MCU for real-time data management [115].

▪ Batteries & Energy Sources

Despite the remarkable progress in wearables, they still rely on external energy sources to power their sensing platforms [71]. While potential solutions like flexible batteries, offer promise for addressing wired power supply issues in WBSNs and WMMMS, they introduce their own set of challenges, such as compromised electrochemical performance, limited feasibility for battery replacement [116], and safety concerns, regarding toxic components [117]. In contrast, the unexploited biomechanical energy within the human body, shows great promise in power reservation, via the development of flexible nanogenerators and self-powered wireless electronics (Fig. 1.71). These advances offer a fresh perspective on wearable electronics, driven by mechanisms like [118]:

- ✓ Energy Harvest (Thermoelectric, Piezoelectric, Triboelectric, Pyroelectric, Hydrovoltaic)
- ✓ Wearable Batteries/Power Systems
- ✓ Energy Storage Components (Flexible super-capacitors and Lithium-ion batteries)
- ✓ Wireless Power Transfer (RF Antennas)
- ✓ Biofuel & Solar Cells

Such pioneering approaches not only solve power-related problems, but also persuade researchers to explore self-powered technologies for wearable devices [7][93].

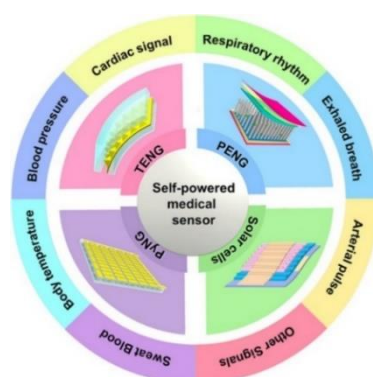


Figure 1.71: Schematic Representation of Self-Powered Medical Sensors [119].

1.2.2.2 Wireless Communication

Wireless technology is vital for the seamless data transmission from biomedical sensors to external receivers, meeting the demands for real-time data bioanalysis. [14][120]. Remote monitoring replaces traditional hospital visits [94], by wirelessly transmitting patient data to medical centers, and alerting clinicians in emergencies, enhancing, therefore, patient care and safety (Fig. 1.72) [70][102]. Consequently, there is a concerted effort in integrating wireless electronics into wearables, and mobile devices, improving their usability and alleviating the prolonged hospital stays [72].

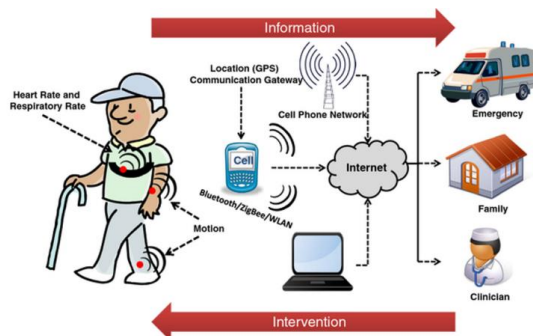


Figure 1.72: Wearable Biosensors capable of remote real-time health data monitoring [70].

Recent developments have given rise to wireless wearable biosensing platforms, integrating wireless technologies like Bluetooth, Wi-Fi, NFC, and RFID (Fig. 1.73) [27]. These innovations enable the wireless interaction between the sensing devices and mobile gadgets, including smartphones, tablets, smartwatches, or laptops [72].

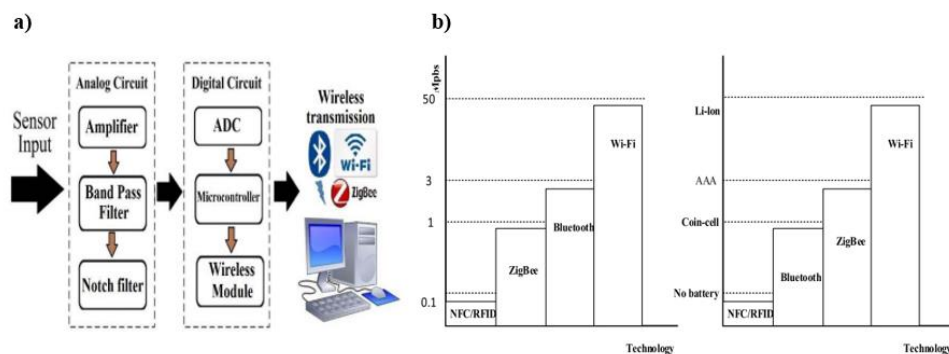


Figure 1.73: a) Schematic representation of the interaction between the sensing device and the outside world via wireless communication technologies [104], b) Graphic representations comparing the wireless communication technologies [99].

Bluetooth

Bluetooth (BT) technology has become increasingly significant in wirelessly connecting devices, primarily due to its cost-effectiveness, compatibility [99][104], and high-speed communication capabilities (1 Mbps) [111]. Operating within a 10-meter distance range, BT employs short-wavelength radio signals, to facilitate energy-efficient data exchange [121]. Notably, Bluetooth operates to globally available RF communication protocols, supporting a wide array of devices, including mobile phones, laptops, and peripherals [99]. Specifically, the communication occurs within the 2.4-5GHz industrial, scientific, and medical (ISM) band, employing electromagnetic (EM) waves for efficient data transmission and rapid speeds. Additionally, with variations like Bluetooth BR/EDR and Bluetooth Low Energy (BLE), BT technology covers a variety of needs. The incorporation of commercial microcontroller modules featuring Bluetooth communication technology, significantly streamlines their integration into existing sensors [116]. While BT remains a favorable choice for many consumer applications, its moderate power consumption requires careful

consideration. Additionally, Bluetooth networking demands the support of prevalent networking protocols like IPv4, IPv6, and IPX, besides other widely used protocols [122]. Beyond its utilization in mobile phones and computers, BT is a favored short-range distance wireless solution for flexible WBSNs and SoCs, allowing patients to enable remote transmission of vital signals, for healthcare monitoring [111].

▪ **Wi-Fi**

Following the IEEE 802.11 standards, Wi-Fi acts as an intermediary link for data transmission between smartphones, sensors and servers. This technology revolutionizes wireless networks and outperforms Bluetooth [99][111]. Despite its high energy consumption, Wi-Fi brings high-speed communication and data security benefits, to Wireless Body Sensor Networks (WBSNs) and Wearable Mobile Medical Monitoring Systems (WMMMS). Furthermore, it provides rapid internet access, through access points (APs), as well as seamless device connectivity, including smartphones, tablets, and laptops. Operating mainly in the 2.4–2.5 GHz and 5.7–5.8 GHz radio bands, Wi-Fi offers broader transmission ranges, and faster data rates, compared to the RFID platforms [99][111]. Noteworthy, Wi-Fi modules often used in flexible electronics and especially WBSNs, include the CC3235SF SoC from Texas Instruments, the ESP32 SoC from Espressif Systems, and the ATSAMW25 module from Microchip [111]. The Wi-Fi's integration in telemedicine and wearables, accelerates the transfer of patients' health data to medical professionals, enhancing both the healthcare efficiency and patient experiences.

▪ **RFID**

RFID technology initially introduced the Machine-to-Machine (M2M) concept, via radio waves for contactless object identification within short ranges [116]. It encompasses transceivers and chips, both necessitating a tag and a reader, for correct functionality. The process involves queries being sent by the reader to the tags, who in return receives the reflected signals. These signals are then processed by a database, which identifies objects within a 10 cm to 200 m range [104]. RFID tags come in three types [104][116]:

1. Active (battery-powered)
2. Passive (battery-free)
3. Semi-Active/Passive (selectively powered).

Additionally, in terms of frequency selection, RFID systems are divided into [116]:

- a. Low-Frequency Identification (LFID), spanning a few hundred Hz to kHz;
- b. High-Frequency Identification (HFID), up to several MHz;
- c. Ultrahigh-Frequency Identification (UHFID), around a thousand MHz;

In essence, RFID's pivotal role is evident in WBSNs, WMMMS, and flexible electronics. Its contactless nature and adaptability, contribute to its versatile integration into flexible materials. These benefits underscore their significance in advancing interconnected and intelligent systems, revolutionizing in healthcare monitoring and applications across various industries.

▪ **NFC**

Near Field Communication (NFC) stands as a short-range wireless data transmission system, enabling electronic devices to communicate wirelessly within a 10 cm radius. Operating at 13.56 MHz, NFC achieves data transfer, at speeds around a few hundred Kbit/sec. This technology utilizes electromagnetic induction [69], working in both active and passive modes for wireless data exchange

[99][116], while serving as a battery-less energy converter [123]. Its compatibility with existing communication methods like RFID and Bluetooth, has led to its popularity in contactless cards, smartphones, WBSNs, WMMMS, among other industries [99].

1.2.3 Internet of Things (IoT), Apps for Data Representation & ESP32 Module

The impact of mobile technology on Biomedical Engineering is noteworthy, especially in enhancing healthcare devices for continuous patient monitoring and instant data accessibility, to medical professionals [124]. The growing healthcare sector, driven by global aging, is exploring solutions like the Medical Internet of Things (mIoTs) [125], which employ budget-friendly sensors and wireless connectivity advancements. This combination, facilitates data collection/processing, and Wi-Fi-accessible services, catering to remote health monitoring, via WBSNs and real-time data storage needs [125][126]. Key to this – for this project – is the ESP32 microcontroller, essential for remote patient monitoring and telemedicine, due to its sensing and wireless capabilities [126]. As mobile apps evolve, they enable real-time doctor-patient communication, via a unified cloud platform, vital in both IoT and healthcare contexts [122]. The integration of IoT into our daily lives, drives a promising healthcare industry, fostering economic growth and innovative solutions. The synergy of IoT and machine learning holds the potential for even further advancements [127].

This unit focuses on recent IoT strides, examining the development of health data display apps for patients and doctors, through mobile gadgets and desktops. Additionally, it highlights the ESP32 microcontroller's role in mIoTs, due to its wireless capabilities within Wireless Body Sensor Networks (WBSN) and Wearable Mobile Medical Monitoring Systems (WMMMS).

1.2.3.1 Internet of Things (IoT)

Remote Patient Monitoring (RPM), employs Internet of Things (IoT) technology to consistently observe the patient's health relaying data, to medical professionals, via the internet. This method facilitates web-based health tracking accessibility, through common browsers [124]. The IoT industry's rapid growth, driven by communication needs, necessitates efficient device connectivity [112]. Therefore, IoT-Cloud medical frameworks ensure secure data sharing, enhancing the patient's healthcare (Fig. 1.74) [125]. In cases requiring for an IoT device to wirelessly connect to IP networks, a prevalent approach involves intermediary gateways, aiding local and IP network connection, via connection protocols like Bluetooth or Wi-Fi [111].

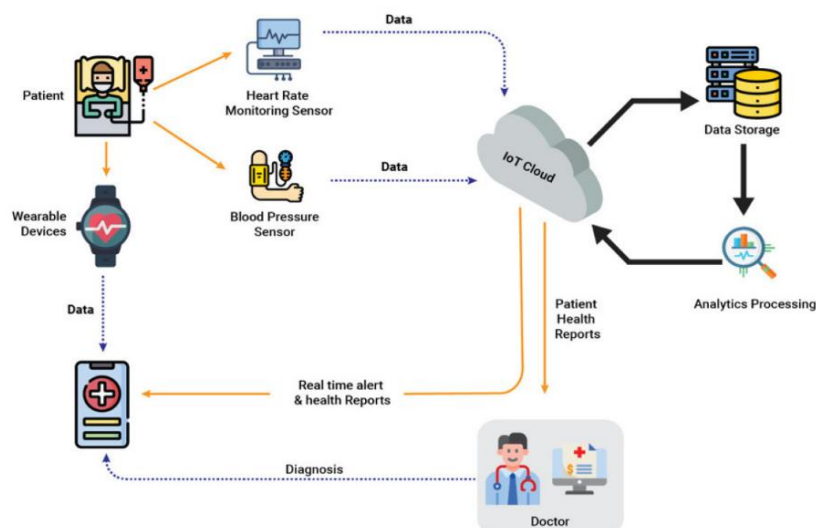


Figure 1.74: Schematic Representation of the IoT-Cloud in remote healthcare monitoring [128].

The optimal functionality of an IoT system, requires certain crucial components to be considered, including (Fig. 1.75) [121]:

- ✓ **Identification:** Each IoT device requires a unique IP address, facilitated by the IPv6 and IPv4 protocols, for its wireless connection real-time data monitoring.
- ✓ **Sensing:** IoT's sensing involves the data collection from the interconnected objects.
- ✓ **Communication:** IoT's diverse communication technologies unite heterogeneous objects, to offer tailored smart services. Protocols like Wi-Fi, Bluetooth, RFID and NFC, enrich this network.
- ✓ **Cloud Platforms:** The cloud serves as a center for data transmission and analysis.



Figure 1.75: IoT Components [121].

Recently, there has been a notable progression in WBSNs and WMMMS, driven by the integration of IoT technologies and applications. For example, a cutting-edge mobile IoT healthcare system, uniting smart phones and 5G for patient risk monitoring, was developed by Nasri and Mtibaa [122]. Moreover, a wearable sensor with wireless capabilities introduced by Kumar et al., enhances road safety, by preventing car accidents. The sensor device, affixed to the driver's hand, measures the body temperature and heart rate. Abnormal readings trigger the control unit to compare against standard values, subsequently activating the vehicle's relay. The corresponding data is continuously transmitted to an IoT cloud, via an ESP8266 Wi-Fi module [129].

Despite its potential, the Internet of Things (IoT) is also accompanied by substantial challenges. One notable limitation involves the constrained memory capacity in numerous IoT nodes, which prevents direct IP-based connections. Another issue pertains to the establishment of a standardized universal connection protocol [122]. Consequently, dependable communication is vital, necessitating for software-hardware integration. Furthermore, the efficient management of numerous IoT devices, presents additional constraints, since the addition of any device, should not degrade the existing one's quality. Therefore, this issue necessitates coordinated efforts to ensure seamless service delivery, through diverse hardware, and communication protocols [121]. Moreover, data integrity and privacy concerns are a key barrier for IoT devices, due to the absence of a standardized IoT security framework, underscoring the need for robust safeguards, for controlled data exchange. Overall, the incorporation of IoT into flexible wearable mobile devices, marks a pivotal advancement, with profound implications. This synergy empowers real-time health monitoring and data-driven insights, catalyzing major shifts, in healthcare and beyond. As these technologies converge, they hold the potential to elevate the quality of life, redefine patient care, and propel innovations across various industries.

1.2.3.2 Android System & Apps for Data Representation

Mobile gadgets are pivotal in wearable and portable biomedical sensing systems, owing to their worldwide utilization, multifunctional attributes, and great connectivity. Smartphones, in particular, have significantly impacted mobile health, and point-of-care (POC) testing, driving notable

advancements in the healthcare sector [12]. Unlike traditional data loggers, smartphones offer a versatile platform as gateways, while their processing units, capitalize their significant computational power, within compact dimensions [70]. With features like high-resolution cameras, memory, display, and a range of wireless connectivity options, smartphones are well-equipped for biomedical sensing tasks [123]. This enables users to upload on the web, their medical status to personalized health centers, granting access to remote medical care.

The evolution of healthcare via mIoT platforms, is evident, through the adoption of Android and Web applications (Fig. 1.76). These tools not only enhance patient safety, but also elevate the overall quality of healthcare operations. Consequently, a comprehensive mobile application empowers the patients' data, by seamlessly integrating them into the IoT framework, offering convenient access to their medical records, and fostering a more informed patient experience.

This integration allows them to:

- a. monitor their health parameters,
- b. monitor their health parameters,
- c. and effortlessly share real-time medical test results.

A vital component in IoT healthcare platform design involves the Multi-Protocol Unit. This unit undertakes a series of steps, like:

- ✓ device detection,
- ✓ assessment of accessory mode support,
- ✓ initiation of accessory mode, if necessary,
- ✓ and establishment of communication through the Android accessory protocol.

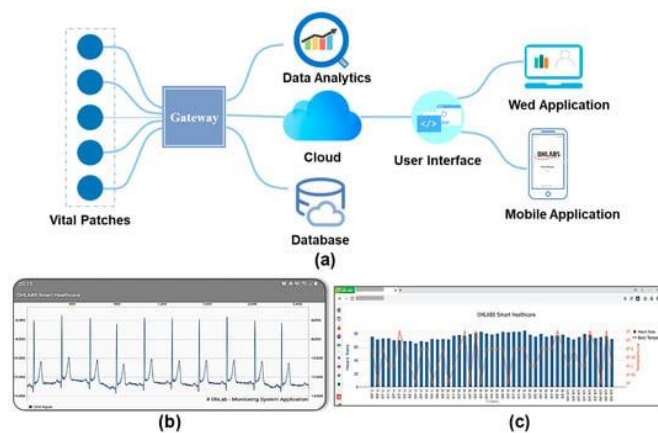


Figure 1.76: Schematic Illustration of an mIoT System [130].

The architecture of the Internet of Things (IoT) platform pays attention to certain key elements: the multi-protocol unit, and the web and mobile apps. The collaboration of these elements facilitates the collection and transmission of the sensor's data, through Android interface and/or web applications, which wirelessly display the data, via Wi-Fi, or Bluetooth wireless technology.

▪ Android Interfaces

The Android interface functions as a channel for data transmission from the Wireless Body Sensor Networks (WBSN) to mobile gadgets, via Wi-Fi or Bluetooth. In order to establish this communication, the app necessitates permissions for web-based data transfer to the remote devices. Within the Android's interface, device specifications and drivers are implemented, while reinforcing the Hardware Abstraction Layer (HAL). This layer holds significant importance, as it establishes the wireless connection, between the Android platform and the hardware. The open-source nature of the

Android Operating System (OS), not only promotes collaboration and innovation within the software community, but also underpins its adaptability, and extensibility. The Android system's Compatibility Test Suite (CTS), ensures reliable application execution. Despite its versatility in smartphones and tablets, the Android OS poses certain challenges, such as reliability, stability, and security. Additionally, despite its flexible framework – under the Apache license that allows source code modification – it exposes certain vulnerabilities, like demand for robust security measures, and intellectual property rights preservation [122]. Leaving these challenges aside, Android's compatibility has enabled the implementation of diverse, user-friendly, health-oriented solutions, that empower individuals to remotely take charge of their well-being. The synergy between Android and wearable biosensors, has paved the way for real-time data collection and analysis.

▪ **Web Applications**

In the field of web applications, the mIoT domain, interfaces with various communication protocols, for web and mobile platforms. Among them, the Hypertext Transfer Protocol (HTTP) emerges as a prevalent selection, due to its widespread server support and compatibility. However, a key drawback of this protocol is its lack of built-in security, as it does not provide any encryption for the data transmitted, between a client and a server. Additionally, the utilization of this protocol in Web applications, faces challenges in maintaining persistent connections for real-time data updates. This results in ongoing requests for new data from the browser to the server, leading to reduced speed, and heightened consumption. Consequently, this protocol proves unsuitable for scenarios where there is a necessity for swift and repeated data updates. On the other hand, Web Sockets is a recent communication protocol, that aligns with the web application standards, for continuous monitoring. This protocol exchanges addressing and handshake mechanisms with the familiar HTTP protocol, making it an ideal candidate for real-time, two-way interaction [122]. Notably advantageous in shared hosting and proxied gateways, Web Sockets demonstrate both compatibility and high-performance capabilities.

1.2.3.3 ESP32 Module

The Espressif ESP32 is a 32-bit microcontroller chip that boasts a dual-core design [125] and stands out as an efficient, and budget-friendly solution for mIoT projects [129], whose cost-effectiveness lies in its advanced system-on-chip (SoC) structure. The ESP32 MCU, incorporates a radio unit that operates at 2.4 GHz for Wi-Fi, and dual-mode Bluetooth Low Energy (BLE) v4.2 radio technology [125][131], all driven by a dual-core Tensilica Xtensa LX6 CPU, using the Harvard Architecture [112]. This CPU houses the microcontroller's internal and external memory (448 kB/ROM, 520 kB/SRAM, two 8 kB RTC memory, and 4MB of flash memory), as well as its peripheral components (eighteen 12-bit ADC pins, four SPI units, two I2C units) (Fig. 1.77). One of the greatest advantages of this platform, is that it offers a power management module (sleep, light sleep, deep sleep mode), to optimize its performance and energy consumption, along with filters and amplifiers for noise-errors elimination. Its GPIO pins serve as interfaces for ADCs/DACs, touch sensors, and other functions such as UART, I2C, and SPI [112], enabling a seamless connectivity with an array of sensors and actuators, making the ESP32 an especially relevant MCU, in healthcare applications [125]. Its programming interface, includes compatibility with both C and C++ languages, alongside a rich set of API libraries, simplifying the software development in environments like the Arduino IDE, and the PlatformIO on Visual Studio Code. These components collectively enable the wireless communication, between medical professionals and patients [112].

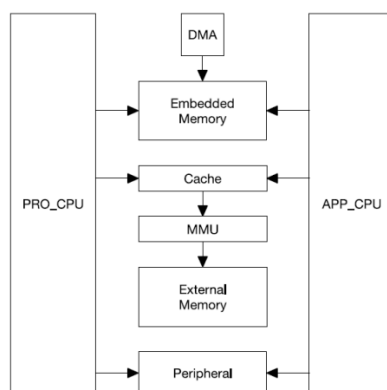


Figure 1.77: Architecture of the ESP32 MCU [112].

In practice, the ESP32 collects health-related data from sensors, and transmits it remotely to IoT platforms. The collected data undergoes processing before being wirelessly transmitted, via the ESP32's Wi-Fi or Bluetooth network, to a central server. The data is usually presented with a password-protected application, which users can access through their computers or mobile devices [132]. This innovative approach redefines how healthcare data is accessed and shared, marking a significant transformation in the medical field.

Many researchers have incorporated the ESP32 MCU into wearable, flexible sensors, enabling remote wireless monitoring and real-time health-related data display, for both patients and doctors. For example, an innovative client-server model developed by Parate and Sharma, for vital body signs tracking via Wi-Fi connection, features two ESP32 Node MCU boards, one serving as the server; which collects the health-related data, and the other as the client (Fig. 1.78a). This technology guarantees secure data transmission through Wi-Fi authentication, and display via the web, making it accessible on various mobile devices and desktops [124]. Another recent advancement presented by Abilesh et al., introduces the iMedBox; a smart medication dispenser (Fig. 1.78b). This device is responsible for health-related reminders and monitoring, facilitated by a smartband onto the patient's arm. This smartband tracks vital health metrics, ensuring uninterrupted connectivity and quick data display facilitated by the ESP32 MCU, which serves as a crucial communication link between the medical experts and patients [133].

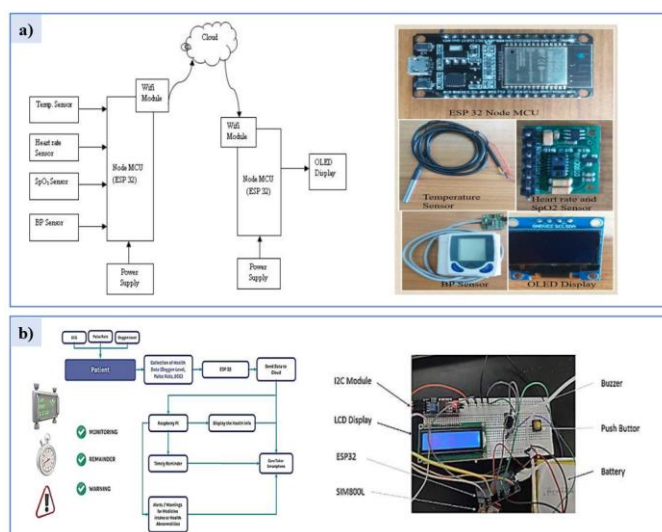


Figure 1.78: a) Schematic Illustration and electronics components used for the development of the client-server model for vital body signs tracking [124], b) Diagram Flow of the iMedBox and visual representation of the prototype circuit [133].

ESP32-WROOM-32 / ESP32-WROOM-32D

The ESP32-WROOM-32 module, seamlessly integrates into custom PCBs, making it a perfect fit for wireless flexible wearable devices in mIoT applications [112]. Its core, being the ESP32-D0WDQ6 SoC, comes with a 4 MB SPI Flash memory. This chip stands out with two adjustable CPU cores, with adjustable clock frequencies, ranging from 80 MHz to 240 MHz. An additional energy-efficient co-processor heightens the power efficiency of the peripheral tasks. The module's rich features encompass capacitive touch sensors, SD card interface, Ethernet, high-performance SPI, UART, I2S, and I2C capabilities [134]. The ESP32-WROOM-32's unique strength lies in its integration with Wi-Fi, and Bluetooth (BLE) modules, enhancing its versatility across applications in various industries. A standout feature, is the chip's minimal sleep current, under 5 μ A, constituting it a viable choice for wearable and battery-powered electronics. This module supports data rates up to 150 Mbps and antenna output power of 20 dBm, [134], emphasizing to its superior performance in integration, power efficiency, and wireless connectivity.

The ESP32-WROOM-32D MCU (Fig. 1.79), emerges as a truly affordable choice for integration into wireless wearable devices, featuring flexible electronics for biomedical applications. The module's dual-core architecture, of 520 KB SRAM [135], 32 MB SPI flash and 40 MHz crystal, not only ensures optimal performance, but also supports the intricate requirements of biomedical data processing [136]. Its capabilities span from low-power sensor networks to high-intensity tasks including voice encoding, music streaming, and MP3 decoding [137]. Within the field of wearable biomedical innovations, the ESP32-WROOM-32D stands as a great example to cutting-edge technology, meeting the intricate demands of human well-being.

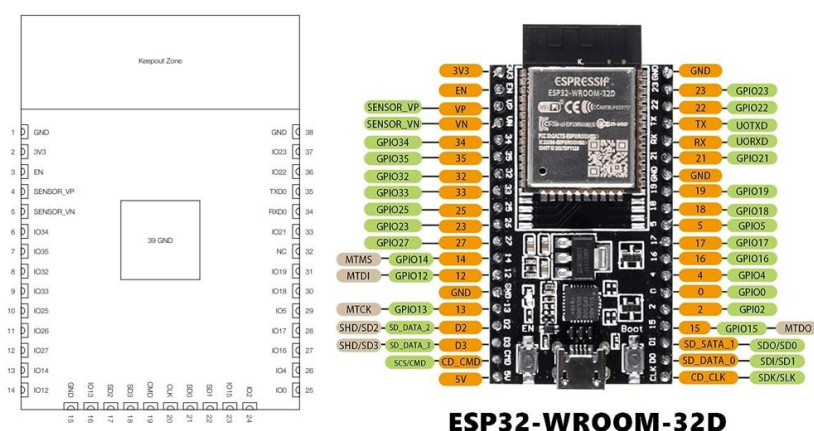


Figure 1.79: ESP32-WROOM-32D Pinout [137][138].

1.3 Flexible Temperature Sensors

The field of health monitoring, has witnessed tremendous interest in the utilization of stretchable and highly responsive, non-invasive temperature sensors, replacing conventional thermometers [109]. These sensors find their significance within wearable systems, used for diagnostic and therapeutic purposes [139]. Skin temperature measurements provide valuable insights into an individual's health condition, ranging from metabolic interpretation, to disease prediction [32]. To fulfill these needs, the development of conformal, intelligent flexible temperature sensors becomes essential [140]. These sensors, boast both heightened sensitivity and a lightweight design, enabling their seamless integration not only to the human skin [19], but also the human organs [140]. Designed with cutting-

edge materials and inventive architectures, flexible temperature sensors, hold substantial potential for diverse applications, including medical electronics, soft robotics, and even bionic skin.

Temperature sensing is highly relevant in various domains, including its crucial role in artificial skin, for touch sensing and long-term physiological monitoring [141], for promptly identifying early health conditions [116][141]. To address this requirement, high sensitivity and low mechanical modulus, are vital for detecting minor temperature fluctuations, and ensuring body compatibility. Additionally, temperature sensors need to possess specific attributes, including stability, robustness, high sensitivity, precise measurement capabilities, flexibility, biocompatibility, repeatability, a lightweight design, rapid response times, and wireless communication capabilities (Fig. 1.80) [72][142]. Furthermore, self-powered temperature sensors extend their operational lifespan by harnessing energy from body heat and movement, contributing to an enhanced user comfort [143].

Flexible temperature sensors are divided into active-matrix and passive-matrix sensors [143]:

- Active-matrix flexible temperature sensors, stand out by incorporating storage components, such as transistors or diodes.
- Passive-matrix flexible temperature sensors, maintain a simpler structural arrangement



Figure 1.80: Flexible Patch for Temperature Monitoring through the IoT, developed by NAMI [144].

Several research developments illustrate the recent advancements of flexible temperature sensors, with a majority of them, incorporating wireless communication technologies to propel their evolution into sophisticated, adaptable devices in smart technology. For instance, Honda et al. introduced an innovative printed smart bandage, which features integrated wireless antennas, microelectromechanical systems (MEMS), and sensors, enabling real-time temperature tracking on the skin [139]. Rao et al., examined an FPGA-based experimental framework, for continuous body temperature tracking and secure data transmission, incorporating measures for data integrity assessment (Fig. 1.81) [101]. Yun et al., proposed a low-power (below 3mW) wireless sensor patch system, for real-time Heart Rate (HR) and Body Temperature (BT) monitoring, via Bluetooth communication (Fig. 1.82) [145]. Additionally, a pioneering approach of Artificial Neural Networks (ANNs)-based Continuous body Temperature Measurement (CBTM) was introduced by Song et al. This device, significantly reduces the sensor's reaction times, while simultaneously enhancing the precision of the CBTM results [146].

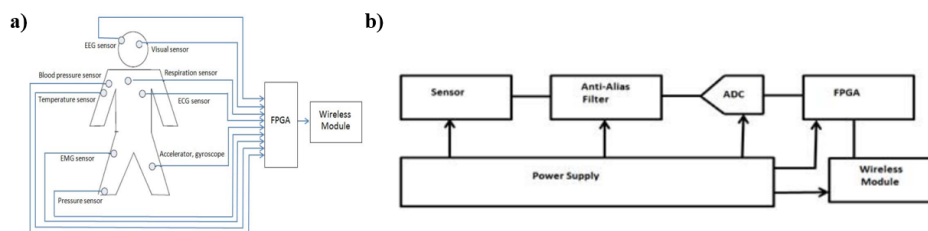


Figure 1.81: a) Representation of the suggested structure for a Wireless Body Sensor Network (WBSN) based on FPGA technology, b) Diagram Flow of the overall FPGA-based system [101].

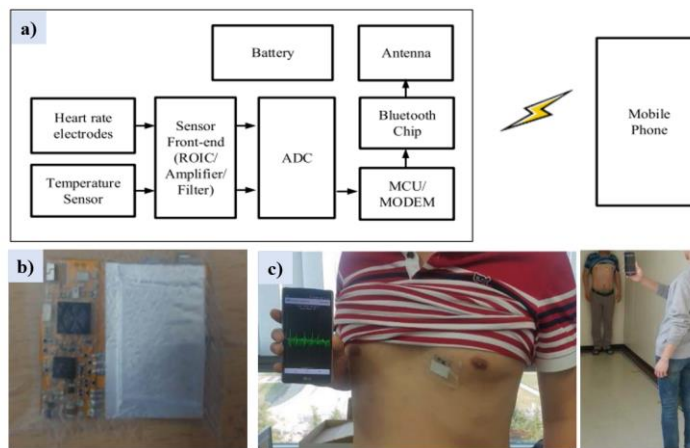


Figure 1.82: Wireless Detection Patch System for real-time Heart Rate (HR) and Body Temperature monitoring via BT communication: **a)** Flowchart of the Sensor Patch, **b)** Visual representation of the Detection Patch, **c)** Visual image of the sensor patch on the body, for real-time data display on the mobile phone [145].

Despite the significant progress of skin temperature detection, there are still several obstacles that continue to exist. One area of concern, lies in the field of medical applications, where a need for greater sensitivity (0.01 °C) is essential, to ensure precise detection, even during the body’s movement [147]. Additional requirements regard detailed temperature mapping, through scalable temperature arrays. Moreover, further limitations refer to quicker response times [146], the incorporation of multiple detection functions, as well as power supply and management [143]. These factors are vital to unlock the full potential of flexible temperature sensors in real-world scenarios.

1.3.1 Skin Temperature

The human body temperature is a dynamic parameter, influenced by both internal and external elements. The intricate thermoregulation mechanism within the human body, guarantees that its temperature remains close to 37 °C; a vital marker for the effective operation of organs, metabolic activities, and the immune system [72]. Therefore, temperature fluctuations may have a big impact on an individual’s physical and mental performance [148], as the body’s temperature regulation system, involves both the internal and the outer parts of the body [149]. Since temperatures in different body areas vary, monitoring them is important for potential illness identification. These variations are influenced not only by internal, but also by external factors (Fig. 1.83) [149]. Realizing the serious health-effects that body temperature might cause, ongoing real-time temperature monitoring is pivotal for the preliminary management of health-related issues, such as fever, inflammation, injuries, and blood circulation [72].

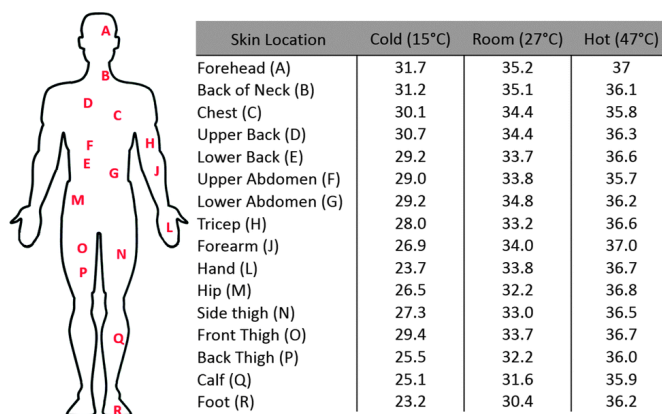


Figure 1.83: Body Temperature variations across various body parts and different ambient conditions [150].

Despite the significant attention of the body temperature's continuous tracking in consumer devices, the measurement of skin temperature often goes unnoticed [151]. Skin not only serves as a protective layer for internal organs, but also possesses impressive abilities, in temperature regulation and sensing stimuli. Moreover, it plays a vital role in indicating the heat dispersion from the body's core, via blood circulation. An essential element in maintaining a steady temperature, involves a stable equilibrium between the heat generation and its release, through body actions like muscle contractions, and sweating [152]. Therefore, a thorough comprehension of the thermoregulation mechanism requires constant observation of both the humidity and surface temperature of the skin [152]. Apart from external conditions [153], clothing functions can also influence the distribution of skin temperature as an extension of its control, reducing the energy needed to maintain a stable body temperature. Moreover, an array of factors, such as exposure to sunlight, contribute to the dynamic interaction, between the skin and its surroundings [154]. Consequently, the accurate readings of skin temperature, often face challenges, arising from multiple factors including the amount of physical activity, and the environment's temperature, necessitating the fabrication of well-calibrated models, that can filter out any disruptive variables, while extracting the clinically valuable insights [151].

The domain of wearable electronic gadgets, arises an urgent requirement for electrically responsive sensors, that not only make direct contact with the human skin, but also exhibit visible indications of temperature fluctuations [155]. Hence, substantial research revolves around the implementation of flexible temperature sensors, that not only provide high precision and dependability when subjected to deformation, but also possess the capacity to reflect these temperature shifts [156]. This essential pursuit, is fueled by the aspiration to establish effective techniques for real-time and non-contact measurement of localized human skin temperature, holding significant potential for overseeing skin temperature in wearable devices [157].

Certain developments in flexible skin temperature sensing devices have emerged recently. McNeill et al., outline the fabrication of a wearable wireless sensor patch system, for continuous epidermal temperature, pressure and humidity measurement, powered by a polymer battery (Fig. 1.84a) [158]. Similarly, Huan et al. designed a wearable wrist device with BLE wireless communication capabilities, to continuously identify gradual skin temperature fluctuations, that could potentially indicate the presence of an illness or infections (Fig. 1.84b) [151]. Furthermore, a highly sensitive electronic skin (E-skin) sensor that simultaneously evaluates and displays the skin's temperature, via a biocompatible hydrogel with thermo-responsive transparency and resistivity adjustments, was introduced by Park et al. [155] Lastly, a study by Lu et al., is related to an inventive method, using a flexible wireless sensor sheet to examine how the finger responds to monitoring temperature and moisture changes. The approach combines a humidity sensor based on ZnIn_2S_4 nanosheets, with a temperature sensor using carbon nanotube/ SnO_2 technology. The integrated sensor is affixed to a volunteer's finger, who experiences both warm ($26\text{ }^\circ\text{C}$) and cold ($> 26\text{ }^\circ\text{C}$) room conditions, transmitting data to a smartphone, via Bluetooth technology (Fig. 1.84c). This method offers potential for continuous real-time monitoring of thermoregulatory processes, through adaptable sensor sheets [152].

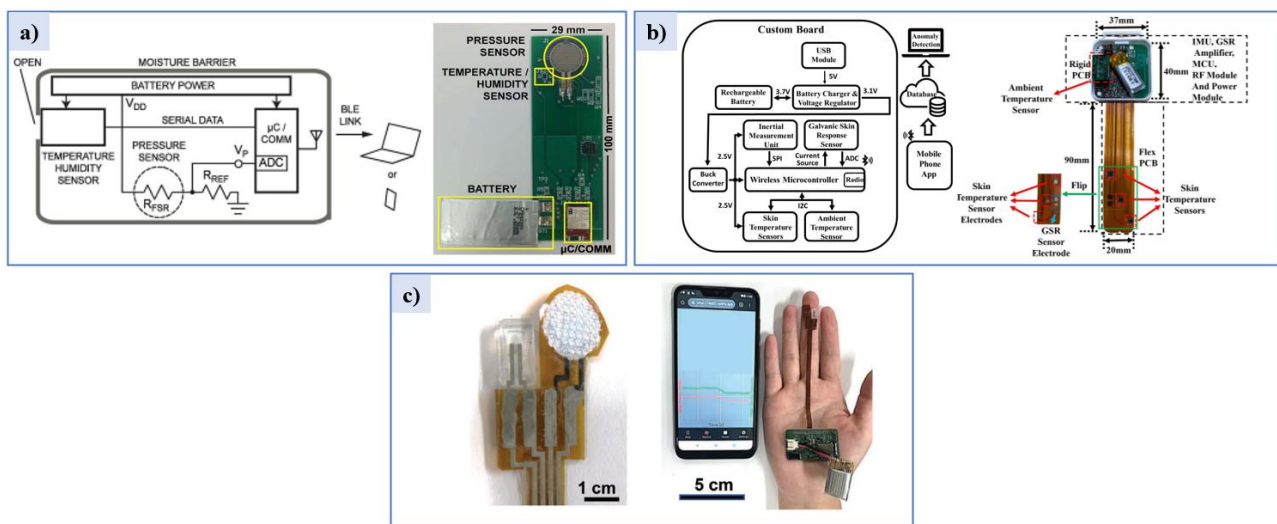


Figure 1.84: a) Circuit Diagram and visual representation of the wearable wireless sensor patch system, for real-time monitoring of the skin’s temperature, pressure and humidity, powered by a polymer battery [158], b) Schematic and visual display of the wearable wrist device with BLE wireless communication capabilities for continuous identification gradual skin temperature changes, for infection identification [151], c) Visual representation of the flexible wireless sensor sheet that examines how the finger responds to thermoregulation and moisture changes [152].

1.3.2 Temperature & Resistance Correlation

The performance of temperature sensors, is remarkably affected by the choice of thermal materials, impacting their sensitivity, stability, response time, accuracy and resolution. Conductive composites, incorporating substances like carbon NPs, NTs, and graphene, offer heightened sensitivity, ease of fabrication, and cost-effectiveness. These composites, exhibit variable resistance-temperature relationships, responding to temperature alterations [32].

The domain of flexible temperature sensors covers a range of categories, including resistance temperature detectors (RTCs), thermistors, thermocouples and thermochromics:

a. Resistance Temperature Detectors

Resistance temperature detectors (RTDs), exhibit proportional changes in resistance in response to temperature variations (Fig. 1.86) [159], serving as widely used flexible temperature sensors, that transform temperature fluctuations into electrical signals. Their functionality can be furtherly improved, through the incorporation of conductive inks, such as graphene and carbon nanotubes [143]. Despite their wide utility in temperature monitoring wearable devices, the interpretation of the data gained from these sensors requires complex electronic structures. These configurations consist of components like amplifiers and ADCs, resulting in a more intricate and expensive manufacturing process [159].

The Temperature Coefficient of Resistance (TCR), holds a significant role in defining a material's temperature sensing effectiveness. It signifies the proportional change in resistance within a 1 °C temperature shift. Higher TCR values are indicative of greater sensitivity in Resistance Temperature Detectors (RTDs), such as those employing Ag nanoparticles (NPs) which are favored due to their excellent conductivity, and cost-efficiency [11][160]. The TCR equation is defined as [160]:

$$Sensitivity = \alpha = \frac{R(T) - R(T_0)}{R(T_0) \cdot (T - T_0)} \quad (Eq. 1)$$

Where:

α = the TCR value

$R(T_0)$ = the resistance value at a reference temperature T_0

ΔR = the resistance difference

ΔT = the temperature difference (K)

When referring to body temperature detection through wearables, the selected sensing material must possess a specific TCR, that provides accurate skin temperature readings within the critical range of 34 to 42 °C, which covers the human body temperature span. Additionally, in order to provide satisfactory daily healthcare needs, the sensor's precision should ideally achieve around 0.1 °C accuracy. However, clinical scenarios demand an even finer precision, at approximately 0.01 °C [109]. A frequent challenge regarding the utilization of RTDs, are the errors arising from the self-heating of resistive wires. This concern is eliminated by the utilization of the Wheatstone Bridge (Fig. 1.85). The design of this structure, includes both a voltage source and two parallel resistor circuits, operating as resistive voltage dividers. To further elevate the accuracy of measurements, alternatives like three-wire or four-wire connections can be considered [160].

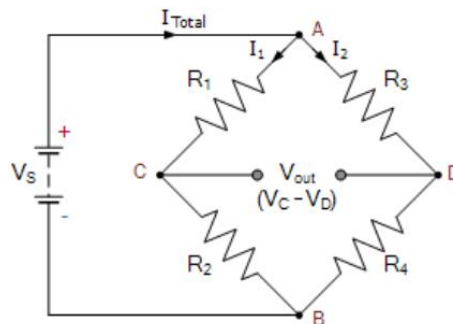


Figure 1.85: Wheatstone Bridge [161].

The relationships for computing the differential potential V_{OUT} and the resistance R_1 of the Wheatstone Bridge are:

$$V_{OUT} = V_C - V_D \cdot \left(\frac{R_2}{R_2 + R_1} - \frac{R_4}{R_4 + R_3} \right) \quad (\text{Eq. 2a})$$

$$\text{and } R_1 = R_2 \cdot \frac{R_3}{R_4} = R_2 \cdot \left(\frac{(V_S - V_{OUT}) \cdot R_3 - V_{OUT} \cdot R_4}{(V_S + V_{OUT}) \cdot R_4 + \Delta V_{OUT} \cdot R_3} \right) \quad (\text{Eq. 2b})$$

b. Thermistors

Thermistors demonstrate non-linear alterations in their resistance, in response to temperature variations, offering precise temperature resolution. Despite their exceptional accuracy in temperature detection, they remain restricted to a narrow range of temperatures, and minute temperature variations [116][160].

Two distinct categories of TCR values are recognized in thermistors: Positive Temperature Coefficient (PTC) and Negative Temperature Coefficient (NTC) (Fig. 1.86) [162].

- Positive Temperature Coefficient (PTC): PTC materials, display an increase in electrical resistance as temperature ascends. Platinum-based materials are notable examples of Positive Temperature Coefficient behavior.

- **Negative Temperature Coefficient (NTC):** NTC materials display a decrease in electrical resistance in response to the rising temperature. The decrease in resistance exhibited by an NTC thermistor is related to the β parameter, which is calculated with the formula provided below:

$$\beta = \frac{\ln\left(\frac{R_{T_0}}{R_{T_1}}\right)}{\frac{1}{T_0} - \frac{1}{T_1}} \quad (\text{Eq. 3})$$

Where:

R_{T_0} = the resistance value at temperature T_0

R_{T_1} = the resistance value at temperature T_1

T_0, T_1 in (K)

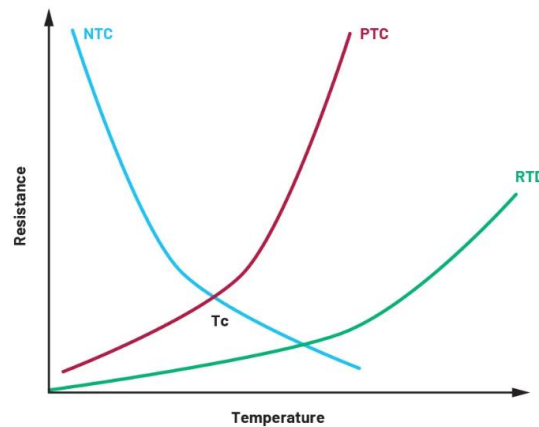


Figure 1.86: NTC vs PTC vs RTDs Graph in response to temperature variations [163].

NTCs find common application in temperature sensors. Examples of NTC behavior, can be observed in metal oxides and semiconductor materials. A notable instance is described by Neella et al., who developed a flexible temperature sensor, by integrating an RGO-Ag nanocomposite film onto Kapton substrate, obtaining a remarkably lower NTC value, than the reported similar graphene films. This film boasted a quicker response time, compared to the existing commercial temperature sensors [162]. Moreover, a groundbreaking flexible and exceptionally sensitive artificial skin for temperature sensing, was developed by Shin et al. This device has been verified as the first NTC sensor displaying the highest sensitivity, regarding its temperature measurements [141].

c. Thermocouples

Thermocouples typically involve of two thermo-elements which generate potential differences, derived from the thermo-electric or Seebeck effect (*Eq.4*) [116].

$$V = S \cdot \Delta T \quad (\text{Eq. 4})$$

Where:

S = the Seebeck coefficient

ΔT = the temperature difference (K)

Their fabrication process on bendable substrates involves MEMS technology, or printing, and coating techniques. Moreover, thermocouples showcase their effectiveness through alloy films. Specifically, when integrated in a circuit, facing different temperatures, these films produce thermo-electric potential, enabling accurate temperature detection. By measuring the temperature-correlated voltage at the film junction – through the Seebeck effect – flexible thermocouples precisely identify any temperature alterations [143].

1.3.3 Thermochromics

Thermochromics (TCs), belong to the category of chromogenics. These materials, possess the exceptional ability to exhibit reversible or irreversible alterations in color, when exposed to external temperature variations. This distinct feature arises from their thermal memory function, enabling them to undergo significant color shifts, upon heating or cooling, establishing their widespread utilization in diverse domains [143] like temperature biosensors, wearables, and smart textiles [164]. An example of TC material is the Polydiacetylene (PDA) (Fig. 1.87), which alters its color from blue to red in response to temperature fluctuations, making it particularly suitable for diverse applications including temperature detection in electronic skin [170]. Nonetheless, the application of TC materials has been filled with concerns regarding their toxicity and their environmental impact. This has prompted the exploration of a new research domain focused on "green" TC materials [164].

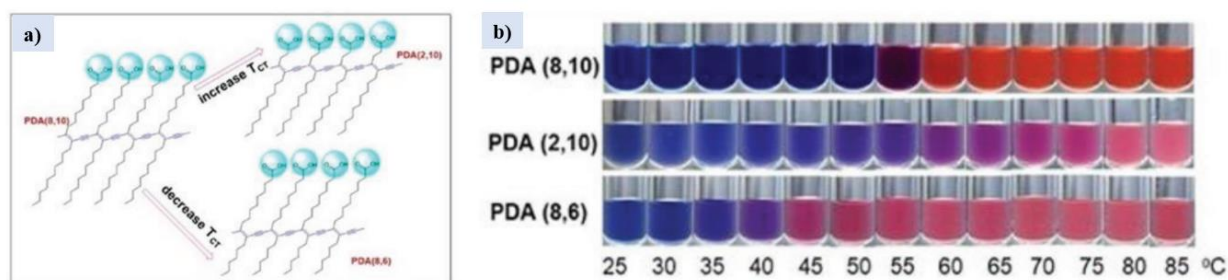


Figure 1.87: Schematic displaying the alterations in the synthesis of polydiacetylene (PDA) and (b) Visual representation of the shift in color of the PDA compounds, upon temperature fluctuations [164].

Thermochromic systems can be divided into two primary categories: The Leuco-Dye system and the Liquid Crystal system. Whereas in terms of their operational mechanism, they can be categorized as Intrinsic system or Doped system [164].

a. Intrinsic System / Doped System

- An **Intrinsic System**, is capable of autonomously forming diverse structures. When exposed to external temperature fluctuations, it undergoes transformations, that lead to its color alteration, or altered spectral properties.
- A **Doped System**, consists of non-TC matrices with integrated TC elements, possibly lacking of certain TC properties. However, the combination of these elements, generates a dynamic system that demonstrates noticeable alterations in color, upon temperature fluctuations.

b. Leuco-Dye System / Liquid Crystal System

- Leuco-Dye TC Systems, rely on temperature-driven chemical transformations [165]. These systems encompass three key elements – the color formers, the developers, and the co-solvents, which collectively, to efficiently elicit color alterations during temperature shifts. Various terms like ‘switching temperature’, ‘discoloration temperature’, and ‘thermochromic temperature’ are used to describe the temperature at which the color change occurs [166]. This class of thermochromics can be directly employed on flexible substrates or textiles.
- Liquid Crystal TC Systems, exhibit color alterations, upon temperature fluctuations, attributed to the changes in their molecular structural arrangement and light interaction [165]. This system provides an alternative mechanism, marked by a gradual discoloration of the material, in contrast to the discrete discoloration witnessed in leuco-dye systems [166].

The incorporation of thermochromic dyes into textiles and flexible substrates, involving printing techniques like screen printing, requires careful consideration. This approach paves the way for innovative design opportunities that combine coloration with electronic engineering. For example, an innovative electrode infused with a layer of thermochromic liquid crystal (TLC), was developed by Thiagalingam et al., to mitigate skin burns (Fig. 1.88) [167]. This integration allows the electrode to swiftly change color within fractions of a second, in response to temperature variations, accurately assessing skin temperatures within a narrow distance. Unveiling a breakthrough, a bio-inspired electronic skin, offering notable stretchability and interactive color transformations was introduced by Xu et al. (Fig. 1.89) [168] This versatile biosensor exhibits remarkable sensitivity, responding to diverse physical stimuli. Its corresponding responses, are visually depicted through a dynamic color shift, transitioning from brown, to green, and resulting in a vivid yellow. This ingenious development, holds promising prospects across multiple domains, including the military and healthcare. Another groundbreaking solution, is a thermotherapeutic device, that merges stretchable strain sensors of three thermochromic dyes, on micro-patterned PDMS surfaces, suggested by Lee et al. (Fig. 1.90). Via controlled mechanical strain-induced electrical resistance changes, the device achieves both customizable color shifts, and controlled heat emission [169].

In summary, thermochromic materials with their temperature-sensitive color changes offer wide a range of applications, spanning from sensors, to smart textiles. With careful formulation, these systems can be tailored for specific temperature ranges, commonly targeting human skin or body temperatures. The ongoing research and development in this field, aims to produce greener and more efficient alternatives, bridging the gap between functionality and environmental responsibility. By harnessing the inherent properties of these materials, designers and researchers are uncovering innovative ways to integrate color responsiveness into diverse fields of engineering and technology.

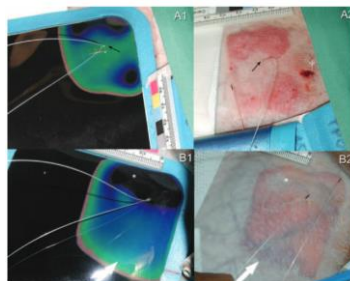


Figure 1.88: Photos A1 and B1 display the TLC probes (black arrows) at peak temperature, whereas A2 and B2 illustrate the corresponding skin burns. In particular, there are three distinct zones that correspond to specific areas on the TLC layer. Severe burns at temperatures $>58^{\circ}\text{C}$ appear as black. Burns at TLC temperatures of 52 to 58°C exhibit blue tones, indicating hyperemia and edema. Skin areas at 50 – 52°C display light blue discoloration. [167].

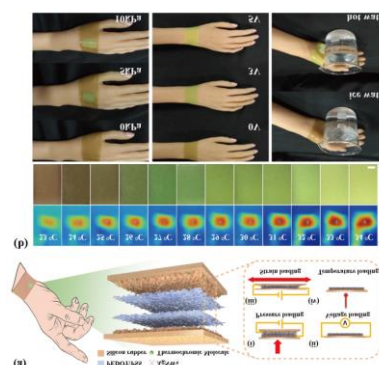


Figure 1.89: a) The design and choice of materials for the bio-inspired colorimetric sensor, b) Thermal and visual image analysis that captures the varying temperature and color alterations in the colorimetric sensor, and visual images showcasing the sensor's responses under different pressures, voltages, and temperatures [168].

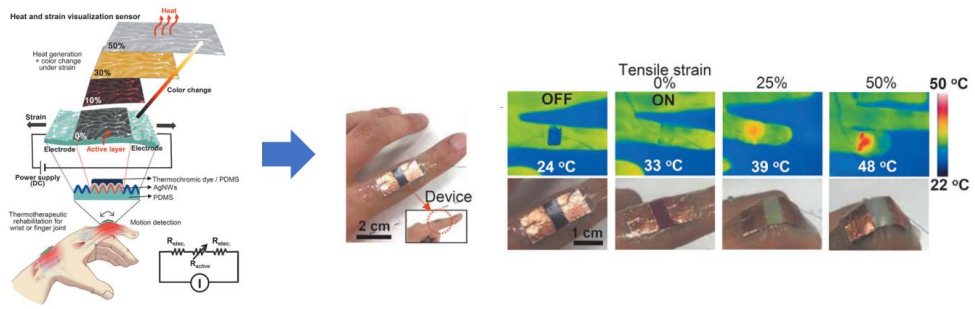


Figure 1.90: Schematic representation of the thermotherapeutic device that merges stretchable strain sensors of three thermochromic dyes on micro-patterned PDMS surfaces, **b)** Visual and thermal image of the changes in temperature and color of the device that is attached onto the finger, while it is moving [169].

2 CHAPTER 2:

Development of a Screen – Print Thermochromic Device for Temperature Sensing

This chapter provides a thorough review of the design evolution, material selection, and fabrication processes, involved in the implementation of the flexible Thermochromic (TC) device, via screen-printing technology. Specifically, three distinct types of TC-based prototype structures were developed, each characterized by a unique activation temperature. The first type features a black TC ink structure with an activation temperature of 31 °C (Thermochromic Screen Printing Ink Black 31°C – SFXC) [171], the second type employs black TC ink with an activation temperature of 47 °C (Thermochromic Screen Printing Ink Black 47°C – SFXC) [172], and the third type utilizes an orange TC structure with an activation temperature of 28 °C (Temperature Responsive Thermochromic Ink - Orange to Neon Yellow – SFXC) [173]. These structures were primarily manufactured on paper substrates, but their fabrication was also extended on PET and Kapton substrates. Following to their fabrication, comprehensive electrical and thermal measurements were also conducted to estimate their sensitivity for temperature detection. In this process, the Keithley 2612 source-meter [174] served as the power source for the internal heating of the TC temperature sensors, while a LabView software controlled the power input to the source-meter. The Temperature to Power/Area (T-P/A) graph determines the amount of heat applied to a specific surface, and the Normalized Resistance Difference to Temperature ($\Delta R/R_0 - T$) graph analysis, allows for the determination of the Temperature Coefficient of Resistance (TCR), which corresponds to the sensitivity rate of these flexible temperature sensors.

2.1 Design of the Layout Masks

Three distinct layout configurations were designed for the TC-based temperature sensors, namely the L1, the L2, and the L3, as illustrated in Fig. 2.1a, 2.1b, 2.1c, respectively. The corresponding masks were subsequently utilized in the screen-printing process to transfer their pattern onto the desired flexible substrate. Accordingly, comprehensive details regarding the specific dimensions of the masks, are provided in Table 2.1.

Out of the three layouts, two of them (L2 and L3), were put into practical use as temperature sensors (Chapter 2.3 – Observations & Remarks). Specifically, the L2 layout was employed for conducting the electrical and thermal measurements to determine the sensitivity of the TC-based temperature sensor's prototype structure. Whereas, the L3 layout was utilized for the temperature recognition via photographic means; an analysis that is extensively discussed, in Chapter 3.

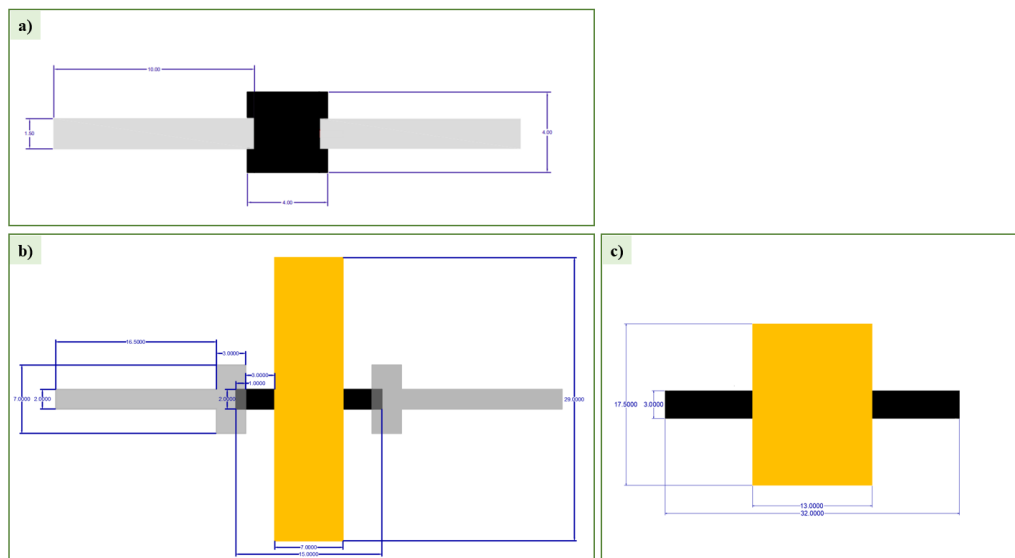


Figure 2.1: a) L1 mask layout (first approach for designing the TC temperature sensor), b) L2 mask layout (second approach for designing the TC temperature sensor) c) L3 mask layout (third and final design of the TC temperature sensor).

Table 2.1: Dimensions for each of the layout masks correspondingly.

Table 2.1: DIMENSIONS FOR EACH MASK LAYOUT (mm)							
	Carbon	Figure	Ag		Figure	TC	Figure
			Track	Pads			
L1	4x4	Fig. 2.1a (black color)	10x1.5	-	Fig. 2.1a (gray color)	-	-
L2	15x2	Fig. 2.1b (black color)	16.5x2	7x3	Fig. 2.1b (gray color)	29x7	Fig. 2.1b (orange color)
L3	32x3	Fig. 2.1c (black color)	-	-	-	17.5x13	Fig. 2.1c (orange color)

a. L1

The fabrication of the L1 layout pattern, comprises of two separate distinct masks:

1. The first one shaped as a square, represents the carbon (resistance) element, measuring 4x4mm (Fig. 2.2a).
2. The second mask consists of two adjacent rectangles, in order to define the Ag (silver-conductive) tracks, with dimensions of 10x1.5mm (Fig. 2.2b).

Both of these masks are meticulously engraved onto gelatin material, and are subsequently overlaid to implement the structure depicted in Fig. 2.1a.

The WAINLUX K6 laser engraver [175] was configured with specific parameters, including a 0.8mm line thickness, 100% power, 90% speed, 79% contrast ratio, and 10 repetitions. It was observed that the line thickness significantly influenced the number of repetitions required. Specifically, thicker lines necessitated fewer repetitions. In this instance, achieving a more precise mask outcome, especially around the corners, might have been possible on the laser engraver, with a reduced repetition count of 8-9.

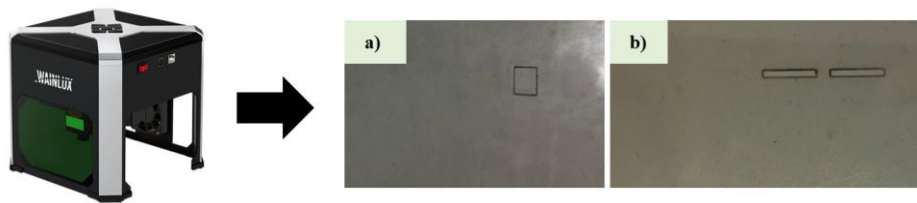


Figure 2.2: a) Laser engraved gelatin mask for the carbon layer of the L1 layout, b) Laser engraved gelatin mask for the Ag layer of the L1 layout.

b. L2

The L2 layout of the TC prototype temperature sensor, comprises three mask layers, implemented via the WAINLUX K6 laser engraver [175]. The laser engraver's software was configured with 100% power, 90% speed, 80% contrast ratio, and 15 repetitions.

Each of the masks displayed in Fig. 2.3, consist of two designs, to generate two samples at once.

1. The first mask is shaped as two electrodes, representing the Ag electrodes, with track dimensions equivalent to 16.5x2mm, and pads dimensions equal to 7x3mm (Fig. 2.3a).
2. The second mask layer features a rectangle positioned between the two Ag electrodes, measuring 15x2mm (Fig. 2.3b). This mask symbolizes the carbon (resistance) material intended for heating, to characterize the TC ink that will be printed subsequently on top.
3. The third mask represents the TC material itself, measuring 29x7mm (Fig. 2.3c). The three masks, are all layered on top of each other, forming the structure illustrated in Fig. 2.1b.

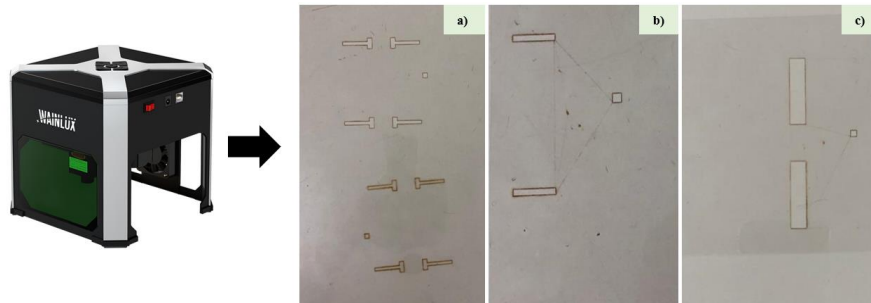


Figure 2.3: L2 layout Laser engraved gelatin mask for a) the Ag layer, b) the Carbon layer, c) the TC layer.

Observations & Remarks

- The laser software was firstly observed to have printed the designed structures in dimensions different from their defaults. The measurements of the designed structures in comparison to the printed structures, are displayed in Table 2.2. Therefore, it was subsequently discovered that the design must be adjusted to fit the dimensions defined by the WAINLUX K6 laser engraver's software. Particularly, it was found out that the engraver employs a scale where every pixel corresponds to 0.5cm, and thus, the design was scaled accordingly.
- Since the L2 layout structure comprises of three mask layers, namely the Carbon Mask, the Ag mask, and the TC Mask, before engraving each mask design, a reference point was utilized, to ensure that the three layers would align precisely, to implement the structure depicted in Fig. 2.1b.

Table 2.2: Design Measurements vs Printed Measurements on the laser engraver of the L2 layout.

Table 2.2: Design Measurements vs Printed Measurements			
	Design Measurements (mm)	Printed Measurements (mm)	Difference (mm)
Carbon	15x2	15x2	0
Ag	Track: 17x2	Track: 16.5x2	0.5x0
	Pads: 7x3	Pads: 7x3	0
TC	35x8	29x7	6x1

c. L3

In contrast to the prior laser-engraved masks, the L3 mask layout adopts a mesh design, that incorporates both the Carbon pattern (32x3mm rectangle – Fig. 2.4a) and the TC pattern (17.5x13mm rectangle – Fig. 2.4b). In addition to the designs employed in the L3 layout configuration, the mesh mask also includes other designs intended for various processes and projects (Fig. 2.4). The L3 designed patterns are duplicated, facilitating the simultaneous screen-printing of two samples, similarly to the L2 configuration’s approach. Moreover, the width of the TC element is smaller, than the L2 layout, as the 29mm width was evidenced as too long, during the heating process. Furthermore, unlike the L2 layout mask consisting of three layers (Carbon, Ag, TC), the L3 mask design employs two layers (Carbon, TC) to expedite the screen-printing process, by eliminating the additional Ag layer. Consequently, the dimensions of the carbon layer in the L3 mask are larger than those in the carbon layer of the L2 laser-engraved mask, as will be furtherly explained in Chapter 2.3.

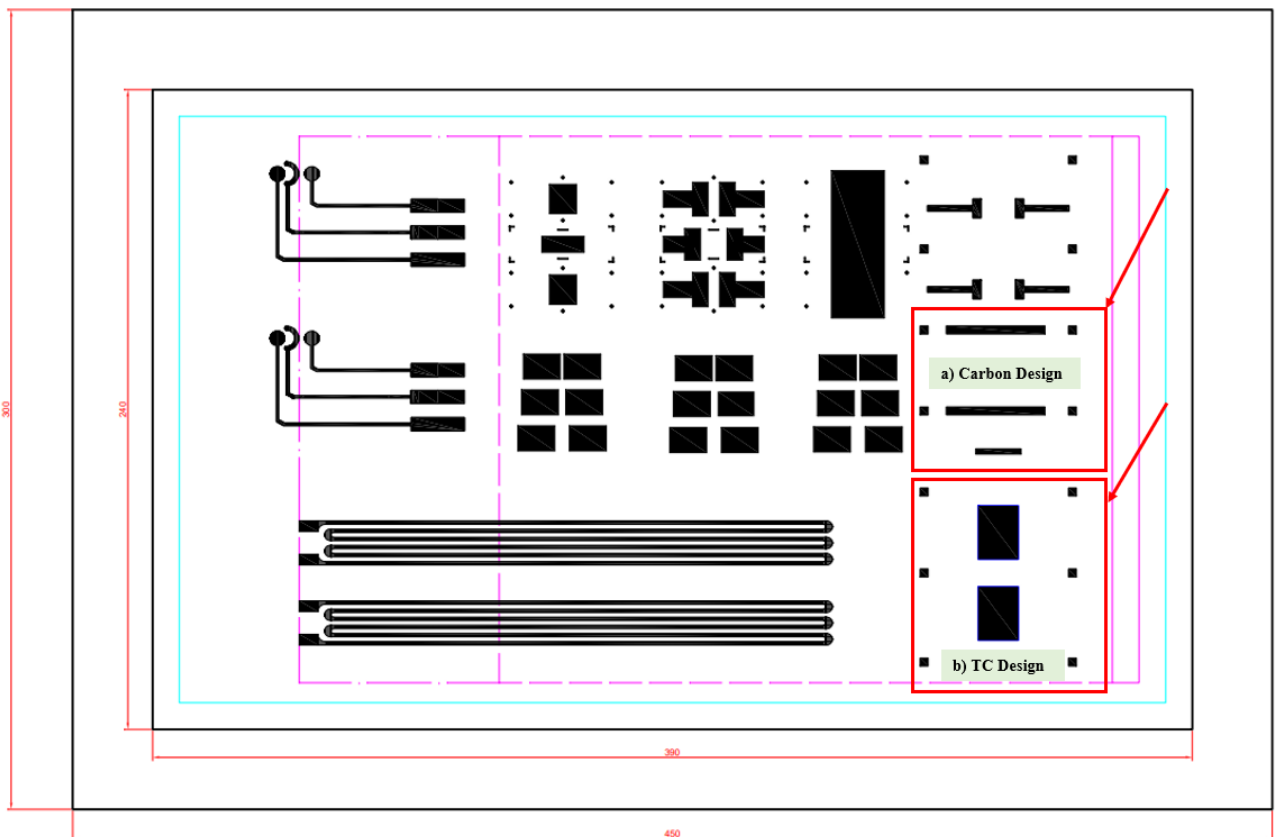


Figure 2.4: Mesh mask layout designs of the Carbon and TC structure: a) Carbon design, b) TC design, of the L2 layout.

2.2 Implementation of the Screen – Printed Device and Materials

This section is dedicated to a comprehensive exploration of the materials employed in the fabrication of the flexible thermochromic temperature sensor, with varying activation temperatures. Furthermore, an in-depth examination of the screen-printing process utilized for the implementation of the L1, L2, and L3 design configurations, is also discussed. In order to offer a thorough understanding of the materials, processes, and outcomes associated with the development of these flexible temperature sensors, an extensive analysis of the optical images for each prototype structure is also provided. This analysis sheds light to the unique characteristics and applications of the TC-based temperature detectors.

2.2.1 Materials and Equipment used for the Temperature Sensing Device

The inks, substrates and equipment used for the fabrication of the thermochromic temperature sensors, are presented in Table 2.3.

Table 2.3: Inks and Substrates and Equipment for TC structures’ fabrication.

INKS		
Name	Use	Figure
Metalon HPR-059, Novacentrix [176]	Heating of the TC structure.	Fig. 2.5a
Metalon HPR-FG77, Novacentrix [177]	Ag electrodes used as tracks for the carbon resistance.	Fig. 2.5b
Thermochromic Screen Printing Ink Black 31°C, SFXC [171]	Implementation of the color changing TC structure. Turns transparent when the temperature exceeds 31 °C.	Fig. 2.5c
Thermochromic Screen Printing Ink Black 47°C, SFXC [172]	Implementation of the color changing TC structure. Turns transparent when the temperature exceeds 47 °C.	Fig. 2.5d
Thermochromic Screen Printing Ink Orange 28°C, SFXC [173]	Implementation of the color changing TC structure. Turns yellow when the temperature exceeds 28 °C.	Fig. 2.5e
SUBSTRATES		
Name	Thickness	Figure
Polyethylene Terephthalate/PET, Goodfellow [178]	0.125mm	Fig. 2.6a
Kapton® HN Film, Goodfellow [179]	0.125mm	Fig. 2.6b
A4 Paper	-	Fig. 2.6c
EQUIPMENT		
Name	Description	Figure
Heating & Dry Heat Sterilization Oven (NUVE FN400) [180]	Curing of the Carbon, Ag, and TC inks	Fig. 2.7a
Screen Printing Semi-Automatic Machine (Ever-bright, S-200HFC) [181]	Screen-printing the TC temperature sensor, onto the flexible substrates	Fig. 2.7b



Figure 2.5: Screen- printing inks: a) Metalon HPR-059, Novacentrix [176], b) Metalon HPS-FG77, Novacentrix [177] c) Thermochromic Screen Printing Ink Black 31°C, SFXC [171], d) Thermochromic Screen Printing Ink Black 47°C, SFXC [172], e) Thermochromic Screen Printing Ink Orange 28°C, SFXC [173].

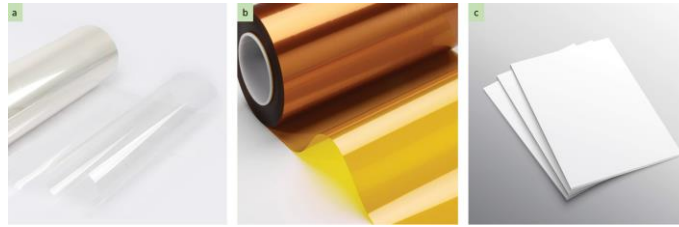


Figure 2.6: Substrates: **a)** Polyethylene Terephthalate/PET, Goodfellow [178], **b)** Kapton® HN Film, Goodfellow [179], **c)** A4 paper.

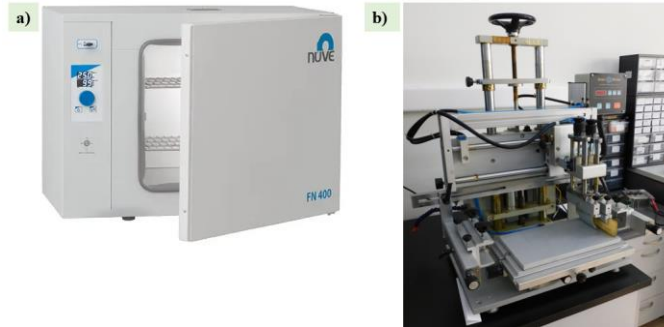


Figure 2.7: Equipment: **a)** Heating & Dry Heat Sterilization Oven (NUVE FN400) [180], **b)** Screen Printing Semi-Automatic Machine (Ever-bright, S-200HFC) [181].

Observations & Remarks

- The black thermochromic inks were supplied in two separate components, namely ink and binder, which needed to be combined in equal proportions (50/50), prior their use.
- The thermochromic (TC) inks were screen-printed directly from the refrigerator due to their thicker consistency, as previous results demonstrated that they become very liquid when used at room temperature, making them unsuitable for screen-printing structures on flexible substrates such as PET, Kapton and paper.
- The carbon and Ag inks by Novacentrix [176][177] were used at ambient temperature and were well-agitated prior to screen printing.

2.2.2 Screen – Printing Process & Optical Characterization

There are two fundamental parts to the screen-printing of the TC temperature sensor on flexible surfaces:

- a.** The mask, is a thin sheet of material which determines the desired design to be printed, and is placed above the substrate.
- b.** The squeegee transfers the ink, which is applied near the design of the mask.

a. L1 Design Mask Layout

In order to fabricate the layout structure illustrated in Fig. 2.1a (L1 layout design), a two-step process was followed, each contributing to the overall structure's functionality.

1. In the initial step, the 4x4mm laser-engraved square mask is utilized (Fig. 2.2a) to screen-print Carbon ink (Metalon HPR-059, Novacentrix – Fig. 2.5a) onto a paper substrate. In this step the carbon resistance element is fabricated, which plays a crucial role in generating a temperature field for the TC element's evaluation. Subsequently, the structure undergoes a curing process at 120 °C (NUVE FN400 – Fig. 2.7a), for a duration of 15 minutes to ensure its stability.
2. In the second phase of this process, the 50x5mm rectangle mask (Fig. 2.2b) is employed for the screen printing of the Ag ink (Metalon HPS-FG77, Novacentrix – Fig. 2.5b), onto the paper

substrate. This step is pivotal in implementing the silver electrodes essential for assuring the efficient interconnection to the external electronic equipment, although it could have also been avoided as demonstrated in the L3 layout design.

A total of three (3) samples were meticulously fabricated, based on the L1 layout configuration. These samples (S1, S2 and S3) are visually represented in Fig. 2.8 which specifically illustrates the two distinct stages of the screen-printing processes for the Carbon and Ag layers, respectively. Comprehensive information regarding the fabrication process of these samples, is meticulously documented in Table 2.4.

Table 2.4: Carbon – Ag – Paper L1 Layout Structure Information about the Screen-Printing Process.

Sample	1 st Carbon Layer			2 nd Ag Layer – Final Configuration of the L1 Layout		
	Repetitions	Details about Squeegee movement	Figure	Repetitions	Details about Squeegee movement	Figure
S1	x3	1 forth, 1 forth, 1 forth	Fig. 2.8a1	x2	1 forth, 1 back	Fig. 2.8b1
S2	x3	1 forth, 1 back, 1 forth	Fig. 2.8a2	x2	1 forth, 1 back	Fig. 2.8b2
S3	x2	1 forth, 1 back	Fig. 2.8a3	x2	1 forth, 1 back	Fig. 2.8b3

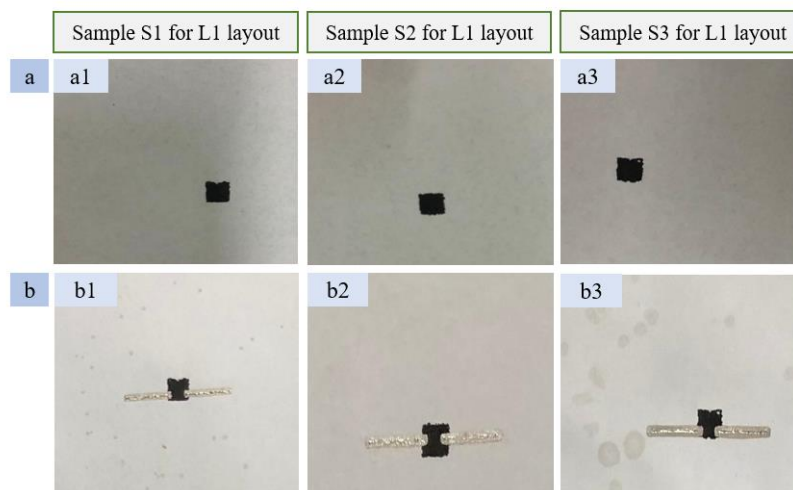


Figure 2.8: 1st and 2nd Layer (Carbon and Ag layer) of the L1 layout temperature sensor prototype, for the S1, S2, and S3 samples.

Observations & Remarks

- Prior to the screen-printing process, each of the gelatin masks was attached to an 80T portrait mesh with paper tape, as depicted in Fig. 2.9a. This method involved aligning the edges of the substrate with the screen-printer’s bed, ensuring precise and consistent placement for every layer, of the final structure.
- Tape was used to secure the paper substrate onto the screen printer, as shown in Fig. 2.9b. However, this approach presented challenges as the paper-tape would occasionally come off during the screen-printing process, resulting in an insecure mask attachment.

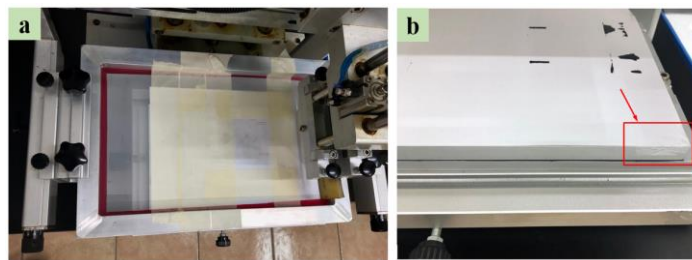


Figure 2.9: a) Laser-Engraved Gelatin Mask paper taped onto an 80T portrait mesh, for screen-printing the desired pattern of the L1 layout, b) Paper substrate secured onto the screen-printer's bed.

b. L2 Design Mask Layout

To implement the structure of the L2 layout depicted in Fig. 2.1b, a three-step process was meticulously followed:

1. Initially, the 15x2mm gelatin mask (Fig. 2.3a) was employed to screen-print the Carbon ink (Metalon HPR-059, Novacentrix – Fig. 2.5a), on paper substrate. Subsequently, the substrate underwent a curing process at 120 °C for a duration of 15 minutes. This step refers to the fabrication of the carbon resistance intended for the heating of the TC element.
2. In the second phase of this process, the Ag mask (Fig. 2.3b) was utilized to screen-print the Ag ink (Metalon HPS-FG77, Novacentrix – Fig. 2.5b), onto the cured substrate. This step is crucial for developing the structure's electrodes. Subsequently, the two-layer structure was cured at 120 °C for 15 minutes.
3. The third layer of the structure involves the fabrication of the 30x6.5mm rectangle (Fig. 2.3c), filled with TC ink. The thermochromic ink was provided by SFXC and includes three variants: Thermochromic Screen Printing Ink Black 31 °C (Fig. 2.5c), Thermochromic Screen Printing Ink Black 47 °C (Fig. 2.5d), and the Temperature Responsive Thermochromic Ink - Orange to Neon Yellow 28 °C (Fig. 2.5e). The former thermochromic ink, was supplied as two separate components, namely the ink and binder, which need to be mixed in equal proportions (50/50), before application. Following this, the three-layer structure underwent a curing process at a temperature of 70 °C for a duration of 15 minutes. This step is crucial to finalize the formation of the structure and activate the thermochromic properties of the ink.

A total of four (5) screen-print functional prototypes were produced, following the L2 layout mask configurations, each of which yielded two samples simultaneously, resulting in a total of ten (10) samples. These samples are visually depicted in Fig. 2.10a, Fig. 2.10b and Fig. 2.10c, illustrating the three distinct stages of the screen-printing processes for the Carbon, Ag, and TC inks, respectively. Detailed information regarding the fabrication process of these samples is thoroughly documented in Table 2.5. This table provides a comprehensive overview of the steps involved in implementing each sample, offering valuable insights into the process and its outcomes.

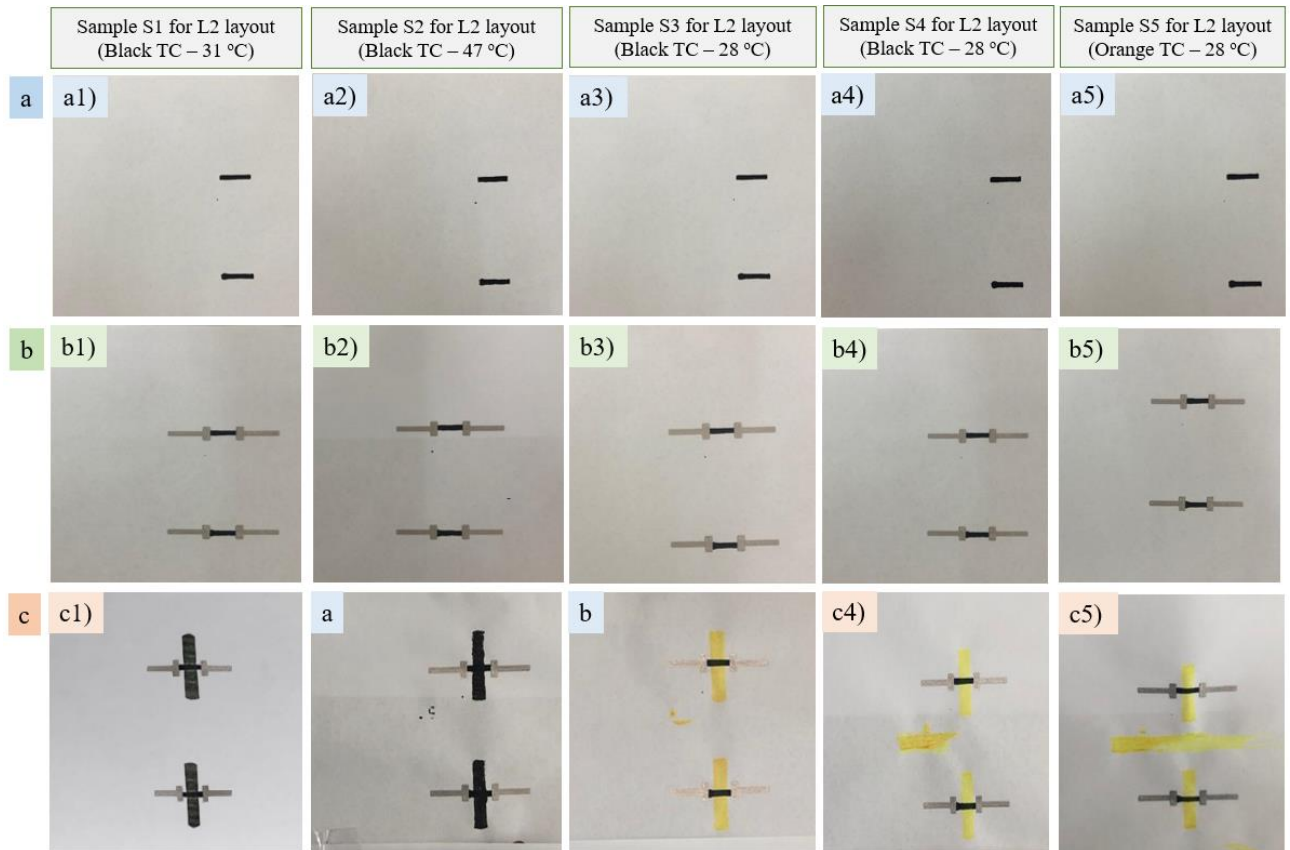


Figure 2.10: 1st, 2nd, and 3rd Layer (Carbon, Ag, TC layers) of the L2 layout temperature sensor prototype, for samples S1, S2, S3, S4, S5.

Table 2.5: Carbon – Ag – TC – Paper L2 Layout Structure Information about the Screen-Printing Process.

Sample	1 st Carbon Layer			2 nd Ag Layer			3 rd TC Layer – Final Configuration of the L2 Layout		
	Repetitions	Details	Figure	Repetitions	Details	Figure	Repetitions	Details	Figure
S1 (Black TC – 31 °C)	x2	1 forth, 1 back	Fig. 2.10a1	x3	1 forth, 1 back, 1 forth	Fig. 2.10b1	x5	1 forth, 1 back, 1 forth, 1 back, 1 forth	Fig. 2.10c1
S2 (Black TC – 47 °C)	x2	1 forth, 1 back	Fig. 2.10a2	x3	1 forth, 1 back, 1 forth	Fig. 2.10b2	x5	1 forth, 1 back, 1 forth, 1 back, 1 forth	Fig. 2.10c2
S3 (Orange TC – 28 °C)	x3	1 forth, 1 back, 1 forth	Fig. 2.10a3	x3	1 forth, 1 back, 1 forth	Fig. 2.10b3	x3	x3 forth	Fig. 2.10c3
S4 (Orange TC – 28 °C)	x3	1 forth, 1 back, 1 forth	Fig. 2.10a4	x3	1 forth, 1 back, 1 forth	Fig. 2.10b4	x3	x3 forth	Fig. 2.10c4
S5 (Orange TC – 28 °C)	x5	1 forth, 1 back, 1 forth, 1 back, 1 forth	Fig. 2.10a5	x3	1 forth, 1 back, 1 forth	Fig. 2.10b5	x4	x4 forth	Fig. 2.10c5

Observations & Remarks

- Each of the gelatin masks was affixed to an 80T mesh portrait, with paper tape as illustrated in Fig. 2.11a. However, this method posed certain issues as the tape would occasionally come off while the screen printer was in operation, resulting in an insecure mask attachment. This issue became particularly critical when screen-printing on PET or Kapton substrates, which, due to their non-absorbent properties, allowed the ink to pass through the laser-engraved mask, without achieving its precise pattern. Similarly, to the previous configuration, the substrates (paper and PET), were secured onto the screen printer's bed using tape, as depicted in Fig. 2.11b. This method involved aligning the edges of the substrate with the screen printer's bed as a reference point, ensuring the consistent and precise implementation of the L2 layout structure as illustrated in Fig. 2.1b.
- In contrast to the successful results obtained via screen-printing the 1st-layer and 2nd-layer configurations on paper (Fig. 2.12a) and PET substrates (Fig. 2.13a), certain challenges occurred when attempting to print the 3rd-layer, which involved the application of TC (Thermochromic) ink (Fig. 2.12b & Fig. 2.13b). This issue stemmed from the Black-Transparent ink (31°C), which had been previously opened and was found to have non-airtight sealing, as well as the insecure mask attachment. According to the ink's datasheet, this particular ink should ideally be used within three months after being opened. These challenges significantly complicated the screen-printing process, primarily because both black TC inks – with a particular emphasis on the Black-Transparent 31°C variant – exhibited a high degree of liquidity, even when combined with the binder mix. Consequently, despite our numerous attempts, and given the insecure laser-engraved mask attachment, achieving precise screen-printing with these inks proved to be a formidable task.
- To overcome these complications, the printing of the third layer was proceeded by screen-printing mostly with the orange-yellow TC ink, which activates at 28 °C. Crucially, the packaging for this particular ink had not been previously opened, ensuring its better performance and consistency.

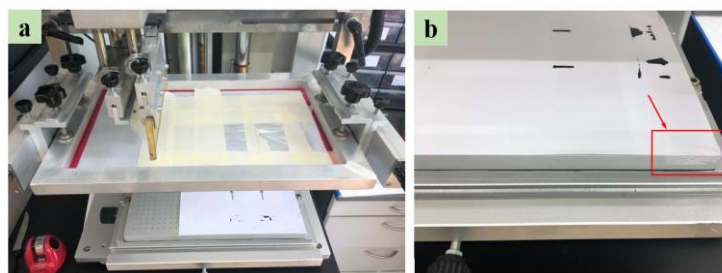


Figure 2.11: a) Laser-Engraved Gelatin Mask paper taped onto an 80T portrait mesh, for screen-printing the desired pattern of the L2 layout, b) Paper substrate secured onto the screen-printer's bed.

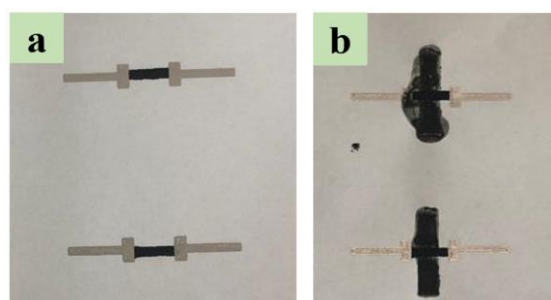


Figure 2.12: a) Screen-printing on paper substrate the 1st and 2nd Layer (Carbon and Ag inks) of the L2 layout configuration, b) Screen-printing on paper substrate the 3rd Layer (Black TC ink – 31 °C) of the L2 layout configuration.

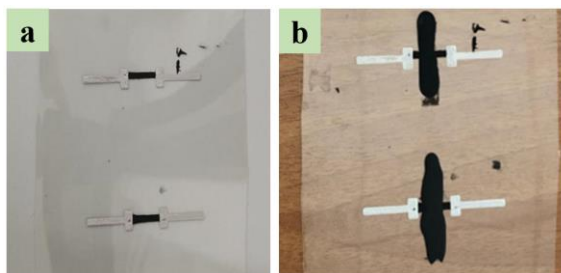


Figure 2.13: a) Screen-printing on PET substrate the 1st and 2nd Layer (Carbon and Ag inks) of the L2 layout configuration, b) Screen-printing on PET substrate the 3rd Layer (Black TC ink – 31 °C) of the L2 layout configuration.

c. Screen-Printing the L3 Design Mask Layout

In this case, the feasibility of screen-printing the L3 design layout on PET and Kapton substrates, via a patterned mesh mask, is investigated (Fig. 2.14). Previous attempts demonstrated that the ink's liquid consistency, as well as the insecure attachment of the laser engraved mask onto the mesh (Fig. 1a, Fig. 1b), resulted in poor print quality (Fig. 2.13b). However, more promising results were obtained when screen-printing on paper substrate, due to its absorbability to liquid inks (Fig. 2.10).

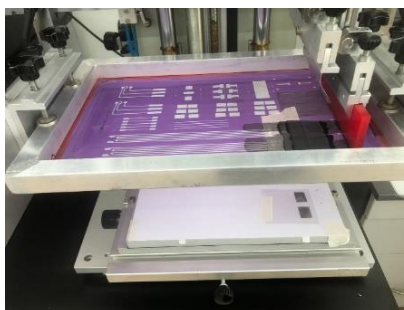


Figure 2.14: New Screen-Print Setup after the printing procedure (mesh mask, red squeegee, print on PET substrate).

The thermochromic (TC) inks used in this case were the black TC inks, with activation temperatures of 31 °C and 47 °C, respectively. The structures of the L3 layout were screen-print on both PET and Kapton substrates, to verify the feasibility of screen-printing the TC inks on non-liquid-absorbent substrates, as well as their proper functionality considering temperature variations. A two-step process was followed to implement the desired thermochromic (TC)-based structure:

1. First, the mesh mask was used to screen-print the carbon ink (Metalon HPR-059, Novacentrix – Fig. 2.5a) onto PET and Kapton substrates. This structure was then cured at 120 °C for 15 minutes.
2. In the second step, the TC structure was printed onto the carbon, which serves as a heater for the heating of the TC material. To do this, the mesh mask was placed firmly into the screen printer, so that the desired pattern was aligned in the middle of the carbon structure that had been previously printed. The final TC structure was cured at 70 °C for 15 minutes.

Two (2) black thermochromic (TC) structures with an activation temperature of 31 °C were fabricated on PET and Kapton substrates, respectively. Similarly, two (2) black thermochromic (TC) structures with an activation temperature of 47 °C were fabricated on the same substrates. More details are provided in Table 2.6.

Table 0.6: Flexible Screen-Print TC Structures with various activation temperatures.

L3 LAYOUT STRUCTURES						
TC INK	SAMPLE AMOUNT		FIGURE		SAMPLE	
	PET	Kapton	PET	Kapton	PET	Kapton
Black (31 °C)	x2	x2	Fig. 2.15a	Fig. 2.15b	S1(a,b)	S2(a,b)
Black (47 °C)	x2	x2	Fig. 2.16a	Fig. 2.16b	S3(a,b)	S4(a,b)

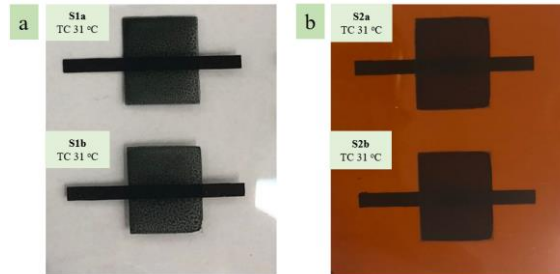


Figure 2.15: Flexible Screen-Print black TC Structures with 31 °C activation temperatures on PET and Kapton substrates, based on the L3 mesh mask layout: **a)** S1a & S1b samples on PET substrate, **b)** S2a & S2b samples on Kapton substrate.

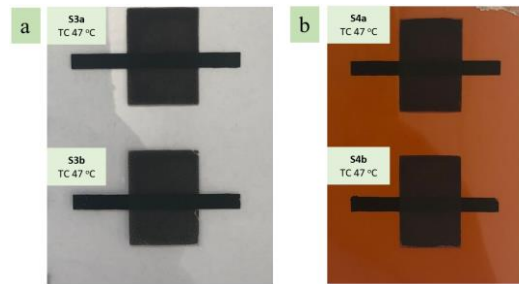


Figure 2.16: Flexible Screen-Print black TC Structures with 47 °C activation temperatures on PET and Kapton substrates, based on the L3 mesh mask layout: **a)** S3a & S3b samples on PET substrate, **b)** S4a & S4b samples on Kapton substrate.

Observations & Remarks

- It was observed that the cleaning of the mesh mask and the number of passes with the squeegee are two important factors that can affect the quality of the screen-print TC structures. By optimizing these factors, clear, uniform prints were achieved, that respond well to changes in temperature.
- The first layer, which includes the carbon ink for the heating of the thermochromic (TC) material, was screen-print with a single pass of the squeegee from right to left direction.
- The second layer, being the TC ink, was screen-print with two passes of the squeegee, both from right to left direction. This was necessary due to the more liquid texture of the TC material.
- Although, the results of the L3 layout temperature sensor prototype, proved to be promising as demonstrated in the above figures, further research is needed to optimize the vulnerabilities of the ink’s formulation as well as the screen-printing process. These include:
 1. Inadequate cleaning of the mesh mask: This can leave residue which can interfere with the printing process.
 2. A non-flat substrate: It may cause the ink to spread unevenly, resulting in a poor-quality print.
 3. The amount of ink used: Too much ink can influence the thermal response of the fabricated flexible temperature sensor

2.2.3 Optical Characterization of the Screen-Print Configurations

This section refers to the optical images captured through the lab's microscope (OLYMPUS | MX Semiconductors – MX51 [185], Fig. 2.17). These images represent each sample in the microscale, to showcase the quality and precision of the fabricated structures, corresponding to each layout design (L1, L2, L3). In all instances, the microscope was utilized with dark filter setting, and a 10x / 0.25 BD lens for image capture.



Figure 2.17: OLYMPUS | MX Semiconductors – MX51 Microscope.

a. Optical Characterization of the Samples with the L1 Design Layout

The optical images provided below, refer to the S1 and S2 samples (Fig. 2.18), which correspond to the L1 design layout of the flexible temperature sensor's prototype. Fig. 2.19 displays the optical characterization of the S1 sample, while Fig. 2.20 showcases the characterization of the S2 sample.

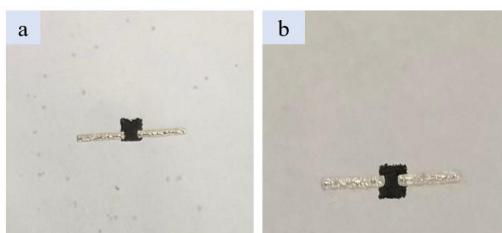


Figure 2.18: Visual representation of the: a) S1 sample, b) S2 sample, with the L1 layout configuration.

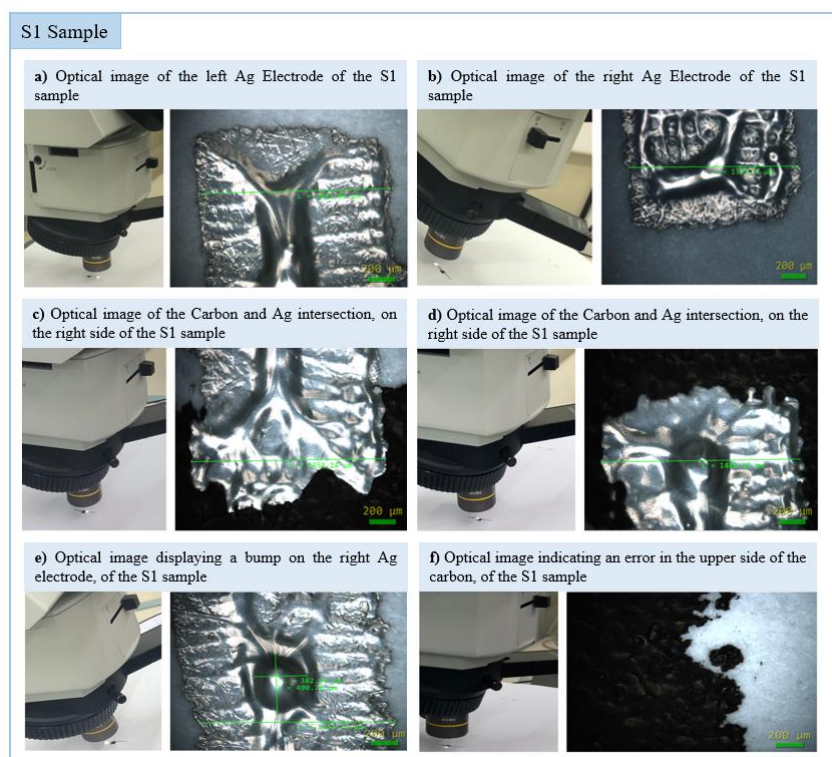


Figure 2.19: Optical Characterization of the S1 sample – L1 layout configuration, with detailed description.

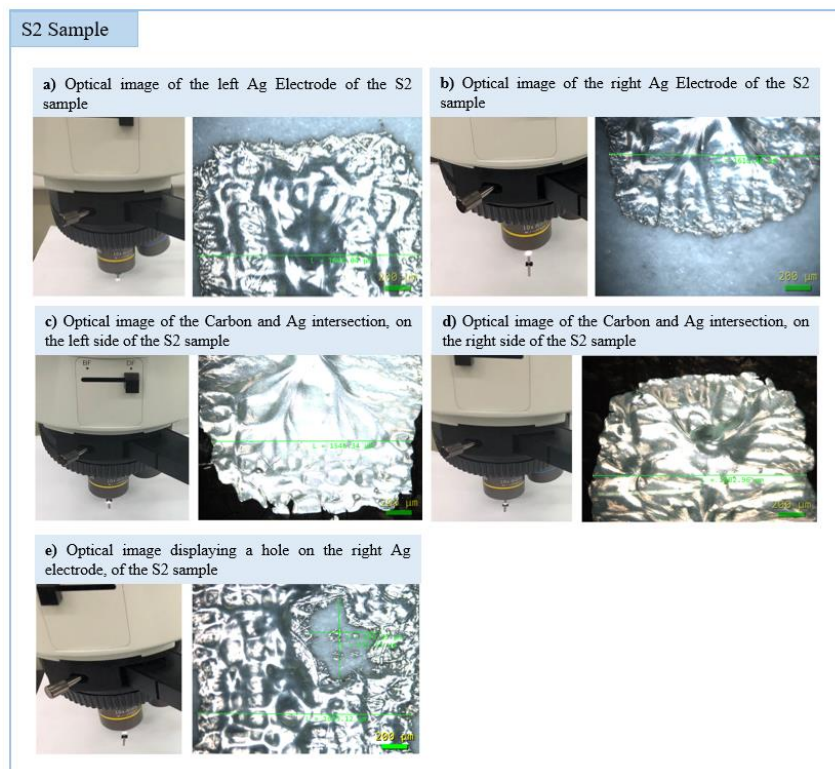


Figure 2.20: Optical Characterization of the S2 sample – L1 layout configuration, with detailed description.

Observations & Remarks

❖ S1 Sample

- As observed in the above images, it is evident that the printed material exhibits a notable amount of roughness, which is expected since the structure is screen-print. Fig. 2.19a and Fig. 2.19b illustrate the top and bottom Ag electrodes, while Fig. 2.19c and Fig. 2.19d display the Carbon-Ag intersection for both the top and bottom electrodes, respectively. Fig. 2.19e highlights a bump formed in the lower Ag electrode, and Fig. 2.19f reveals an imperfection in the carbon’s shape, which is also observed without the microscope, in Fig. 2.18a.

❖ S2 Sample

- Similarly, to the S1 sample, the images presented above for the S2 sample, also reveal significant roughness in the printed material. Fig. 2.20a and Fig. 2.20b provide a visual representation of the upper and lower Ag electrodes, while Fig. 2.20c and Fig. 2.20d display the Carbon-Ag intersection for both the top and bottom electrodes, respectively. Fig. 2.20e highlights a hole in the lower electrode, which is also visible to some extent. This hole may potentially affect the accuracy of the thermal measurements conducted on the structure, during its heating.

b. Optical Characterization of the Samples with the L2 Design Layout

The optical images below, refer to the S2 (Fig. 2.21a – Black TC 47 °C) and S3 sample (Fig. 2.21b – Orange TC 28 °C), corresponding to the L2 design layout of the flexible temperature sensor’s prototype. The optical images in Fig. 2.22 correspond to the S1 sample. Whereas the optical characterizations in Fig. 2.23 correspond to the S2 sample.

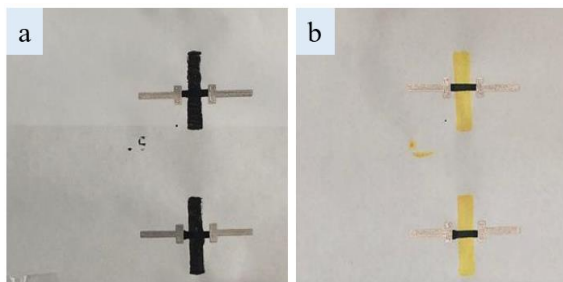


Figure 2.21: Visual representation of the: **a)** S2 sample utilizing the Black TC (47 °C), **b)** S3 sample, utilizing the Orange TC (28 °C) with the L2 layout configuration.

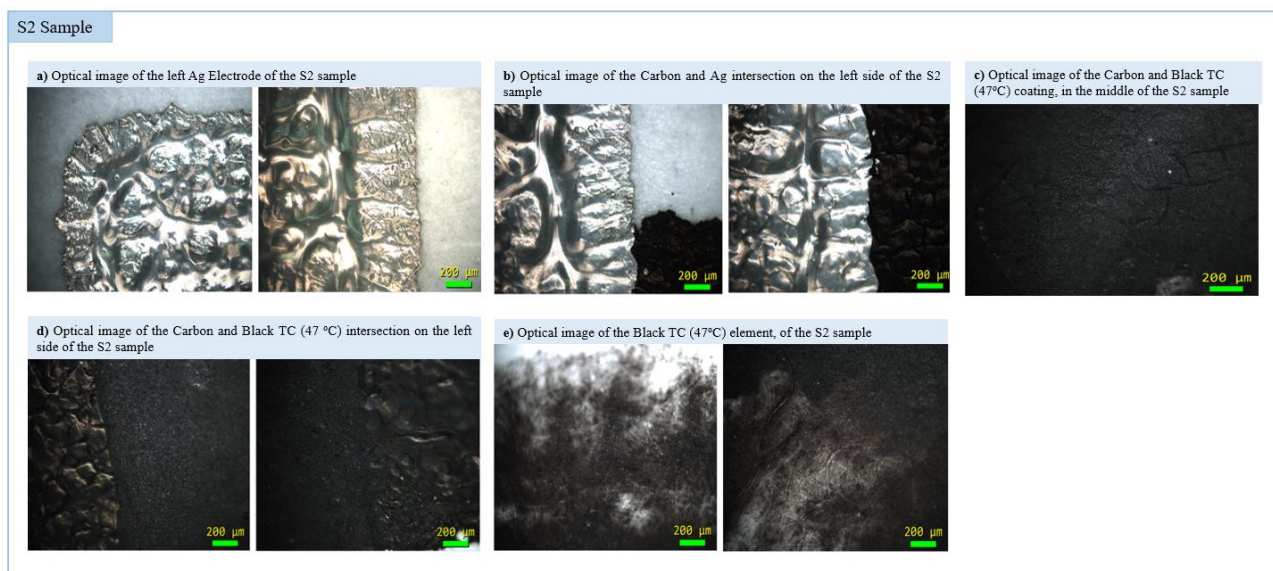


Figure 2.22: Optical Characterization of the S1 sample utilizing the Black TC (47 °C) – L2 layout configuration, with detailed description.



Figure 2.23: Optical Characterization of the S2 sample utilizing the Orange TC (28 °C) – L2 layout configuration, with detailed description.

Observations & Remarks

❖ S2 Sample

- The optical images presented in Fig. 2.22, offer a visual representation of the surface characteristics the S2 sample. As expected, some degree of roughness caused by the screen-printing process, is noticeable. Fig. 2.22a specifically focuses on the top corner and right side of the bottom Ag electrode. In Fig. 2.22b, the Carbon-Ag intersection for the bottom electrode is observed, while Fig. 2.22c and Fig. 2.22d depict the Carbon-TC coating and the intersection between them, respectively. Notably, in Fig. 2.22e, it is evident that the black TC material – unlike the other two components – does not exhibit any surface roughness when applied to the paper substrate, due to its liquid consistency. Additionally, Fig. 2.22e highlights the non-linear spreading of the Black TC material on the lower side of the paper substrate, a result of its liquid nature prior curing at 70 °C, for a duration of 15 minutes.

❖ S3 Sample

- Similarly, to the S2 sample, the optical characterizations in Fig. 2.23, also reveal surface roughness onto the S3 sample. Fig. 2.23a reveals the sides of the bottom Ag electrode, while Fig. 2.23b displays the Carbon-Ag coating for the bottom electrode. Fig. 2.23c illustrates the Carbon-TC coating and intersection, respectively, and Fig. 2.23d displays the orange TC material. These images collectively offer insights into the surface characteristics of the S2 sample.

c. Optical Characterization of the Samples with the L3 Design Layout

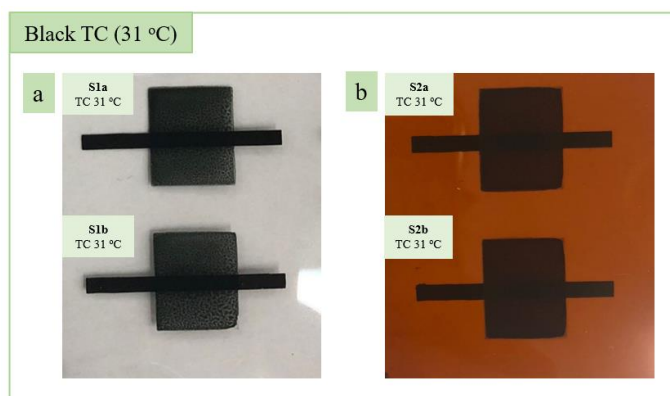


Figure 2.24 Visual representation of the: **a)** S1 sample utilizing the Black TC (31 °C) on PET substrate, **b)** S2 sample, utilizing the Black TC (31 °C) on Kapton substrate, with the L3 layout configuration.

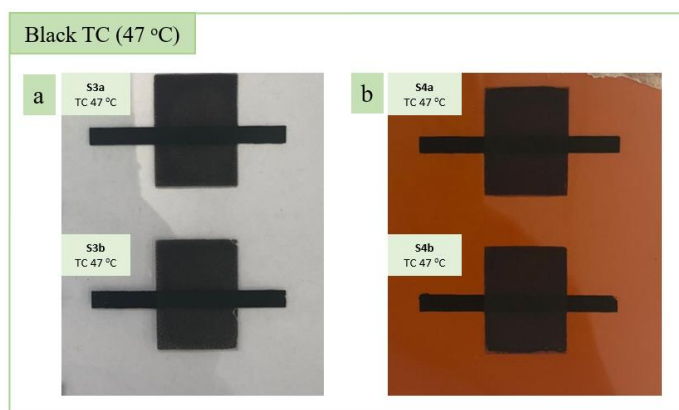


Figure 2.25 Visual representation of the: **a)** S3 sample utilizing the Black TC (47 °C) on PET substrate, **b)** S2 sample, utilizing the Black TC (47 °C) on Kapton substrate, with the L3 layout configuration.

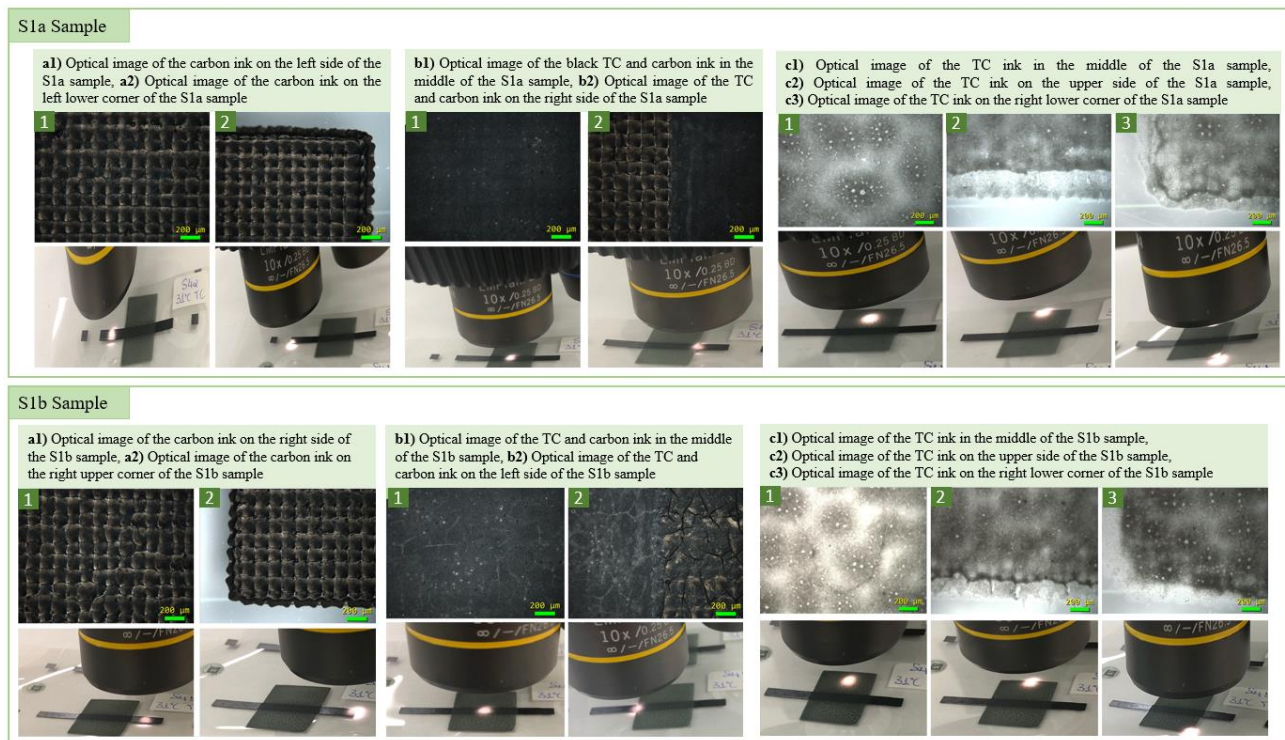


Figure 2.26: Optical Characterization of the S1a and S1b samples utilizing the Black TC (31 °C), on PET surface – L3 layout configuration, with detailed description.

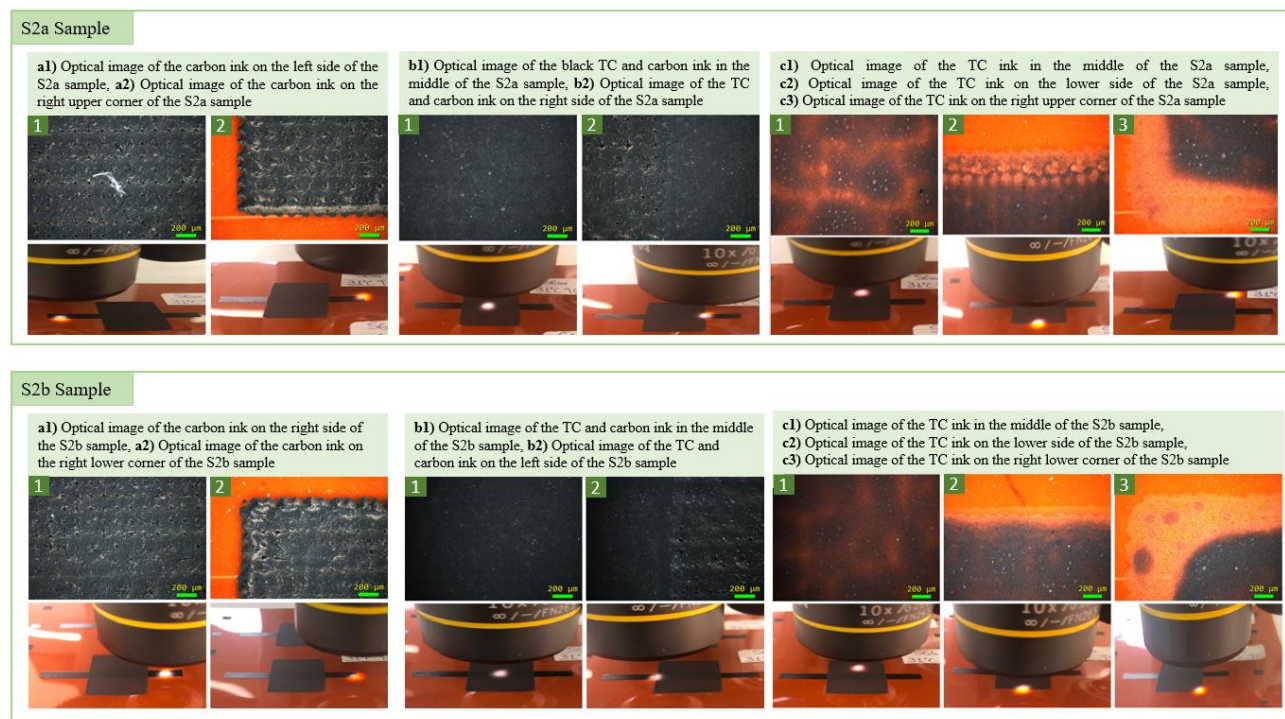


Figure 2.27 Optical Characterization of the S2a and S2b samples utilizing the Black TC (31 °C), on Kapton surface – L3 layout configuration, with detailed description.

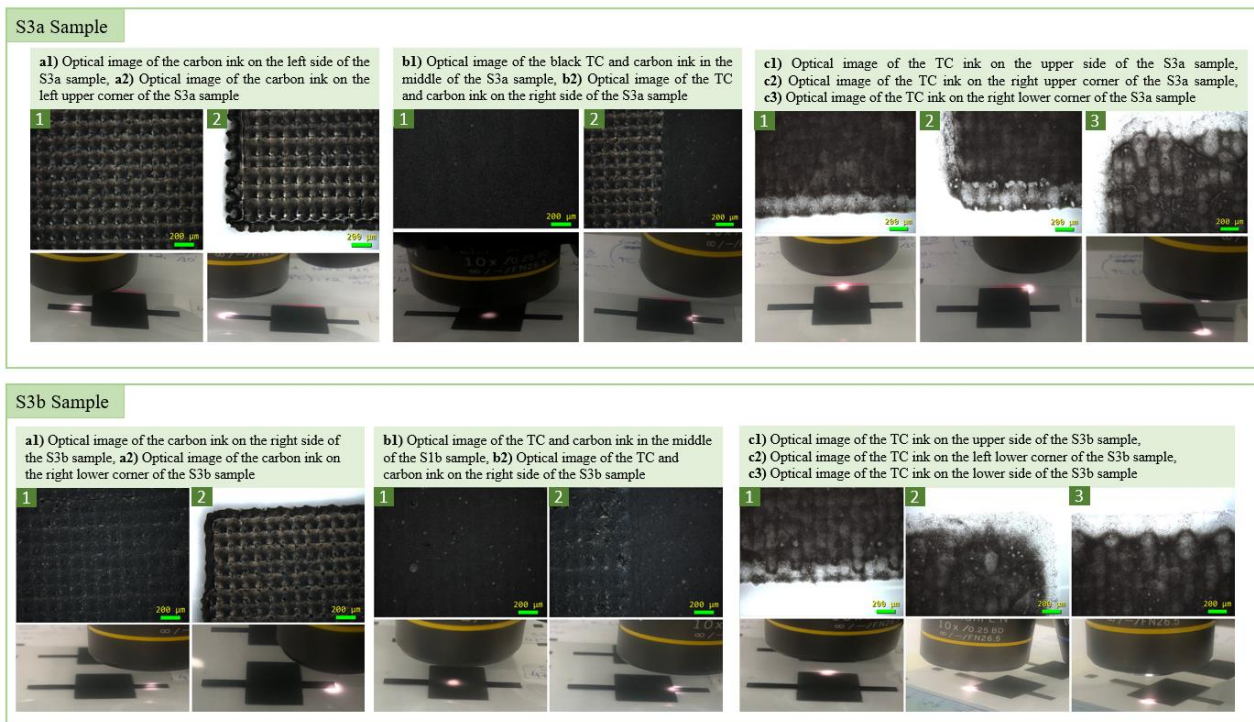


Figure 2.28: Optical Characterization of the S3a and S3b samples utilizing the Black TC (47 °C), on PET surface – L3 layout configuration, with detailed description.

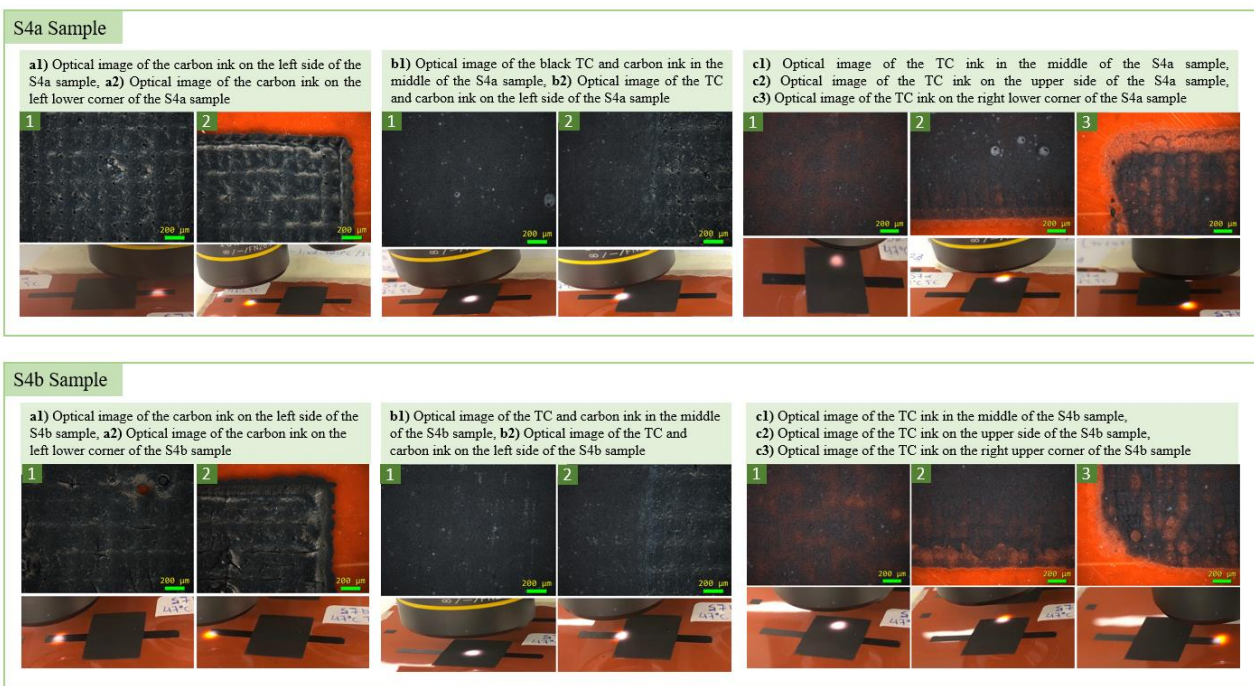


Figure 2.29: Optical Characterization of the S4a and S4b samples utilizing the Black TC (47 °C), on PET surface – L3 layout configuration, with detailed description.

****Observations & Remarks****

❖ S1 & S2 Samples – Black TC 31°C on PET and Kapton Substrates

- Based on the optical images presented above which depict both samples on PET and Kapton substrates, it becomes apparent that certain regions of the carbon ink exhibit a mesh-like pattern, characterized by small square structures, indicative of surface irregularities. Conversely, in some areas, the carbon component appears smoother and more compressed. This variability can be attributed to the differential pressure exerted by the mesh mask and the squeegee on the substrate

during the screen-printing process. This leads to the non-uniformly distributed carbon ink across the entire surface.

- A comparison of the optical images of the S1a and S1b TC structures on PET substrates (Fig. 2.26) indicates that the printings are of good quality. However, a minor scratch is observed on the S1b structure (Fig. 2.30a). This scratch may be the cause of the small defects on the PET substrate from the manufacturer, or it may have occurred during the screen-printing procedure. Therefore, it is recommended to examine the PET substrate for any small imperfections via the microscope, prior to a screen-printing procedure.
- The optical images of the S2a screen-print sample display a hole on its left side, where carbon ink is printed (Fig. 2.30b). This flaw may affect our measurements when heat is applied to the sample via the prober. However, the optical images of the S2b screen-print sample indicate that no visible scratches or holes are displayed on the carbon ink (Fig. 2.27 – S2b Sample).
- Keeping the abovementioned observations in mind, it could be said that out of these four (4) samples, S1b and S2b are the samples with the best screen-printing outcome.

❖ S3 & S4 Samples – Black TC 47°C on PET and Kapton Substrates

- The optical characterizations of the S3a and S3b samples (Fig. 2.28) indicate that they are of relatively good quality. However, there are some noticeable defects that should be noted. Regarding the S3b sample, there is a deformity in the printing of the right upper corner of the TC element (Fig. 2.31), although it is not likely to affect the measured data, when the sample is heated.
- The optical images of the S4a and S4b samples (Fig. 2.32a) do not indicate any holes. However, there is a deformity in the right upper corner of the carbon ink structure of the S4b sample (Fig. 2.32b). Specifically, the corner has not been printed correctly, probably because of the poorly cleaned mesh mask, whose residue can prevent the ink from being printed correctly.

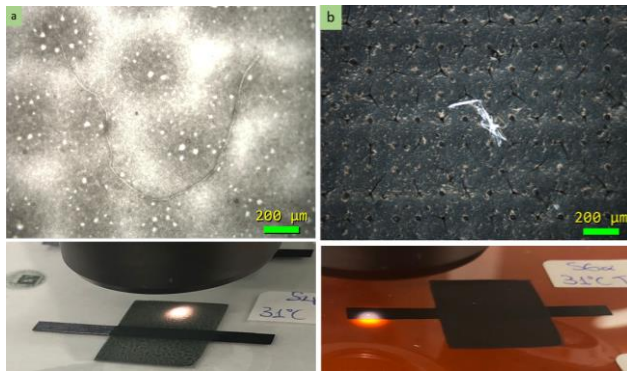


Figure 2.30: Errors on S1b and S2a samples: **a)** Scratch within the black TC ink in the middle of the S1b sample, **b)** Hole on the left side of the S2a sample.

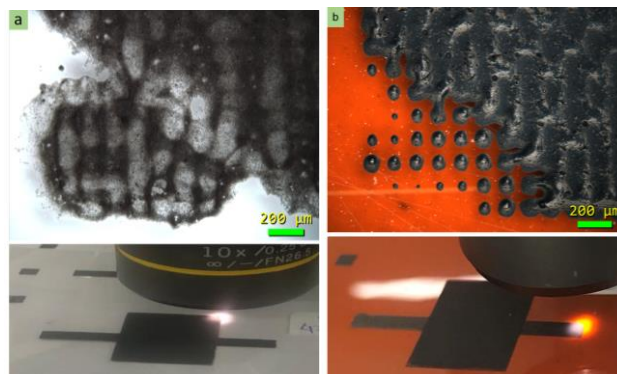


Figure 2.31: Errors on S3b and S4b samples, **a)** Deformity in the screen-printing outcome on the left upper corner of the Black TC ink of S3b sample, **b)** Voids on the right upper corner of the carbon ink structure of S4b sample.

2.3 Electrical – Thermal Measurements

The primary objective of this paragraph is to assess the heat responsiveness of Thermochromic materials at various activation temperatures, across the three distinct layout design prototypes. This assessment is conducted by employing internal heating (the heating induced by the internal carbon heater [182]), in order to identify the most suitable prototype for use as a flexible skin temperature sensor, utilizing TC inks. To accomplish this, the measurements and characterizations were conducted within a probe station, equipped with an integrated hot-plate (Fig. 2.32b). To precisely regulate the power supplied to the hot-plate, a LabView software program was developed, while probes were employed to apply the power to specific regions of each sample. The Keithley 2612 source-meter [174] served as the power source and was connected with both the software and the probe station (Fig. 2.32a). The temperature measurements for each sample were obtained using an IR thermal camera (UNI-T PRO - UTI690B / Professional Thermal Imager – Fig. 2.33a) [183], as well as the High precision Thermal IR Camera (FLIR SC655) (Fig. 2.33b) [184].

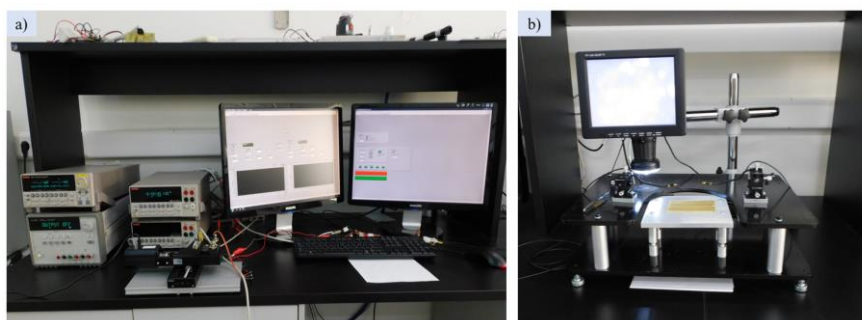


Figure 2.32: Equipment used for the internal heating of the TC flexible structures: **a)** Keithley source-meter [174] and LabView Software, **b)** probe station with integrated hot-plate.

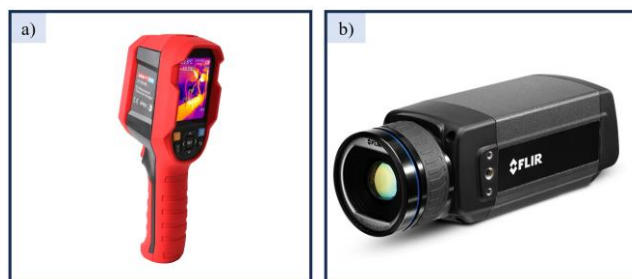


Figure 2.33: IR thermal cameras for thermal measurements: **a)** UNI-T PRO - UTI690B / Professional Thermal Imager [183], **b)** High precision Thermal IR Camera (FLIR SC655) [184].

2.3.1 Temperature – Power/Area and Resistance – Temperature Graphs

This section, presents the detailed Temperature – Power/Area and Resistance – Temperature graphs, for each of the three designed layouts that have been developed. These graphs offer comprehensive insights into the temperature-related performance and resistance characteristics of each individual sample, facilitating a more in-depth understanding of the comparative performance and behavior of the three developed prototype configurations.

a. Graphs corresponding to the L1 layout configuration – Internal Heating of the samples

The data-tables (Table 2.7) and graphs provided below, refer to the performance of the S1, S2, and S3 samples, when internal heating is applied, via the probe station (Fig. 2.34). In this case the UNI-T PRO - UTI690B / Professional Thermal Imager [183] was used for the temperature's identification, during the internal heating process of each sample.

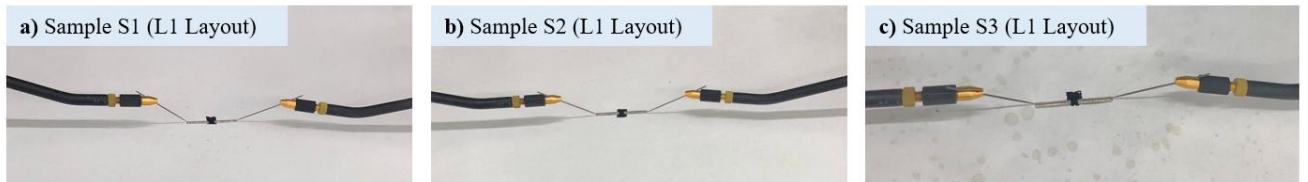
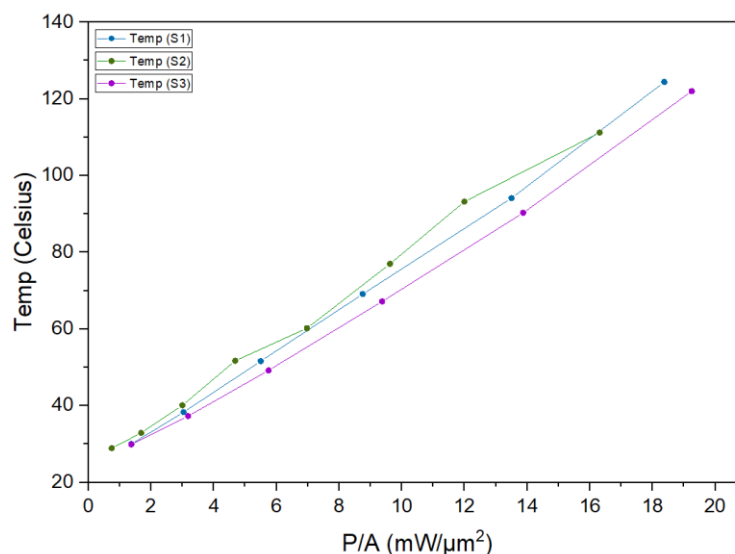


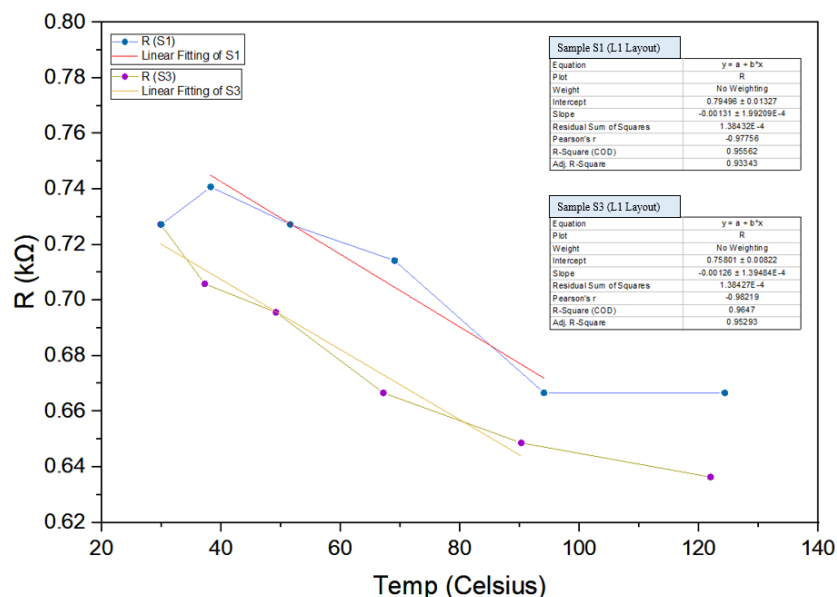
Figure 2.34: Visual representation of the: a) S1 sample, b) S2 sample, c) S3 sample with the L1 layout configuration, onto the hot-plate for internal heating.

Table 2.7: Data gained from the Internal Heating of S1, S2 and S3 Sample, respectively.

S1 Sample						
Volt (V)	Temperature (°C)	I (mA)	P (mW)	Power/Area (mW/μm ²)	R (kΩ)	ΔR/R ₀
4	30	5.5	22	1.375	0.72727	0.01818
6	38.3	8.1	48.6	3.0375	0.74074	0
8	51.6	11	88	5.5	0.72727	0.01818
10	69.1	14	140	8.75	0.71429	0.03571
12	94.1	18	216	13.5	0.66667	0.1
14	124.4	21	294	18.375	0.66667	0.1
S2 Sample						
Volt (V)	Temperature (°C)	I (mA)	P (mW)	Power/Area (mW/μm ²)	R (kΩ)	ΔR/R ₀
4	28.9	3	12	0.75	1.33333	0
6	32.9	4.5	27	1.6875	1.33333	0
8	40.1	6	48	3	1.33333	0
10	51.7	7.5	75	4.6875	1.33333	0
12	60.2	9.3	111.6	6.975	1.29032	0.03226
14	77	11	154	9.625	1.27273	0.04545
16	93.2	12	192	12	1.33333	0
18	111.2	14.5	261	16.3125	1.24138	0.06897
S3 Sample						
Volt (V)	Temperature (°C)	I (mA)	P (mW)	Power/Area (mW/μm ²)	R (kΩ)	ΔR/R ₀
4	29.9	5.5	22	1.375	0.72727	0
6	37.3	8.5	51	3.1875	0.70588	0.0303
8	49.2	11.5	92	5.75	0.69565	0.0448
10	67.2	15	150	9.375	0.66667	0.08586
12	90.3	18.5	222	13.875	0.64865	0.11138
14	122	22	308	19.25	0.63636	0.12879



Graph 2.1: Temperature – Power/Area (T-P/A) Graph for S1, S2 S3, samples - L2 Layout.



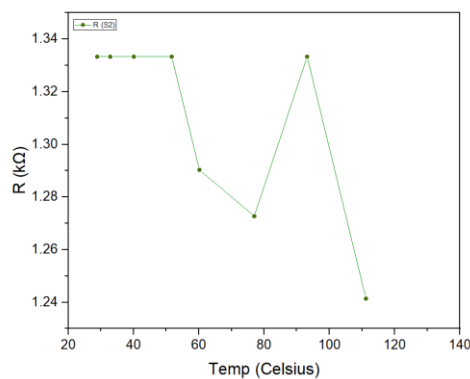
Graph 2.2: Resistance – Temperature (R-T) Graph for S1, S2 S3, samples - L2 Layout.

Observations & Remarks

- Since different samples may exhibit varying temperature readings when subjected to the same voltage level, "Power" is a variable commonly associated with a particular temperature reading. Consequently, the Power/Area (P/A) data provides insight into the concentration amount of heat, within a given surface area. This metric reveals that larger surfaces require a greater amount of power to achieve a specific temperature, while smaller surfaces require less power to attain the same temperature level. Such information is valuable for understanding the thermal behavior of various surface sizes and optimizing the heating processes accordingly.
- Upon careful examination of the S2 sample (Fig. 2.8b2) and a comparative analysis with the S1 and S3 samples (Fig. 2.8a2 and Fig. 2.8c2), it becomes apparent that there may be structural irregularities within the sample. Specifically, the electrode placement in S2 appears to be positioned precisely at the middle of the carbon element, whereas in the case of the other two samples, the electrodes are located relatively lower. Consequently, this variation results in a distinct difference in the heating carbon area between the S2 sample and the other two samples, which is particularly noticeable when examining the Temperature-Power/Area (T-P/A) and Resistance – Temperature (R-T) graphs (Graph 2.1, Graph 2.2). Graph 2.1 represents the relationship between the temperature and power, in response to the area (T-P/A) of the S1, S2, and S3 samples. Notably, in Table 2.7 the recorded currents for S1 and S3 samples are identical, whereas the current data for S2 is almost half the value, from the other two samples. Therefore, the power data derived from the S2 sample appears to be only half the power generated from S1 and S3 samples. This discrepancy in power performance may be attributed to multiple factors, most notably the placement of the Ag contacts on the carbon element, as well as the concentration of carbon ink.
- The R-T graph illustrates the relationship between the resistance and temperature of the S1 and S3 samples. As depicted in Graph 2.2, it is evident that the resistance data for both the S1 and S3 samples are quite similar. This similarity is further evident when examining the slopes of both graphs, which represent a nearly identical behavior, being equal to $Slope_{S1} = -0.00131 \pm 1.99E-4$ (kΩ / °C) and $Slope_{S3} = -0.00126 \pm 1.39E-4$ (kΩ / °C). This observation aligns with the identical power values presented in Table 2.7. Notably, the resistance behavior of sample S2 – as illustrated

in [Graph 2.3](#) – displays an unusual resistance pattern from that of S1 and S3, leading to its exclusion from the overall R-T graph. Remarkably, the resistance of S2 is twice that of both S1 and S3, a characteristic also evident in the power values depicted in [Table 2.7](#) and the corresponding graphs.

- Due to the fact that the highly conductive silver (Ag) electrodes were unevenly placed onto the carbon element, the heating of the carbon’s area was varying, as the areas closer to the Ag electrodes experienced more heat than others ([Fig. 2.35](#)). Consequently, this design is unsuitable for effectively heating the thermochromic (TC) material, as well as its consideration as a prototype for flexible skin temperature sensors based on TC inks.
- To address these challenges, the L2 layout design was developed. In this design, the Ag electrodes are designed and positioned accurately, to cover the entire width of the carbon element. This modification ensures that the thermochromic material not only fully covers the carbon area but also, due to its extended length, exceeds its coverage area.



Graph 2.3: R-T Graph of the S2 sample, showing non-linearity and an unusual pattern.

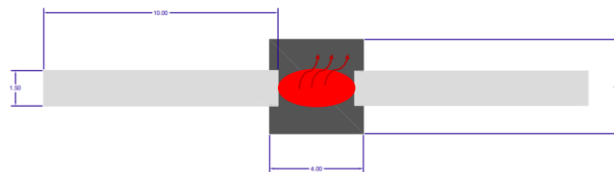


Figure 2.35: L1 layout configuration. This design is inappropriate for the heating of the TC element, as only a specific area of the carbon resistance is heated, when power is applied.

b. Graphs corresponding to the L2 layout configuration – Internal Heating of the samples

The following data tables and graphs pertain to the performance evaluation of the S1, S2 and S3 samples regarding the L2 layout design, under internal heating application through the probe station, as illustrated in [Fig. 2.36](#). In this particular scenario, the process involved utilizing the FLIR SC655 Thermal Machine Vision Camera [184], for the temperature’s precise assessment and identification during the internal heating process.

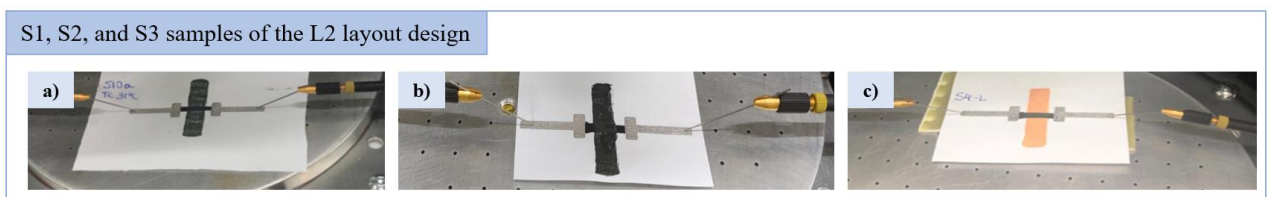


Figure 2.36: Visual representation of the: a) S1 sample (Black TC 31 °C), b) S2 sample (Black TC 47 °C), c) S3 sample (Orange TC 28 °C), with the L2 layout configuration, onto the hot-plate for internal heating.

▪ Internal Heating of the S1 sample

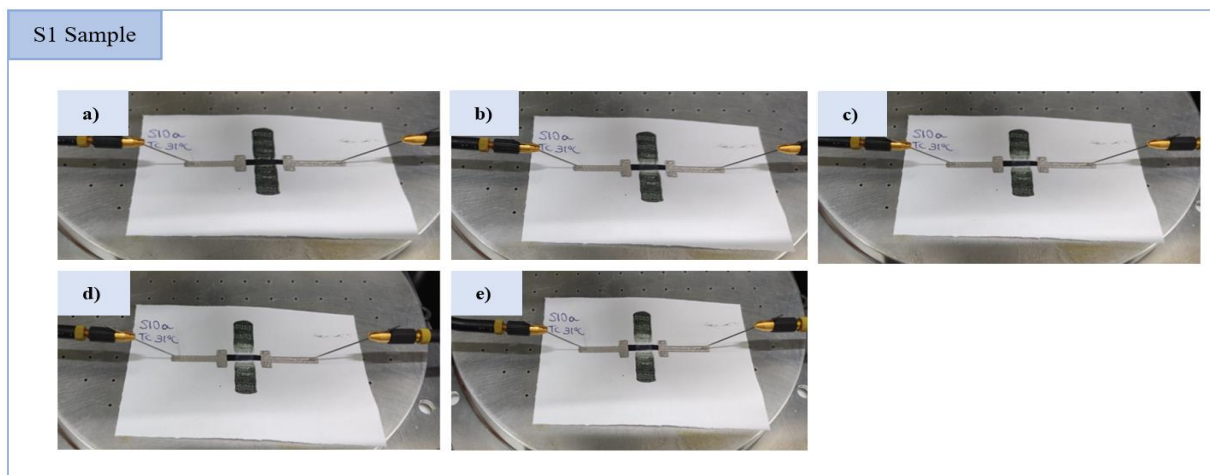


Figure 2.37: Discoloration process of the S1 sample (Black TC 31 °C), with the application of various power rates.

Table 2.8: Data gained from the Internal Heating of S1 Sample

S1 Sample (Black TC, 31 °C)						
Volt (V)	Figure	Temperature (°C)	I (mA)	Power/Area (mW/μm ²)	R (kΩ)	ΔR/R ₀
1	Fig. 2.37a	27.3	0.15	7.38916E-4	6.66667	0
10	Fig. 2.37b	29.8	1.5	0.07389	6.66667	0
15	Fig. 2.37c	34	2.26667	0.16749	6.61765	0.00735
20	Fig. 2.37d	40	3.05	0.30049	6.55738	0.01639
25	Fig. 2.37e	48.1	3.96	0.48768	6.31313	0.05303

▪ Internal Heating of the S2 sample

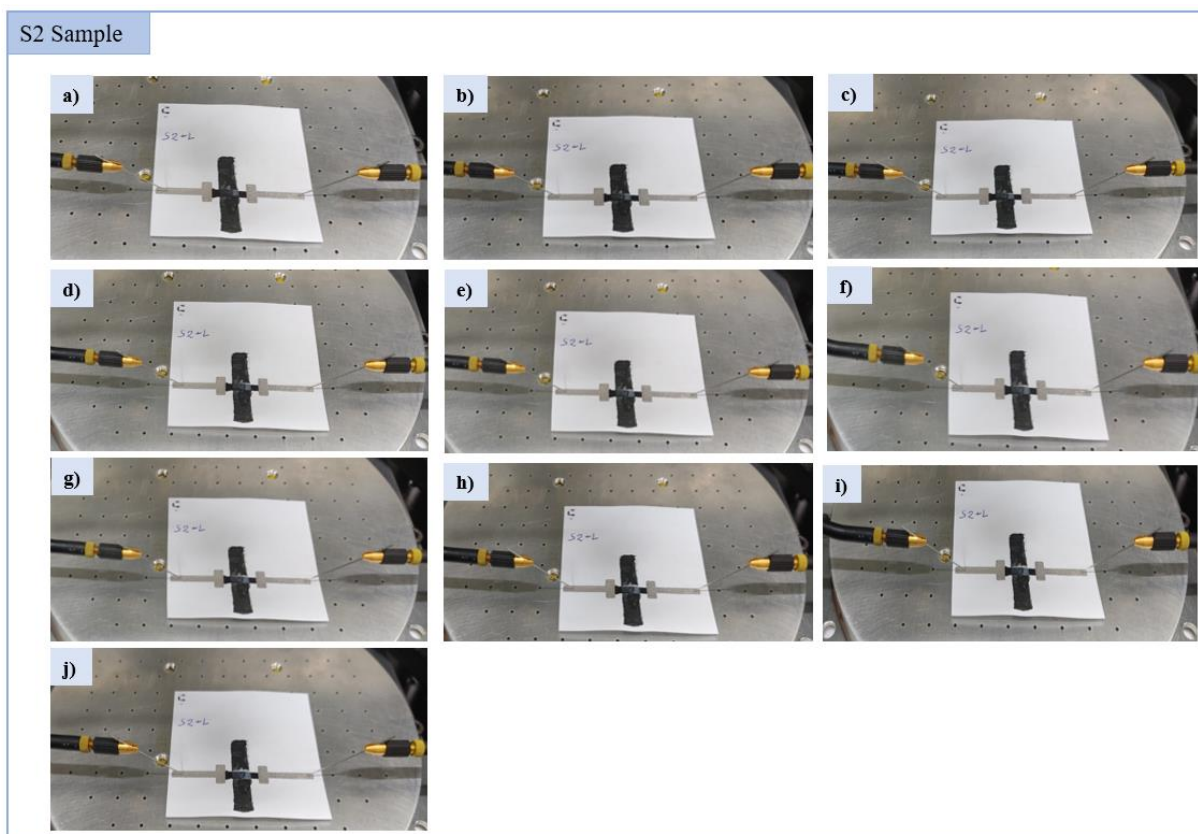


Figure 2.38: Discoloration process of the S2 sample (Black TC 47 °C), with the application of various power rates.

Table 2.9: Data gained from the Internal Heating of S2 Sample

S2 Sample (Black TC, 47 °C)						
Volt (V)	Figure	Temperature (°C)	I (mA)	Power/Area (mW/μm ²)	R (kΩ)	ΔR/R _o
25	Fig. 2.38a	36.5	1.96	0.24138	12.7551	0
30	Fig. 2.38b	40.5	2.36667	0.34975	12.67606	0.0062
31	Fig. 2.38c	41.7	2.45161	0.37438	12.64474	0.00865
35	Fig. 2.38d	45.8	2.8	0.48276	12.5	0.02
36	Fig. 2.38e	47	2.88889	0.51232	12.46154	0.02302
37	Fig. 2.38f	48.2	2.97297	0.54187	12.44545	0.02428
39	Fig. 2.38g	51	3.15385	0.60591	12.36585	0.03052
41	Fig. 2.38h	53.6	3.34146	0.67488	12.27007	0.03803
42	Fig. 2.38i	55	3.42857	0.70936	12.25	0.0396
43	Fig. 2.38j	56.7	3.51163	0.74384	12.24503	0.03999

Internal Heating of the S3 sample

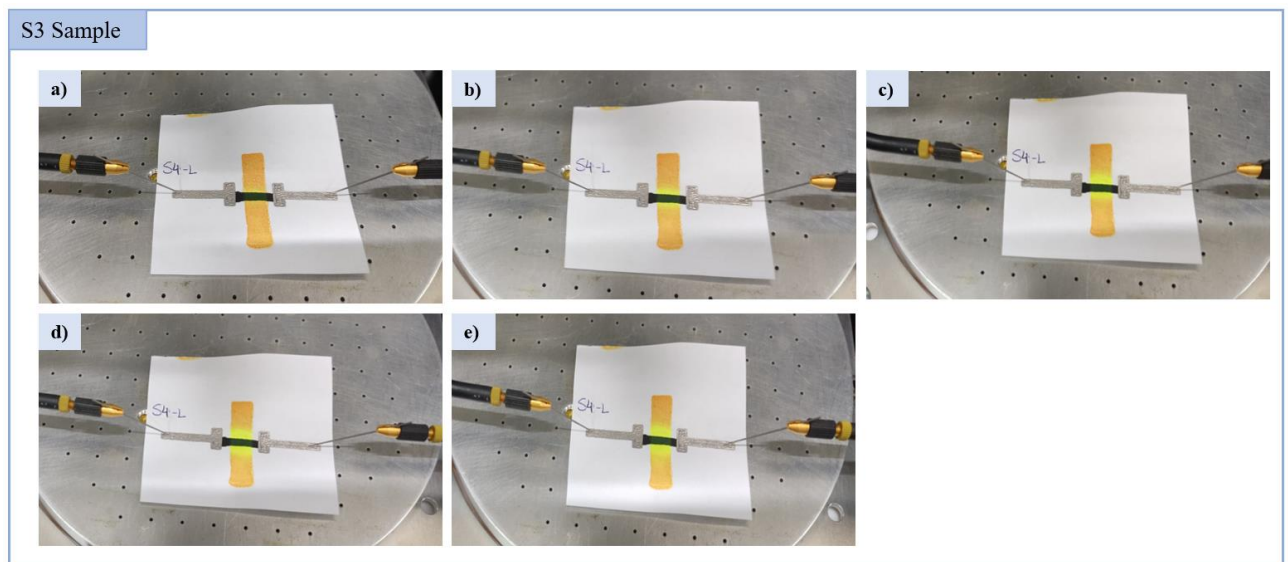
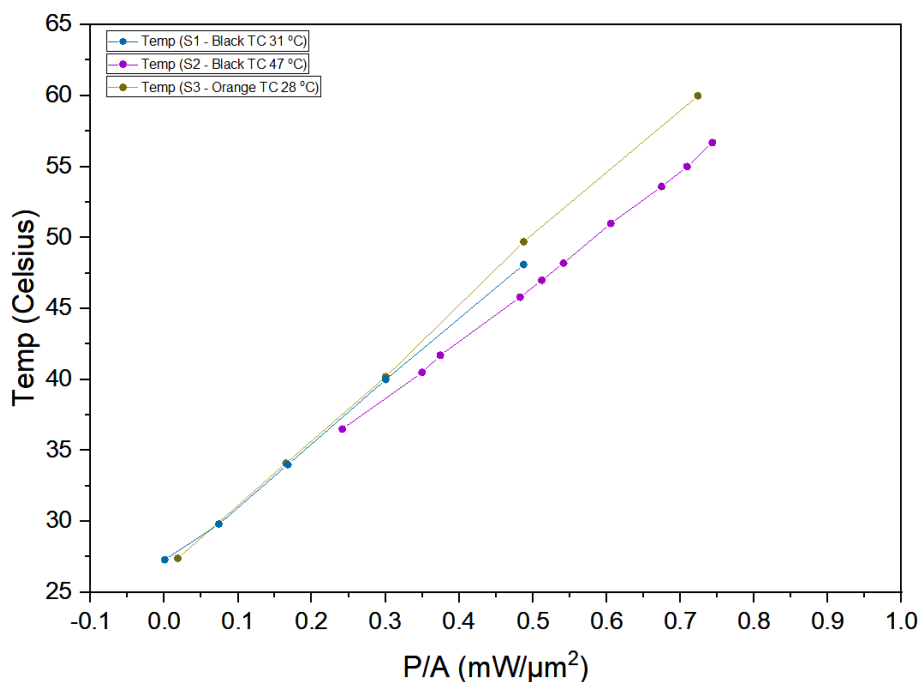


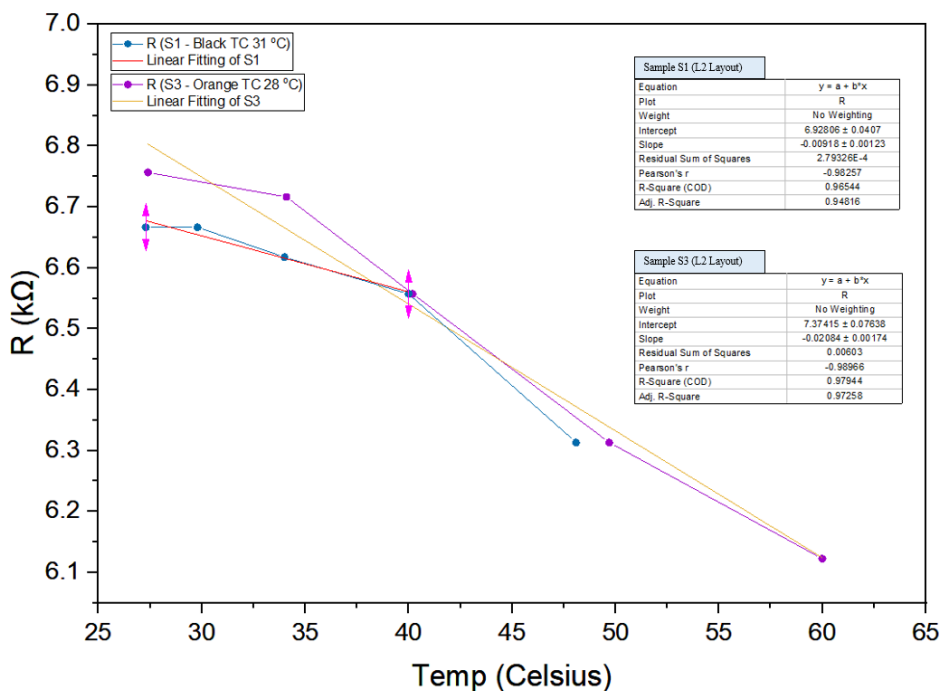
Figure 2.39: Discoloration process of the S3 sample (Orange TC 28 °C), with the application of various power rates.

Table 2.10: Data gained from the Internal Heating of S3 Sample.

S3 Sample (Orange TC, 28 °C)						
Volt (V)	Figure	Temperature (°C)	I (mA)	Power/Area (mW/μm ²)	R (kΩ)	ΔR/R _o
5	Fig. 2.39a	27.4	0.74	0.01823	6.75676	0
15	Fig. 2.39b	34.1	2.23333	0.16502	6.71642	0.00615
20	Fig. 2.39c	40.2	3.05	0.30049	6.55738	0.03041
25	Fig. 2.39d	49.7	3.96	0.48768	6.31313	0.06765
30	Fig. 2.39e	60	4.9	0.72414	6.12245	0.09673



Graph 2.4: Temperature – Power/Area (T-P/A) for the S1 (Black TC 31 °C), S2 (Black TC 47 °C) and S3 Samples (Orange TC 28 °C).

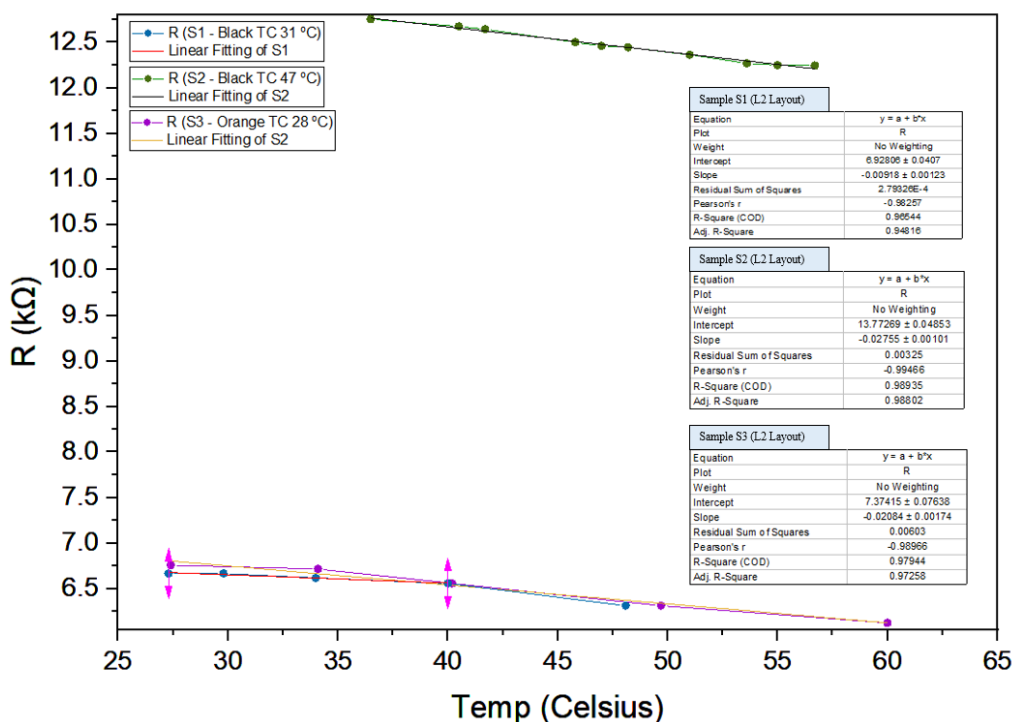


Graph 2.5: Resistance – Temperature (R-T) Graph for the S1 (Black TC 31 °C) and S3 Samples (Orange TC 28 °C).

Observations & Remarks

- **Graph 2.4**, illustrates the Temperature-Power/Area (T-P/A) relationship. Specifically, the T-P/A graph indicates that, while a particular level of power is linked to a specific temperature reading, various samples may not produce the same temperature reading, when subjected to the same amount of power. The linearity of the S1 and S3 samples is of significant interest, since the same amount of power, almost generates the same amount of heat, as evidenced by [Table 2.8](#) and [Table 2.10](#). This consistent thermal behavior is attributed to the matching geometric characteristics of both samples, as well as the quantity of carbon ink serving as a heating element for the TC material.

- Graph 2.5** presents the Resistance-Temperature relationship for the S1 and S3 samples, with activation temperatures of 31°C (Black-Transparent) and 28 °C (Orange-Yellow), respectively. The slopes in this graph differs a lot for each of the samples, with the S1 sample’s being equal to $Slopes_{S1} = -0.00918 \pm 0.00123$ (kΩ / °C), and the S3 sample’s equal to $Slopes_{S3} = -0.02084 \pm 0.00174$ (kΩ / °C). This limitation may be due to the triple curing process of the carbon element, potentially altering its electrical characteristics. This constraint could be avoided by introducing a barrier layer on top of the carbon resistance, to maintain the stability of its electrical properties. Another viable solution could involve estimating the TCR of the carbon resistance, prior screen-printing the Ag and TC layers on top of it. The S2 sample showcases a twice resistance value, in contrast to the other two samples (**Graph 2.6**). This constraint might be due to the amount of carbon ink of the S2 sample, in comparison to the S1 and S3 samples. Moreover, as closely evidenced by **Fig. 2.38**, the TC element of S2 sample reveals an uneven distribution, with some areas showing thicker amounts of TC ink than others. This irregularity is not observed in the prints of the other two samples, which exhibit a more consistent pattern in their graphical representations. However, it is worth noting that the slope of the S2 sample is close to the slope value derived from the S3 sample, being equal to $Slopes_{S2} = -0.02755 \pm 0.00101$ (kΩ / °C). This observation correctly signifies that when the resistance value of the S2 sample is twice that of the S3 sample, it results in a slightly larger slope. To address any of the challenges effectively, it is imperative to execute the screen-printing process with meticulous precision, to ensure uniformity and consistency in the TC element deposition. This will enable us to acquire more valuable and accurate data, essential for the development of the temperature sensor's prototype.



Graph 2.6: Temperature – Power/Area (T-P/A) Graph for the S1 (Black TC 31 °C), S2 (Black TC 47 °C) and S3 Samples (Orange TC 28 °C) – Representation of the double resistance values of the S2 sample, in comparison to the S1 and S3 samples

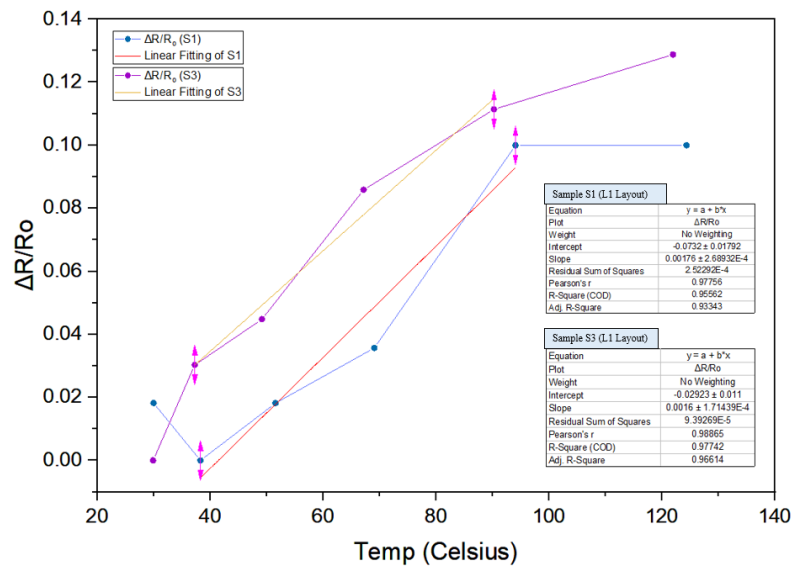
2.3.2 Temperature Coefficient of Resistance

This section is focused on the Temperature Coefficient of Resistance (TCR) of the samples, of the three distinct layout configurations, L1, L2 and L3, respectively. The objective here is to identify the most optimal configuration for fabricating a flexible skin-temperature sensor utilizing Thermochromic elements. This investigation seeks to determine which layout configuration offers the best performance and reliability for the development of such a sensor by providing valuable insights into achieving its desired functionality and effectiveness.

The TCR ($^{\circ}\text{C}^{-1}$) is calculated by evaluating the slope of the Resistance-Temperature curve or line, and is defined as the change in resistance (ΔR) divided by the initial resistance (R_0) for a specific temperature change (ΔT) [186]:

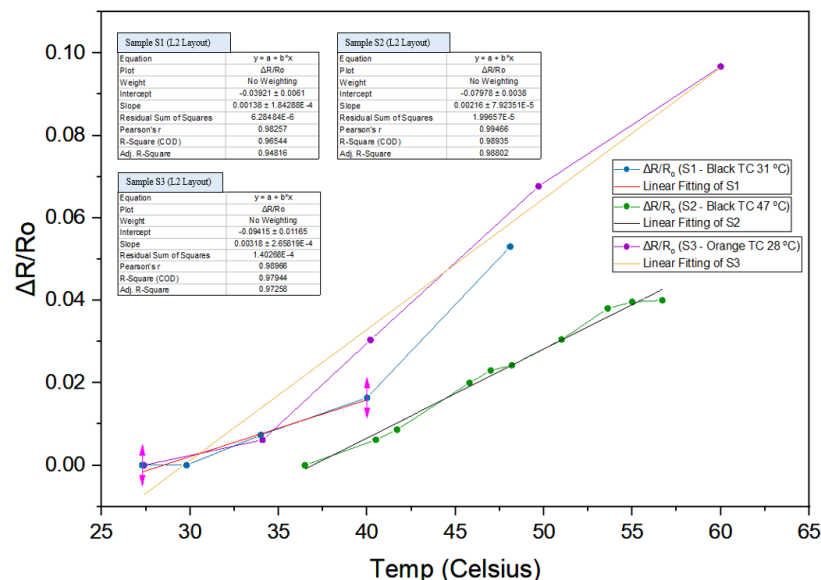
$$TCR = a = \frac{\left(\frac{\Delta R}{R_0}\right)}{T} \quad (\text{Eq. 5})$$

a. TCR of S1 and S2 samples of the L1 layout design



Graph 2.7: TCR ($\Delta R/R_0 - T$) Graph for samples S1 and S3 with the L1 layout configuration.

b. TCR of S1, S2 and S3 samples of the L2 layout design



Graph 2.8: TCR ($\Delta R/R_0 - T$) Graph for samples S1 and S3 with the L2 layout configuration.

Observations & Remarks

L1 Layout:

- As observed in [Table 2.6](#), samples S1, S2 and S3 display a negative temperature coefficient (NTC) because of their constantly decreasing resistance, with the increasing temperature. Therefore, 'R_o' represents the highest resistance value obtained from each sample in [Table 2.6](#), and the changes in resistance (ΔR) values are calculated by subtracting 'R_o' (= the highest resistance) from each resistance 'R'. The ' $\Delta R/R_o - T$ ' graph ([Graph 2.7](#)), reveals a $TCR_1 = 0.00176 \pm 2.69E-4$ ($^{\circ}C^{-1}$), and a $TCR_3 = 0.0016 \pm 1.71E-4$ ($^{\circ}C^{-1}$), for sample S1 and S3, respectively. The Temperature Coefficient of Resistance (TCR) values for both the S1 and S3 samples are nearly identical, demonstrating the consistent behavior of the carbon resistance when exposed to temperature variations. As previously mentioned, sample S2 is not taken into consideration, since it displays an unusual resistance pattern from that of the S1 and S3 samples.

L2 Layout:

- [Graph 2.8](#) displays the Temperature Coefficient of Resistance (TCR), obtained from the $\Delta R/R_o -$ Temperature correlation. 'R_o' is defined as the highest resistance value, due to the negative temperature coefficient (NTC) behavior of all S1, S2, and S3 samples. This observation is also presented thoroughly in [Table 2.7](#), [Table 2.8](#), and [Table 2.9](#), for each sample respectively. The ΔR values were calculated by subtracting 'R_o' from each 'R'. All samples exhibit a negative TCR since the resistance values decrease with the increasing temperature. Each sample exhibits a TCR equal to $TCR_1 = 0.00138 \pm 1.84E-4$ ($^{\circ}C^{-1}$) for sample S1, $TCR_2 = 0.00216 \pm 7.91E-5$ ($^{\circ}C^{-1}$) for sample S2, $TCR_3 = 0.00318 \pm 2.66E-4$ ($^{\circ}C^{-1}$) for sample S3. As previously mentioned, the lack of a barrier layer (e.g., PEDOT: PSS) to preserve the stability of the carbon resistance's electrical properties, might be the cause of the varying TCR values. Therefore, a viable solution would conduct the measurements both before and after screen-printing the Ag and TC layers, to compare the stability of the TCR values.

3 CHAPTER 3:

Optical Temperature detection of the TC Device

This chapter presents the correlation analysis between the thermal and optical field of the S3a and S4a samples with the L3 layout design, on PET and Kapton substrates, respectively. These samples consist of a black thermochromic (TC) ink with an activation temperature of 47 °C on top of a printed carbon heater (Fig. 3.1a, Fig. 3.1b). To conduct the analysis, internal heating is applied through the carbon element to both samples, via the probe station. The probes are in contact with the carbon layer of the TC-based structure, which functions as a heater for the thermochromic ink. The main objective of this study is to establish a correlation between the thermal and optical fields under a wide temperature range, as well as a narrow temperature range that closely aligns with the activation temperature of these samples. The correlation between the thermal and optical field is conducted through a thermal IR camera (High precision Thermal IR Camera - FLIR SC655 [184]) and a high-resolution camera.

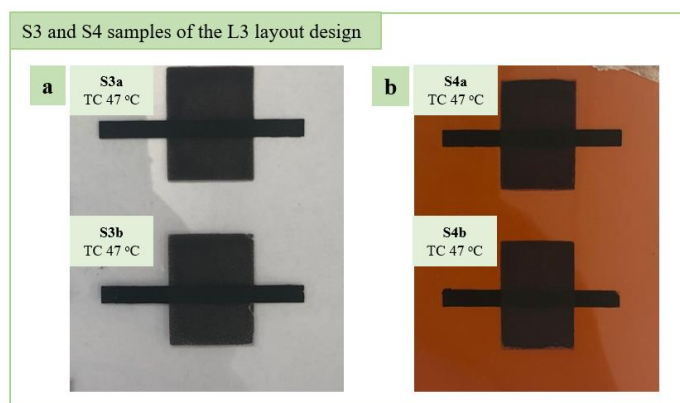


Figure 3.1: a) S3a Sample: Black TC with 47 °C activation temperature on PET Substrate, b) S4a Sample: Black TC with 47 °C activation temperature on Kapton Substrate.

3.1 Temperature Determination – Correlation of the Thermal and Optical Field

The setup of the temperature determination via photography involves several components, including:

1. a LabView software program responsible for regulating the supplied power to the hot-plate,
2. the probe station with the integrated hot-plate,
3. the Keithley 2612 source-meter [174] which functions as the power source and is connected to both the software and the prob-station.

The temperature of each sample was determined through an IR thermal camera (FLIR SC655 [184]), whose software not only provides thermal data, but also offers a correlation between the temperature and the pixels within the selected area of interest. In particular, it was observed that the 35mm carbon's element length corresponds to 159 pixels. The ImageJ software [187] was employed to process the optical images, captured by either a high-resolution camera. By using this software, the grayscale data was extracted from the specific area of the image of interest. This data underwent additional processing in OriginPro software, by OriginLab [188] to implement the correlation graphs.

Given that both the thermal and optical image data were expressed in terms of pixels, a correlation between the maximum recorded temperature and its corresponding pixels in the thermal image, was established. This connection was also correlated with the maximum grayscale value – representing the lightest color – in the optical image. All pixels were converted into distance values in millimeters. This conversion involved measuring the actual width of the TC (thermochromic) element, and determining how many pixels in the FLIR software correspond to that measured dimension, as our measurements were specifically taken within that particular area.

3.1.1 Measurements of the TC Device with the Thermal (IR) and a High-Resolution Camera

In both the S3a and S4a samples, temperature distribution graphs were generated along the width of the TC (thermochromic) element. Two sets of temperature variations were conducted for each sample, in response to the activation temperature of the TC element (47 °C). In the former analysis both of the samples were examined at wide a temperature range of 50 °C, 60 °C, and 70 °C. In the later analysis, however, a narrow temperature measurement range that closely aligns with the activation temperature value of the samples, was intentionally selected. In this specific scenario, the samples were studied at temperatures of 40 °C, 43 °C, 46 °C, 49 °C, and 52 °C.

Table 3.1, provides the temperature values for each of the two distinct temperature range scenarios, being:

- a) a wide temperature range,
- b) a narrow temperature range that closely aligns with the 47 °C activation temperature of the TC element.

This table also includes the corresponding power inputs necessary to attain these specific temperature levels.

Table 3.1: Power applied to get the desired temperatures, for each of the two temperature range scenarios, respectively.

1st Scenario: Wide temperature range		
Temperature (°C)	Power (W)	
	S3a sample (PET substrate)	S4a sample (Kapton substrate)
50	0.224	0.479
60	0.358	0.678
70	0.497	0.987
2nd Scenario: Narrow Temperature range that closely aligns with the 47 °C activation temperature of the TC element		
Temperature (°C)	Power (W)	
	S3a sample (PET substrate)	S4a sample (Kapton substrate)
40	0.115	0.219
43	0.148	0.294
46	0.161	0.384
49	0.198	0.451
52	0.233	0.522

3.1.2 Data Processing & Correlation Graph of the Thermal and Optical Field of the TC device

This paragraph presents the temperature distribution across the TC element of both the S3a and S4a samples for each of the two scenarios, indicated in the previous paragraph (Fig. 3.2 and Fig. 3.10). Additionally, the thermal and optical correlation graphs, are also included to complement our findings. These graphs establish the relationship between the thermal and optical distribution field, providing a comprehensive understanding of both the samples' behavior under different temperature conditions.

a) 1st Scenario: Wide temperature range

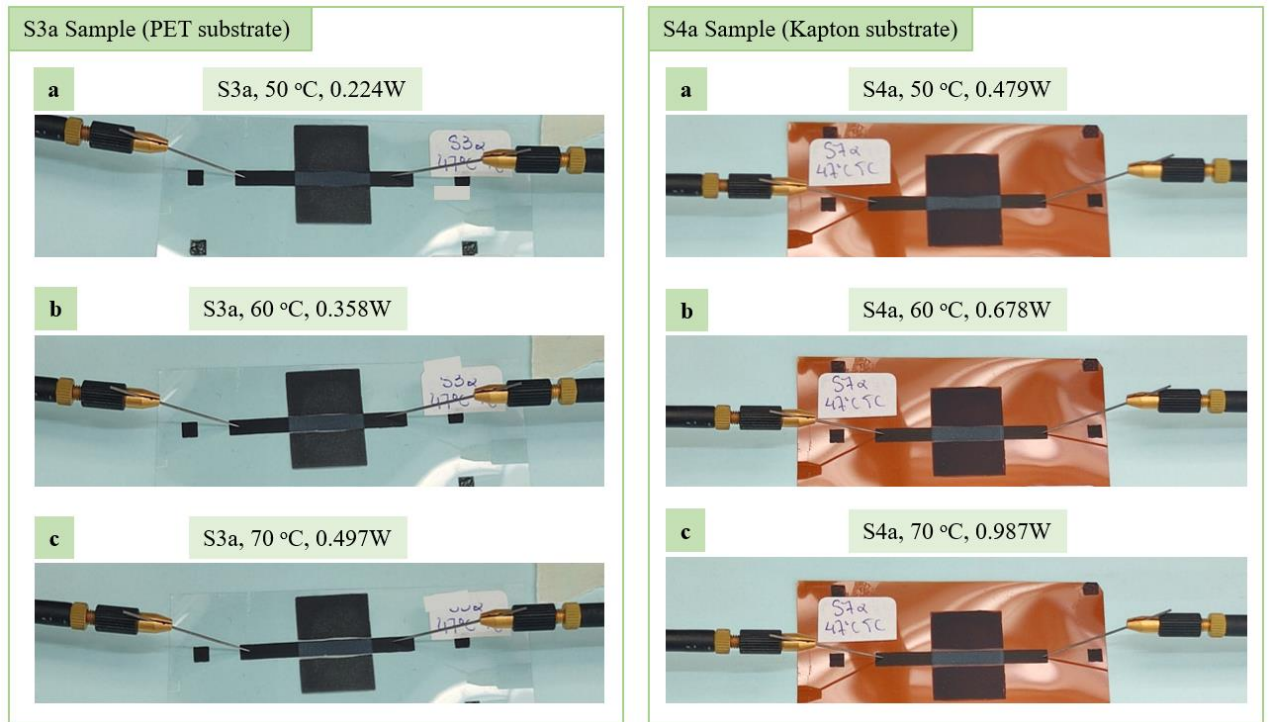


Figure 3.2: Internal Heating phases of the S3a and S4a samples, on PET and Kapton substrates respectively: a) 50 °C, b) 60 °C, c) 70 °C.

Each of the provided graphs below features three or four distinct curves. The first two curves depict the thermal data, with the green curve representing the data obtained from the IR camera and the corresponding Gaussian curve (red curve). The third curve, in blue color, illustrates the optical data captured with a high-resolution camera, and fourth curve displays the corresponding Gaussian curve (purple curve).

On the vertical (y-axis) of these graphs, the temperature readings across the selected width of the ThermoChromic (TC) element, is presented. This includes the data derived from both the IR camera and the high-resolution camera. The temperature evaluation for the optical field was acquired indirectly. In particular, the acquired grayscale data was subsequently converted into temperature data. Meanwhile, the horizontal (x-axis), displays the width distance of the TC element, expressed in millimeters. This distance corresponds to the pixels identified in the IR camera.

■ S3a Sample: Thermal & Optical Field Correlation Graph with Gaussian Fittings

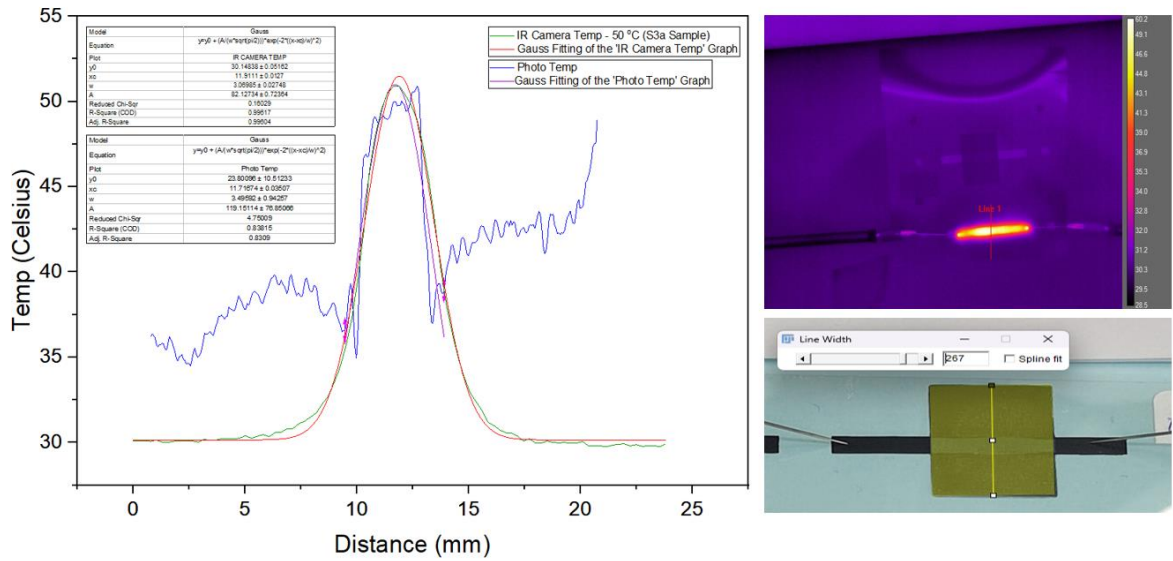


Figure 3.3: Thermal & Optical Field Correlation Graph of the S3a sample with Gaussian Fittings for 50 °C temperature.

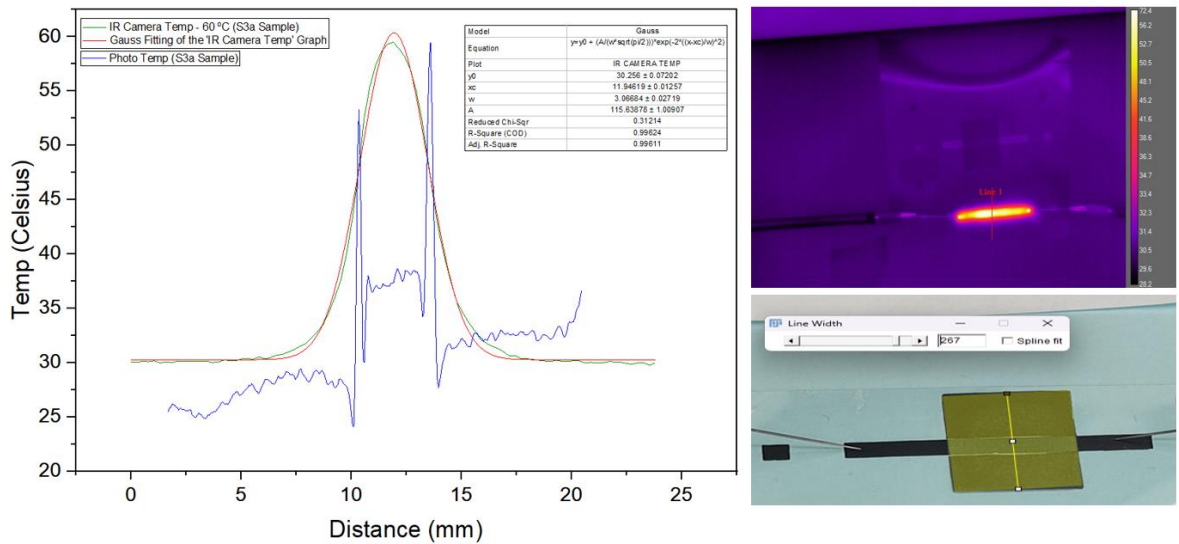


Figure 3.4: Thermal & Optical Field Correlation Graph of the S3a sample with Gaussian Fittings for 60 °C temperature.

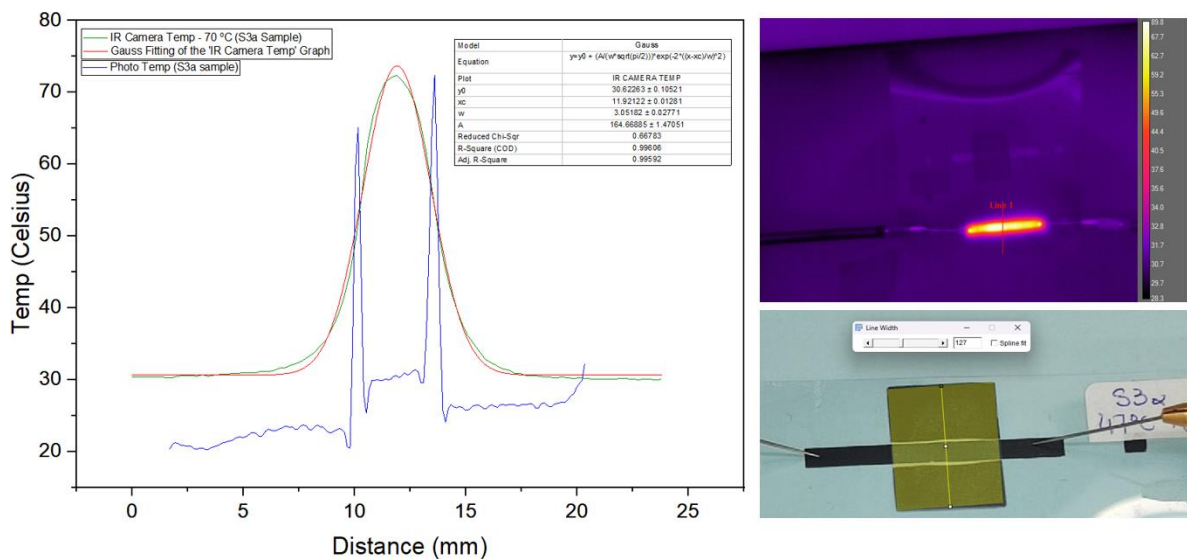


Figure 3.5: Thermal & Optical Field Correlation Graph of the S3a sample with Gaussian Fittings for 70 °C temperature.

▪ S4a Sample: Thermal & Optical Field Correlation Graph with Gaussian Fittings

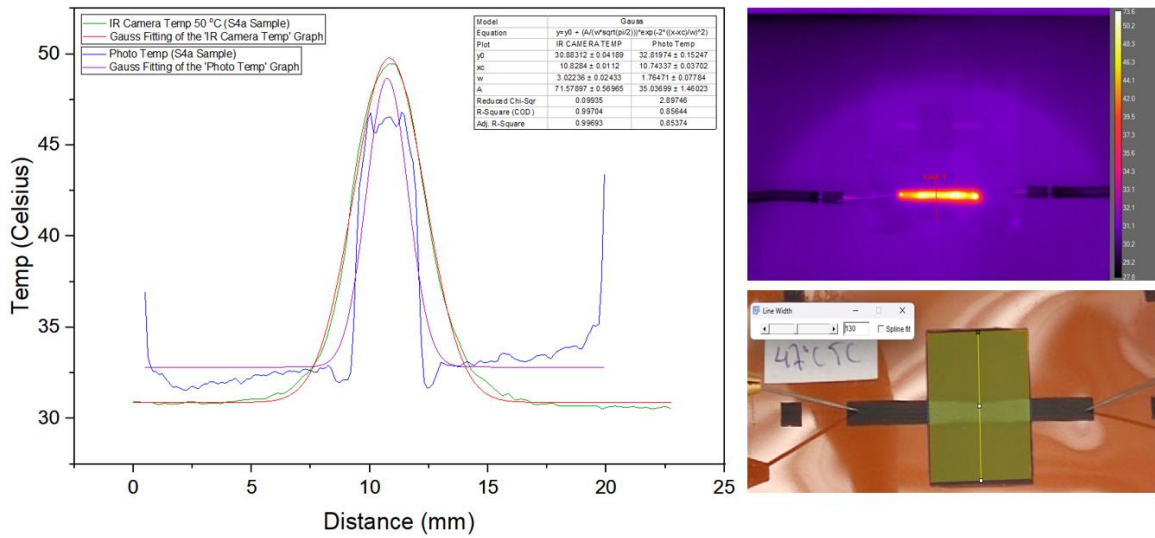


Figure 3.6: Thermal & Optical Field Correlation Graph of the S4a sample with Gaussian Fittings for 50 °C temperature.

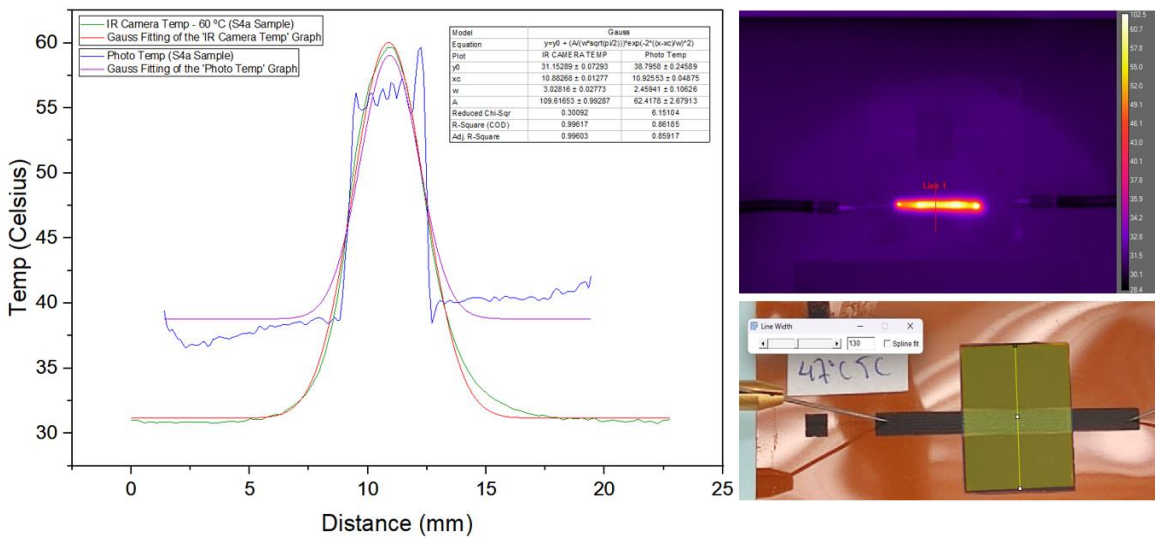


Figure 3.7: Thermal & Optical Field Correlation Graph of the S3a sample with Gaussian Fittings for 60 °C temperature.

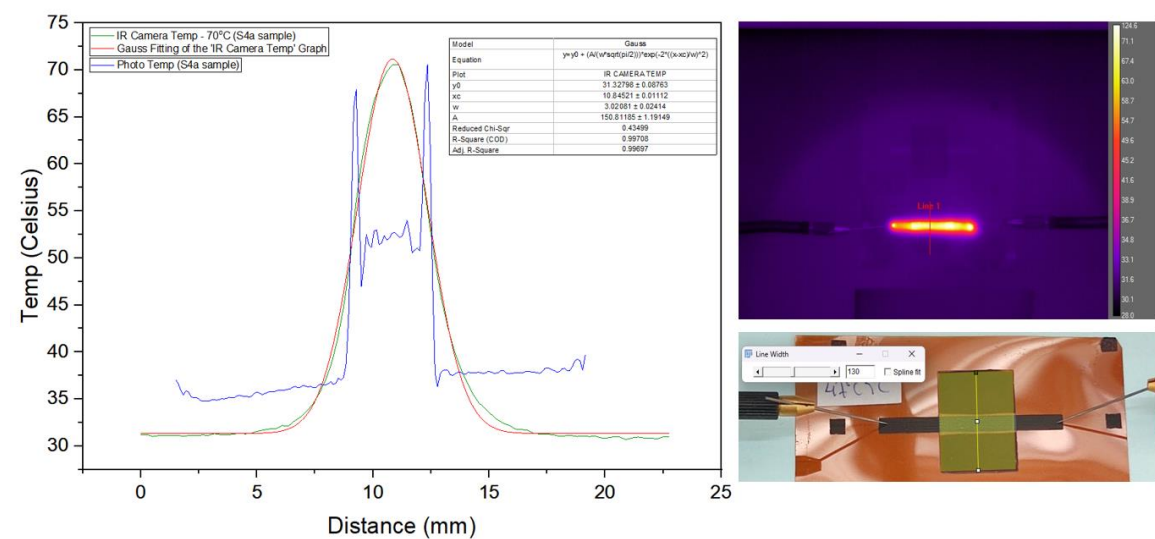


Figure 3.8: Thermal & Optical Field Correlation Graph of the S3a sample with Gaussian Fittings for 70 °C temperature.

Observations & Remarks – 1st Scenario▪ **S3a Sample**

- The field correlation graphs presented above (Fig. 3.3, Fig. 3.4, Fig. 3.5), depicting the thermal and optical images captured at different temperatures (50 °C, 60 °C, and 70 °C), reveal a notable distinction between the graph derived from the optical image and the one obtained from the thermal image. This discrepancy arises from the behavior of the Thermochromic element during heating above its activation temperature of 47 °C, causing it to become transparent in color. This feature along with the transparency of the PET substrate, exposes everything that is beyond the area of the underlying black carbon material. Consequently, the transparency issue significantly impacts the graphs obtained from the optical field, which is particularly noticeable in Fig. 3.4 (60 °C) and Fig. 3.5 (70 °C), where two spikes appear. These spikes, correspond to the transparent TC element at the two sides the carbon resistance. If the carbon beneath the TC element were not visible, the graph from the optical image would exhibit a similar pattern to the one derived from the thermal field, as long as the maximum induces temperature was below the activation temperature.
- To address this issue effectively, potential solutions were proposed:
 1. The first suggestion was to conduct new printings with multiple layers of the thermochromic (TC) ink, ensuring that the underlying carbon remains covered when the sample is subjected to heating. By increasing the number of TC layers, the transparency issue can be mitigated. However, this solution introduced additional challenges, notably regarding the quality of the TC-based structure. This is due to the increased volume of TC ink, which posed issues even after the curing process, as the TC element retained a gel-like consistency. Additionally, diffusion may occur to the multi-layer structure, which may affect the properties of each printed device.
 2. Another viable approach involved introducing an intermediary layer between the carbon and the TC element. This middle layer, consisting of an additional ink coating, would serve as a protective barrier. Consequently, even during the color changes of the TC element, the carbon resistance beneath it would remain indistinguishable, thanks to the presence of this intervening ink layer. As illustrated in Fig. 3.9, this approach demonstrated its effectiveness. However, the optical image displayed a uniform field, resulting in a square pulse in the grayscale graph, rather than the anticipated Gaussian behavior due to the homogenous field of the selected area of the sample.
- The 2nd Scenario was conducted, in order to study the TC behavior close to the activation temperature. The aim was not to improve the 1st Scenario, but to extract the info that was missing due to high-temperature values. In this case, internal heating of the S3a and S4a samples was conducted within a temperature range that closely aligns with the 47 °C activation temperature of the TC element.

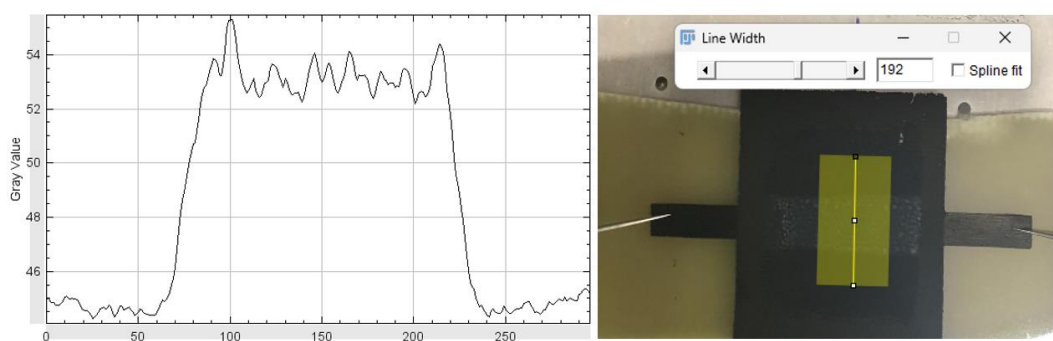


Figure 3.9: Grayscale graph of the optical image for a sample with intermediate black ink layer between the Carbon resistance and TC element, to mitigate the exposure of the underlying carbon resistance.

▪ S4a Sample

- Based on the provided thermal and optical images of the S4a sample on Kapton substrate, captured at different temperatures (50 °C, 60 °C, and 70 °C), it is evident that compared to the S3a sample, the graphs representing the data obtained from the optical field are more accurately aligned with the corresponding data obtained from the thermal field (Fig. 3.6 – 50 °C and Fig. 3.7 – 60 °C). This improved correlation is attributed to the Kapton substrate used in the S4a sample. Namely, when the thermochromic (TC) element becomes transparent, it adopts the brownish color of Kapton, leading to more satisfactory results in the graphs.
- However, as presented in Fig. 3.8, when internal heating at 70 °C was applied to the S4a sample, the two spikes were evident again, due to the exposure of the carbon resistance when the TC element's transparency area exceeded the carbon's area.

b) 2nd Scenario: Narrow Temperature range that closely aligns with the 47 °C activation temperature of the TC element

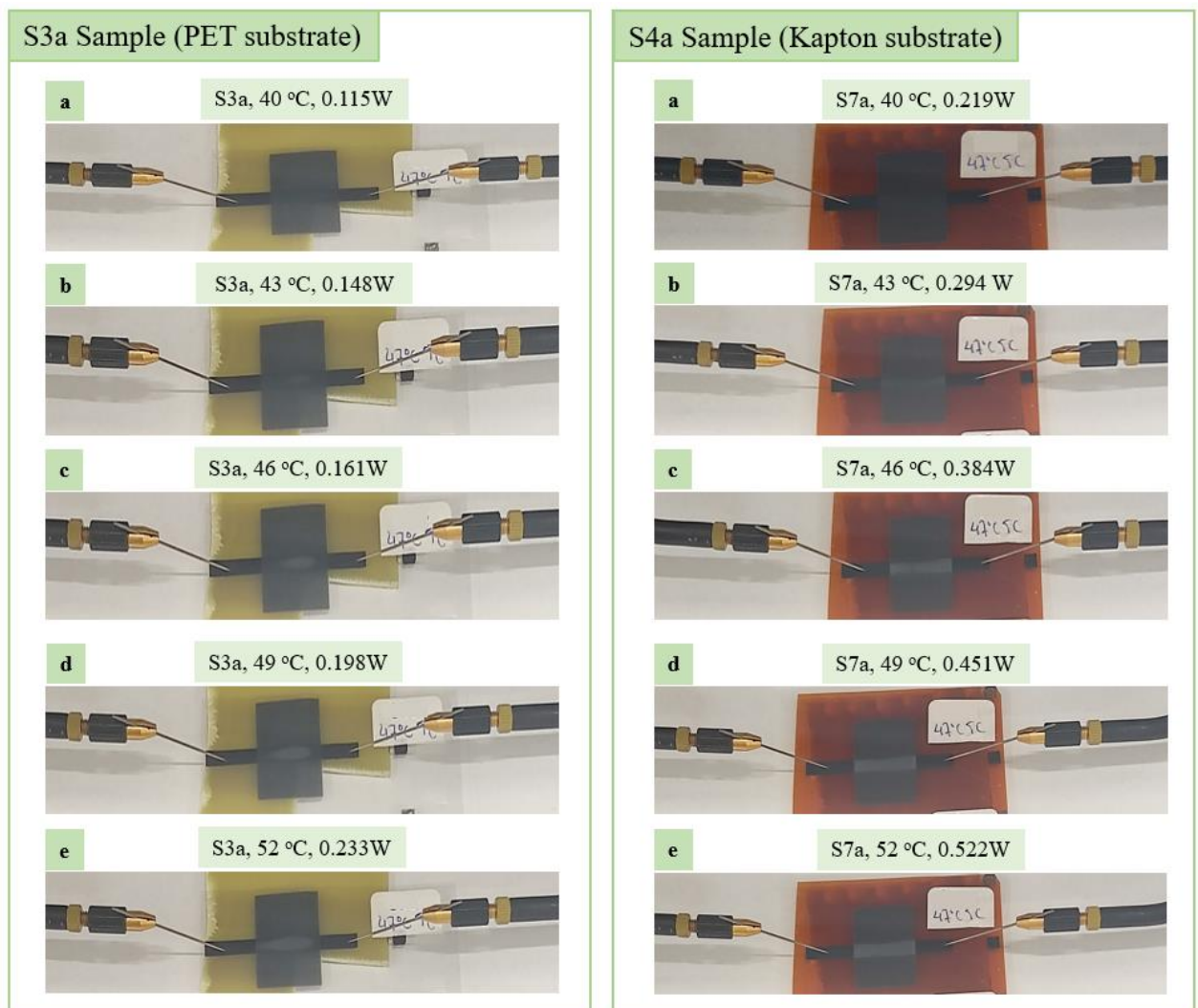


Figure 3.10: Internal Heating phases of the S3a and S4a samples, on PET and Kapton substrates respectively: a) 40 °C, b) 43 °C, c) 46 °C, d) 49 °C, e) 52 °C.

Each of the provided graphs below, features four distinct curves. The first two curves depict the thermal data, with the black curve representing the data obtained from the IR camera and the corresponding Gaussian curve (red curve). The third curve, in green, illustrates the optical data captured with a high-resolution camera, and the corresponding Gaussian curve (blue curve). On the vertical (y-axis) of these graphs, the temperature readings for each area of the ThermoChromic (TC) element, is presented. This includes the mean temperature data of a specific area of the sample, derived from both the IR camera and the high-resolution camera. The temperature evaluation for the optical field was acquired indirectly. In particular, the acquired grayscale data was subsequently converted into temperature data. Meanwhile, the horizontal (x-axis), displays the width distance area of the TC element, expressed in millimeters. This width distance corresponds to the pixels identified in the IR camera for that specific width area.

▪ **S3a Sample: Thermal & Optical Field Correlation Graph with Gaussian Fittings**

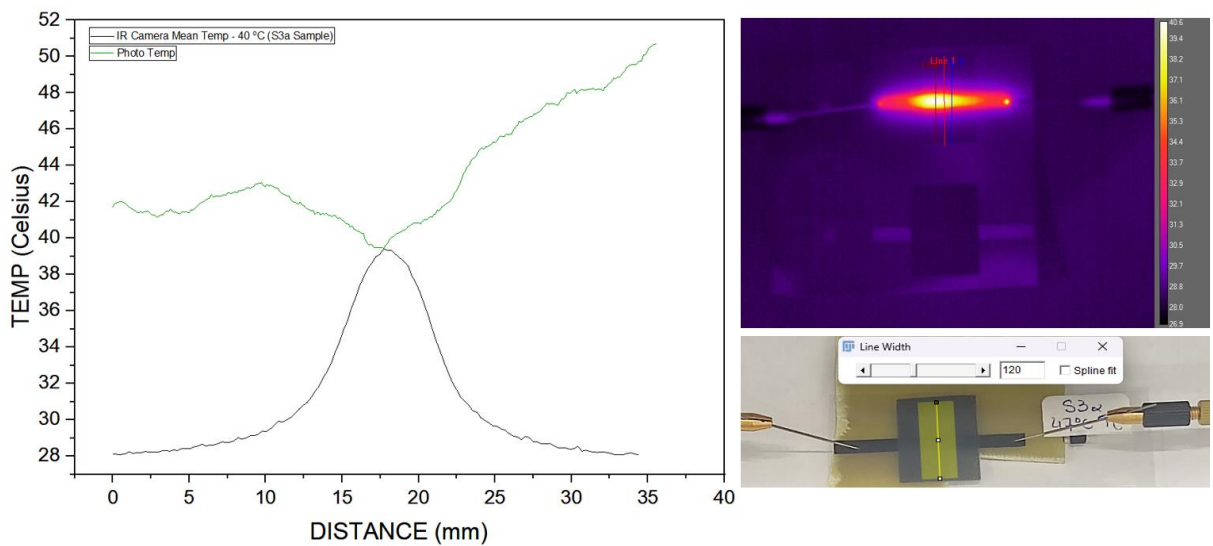


Figure 3.11: Thermal & Optical Field Correlation Graph of the S3a sample with Gaussian Fittings for 40 °C temperature.

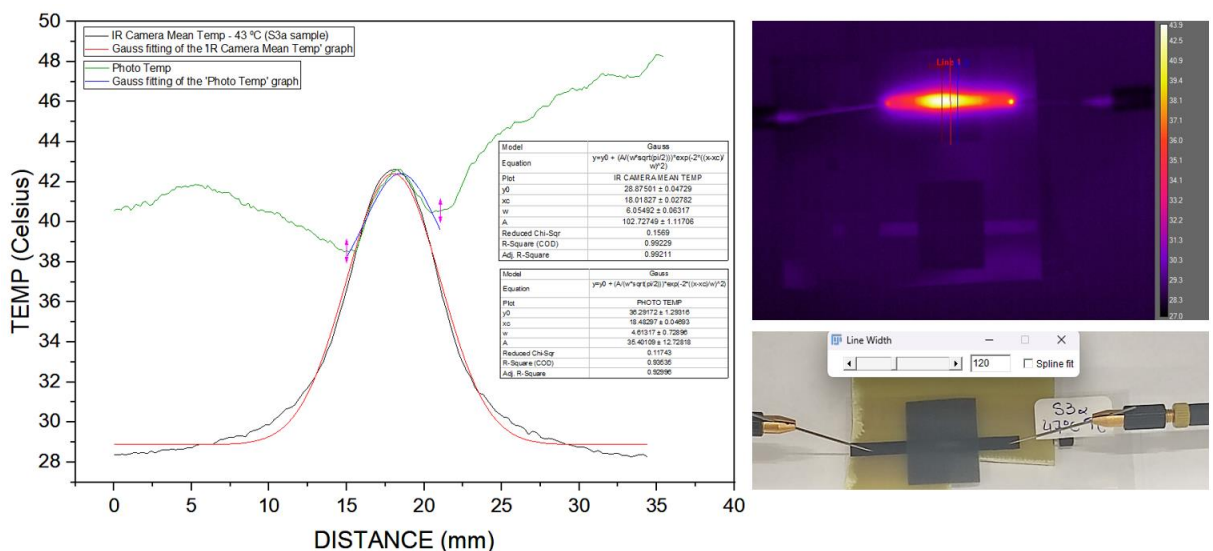


Figure 3.12: Thermal & Optical Field Correlation Graph of the S3a sample with Gaussian Fittings for 43 °C temperature.

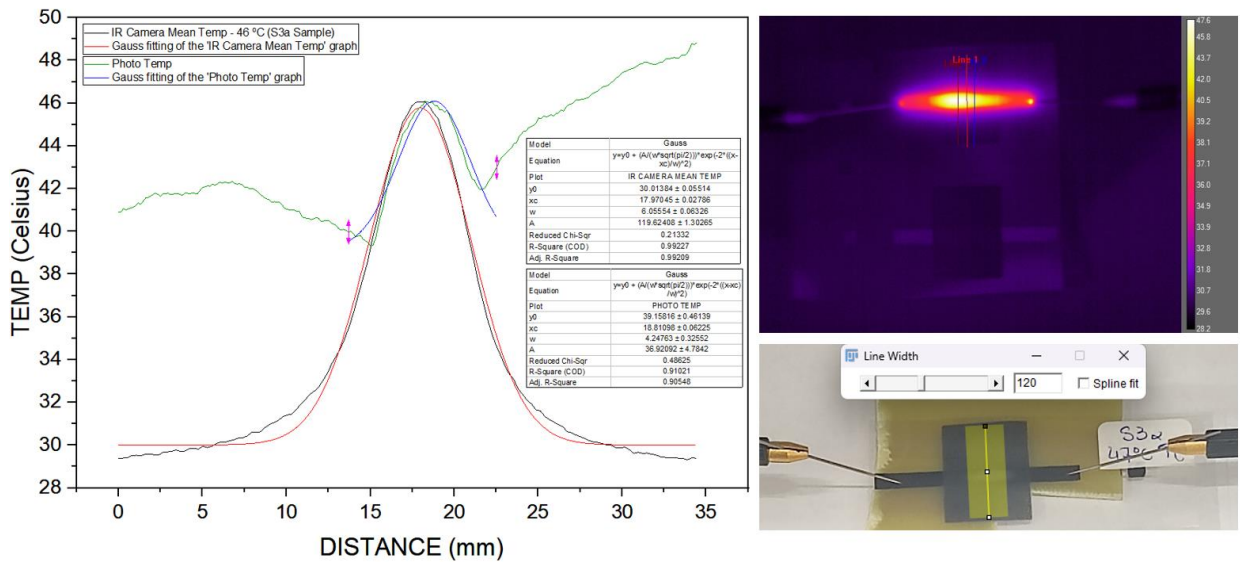


Figure 3.13: Thermal & Optical Field Correlation Graph of the S3a sample with Gaussian Fittings for 46 °C temperature.

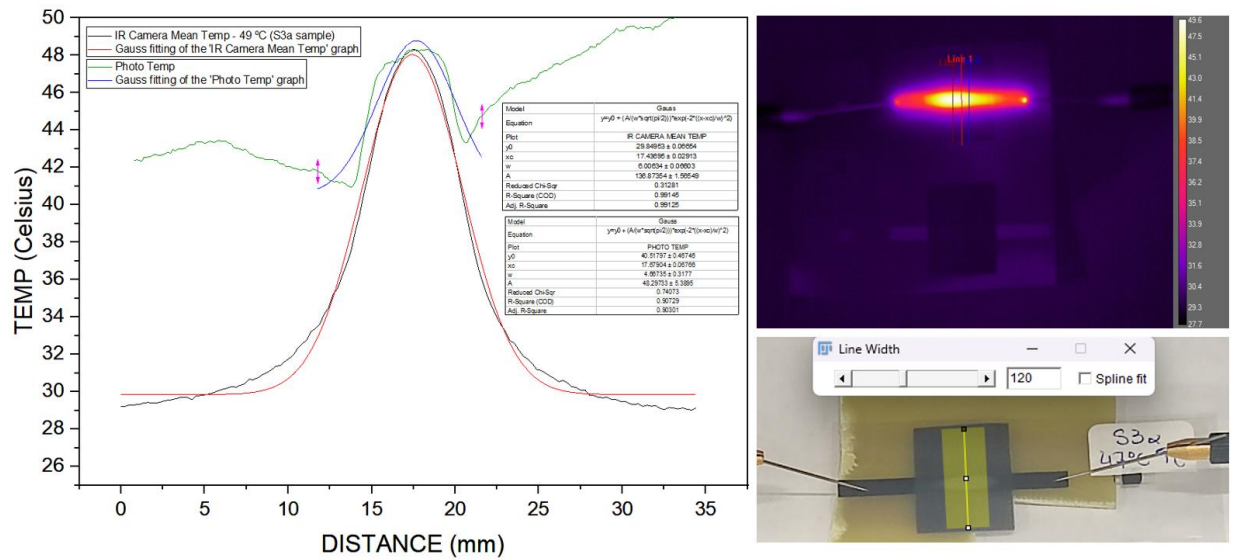


Figure 3.14: Thermal & Optical Field Correlation Graph of the S3a sample with Gaussian Fittings for 49 °C temperature.

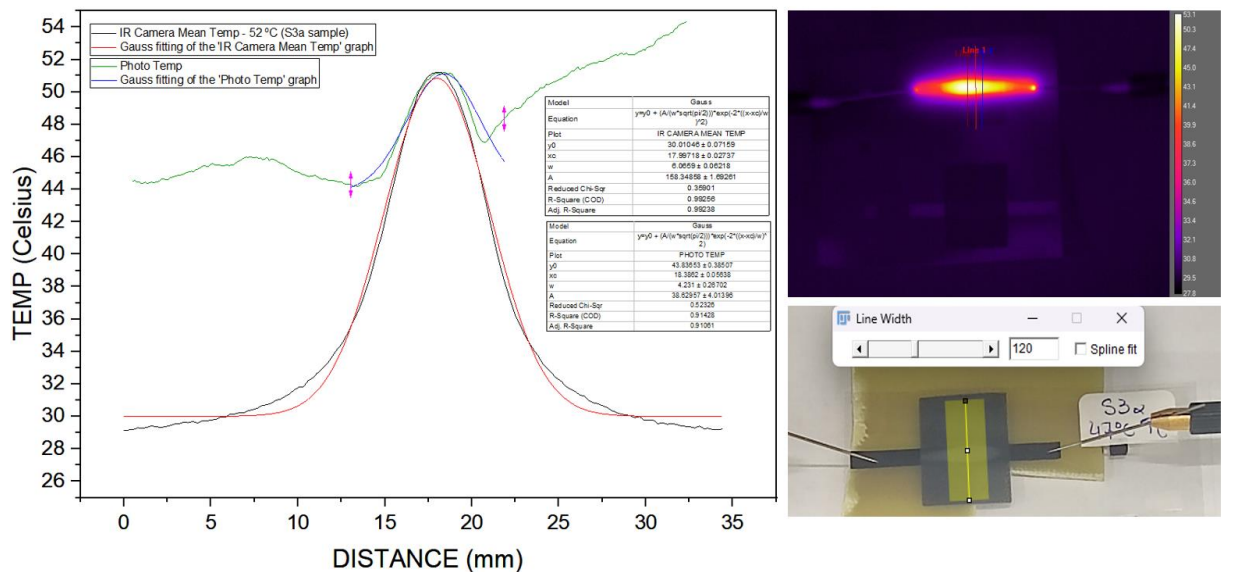


Figure 3.15: Thermal & Optical Field Correlation Graph of the S3a sample with Gaussian Fittings for 40 °C temperature.

■ S4a Sample: Thermal & Optical Field Correlation Graph with Gaussian Fittings

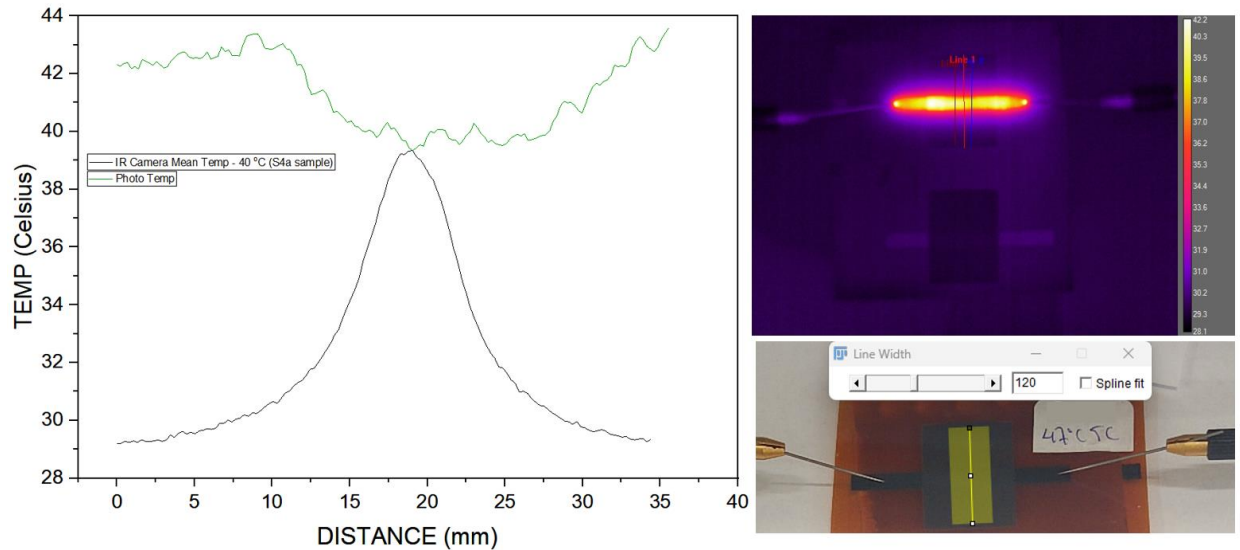


Figure 3.16: Thermal & Optical Field Correlation Graph of the S4a sample with Gaussian Fittings for 40 °C temperature.

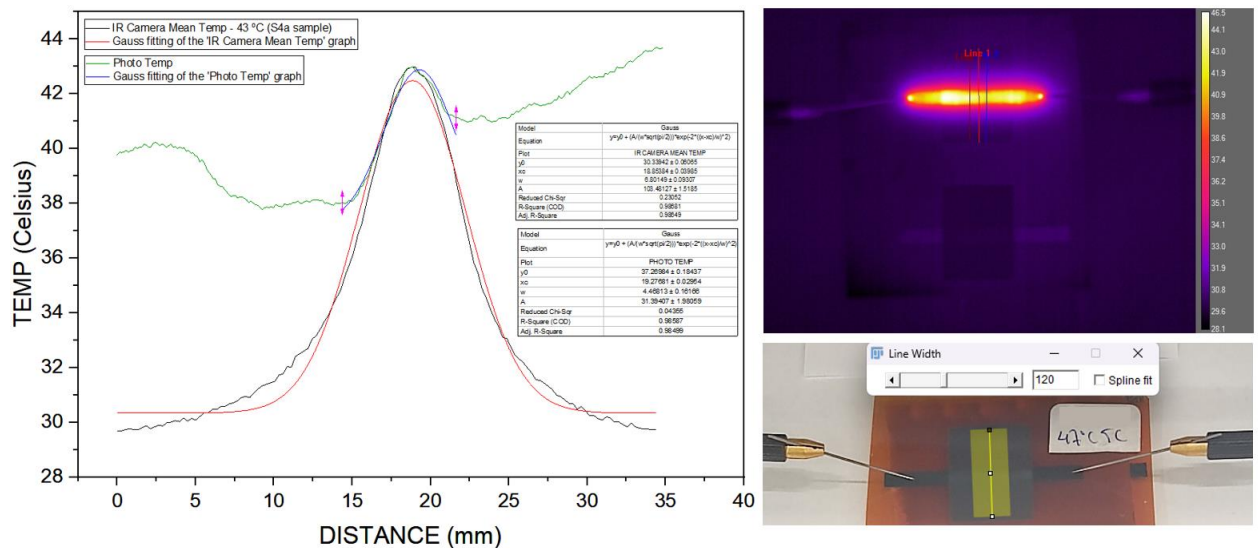


Figure 3.17: Thermal & Optical Field Correlation Graph of the S4a sample with Gaussian Fittings for 43 °C temperature.

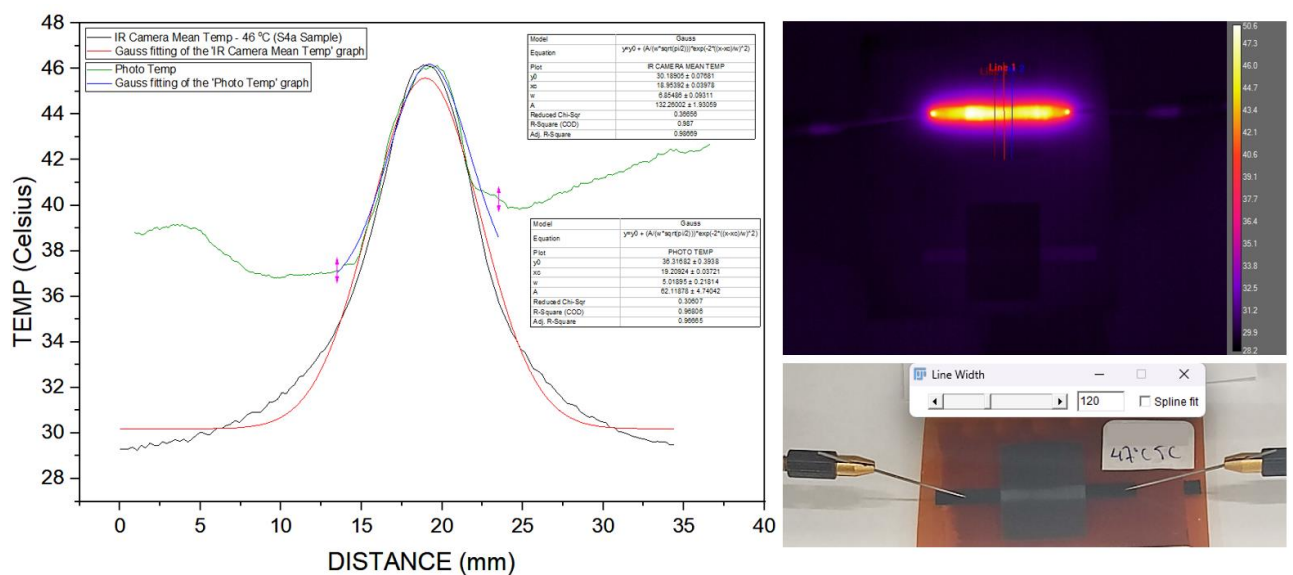


Figure 3.18: Thermal & Optical Field Correlation Graph of the S4a sample with Gaussian Fittings for 46 °C temperature.

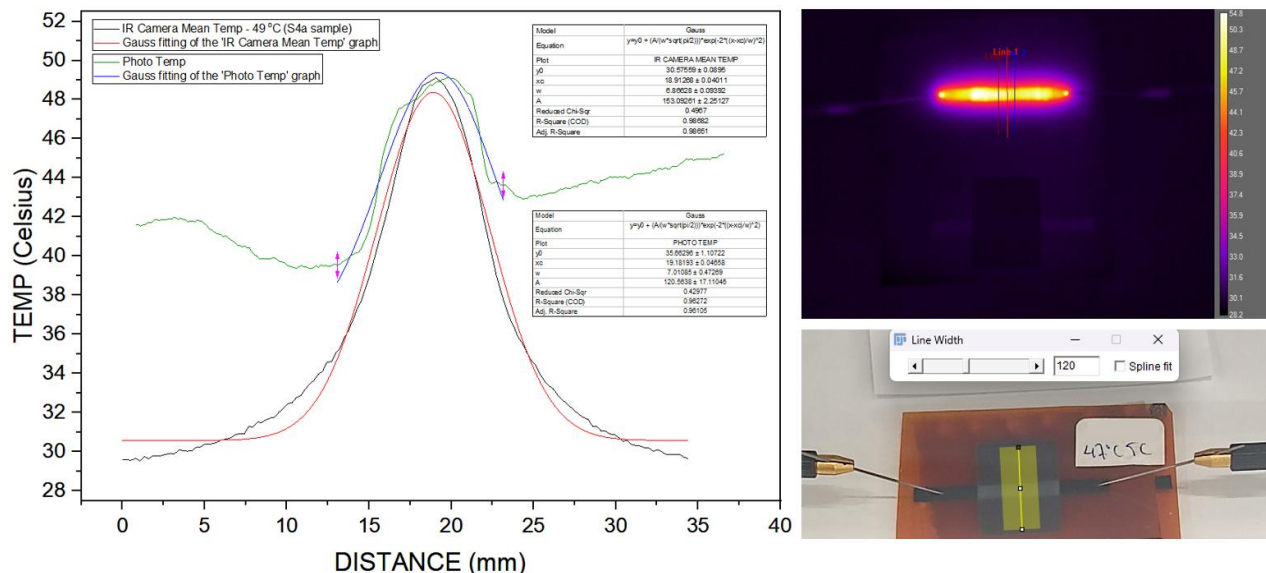


Figure 3.19: Thermal & Optical Field Correlation Graph of the S4a sample with Gaussian Fittings for 49 °C temperature.

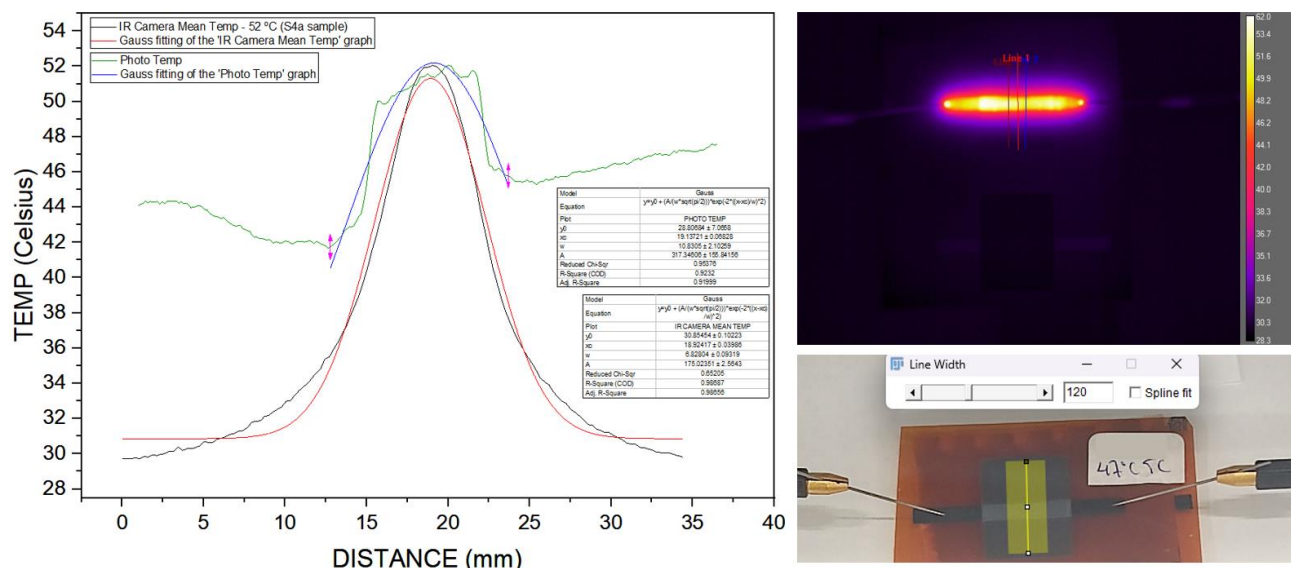


Figure 3.20: Thermal & Optical Field Correlation Graph of the S4a sample with Gaussian Fittings for 52 °C temperature.

Observations & Remarks – 2nd Scenario

▪ S3a Sample

- In contrast to the 1st Scenario, where the analysis of the structure's thermal image, was limited to a single vertical line across the TC element's width (Fig. 3.3 – Fig. 3.5, IR images), in the current approach, three discrete vertical lines were positioned across a specified area of interest of the TC element. As these lines exhibit distinct temperature readings from one another, a mean temperature value for every pixel was derived from these measurements, employed thereafter to the thermal graph analysis.
- The specific graphs, represent the correlation between the thermal and optical images, which were acquired through the FLIR camera and a high-resolution camera, respectively. According to the findings outlined in the 1st Scenario, the thermal and optical images captured at temperatures 50 °C, 60 °C, and 70 °C, manifested a discernible distinction between the graph derived from the optical image, and that originating from the thermal image (Fig. 3.3 – Fig. 3.5). This arises from the behavior of the Thermochromic (TC) element during the heating process, leading to its transparency, and thereby revealing the underlying carbon material. Consequently,

in this study, the measurements were conducted within a proximate temperature range to the activation temperature of the TC element, specifically at 47 °C. This scenario case was employed to examine more thoroughly the behavior of the TC element in temperatures that closely align with its activation temperature.

- In this scenario, the discoloration of the TC element below the carbon's area is observed up to 52 °C (Fig. 3.15). Beyond this temperature point, further heating of the TC element, causes its area of discoloration to surpass that of the carbon material. This, in return, impacts the graphs derived from the optical field.
 - As depicted in Fig. 3.11, when the temperature is maintained at 40 °C, there is no evident transparency in the Thermochromic (TC) structure. This aligns with our expectations, since the activation temperature for the TC material is approximately 47 °C. This observation is further substantiated by the corresponding graph generated from the optical image, which does not reveal any indication of a color change in the TC material, under these conditions.
 - Fig. 3.12 – Fig. 3.15, display the thermal and optical correlation graphs of the sample's heating at 43 °C, 46 °C, 49 °C, and 52 °C. Notably, at 43 °C the Thermochromic (TC) element initiates its transparent transition (Fig. 3.12). Noteworthy behavior emerges as the temperature ascends within the 47 °C range, up to 52 °C; where the transparent area of the TC element nearly matches the heater's area. Consequently, all graphs exhibit a similar pattern, where the transparency observed in the optical image corresponds to the maximum temperature conducted to the TC structure.
 - In Fig. 3.13 (internal heating at 46 °C) however, the maximum area observed in the graph derived from the optical image, does not precisely align with the maximum area of temperatures detected in the thermal image. This is a potential error that may not have been accounted, during the conversion process of the optical field, from Grayscale Data to Temperature Data.
- S4a Sample
- Similar to the S3a sample, the S4a sample was heated at 40 °C, 43 °C, 46 °C, 49 °C, and 52 °C. Therefore, the presented graphical representations of the S4a sample, exhibit a similar pattern to the thermal-optical correlation graphs of the S3a sample. Meaning that, from 43 °C until 52 °C, the transparent area of the TC element nearly matches the heater's area (Fig. 3.17 – Fig. 3.20). Therefore, the maximum temperature conducted to the TC structure, corresponds to its area of transparency.
 - At an internal heating of 52 °C (Fig. 3.20), an almost square pulse is observed at the Thermal & Optical Correlation Graph of the S4a sample, rather than the expected Gaussian behavior. This is due to the combination of the Kapton's color and the transparency of the TC element, which adopts the brownish color of Kapton, resulting to a more homogenous optical field between the TC element and the carbon resistance.

Observations & Remarks about TCR of the L3 layout samples – 2nd Scenario

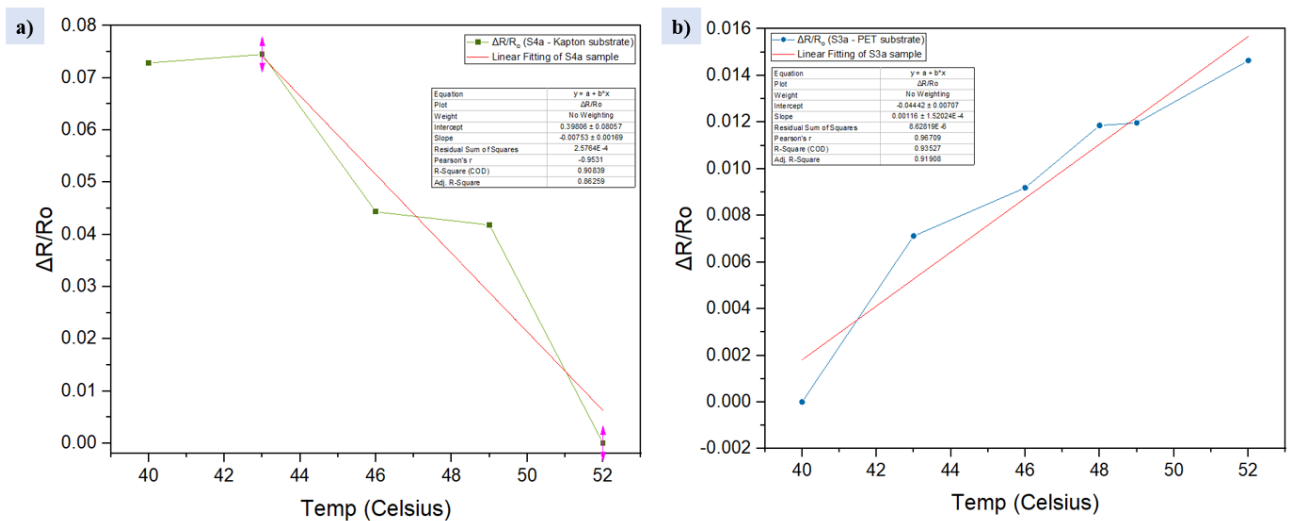
- The Temperature Coefficient of Resistance (TCR) observed in S4a sample (Kapton substrate), exhibits a Positive Temperature Coefficient (PTC) behavior (Graph 3.1a, Table 3.2 – S4a Sample), which contradicts the Negative Temperature Coefficient (NTC) behavior, observed in Chapter 2 for the samples with the L1 and L2 geometries. This discrepancy may be attributed to the fact that the first layer of the S4a sample, consisting of the carbon resistance – which was initially cured at 120 °C – underwent a second curing process, to integrate the second TC layer, placed on top of it. This dual curing process may have altered the electrical characteristics of the carbon resistance layer when mixed with the TC layer. However, relying solely on this observation may not be sufficient enough. Consequently, another significant factor contributing

to the S4a sample's PTC behavior can be attributed to the chemical composition of the Kapton substrate and the way in which the carbon element is layered onto it, following the screen-printing and curing processes.

- The TCR of the S3a sample (PET substrate), exhibits a NTC behavior, similarly to the samples examined in Chapter 2, relating the L1 and L2 layout designs. This TCR value is equal to $TCR = 0.00116 \pm 1.52E-4$, as presented in Graph 3.1b.

Table 3.2: Data gained from the Internal Heating of S3a and S4a Samples.

S3a Sample (PET Substrate)						
Volt (V)	Temperature (°C)	I (mA)	P (mW)	Power/Area (mW/μm ²)	R (kΩ)	ΔR/R ₀
23	40	5	115	0.52036	4.6	0
26	43	5.69231	148	0.66968	4.56757	0.00712
28	46	6.14286	172	0.77828	4.55814	0.00918
30	49	6.6	198	0.89593	4.54545	0.01197
32.5	52	7.16923	233	1.0543	4.53326	0.01464
S4a Sample (Kapton Substrate)						
Volt (V)	Temperature (°C)	I (mA)	P (mW)	Power/Area (mW/μm ²)	R (kΩ)	ΔR/R ₀
35	40	6.26286	219.2	0.99186	5.5885	0.07286
40.5	43	7.25926	294	1.33032	5.57908	0.0745
47	46	8.17021	384	1.73756	5.7526	0.04434
51	49	8.84314	451	2.04072	5.76718	0.0418
56	52	9.32143	522	2.36199	6.00766	0



Graph 3.1: TCR ($\Delta R/R_0 - T$) Graphs: **a)** PTC behavior of S4a sample (Kapton substrate), **b)** NTC behavior of S3a sample (PET substrate).

*** Future Considerations and Improvements ***

- In both scenarios, the graphs that demonstrate the correlation between the thermal and optical properties in the selected area of the Thermochromic (TC) element, it is observed that the highest temperature detected by the FLIR professional thermal camera matches the maximum temperature captured by the high-resolution camera. However, there is a notable disparity in the thermal-optical correlation within specific regions. This misalignment is noticeable both before the beginning of the temperature increase, and after the temperature drop. Particularly, in the 1st Scenario, this discrepancy is evident in the regions situated below 9mm and above 12.5mm along the x-axis (Fig. 3.3 – Fig. 3.8). In the case of the 2nd Scenario, these disparities are observed in the areas below 13mm and above 23mm (Fig. 3.12 – Fig. 3.15 and Fig. 3.17 – Fig. 3.20). This

constraint might arise from the positioning of the high-resolution camera along the y-axis, which is oriented vertically to the carbon element. This orientation, resulted in shadowing the areas where the observed misalignment occurred. To address this issue effectively, a recommended solution would involve repositioning the camera directly above the sample, with a particular emphasis on situating it closer to its top left corner, minimizing therefore, any undesirable shadow effects. Alternatively, another viable approach would be to normalize the data from these specific regions, and aligning them with the data captured by the FLIR professional camera.

- One of the most notable challenges of the measurement process, involves achieving precise identification between the selected region on the thermal and optical fields. This issue introduces certain constraints, including offsets between the thermal and optical data, on both the horizontal and vertical scales of the graphs. This concern could be limited if both the FLIR camera and the high-resolution camera were positioned at the exact same spot, and with the same zoom settings. This approach would ensure the precise amount rows and columns, of the data array, captured by these images. Consequently, by performing a subtraction operation, the specific area of interest within the Thermochromic (TC) element could be extracted. This solution of course, requires further discussion, as well as trials to assure its validity.

4 CHAPTER 4:

Final Printed Electronic Temperature Sensing Device – Wireless Communication

This chapter provides a description of the electronic setup employed for the implementation of a flexible skin temperature sensor. The primary objective of this setup is to enable human-machine interfaces for real-time monitoring of the data collected by the sensor. Additionally, the chapter explores the means through which this data is displayed, utilizing wireless communication protocols such as Wi-Fi, IoT, and Bluetooth. These communication technologies have been specially programmed and designed to present in a user-friendly manner the data generated by our sensor. Furthermore, the chapter offers a comprehensive comparison of the three wireless technologies mentioned above. This comparison delves into the advantages and disadvantages associated with each of these technologies, giving insight into their suitability for the specific requirements of the sensor system. In essence, this chapter sheds light on the technological infrastructure that evolves the remote functionality and usability of the flexible skin temperature sensor.

4.1 Electronic Setup of the Temperature Sensing Device

The electronic setup is a fundamental aspect of the flexible skin temperature sensor system, encompassing the essential hardware and associated electronic components. It plays a pivotal role in acquiring, processing, and transmitting data, enabling the sensor to provide accurate and timely temperature insights. Consequently, it is beneficial to delve into the specific components of this setup, and the way they collectively contribute to the sensor's overall performance and user interface. In [Table 4.1](#), a comprehensive list of the electronic components ([Fig. 4.1](#)) employed in the prototype of the electronic setup for the flexible skin-temperature sensing device, is provided. These components collectively form the prototype circuit illustrated in [Fig. 4.2](#), which facilitates human-machine interfaces, by allowing for real-time monitoring of the temperature data recorded by the flexible sensor.

Table 4.1: Electronic Components for Electronic Setup Prototype of the Temperature Sensing Device.

Electronic Components for Electronic Setup Prototype of the Temperature Sensing Device		
Name	Details – Function in the circuit	Figure
ESP32-WROOM-32D MCU [189]	Integration of the flexible skin-temperature sensor into a wireless wearable device	Fig. 4.1a
NTC 10K 1% B3950 Thermistor [190]	Real-time measurement of the environmental temperature	Fig. 4.1b
Metal Film Resistor 10K (x1) [191]	Used as a voltage divider for the accurate measurement of the environmental temperature acquired by the NTC 10K 1% B3950 Thermistor	Fig. 4.1c
Metal Film Resistor 3K3 (x1) [192]	Wheatstone bridge setup	Fig. 4.1d
Metal Film Resistor 6K8 (x2) [193]	Wheatstone bridge setup	Fig. 4.1e
Breadboard 830 Tie Point [194]	Electronic component integration	Fig. 4.1f
Jumper Wires [195]	Data transmission and communication between the electronic components	Fig. 4.1g

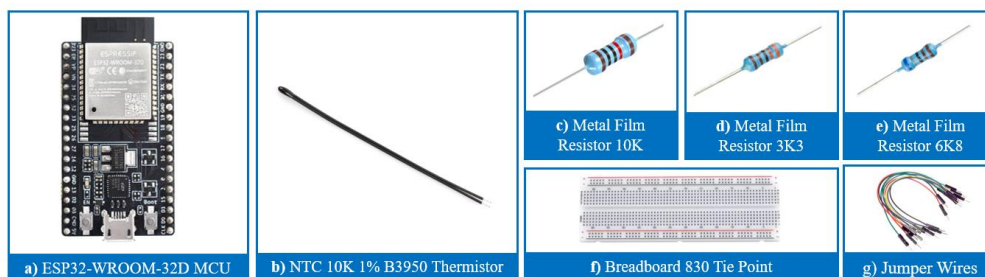


Figure 4.1: Electronic Components for Electronic Setup Prototype of the Temperature Sensing Device.

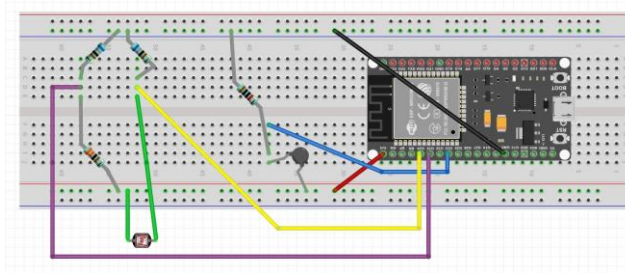


Figure 4.2: Electronic Setup Circuit prototype for accurately measuring the temperature acquired from the flexible TC-based temperature sensor.

4.1.1 Electronic Setup Circuit Prototype Explanation

As illustrated in Fig. 4.2, the prototype of the electronic circuit comprises three distinct parts, each working collaboratively to achieve precise temperature measurements from the flexible TC-based skin-temperature sensor. These electronic parts are as follows:

a) The ESP32-WROOM-32D

The ESP32-WROOM-32D serves as the central component of the system, controlling the connection and coordination of all electronic elements, to accurately measure any voltage signal and resistance/temperature-related data. It also features wireless interfaces, allowing the seamless integration of the flexible skin-temperature sensor into a wireless wearable device, which facilitates real-time data monitoring, through mobile devices and desktops.

b) The voltage divider for the NTC Thermistor

The NTC 10K Thermistor, is utilized to validate the environment’s temperature, which is afterwards used as a reference temperature for the flexible sensor’s temperature reading. However, in order to measure the environment’s temperature, the corresponding resistance needs to be measured initially. Therefore, as illustrated in Fig. 4.2, one terminal of the thermistor is connected to the V_{CC} pin and the other terminal is connected to the ground, using a known value resistor (being the Metal Film Resistor $10K\Omega$). Since the ESP32-WROOM-32D MCU has a build in ADC, the resistance can be directly calculated, via the voltage divider (Fig. 4.3), as represented in Eq. 6 [196]:

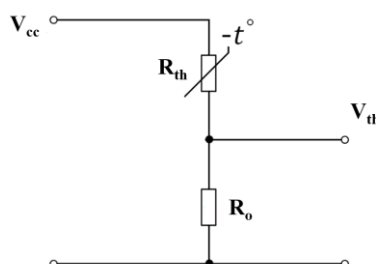


Figure 4.3: Voltage Divider for the accurate measurement of the thermistor’s resistance (R_{th}) [196].

$$V_{th} = V_{CC} \cdot \frac{R_o}{R_o + R_{th}} \Leftrightarrow R_{th} = R_o \cdot \left(\frac{V_{CC}}{V_{th}} - 1 \right) \quad (\text{Eq. 6})$$

Where:

R_{th} = the resistance of the thermistor.

R_o = the resistance of known value (Metal Film Resistor 10K Ω).

V_{CC} = the voltage input value.

V_{th} = the voltage divider potential calculated by the ADC unit of the ESP32-WROOM-32D MCU.

The corresponding environment's temperature is measured by the formula presented below (Eq. 7) [197]:

$$R_{th} = R_o \cdot e^{-B \left(\frac{1}{T_o} - \frac{1}{T_{th}} \right)} \Leftrightarrow$$

$$\frac{1}{T_{th}} = \frac{1}{T_o} + \frac{1}{B} \cdot \ln \left(\frac{R_{th}}{R_o} \right) \quad (\text{Eq. 7})$$

Where:

T_{th} = the constantly changing environmental temperature, captured by the thermistor.

T_o = the reference temperature of the thermistor.

B = the Beta value of the thermistor (this value demonstrates the curve shape of the Resistance – Temperature graph, Eq. 3).

R_{th} = the resistance of the thermistor.

R_o = the resistance of known value (Metal Film Resistor 10K Ω).

c) The Wheatstone Bridge for the Flexible Temperature Sensor

The Wheatstone Bridge accurately calculates the resistance of the TC-based flexible temperature sensor. In this setup, the Wheatstone Bridge consists of the flexible sensor and three known resistances ($R_2 = 3.3 \text{ K}\Omega$, $R_3 = R_4 = 6.8 \text{ K}\Omega$), as presented in Fig. 4.4 [198][199]. The built-in ADC unit in the ESP32-WROOM-32D, directly calculates the V_1 and V_2 potentials, formed by the two voltage dividers of the Wheatstone Bridge.

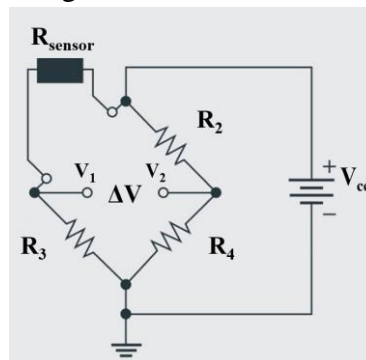


Figure 4.4: Wheatstone Bridge used for accurately measuring the resistance of the flexible temperature sensor [198].

The equations below [198][199], calculate both the potential difference across the bridge and the resistance value of the flexible temperature sensor.

$$V_1 = \frac{R_3}{R_3 + R_{sensor}} \cdot V_{CC} , V_2 = \frac{R_4}{R_4 + R_2} \cdot V_{CC} \quad (\text{Eq. 8})$$

$$\Delta V = V_1 - V_2 = \left(\frac{R_3}{R_3 + R_{sensor}} - \frac{R_4}{R_4 + R_2} \right) \cdot V_{CC} \quad (\text{Eq. 9})$$

$$R_{sensor} = R_3 \cdot \left(\frac{V_{cc} \cdot R_2 - \Delta V \cdot R_2 - \Delta V \cdot R_4}{V_{cc} \cdot R_4 + \Delta V \cdot R_2 + \Delta V \cdot R_4} \right) \quad (\text{Eq. 10})$$

Where:

V_1 = the potential value, between the R_3 and the R_{sensor} .

V_2 = the potential value, between the R_4 and the R_2 .

ΔV = the potential difference between the V_1 and V_2 .

R_2, R_3, R_4 = resistances of the Wheatstone bridge (Metal Film Resistors 3K3 (x1), 6K8 (x2)).

R_{sensor} = the resistance of the flexible temperature sensor.

Subsequently, the R_{sensor} is converted into an accurate temperature reading, using the following mathematical relationship [200]:

$$\text{- If } R_{th} > R_{sensor}: \quad R_{sensor} = R_{th} \cdot (1 + a \cdot (T_{sensor} - T_{th})) \Leftrightarrow$$

$$T_{sensor} = \frac{R_{th} - R_{sensor}}{a \cdot R_{th}} + T_{th} \quad (\text{Eq. 11a})$$

$$\text{- If } R_{th} < R_{sensor}: \quad R_{sensor} = R_{th} \cdot (1 + a \cdot (T_{th} - T_{sensor})) \Leftrightarrow$$

$$T_{sensor} = \frac{R_{sensor} - R_{th}}{a \cdot R_{th}} + T_{th} \quad (\text{Eq. 11b})$$

Where:

T = the constantly changing temperature, captured by the flexible temperature sensor.

T_{th} = the constantly changing environmental temperature, captured by the thermistor.

R_{sensor} = the resistance of the flexible temperature sensor.

R_{th} = the resistance of the constantly changing environmental temperature, captured by the thermistor.

a = the temperature coefficient of resistance of the flexible temperature sensor.

4.1.2 C++ Code Explanation for Skin-Temperature Detection

The main objective of the C++ code for calculating the temperature detected by the flexible temperature sensor is summarized as follows:

1. Initialization of the global variables according to the electronic setup presented in Fig. 4.2 (Fig. 4.5).
2. Initialization of the ADC resolution for the ESP32 MCU, as well as the Baud Rate for serial communication (Fig. 4.6).
3. Calculation of the potential derived from the voltage divider (V_{th}) between the Metal Film Resistors 10K and the NTC 10K 1% B3950 Thermistor, through the ESP32 ADC resolution relationship (Fig. 4.7).
4. Calculation of the thermistor's resistance (R_{th}) via Eq. 6 (Fig. 4.7).
5. Determination of the ambient temperature detected by the thermistor (T_{th}) (Eq. 7, Fig. 4.7).
6. Calculation of the potential derived from the two voltage dividers (V_1, V_2) within the Wheatstone Bridge (Eq. 8), and subsequent estimation of their differential potential (V) (Eq. 9) (Fig. 4.8).
7. Computation of the resistance of the flexible temperature sensor (R_{sensor}), via Eq. 10 (Fig. 4.8).
8. Estimation of the temperature detected by the flexible temperature sensor (T_{sensor}), through Eq. 11a or Eq. 11b (Fig. 4.8)

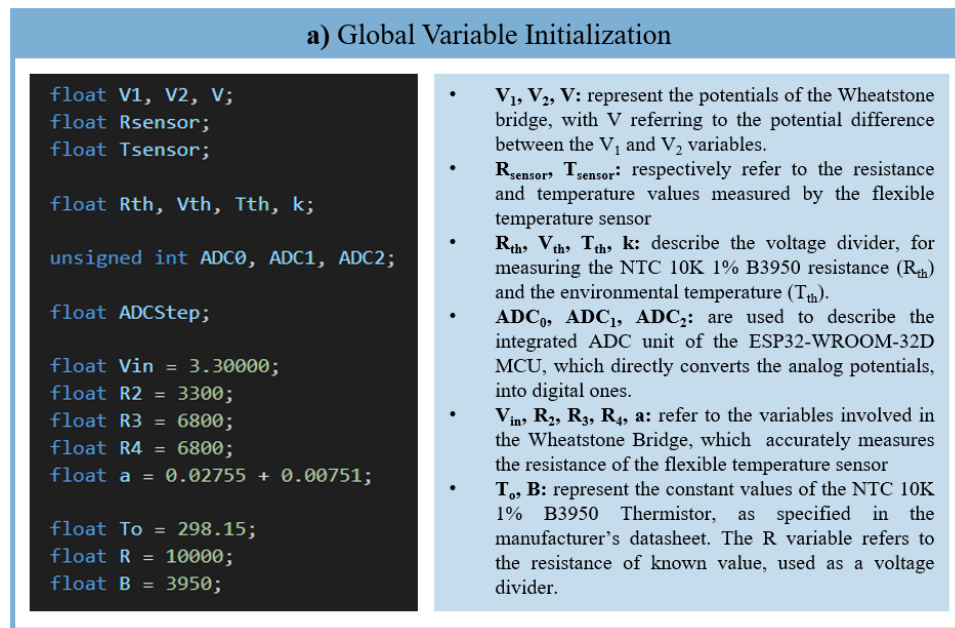


Figure 4.5: Global Variable Initialization and Explanation.

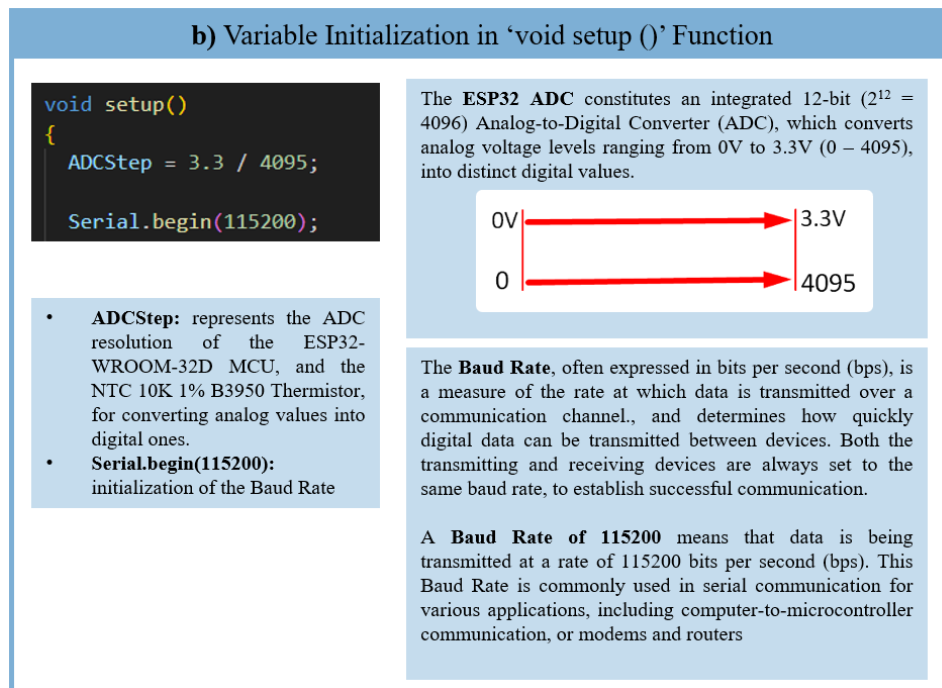


Figure 4.6: Variable Initialization and Explanation, in 'void setup()' function.

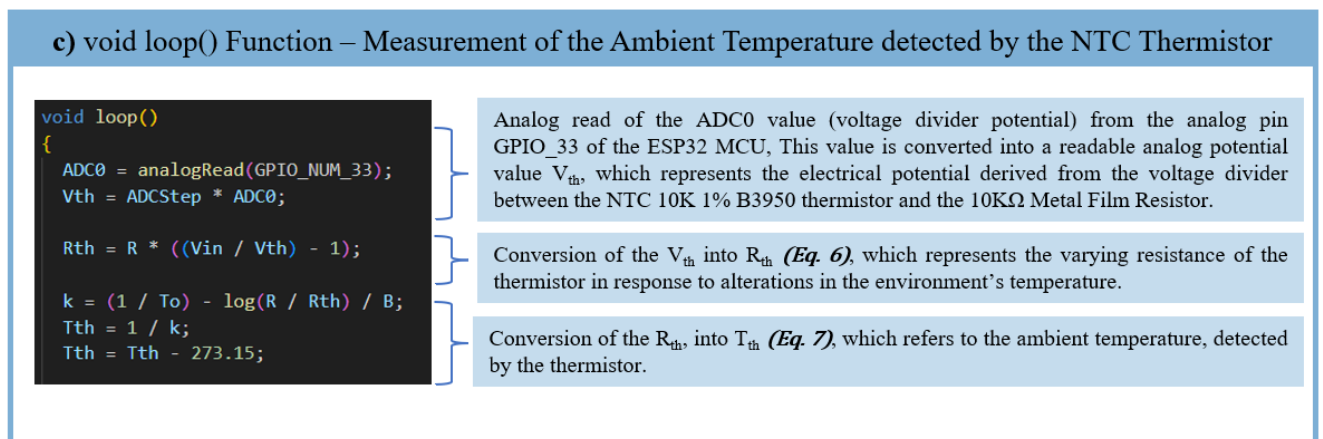


Figure 4.7: Ambient Temperature Estimation and Explanation, in 'void loop()' function.

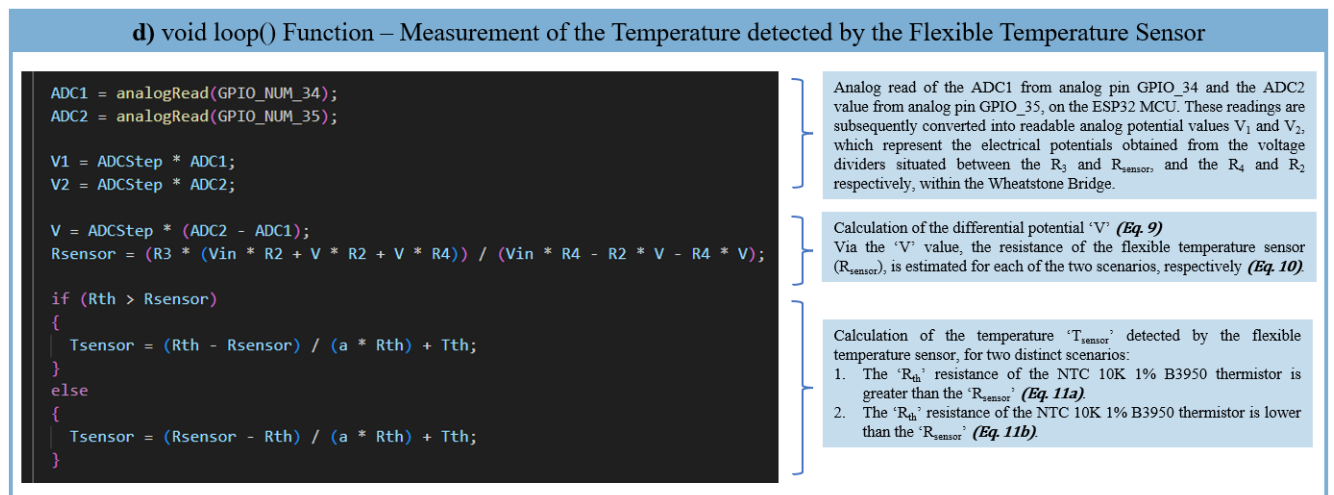


Figure 4.8: Estimation and Explanation of the temperature by the flexible temperature sensor, in 'void loop()' function.

Observations & Remarks

- The ESP32 ADC has limitations when it comes to voltage measurement. Specifically, it cannot measure directly voltages that exceed 3.3V. Additionally, it exhibits a non-linear behavior, with no sensitivity between 3.2V – 3.3V, and very low voltage values, like 0V – 0.1V (Fig. 4.9) [201].
- If the ESP32 MCU included a differential measurement component (e.g., ARM microcontroller), the differential voltage 'V' could have been directly measured.
- The NTC (Negative Temperature Coefficient) 10K B3950 thermistor exhibits a resistance value of 10K Ω at a temperature of 25 °C. The manufacturer's Temperature-Resistance data for this thermistor can be found in Table 4.2 [202].
- In this electronic setup configuration, a sample with the L3 layout design, on Kapton substrate was utilized. This sample consisted of a black TC element with an activation temperature of 47 °C (Fig. 4.10). The slope $a = 0.02755 + 0.00751$ (k Ω /°C) was intentionally selected to ensure that the flexible temperature sensor accurately reflected the skin temperature readings, in response to ambient temperature changes (Fig. 4.11a). Following the comprehensive analysis of the TCR values extracted from the Chapter 2 graphs, the most suitable value emerged from the S2 sample on paper substrate with the L2 layout configuration (Graph 2.6), measuring at $0.02755 + 0.00101$ (k Ω /°C). However, it is important to note that in this electronic setup, a sample with the L3 layout configuration on Kapton substrate, was employed. Therefore, a skin temperature reading of 39.69 °C was detected at an ambient temperature of 25 °C, as illustrated in Fig. 4.11b. This measurement showcases that the TCR value of the sample with the Kapton substrate, should be identical to the one derived from the S2 sample on paper substrate, due to the variation of fabrication processes. Consequently, a calibration of the TCR value was necessary. More specifically, this calibration involved adjusting the TCR value by increasing its offset by 0.0065 (k Ω /°C). As a result, the recorded skin temperature was equal to 36.69 °C, under the same ambient conditions. This particular skin temperature value, corresponds to the typical skin temperature of a human at reasonable ambient temperatures, which is why it was especially chosen.
- Following the assessment of the sensor's performance at an ambient temperature of 25 °C, the next objective was to evaluate its functionality at higher temperatures, specifically above 40 °C, to observe the transparency of the black TC element. To achieve this, an external heater was employed to generate heat. The external heater was placed above both the flexible sensor and the thermistor, resulting in a non-homogenous heating of both the thermistor and the flexible device. With this configuration, the thermistor could detect the temperature increase, while the

thermochromic (TC) sensor registered this temperature by transitioning to a transparent color. Once the TC element became transparent, the corresponding data was recorded (Fig. 4.12). As depicted in Fig. 4.12b, the ambient temperature reached about 40.67 °C, and the temperature measured by the flexible sensor registered at 42.51 °C. At this temperature, the transparency of the TC element became evident. This observation aligns with our earlier findings in Chapter 3 (Observations & Remarks – 2nd Scenario, S4a Sample), where the TC element transitioned from black to transparent at 43 °C, contrary to the manufacturer's datasheet. The skin-temperature value derived from the flexible sensor (approximately 42.51 °C), appears reasonable considering someone’s exposure to the sun and an ambient temperature of 40.67 °C.

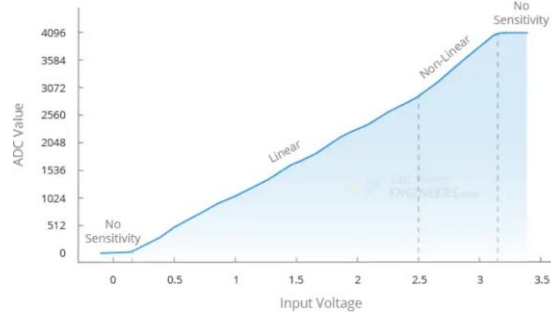


Figure 4.9: ESP32 ADC Non-Linear Graph [201].

Table 4.2: Temperature-Resistance data of the NTC 10K B3950 thermistor, provided by the manufacturer [202].

Resistance @ 25°C = 10KΩ				B _{3950K}			
T(°C)	R(KΩ)	T(°C)	R(KΩ)	T(°C)	R(KΩ)	T(°C)	R(KΩ)
-40	277.2	1	30.25	42	4.915	83	1.128
-39	263.6	2	28.82	43	4.723	84	1.093
-38	250.1	3	27.45	44	4.539	85	1.059
-37	236.8	4	26.16	45	4.363	86	1.027
-36	224.0	5	24.94	46	4.195	87	0.9955
-35	211.5	6	23.77	47	4.034	88	0.9654
-34	199.6	7	22.67	48	3.880	89	0.9363
-33	188.1	8	21.62	49	3.733	90	0.9083
-32	177.3	9	20.63	50	3.592	91	0.8812
-31	167.0	10	19.68	51	3.457	92	0.8550
-30	157.2	11	18.78	52	3.328	93	0.8297
-29	148.1	12	17.93	53	3.204	94	0.8052
-28	139.4	13	17.12	54	3.086	95	0.7816
-27	131.3	14	16.35	55	2.972	96	0.7587
-26	123.7	15	15.62	56	2.863	97	0.7366
-25	116.6	16	14.93	57	2.759	98	0.7152
-24	110.0	17	14.26	58	2.659	99	0.6945
-23	103.7	18	13.63	59	2.564	100	0.6744
-22	97.9	19	13.04	60	2.472	101	0.6558
-21	92.50	20	12.47	61	2.384	102	0.6376
-20	87.43	21	11.92	62	2.299	103	0.6199
-19	82.79	22	11.41	63	2.218	104	0.6028
-18	78.44	23	10.91	64	2.141	105	0.5858
-17	74.36	24	10.45	65	2.066	106	0.5694
-16	70.53	25	10.00	66	1.994	107	0.5535
-15	66.92	26	9.575	67	1.926	108	0.5380
-14	63.54	27	9.170	68	1.860	109	0.5229
-13	60.34	28	8.784	69	1.796	110	0.5083
-12	57.33	29	8.416	70	1.735	111	0.4941
-11	54.50	30	8.064	71	1.677	112	0.4803
-10	51.82	31	7.730	72	1.621	113	0.4669
-9	49.28	32	7.410	73	1.567	114	0.4539
-8	46.89	33	7.106	74	1.515	115	0.4412
-7	44.62	34	6.815	75	1.465	116	0.4290
-6	42.48	35	6.538	76	1.417	117	0.4171
-5	40.45	36	6.273	77	1.371	118	0.4055
-4	38.53	37	6.020	78	1.326	119	0.3944
-3	36.70	38	5.778	79	1.284	120	0.3835
-2	34.97	39	5.548	80	1.243	121	0.3730
-1	33.33	40	5.327	81	1.203	122	0.3628
0	31.77	41	5.117	82	1.165	123	0.3530

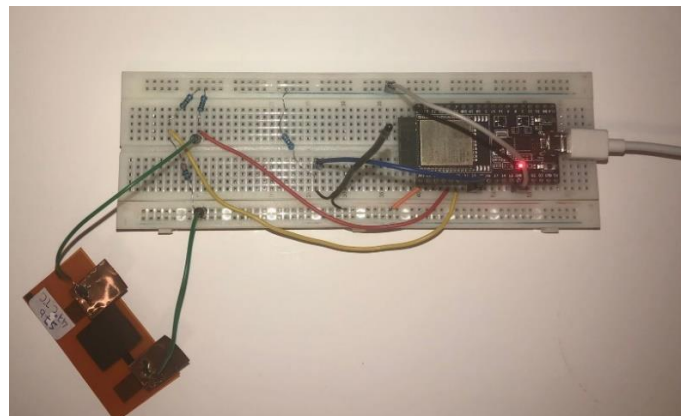


Figure 4.10: Electronic setup with the flexible temperature sensor at an ambient temperature of 25 °C (Black TC 47 °C on Kapton substrate – L3 layout design).

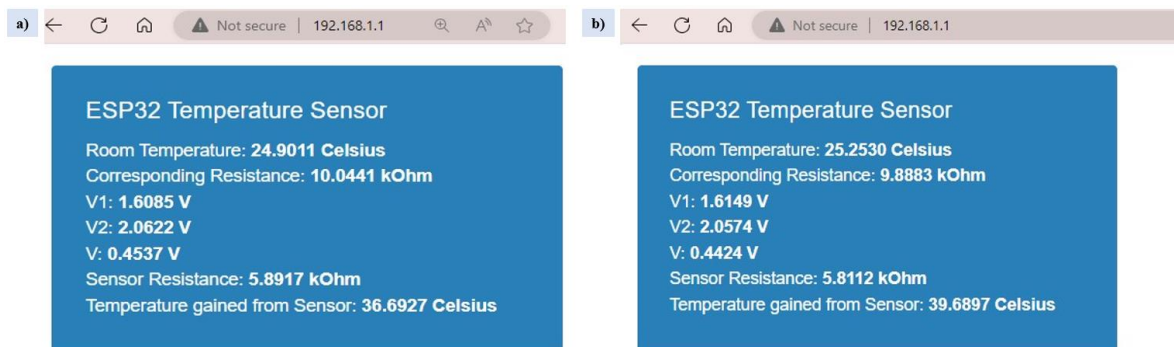


Figure 4.11: Data displayed via a Web Server user interface: **a)** $a = 0.02755 + 0.00751 \text{ (k}\Omega/\text{C}^\circ\text{)}$, **b)** $a = 0.02755 + 0.00101 \text{ (k}\Omega/\text{C}^\circ\text{)}$.

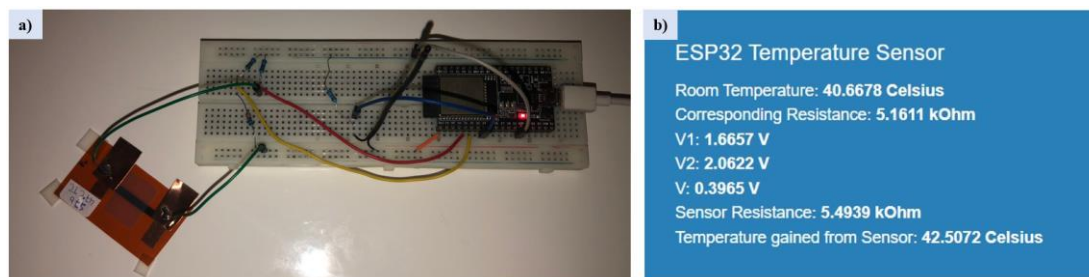


Figure 4.12: Ambient temperature of 41 °C: **a)** Electronic setup with the flexible temperature sensor – transparency of the black TC element, **b)** Corresponding data displayed via a Web Server user interface.

4.2 Wireless Communication

The successful implementation of Wi-Fi, IoT, and Bluetooth communication protocols has expanded the capabilities of the flexible temperature sensor, allowing it to function as a wearable device for real-time data monitoring, for both patients and medical experts. In the following sections, the programming of these three wireless communication protocols, is extensively described. Furthermore, a thorough comparative analysis of these communication methods, is also included, to evaluate their respective advantages and drawbacks, providing valuable insights for future developments in the field of healthcare and remote patient monitoring.

4.2.1 Web Server App

The ESP32 supports Wi-Fi connectivity, thus, a web server application was developed, which is not only applicable for mobile devices but also laptops, computers, and any other device that connects to the internet and can access a web browser.

Through this implementation the ESP32 MCU is configured to act both as an Access Point (AP) [204], as well as a Web Server. As an AP it assigns a unique IP Address that allows communication among the connected devices, while the Web Server monitors incoming HTTP requests and sends HTTP responses, including HTML, CSS, JavaScript or any other web content.

With this configuration, the ESP32 is given a set of variables for setting up the Wi-Fi connection and an IP Address where connected devices can access web content via HTTP (Fig. 4.13).

```

/* Set SSID & Password */
const char *ssid = "ESP32"; // SSID
const char *password = "12345678"; // Password

/* Set IP Address details */
IPAddress local_ip(192, 168, 1, 1);
IPAddress gateway(192, 168, 1, 1);
IPAddress subnet(255, 255, 255, 0);

WebServer server(80);
    
```

Figure 4.13: Initial variables required for setting up the Wi-Fi connection and Web Server.

Once the server starts, users can connect to the Wi-Fi provided by the ESP32 using the preset password (Fig. 4.14a) and navigate to the corresponding IP Address, via a web browser. The root page of that HTTP request sends an HTML, CSS and JavaScript response body, that loads a user interface to the browser, displaying the transmitted data from the ESP32 (Fig. 4.14b). The way data gets retrieved and updated is through an API Endpoint configured in the ESP32, which responds with a JSON object, that contains all the required data values. To achieve a constant update of the values, an interval method has been used in JavaScript that gets executed every 1000ms (1 second). Each time the method is run, a new response from the API gets retrieved, parsed and displayed onto the screen in the main route.

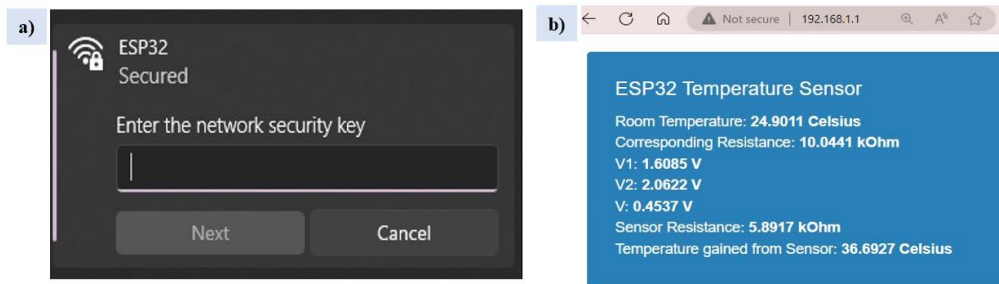


Figure 4.14: a) Wi-Fi network of the ESP32, with a protected password, b) Web server user interface, via the web browser.

Code Explanation

To setup the AP and Web Server for the ESP32, an SSID and Password must be configured for the device (Fig. 4.13), in order to broadcast the Wi-Fi with a valid name and a password for extra protection. Additionally, an IP Address had to be initialized so that the ESP32 can allow other devices to connect properly and securely. As mentioned, in the root path of the web server, the ESP32 responds with web content that consists of the HTML (Fig. 4.15), CSS (Fig. 4.16) and JavaScript (Fig. 4.17) code and gets rendered to the client browser as a user interface.

a) HTML Content

```

<div class="card">
  <h1>ESP32 Temperature Sensor</h1>
  <p>Room Temperature: <span id="tth-element">0 Celsius</span></p>
  <p>Corresponding Resistance: <span id="rth-element">0 kOhm</span></p>
  <p>V1: <span id="adc1-element">0 V</span></p>
  <p>V2: <span id="adc2-element">0 V</span></p>
  <p>V: <span id="adc-element">0 V</span></p>
  <p>Sensor Resistance: <span id="rsensor-element">0 kOhm</span></p>
  <p>Temperature gained from Sensor: <span id="tsensor-element">0 Celsius</span></p>
</div>
    
```

Figure 4.15: HTML Content, the structure of the web content that gets retrieved from the HTTP response.

b) CSS - Styling

```
const char MAIN_page[] PROGMEM = R"=====(
<!DOCTYPE html>
<html>
<head>
  <style>
    * {
      margin: 0;
      padding: 0;
      font-family: Arial, Helvetica, sans-serif;
      color: #fff;
    }

    h1 {
      font-size: 16pt;
      font-weight: 400;
      margin-bottom: 15px;
    }

    p {
      margin-bottom: 5px;
      font-size: 12pt;
      font-weight: 400;
    }

    span {
      font-weight: 600;
    }

    .card {
      max-width: 450px;
      min-height: 250px;
      background: #2980b9;
      padding: 30px;
      box-sizing: border-box;
      color: #fff;
      margin: 20px;
      border-radius: 4px;
    }
  </style>
</head>

```

Figure 4.16: CSS Styling of the web content that gets retrieved from the HTTP response.

c) JavaScript Logic

```
<script>
setInterval(function () {
  // Call a function repetatively with 2 Second interval
  getData();
}, 2000); // 2 Seconds update rate

function getData() {
  fetch("/data", {
    method: 'GET',
  })
  .then((res) => {
    if (res.ok) return res.json();
  })
  .then((data) => {
    document.getElementById("tth-element").innerHTML = data.tth + " Celsius";
    document.getElementById("rth-element").innerHTML = data.rth + " kOhm";

    document.getElementById("adc1-element").innerHTML = data.adc1 + " V";
    document.getElementById("adc2-element").innerHTML = data.adc2 + " V";
    document.getElementById("adc-element").innerHTML = data.adc + " V";
    document.getElementById("rsensor-element").innerHTML = data.rsensor + " kOhm";
    document.getElementById("tsensor-element").innerHTML = data.tsensor + " Celsius";
  });
}
</script>

```

Figure 4.17: JavaScript code, for the logic of the web content that gets retrieved from the HTTP response.

The route navigation is handled by the handler methods (Fig. 4.18).

- **void handleRoot():** Responds with the HTML content, which in turn is responsible for rendering the UI (User Interface) within the web browser.
- **void handleData():** Is responsible for generating the JSON object that is gathered from the API call through the “/data” path, with the up-to-date values incorporated in the response.

```

void handleRoot()
{
  String mainPage = MAIN_page;
  server.send(200, "text/html", mainPage);
}

void handleData()
{
  String response = "{\"tth\":\\"" + String(Tth, 4) + "\",\"rth\":\\"" + String(Rth/1000, 4) +
    "\",\"adc1\":\\"" + String(V1, 4) + "\",\"adc2\":\\"" + String(V2, 4) + "\",\"adc\":\\"" + String(V, 4) +
    "\",\"rsensor\":\\"" + String(Rsensor/1000, 4) + "\",\"tsensor\":\\"" + String(Tsensor, 4) + "\"}";

  server.send(200, "application/json", response);
}

```

Figure 4.18: Handlers for the routing of the web server.

The final steps of the setup configuration are to subscribe the SSID and Password to the ESP32 and set the handler methods to a valid path (Fig. 4.19). The “handleRoot” will be accessible via the “/” path and the “handleData” will be accessible via the “/data” path.

```

WiFi.softAP(ssid, password);
WiFi.softAPConfig(local_ip, gateway, subnet);

delay(100);

server.on("/", handleRoot);
server.on("/data", handleData);

```

Figure 4.19: Subscribe the SSID and Password the Wi-Fi library and set the handlers to valid paths for the web server.

4.2.2 IoT App

The IoT implementation is similar to the Web Server, however, the ESP32, is not configured to act as an AP (Access Point), but as a STA (Station) [205]. Consequently, the device gets connected to an existing Wi-Fi in order to send and receive HTTP requests. Furthermore, an online platform called ‘Arduino Cloud’ was used to make the development process easier and offer a better UI (User Interface) design [206], via the integrated dashboard panel.

Since the Arduino Cloud Platform offered most flexibility through a drag-and-drop mode, coding was only required for the calculation and representation of the temperature values.

Once the ESP32 was connected, the variables and dashboard components had to be designed via the Arduino Cloud, to visually display the data. This process was accomplished through the list of components, which were already included in the free tier plan of the Arduino Cloud. Finally, after designing the dashboard and uploading the code to the ESP32, graphs and other components, the data was displayed to the screen (Fig. 4.20a). In addition, a mobile application offered by the Arduino Cloud called “IoT Remote” was utilized to access the data from anywhere in the world, as long as the ESP32 remained connected to the internet (Fig. 4.20b).

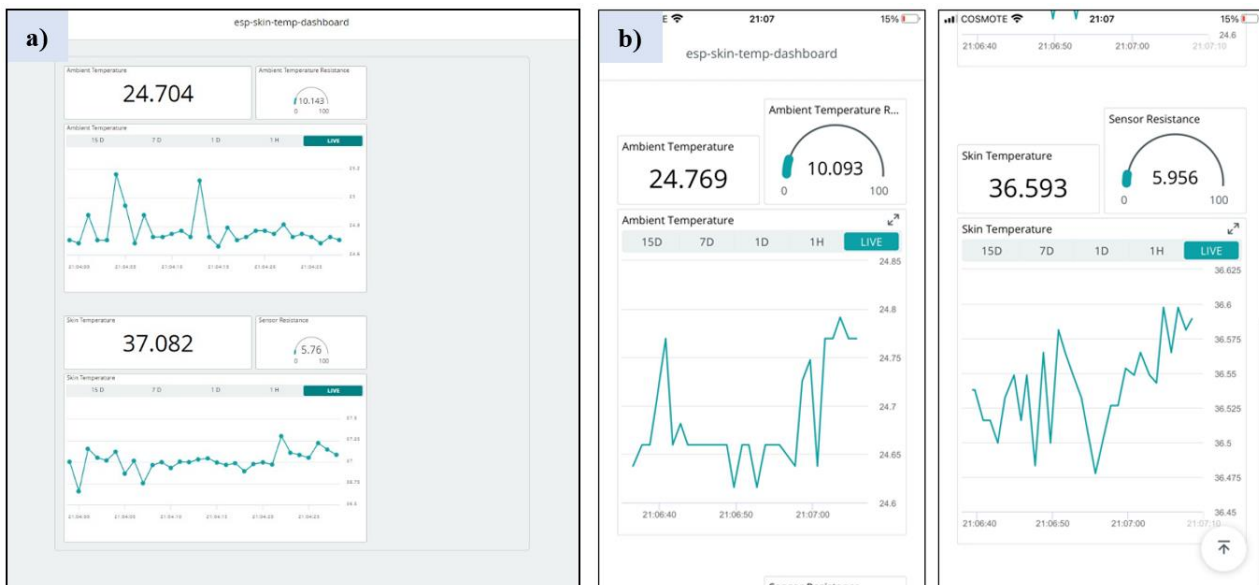


Figure 4.20: a) IoT Desktop dashboard that displays live data of the ESP32, b) IoT mobile application dashboard that displays live data of the ESP32.

▪ **Code Explanation**

Even though the implementation of the IoT and the Web Server were similar, setting up the ESP32 to work with Arduino Cloud (IoT) was quite different, since all variables and user interface (including components) were offered by the Arduino Cloud Platform’s interface. Initially, four (4) cloud variables were set in the platform, namely “roomTemperature”, “roomTempResistance”, “sensorResistance” and “tempGainedFromSensor” (Fig. 4.21a). The code for these variables gets automatically generated by the platform in the Cloud Editor, which is also mentioned in a large section comment on top of the code (Fig. 4.21b).

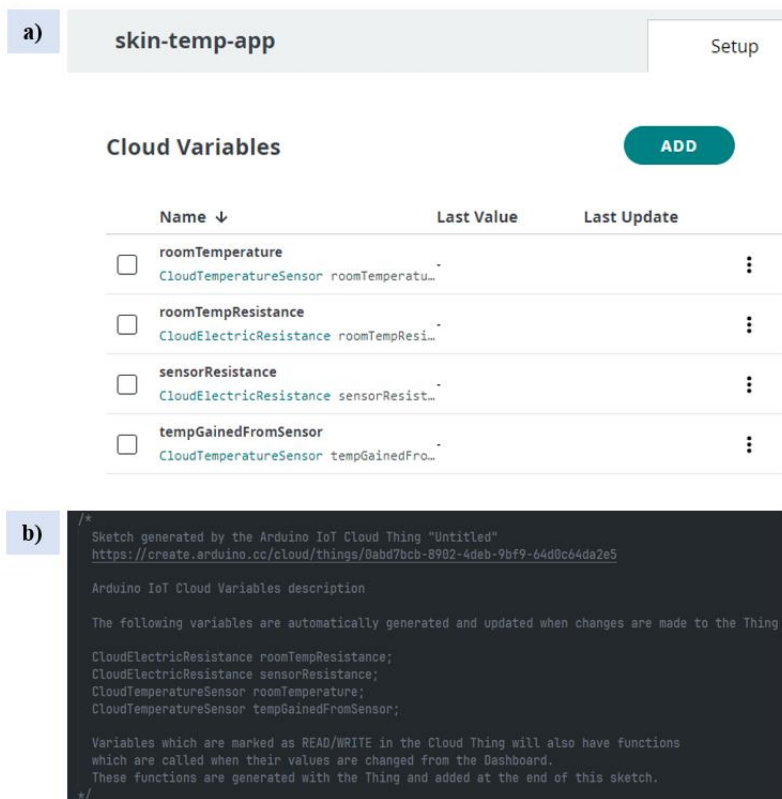


Figure 4.21: a) Cloud variables created in the Arduino Cloud Platform, b) Generated code comment ensuring developers that variables are automatically generated.

After initializing the variables, a dashboard where the data is visualized was designed, using two Chart components, two Gauge components and two Value components (Fig. 4.20). The Chart components are responsible for displaying in a graph the progression of the ambient and skin temperatures in Celsius, the Gauge components are responsible for visualizing the measurements of the thermistor and sensor resistances, while the Value components are simply a representation of the latest value of the graph for the temperatures.

Once both the variables and the dashboard for the IoT Application were finalized, the ESP32 had to be connected to a Wi-Fi network through the Platform's interface (Fig. 4.22). To achieve the connection, a Wi-Fi name, password and secret key had to be inputted. The secret key was provided upon selecting the ESP32 model.

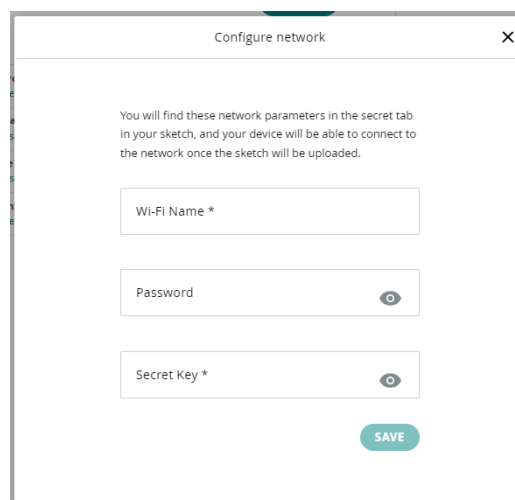


Figure 4.22: Arduino Cloud Platform – Connect to a Wi-Fi Network window.

Finally, since every setup step was completed in the Arduino Cloud Platform's interface, the only thing to do was specify the values that each "cloud variable" is going to represent (Fig. 4.23).

```
roomTemperature = Tth;  
roomTempResistance = Rth/1000;  
sensorResistance = Rsensor/1000;  
tempGainedFromSensor = Tsensor;
```

Figure 4.23: Assigning the measurement values to the IoT variables initialized on the platform.

4.2.3 Bluetooth App

The ESP32-WROOM-32D integrates Bluetooth Low Energy (BLE) technology [207], enabling the transmission of data to mobile devices. As a result, a Bluetooth application has been developed to facilitate remote real-time temperature monitoring and the display of data captured by the flexible temperature sensor.

The ESP32 incorporates a unique identification number, referred to as a UUID (Universal Unique Identifier) [208]. The UUID is defined for two (2) different things in the ESP32, namely Services and Characteristics [209]. The Service UUID is used to identify a specific service offered by the ESP32 device and acts as an identifier that allows other BLE devices to discover and recognize the services.

The main Service in the ESP32 is to transmit ambient and skin temperature data, achieved via 'characteristics'. Characteristics are specific data points included in a service and can define the type of data being transmitted, its properties (e.g., Read, Read & Write, etc.), and the actual data value.

They are used to exchange data between the ESP32 and any other connected device. Because there are two main data values that the ESP32 transmits, namely ambient and skin temperature, each characteristic has also been given its own UUID in order to separate each value from the other. This makes it easy for other BLE devices to discover, as well as interact with each characteristic individually. In order to effectively read the data transmitted by the ESP32 a mobile application has been developed with the unique purpose of communicating with the device (Fig. 4.24). The technology used for developing the application was React-Native [210], via a framework called Expo [211] to expedite and assist with the development process. React-Native is a JavaScript framework based on React, that offers developers the ability to design mobile applications for any OS (Operating System). Therefore, the same codebase, can work on any device, no matter if it is an Android or an IOS (iPhone).

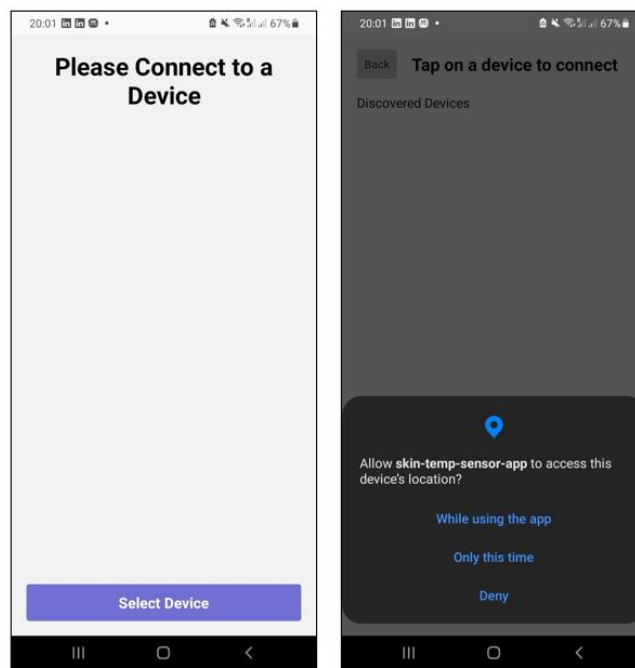


Figure 4.24: Bluetooth mobile application, first look and Bluetooth/Location permissions.

The mobile application considers all the UUIDs defined in the ESP32 and works around those to discover and communicate with the device, thus, allowing seamless communication between them. It works by first scanning for BLE devices that have the same Service UUID as the defined one in the ESP32 device. Secondly, it offers a list of all discovered devices based on that criteria and allows the user to tap and connect (Fig 4.25a). Thirdly, once a connection has been succeeded and the application gets paired with the device, it makes use of the defined Characteristics UUIDs to read the transmitted data from the ESP32. It then uses a library called “base64” to decode the received value from the characteristics, into a floating-point number which can be understood by the user, since the transmitted data from the ESP32 is encoded with base64 [212]. Finally, it displays the readable value to the application and updates it in intervals of 1000ms (1 second) as configured in the ESP32 device (Fig 4.25b). The update timeframe is the result of the notification property of the characteristics in combination of the delay specified for each data transmission.

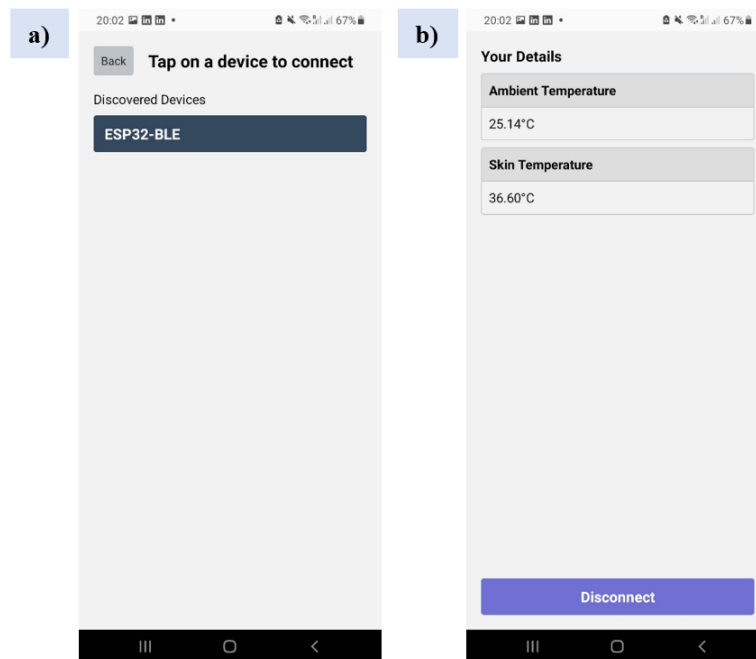


Figure 4.25: a) Bluetooth mobile application: a) list of discovered and connectable ESP32 devices, b) display of live data after successful Bluetooth pairing.

▪ Code Explanation

a) ESP32-WROOM-32D BLE Initialization

In order for the device to work properly, implementing Bluetooth Low Energy for the ESP32, requires multiple steps of configuration in the code. Firstly, there are four libraries that needed to be included for the code to work (Fig. 4.26), each related to the BLE functionality and crucial for the BLE application.

```
#include <BLEDevice.h>
#include <BLEServer.h>
#include <BLEUtils.h>
#include <BLE2902.h>
```

Figure 4.26: Required imports for the ESP32 code with Bluetooth.

Secondly, three constant variables for the UUIDs had to be defined for the device, one for the Service and two for the Characteristics (Fig. 4.27). In addition to the UUIDs, variables for the service and characteristics as points, had to also been set at the top of the code (Fig. 4.28), to refer to the UUIDs when initialized.

```
#define SERVICE_UUID "0000180A-0000-1000-8000-00805F9B34FB"
#define AMBIENT_TEMPERATURE_CHARACTERISTIC_UUID "00002A6E-0000-1000-8000-00805F9B34FB"
#define SKIN_TEMPERATURE_CHARACTERISTIC_UUID "00002A6F-0000-1000-8000-00805F9B34FB"
```

Figure 4.27: Defined UUIDs for Service and Characteristics.

```
BLEServer *pServer = NULL;
BLECharacteristic *pAmbientTempCharacteristic = NULL;
BLECharacteristic *pSkinTempCharacteristic = NULL;
```

Figure 4.28: Defined pointers for the characteristics, which will later hold data values to be transmitted.

Thirdly, in the initialization process (Fig. 4.29), when setting up the ESP32 with BLE there needs to be a configuration of steps, where all variables are initialized and subscribed to their methods, respectively.

- The first step includes naming the ESP32 (Fig. 4.29 – a). This name serves the purpose of making the device easily identifiable when detected, ensuring that it is displayed with its designated name in the list of scanned devices.
- The next step involves creating the server (Fig. 4.29 – b),
- Subscribing a service on to that server (Fig. 4.29 – c),
- and subscribing the characteristics on to that service using the previously defined UUIDs (Fig. 4.29 – d).

The final step holds significant importance for the initialization of the ESP32's functionality and its data transmission to the devices that have been paired with it. Since the data to be transmitted is determined by the measurements taken on the ESP32, there is no need for the paired devices to modify this value. Consequently, the properties for the characteristics have been configured as "read-only." This signifies that other devices can access and retrieve the data, but are unable to alter or update it.

```
a) BLEDevice::init("ESP32-BLE");
b) pServer = BLEDevice::createServer();
c) BLEService *pService = pServer->createService(SERVICE_UUID);
d) pAmbientTempCharacteristic = pService->createCharacteristic(
    AMBIENT_TEMPERATURE_CHARACTERISTIC_UUID,
    BLECharacteristic::PROPERTY_READ |
    BLECharacteristic::PROPERTY_NOTIFY);
    pSkinTempCharacteristic = pService->createCharacteristic(
    SKIN_TEMPERATURE_CHARACTERISTIC_UUID,
    BLECharacteristic::PROPERTY_READ |
    BLECharacteristic::PROPERTY_NOTIFY);
```

Figure 4.29: Initializing all the defined variables and enabling the device to work with BLE.

After everything has been properly configured, the necessary values are assigned to the pointer variables associated with the characteristics, along with a notify method that guarantees that the ESP32 transmits updates each time there is a change in these values (Fig. 4.30).

```
// Ambient Temperature
pAmbientTempCharacteristic->setValue((uint8_t *)&Tth, sizeof(Tth));
pAmbientTempCharacteristic->notify();

// Skin Temperature
pSkinTempCharacteristic->setValue((uint8_t *)&Tsensor, sizeof(Tsensor));
pSkinTempCharacteristic->notify();
```

Figure 4.30: Passing the measurements into the initialized variables for the Characteristics pointers.

b) BLE Mobile Application

Once the ESP32 BLE coding part was completed, a mobile application had to be developed in order to establish a wireless connection for reading the values from the ESP32.

In the mobile application, the same UUIDs defined for the service and characteristics in the ESP32, were also defined and exported in the application source code (Fig. 4.31). This approach ensures that the application exclusively identifies and connects to the ESP32 when scanning for Bluetooth Low Energy (BLE) devices. Once connected, the data can be accessed through the characteristics using the Characteristics UUIDs, which is a less resource-intensive process compared to discovering these characteristics from scratch.

```

const SERVICE_UUID = "0000180A-0000-1000-8000-00805F9B34FB";
const AMBIENT_TEMPERATURE_CHARACTERISTIC_UUID =
  "00002A6E-0000-1000-8000-00805F9B34FB";
const SKIN_TEMPERATURE_CHARACTERISTIC_UUID =
  "00002A6F-0000-1000-8000-00805F9B34FB";

export {
  SERVICE_UUID,
  AMBIENT_TEMPERATURE_CHARACTERISTIC_UUID,
  SKIN_TEMPERATURE_CHARACTERISTIC_UUID,
};

```

Figure 4.31: Defined UUIDs for the mobile application, in order to communicate with the ESP32.

When developing mobile applications, there are numerous challenges associated with managing internal APIs, primarily due to the requirement of implementing permissions [213]. Therefore, the application cannot work without the user granting permission for accessing the location services, thus allowing access to Bluetooth as well, which needs the app to function properly. The implementation of such a permission request is achieved manually (Fig. 4.32), and while it may vary from one application to another, the common principle is to verify that the permission status is "granted", before proceeding.

```

const requestPermissions = async () => {
  if (Platform.OS === "android") {
    if ((ExpoDevice.platformApiLevel ?? -1) < 31) {
      const granted = await PermissionsAndroid.request(
        PermissionsAndroid.PERMISSIONS.ACCESS_FINE_LOCATION,
        {
          title: "Location Permission",
          message: "Bluetooth Low Energy requires Location",
          buttonPositive: "OK",
        }
      );
      return granted === PermissionsAndroid.RESULTS.GRANTED;
    } else {
      const isAndroid31PermissionsGranted =
        await requestAndroid31Permissions();
      return isAndroid31PermissionsGranted;
    }
  } else {
    return true;
  }
};

```

Figure 4.32: Regulating permissions for the mobile application (Bluetooth & Location/GPS).

Once the permission is granted, the application can initiate a scan for available devices to establish a BT connection (Fig. 4.33). However, since this application is developed to be paired with the ESP32 exclusively, a specific parameter is provided to the scan function to restrict the scan results to the Service UUID of the ESP32 (Second line of Fig. 4.33).

```

const scanForPeripherals = () => {
  bleManager.startDeviceScan([SERVICE_UUID], null, (error, device) => {
    if (error) {
      console.log(error);
    }
    if (device) {
      setAllDevices((prevState: Device[]) => {
        if (isDuplicateDevice(prevState, device)) {
          return [...prevState, device];
        }
        return prevState;
      });
    }
  });
};

```

Figure 4.33: Method for scanning BLE (ESP32) devices for the mobile application.

Since the scanning method does not inherently detect whether a device had already been detected, it will keep populating the list of scanned devices with the same device. To address this issue, a method for detecting duplicate devices has been implemented (Fig. 4.34). This function compares the identification number of any new device with those already in the list. Therefore, if the identification number matches, it will ignore the current device, whereas if the device is not found within the list, it is then added to it.

```
const isDuplicateDevice = (devices: Device[], nextDevice: Device) =>
  devices.findIndex((device) => nextDevice.id === device.id) > -1;
```

Figure 4.34: Method for ensuring no duplicate devices get added to the results of discovered devices in the mobile application.

Once the scan has discovered one or more devices, the application is able to connect and pair with any of them (Fig. 4.35). In this process, the connection method first stores the selected device into a state (saves it) and then begins to scan for the available services and characteristics associated with the selected device. Afterwards, the device scanning process is halted, and the application begins the process of streaming the temperature-related data to the chosen device.

```
const connectToDevice = async (device: Device) => {
  try {
    const deviceConnection = await bleManager.connectToDevice(device.id);
    setConnectedDevice(deviceConnection);
    await deviceConnection.discoverAllServicesAndCharacteristics();
    bleManager.stopDeviceScan();
    startStreamingData(deviceConnection);
  } catch (e) {
    console.log("FAILED TO CONNECT", e);
  }
};
```

Figure 4.35: Method for connecting and pairing with the selected BLE (ESP32) device.

The data streaming method (Fig. 4.36) ensures that a device exists and is paired with the mobile application. Subsequently it uses both the Service UUID and characteristic UUID associated with each data value to retrieve the ambient and skin temperature readings through the "onDataUpdate" method. (Fig. 4.37).

The "onDataUpdate" method, determines which data value requires updating based on the type specified as an argument, either "ambient" or "skin". These are custom values, specifically defined in the application, to guarantee that the correct value gets updated on the screen. However, another critical step is essential to ensure the proper display of values, and that entails decoding the received data from the characteristics.

```
const startStreamingData = async (device: Device) => {
  if (device) {
    device.monitorCharacteristicForService(
      SERVICE_UUID,
      AMBIENT_TEMPERATURE_CHARACTERISTIC_UUID,
      (err, char) => onDataUpdate("ambient", err, char)
    );
    device.monitorCharacteristicForService(
      SERVICE_UUID,
      SKIN_TEMPERATURE_CHARACTERISTIC_UUID,
      (err, char) => onDataUpdate("skin", err, char)
    );
  } else {
    setAmbientTemp(-1);
    setSkinTemp(-1);
  }
};
```

Figure 4.36: Method for allowing transmission of the data from the BLE device (ESP32) to the mobile application via Characteristics.

```

const onDataUpdate = (
  type: "ambient" | "skin",
  error: BleError | null,
  characteristic: Characteristic | null
) => {
  if (error) {
    console.log(error);
    return -1;
  } else if (!characteristic?.value) {
    console.log("No Data was recieved");
    return -1;
  }

  if (type === "ambient") {
    const rawData = decodeBinaryValue(characteristic.value);
    setAmbientTemp(rawData);
  } else if (type === "skin") {
    const rawData = decodeBinaryValue(characteristic.value);
    setSkinTemp(rawData);
  }
};

```

Figure 4.37: Method for updating the mobile application values every time the BLE (ESP32) device's data changes.

In order to decode these values, a custom method named "decodeBinaryValue" has been developed (Fig. 4.38). This method accepts the raw characteristic value and returns a decoded value that is easily read by the user. Given that the ESP32 transmits floating-point numbers, the "base64" library is utilized to facilitate the conversion of the value from base64 encoding back into a floating-point number, through the "readFloatLE" method.

```

import {Buffer} from 'buffer';

const decodeBinaryValue = (base64Value: string) => {
  const decodedBinary = Buffer.from(base64Value, 'base64');
  const value = decodedBinary.readFloatLE(0);
  return value;
};

export default decodeBinaryValue;

```

Figure 4.38: Method for decoding the transmitted data into readable numeric (float) values.

4.3 Comparison of the Three Technologies (Web Server, IoT and Bluetooth App)

- With the web service, users are required to disconnect from their main Wi-Fi connection and connect to the ESP32's Hotspot. This essentially isolates users from the broader internet, as the only accessible data is that served by the ESP32 server. The process involves several steps, including disconnecting from the current Wi-Fi network, connecting to the ESP32 hotspot, opening a web browser, and navigating to the local hotspot, which is represented by an IP address. This technology, therefore, confronts certain challenges including the memorization of the IP address – particularly if not saved – introducing a complex and time-consuming procedure for gaining access to temperature-related data. Despite its constraints, Wi-Fi technology provides faster data transfer, whereas Bluetooth is more appropriate for short-range connections between devices which focus on energy efficiency.
- The Internet of Things (IoT) presents an appealing concept for maintaining uninterrupted access to data. However, there is a fundamental requirement in the case of ESP32 devices, which necessitates a constant internet connection to facilitate data display. This requirement may not align with the preferences and circumstances of many users. Moreover, the current approach lacks simplicity in connecting the ESP32 to the internet, as it mandates users to engage in manual configuration via their Cloud accounts. This process can be perceived as less efficient, potentially posing challenges for those seeking a seamless and straightforward experience. Nevertheless,

considering that many users can be connected to the same Cloud platform, they can gain real-time access to the same the temperature data. This particular advantage proves extremely valuable for individuals that due to medical reasons are confined to their homes. In such cases, both healthcare professionals and family members can remotely access the patient's health-related data, facilitating continuous remote monitoring and care.

- Using Bluetooth, all issues mentioned above are solved, as the ESP32 can maintain a constant Bluetooth broadcasting at all times, which makes it easy to access anytime the data quickly, using the mobile app. However, Bluetooth is intended for short-range, low-power, personal area network (PAN) connections. Meaning that, in contrast to the IoT technology, doctors can't get direct access into a patient's data.
- In evaluating these technologies, it is imperative to recognize that each possesses its unique set of merits and limitations. Consequently, the choice of wireless technology for data presentation depends on several crucial factors. These include the specific health parameters detected from the sensor, the current health condition of the patient, and the intended use of the sensor, whether it serves as a personal health gadget or a medical device. When the sensor serves personal health monitoring needs, Bluetooth technology emerges as a well-suited option. Its seamless connectivity, coupled with lower power consumption, lends itself admirably to individual users seeking convenience and accessibility. On the other hand, in cases where the sensor assumes a medical role, such as continuous patient monitoring, the Internet of Things (IoT) Cloud Platform presents as the more suitable choice. This facilitates comprehensive data evaluation and remote access, proving invaluable to medical experts, in delivering timely and informed care. Hence, the choice of wireless technology should be a deliberate one, tailored to the specific context and requirements of the healthcare scenario at hand.

5 Conclusions – Future Work

- In this work a flexible temperature sensor based on thermochromic inks was fabricated with screen-printing technology. Several critical parameters, including, the sensor's structure, the substrate material, the thermal-electrical and thermal-optical properties, as well as the overall performance, were evaluated to ensure the sensor's successful implementation. Three distinct layout designs (L1, L2, L3), were extensively implemented and examined. The experimental measurements that correlate the resistance with the temperature developed in the flexible device (Chapter 2), presented a varying temperature coefficient of resistance (TCR) for each sample, which was experimentally found to have a negative temperature coefficient (NTC) behavior. The analysis was followed by the correlation of the thermal field of the sensor through a thermal (IR) camera, with the optical field via photography, for the samples with the L3 layout configuration with an activation temperature of 47 °C, on polymer substrates (Chapter 3). This analysis showcased that according to the findings outlined in the 1st Scenario (Wide Temperature Range), the thermal and optical images captured at temperatures 50 °C, 60 °C, and 70 °C, manifested a discernible distinction between the graph derived from the optical image, and that originating from the thermal image (Fig. 3.3 – Fig. 3.5). This arises from the behavior of the Thermochromic (TC) element during the heating process, leading to its transparency, and thereby revealing the underlying carbon material, when its area of discoloration exceeds the carbon element's area. The 2nd Scenario (Narrow Temperature range) was conducted to get a closer view of the sample's behavior at temperatures that closely align with the 47 °C activation temperature of the TC element. It was observed that at 43 °C the Thermochromic (TC) element initiated its transparent transition (Fig. 3.12). Notably, the discoloration of the TC element below the carbon's area was observed up to 52 °C (Fig. 3.15). Consequently, all graphs exhibited a similar pattern, where the transparency observed in the optical image, corresponded to the maximum temperature conducted to the TC structure. In combination with the fabricated sensor, an electronic setup based on the ESP32-WROOM-32D microcontroller, a voltage divider and a Wheatstone bridge, was also developed (Chapter 4). In this setup, the microcontroller read the resistance of the sensor and used its temperature coefficient of resistance, to calculate the detected temperature which then, logs it. After a comprehensive examination of the TCR values extracted from the Chapter 2 a value of $0.02755 + 0.00751$ (k Ω /°C), was specifically chosen for the 47 °C activation temperature TC sensor with the L3 geometry, resulting in a skin temperature value of 36.69 °C under a 25 °C ambient temperature. This particular skin temperature value corresponds to the typical skin temperature of a human at reasonable ambient temperatures. Furthermore, the sensor's functionality at higher temperatures, specifically above 40 °C, was also presented. To achieve this, an external heater placed above both the flexible sensor and the thermistor, generated non-homogenous heating. This setup allowed the thermistor to detect the temperature increase, while the thermochromic (TC) sensor registered this temperature by transitioning to a transparent color. In this case, the ambient temperature reached about 40.67 °C, and the temperature measured by the flexible sensor registered at 42.51 °C. The recorded data was displayed in real-time to the user via a web server, IoT, or Bluetooth application. This device provides a solid foundation for the development of new types of flexible temperature sensors, holding significant promise both in the medical field and patient care.
- Flexible skin temperature sensors utilizing thermochromic (TC) inks hold substantial promise in the realm of healthcare and technology. They provide various advantages including enhanced

comfort and wearability, precise and real-time data, accessibility, convenience, remote monitoring and early detection. More specifically, flexible sensors integrated with thermochromic inks, adhere comfortably to the skin's surface, ensuring a non-intrusive monitoring experience. This enables individuals to wear them for extended periods without discomfort, making them ideal candidates for continuous temperature monitoring. Additionally, the ability of TC inks to change color in response to temperature fluctuations, allows for highly accurate temperature measurements. This level of precision is crucial for monitoring various health conditions, such as fever, or heat stroke. Furthermore, these sensors can be integrated into wearable devices, including smartwatches or adhesive patches, allowing for an accessible and user-friendly experience. The real-time data from these sensors can be transmitted wirelessly to healthcare professionals, facilitating remote monitoring, as well as immediate alerts of patients' health conditions.

- The temperature recognition via photography as detailed in Chapter 3, provides a more accurate and comprehensive insight into a patient's skin-temperature profile. In particular, the combined data derived from the thermal and optical field, facilitate the implementation of a thermal map of the skin. This thermal mapping allows for the identification of the body areas that are warmer or cooler than normal, indicating a sign of a variety of health conditions. Furthermore, to enhance the depth of analysis, additional measurements could be conducted, regarding the dynamic behavior of the fabricated samples. This assessment may yield valuable information about the TC element's dynamic response, when exposed to temperature variations.
- Although the successful implementation of a flexible skin-temperature sensor prototype based on TC inks, was generally achieved, certain challenges persisted. The primary challenge revolves around the fluctuations observed in the Resistance-Temperature (R-T) graphs and the Temperature Coefficient of Resistance (TCR) values of the samples. These variations probably stem from the direct screen-printing of the TC layer onto the Carbon layer, particularly in the L2 and L3 layout configurations. Therefore, to ensure the reliability of the temperature measurements, several strategies can be considered for future enhancements:
 1. One promising approach is the incorporation of a barrier layer, such as PEDOT: PSS, between the TC layer and the Carbon layer. This intermediary layer can help mitigate the interference caused by the direct contact between these layers, resulting in more stable Resistance-Temperature (R-T) graphs and Temperature Coefficient of Resistance (TCR) values.
 2. Another strategy involves conducting thermal measurements both before and after the screen-printing of the TC layer. By comparing the pre- and post-printing – of the TC layer – measurements, the deviations caused by the application of the TC ink, could be better assessed.
- An additional concept for advancing the development of this device involves transforming it into a flexible printed circuit board (PCB), integrated with a printed battery. This configuration represents a significant step towards elevating the prototype sensor into a wearable device, with the ability to provide real-time data monitoring. By integrating the necessary components into a flexible PCB, the sensor gains a more streamlined and compact design, ideal for wearability. Moreover, the inclusion of a printed battery ensures continuous power supply, enabling extended operational periods for uninterrupted monitoring. Furthermore, it is imperative to explore the testing of this advanced configuration on a fake-skin surface. Conducting measurements on fake-

skin models would serve to validate the sensor's ability to accurately detect and record realistic skin-temperature data.

- Additional improvements could be made to the Bluetooth Low Energy implementation for the mobile application, by integrating an online central database. This database would facilitate user authentication (login) via their account, and maintain an online profile with their real time data. Furthermore, when the mobile device is connected to the internet, the application could send requests to a server and upload data to the database. In addition, a separate application or website could be developed in order to monitor the database, allowing medical experts to gain access to each patient's data, considering their consent and permission. This approach could effectively address the close-range Bluetooth communication constraint, in the current BLE implementation.

6 FINAL REMARKS – Learning Outcomes

This project has significantly contributed to the expansion of my knowledge by providing hands-on experience with various laboratory equipment and technologies. This included the fabrication of flexible sensors via screen-printing process, the operation of the Keithley 2612 source-meter and the probe station for precise sample measurements, and the utilization the OLYMPUS | MX Semiconductors – MX51 optical imager to capture high-quality optical images of the samples. Furthermore, this project introduced me to the application of thermal infrared (IR) cameras for temperature detection within the samples, when subjected to internal heating, allowing for more comprehensive data analysis. In addition to my involvement in flexible sensor fabrication and electrical/thermal measurements, I acquired further knowledge about microcontrollers, with a particular focus on the ESP32, and its programming. This extended my expertise in the field of embedded systems and equipped me with practical experience in coding and interfacing with microcontrollers. Lastly, beyond the technical aspects, I had the opportunity to explore the development of applications with wireless communication protocols. This multifaceted project not only boasted my technical capabilities, but also expanded my problem-solving and project management skills, providing me with a well-rounded educational experience.

References

- [1] Zhou, N., Liu, T., Wen, B., Gong, C., Wei, G., & Su, Z. (2020). Recent Advances in the Construction of Flexible Sensors for Biomedical Applications. *Biotechnology Journal*, 15(12), 2000094. <https://doi.org/10.1002/biot.202000094>
- [2] Bhattacharya, S., Agarwal, A. K., Chanda, N., Pandey, A., & Sen, A. K. (2018). Environmental, chemical and medical sensors. *Energy, Environment, and Sustainability*. <https://doi.org/10.1007/978-981-10-7751-7>
- [3] Kenry, Yeo, J. C., & Lim, C. T. (2016). Emerging flexible and wearable physical sensing platforms for healthcare and biomedical applications. *Microsystems & Nanoengineering*, 2(1). <https://doi.org/10.1038/micronano.2016.43>
- [4] Wu et al., (2022). Optical flexible biosensors: From detection principles to biomedical applications. *Biosensors and Bioelectronics*, 210, 114328. <https://doi.org/10.1016/j.bios.2022.114328>
- [5] Qian, S., Cui, Y., Cai, Z., & Li, L. (2022). Applications of smartphone-based colorimetric biosensors. *Biosensors and Bioelectronics: X*, 11, 100173. <https://doi.org/10.1016/j.biosx.2022.100173>
- [6] Shi, H., Cao, Y., Xie, Z., Zhao, Y., Zhang, C., & Chen, Z. (2022). Multi-parameter photoelectric data fitting for microfluidic sweat colorimetric analysis. *Sensors and Actuators B-chemical*, 372, 132644. <https://doi.org/10.1016/j.snb.2022.132644>
- [7] Lee, J., Jeon, S., Seo, H., Lee, J. T., & Park, S. (2021). Fiber-Based sensors and energy systems for wearable electronics. *Applied Sciences*, 11(2), 531. <https://doi.org/10.3390/app11020531>
- [8] Kwon, D. Y., & Myoung, J. (2020). Wearable and semitransparent Pressure-Sensitive Light-Emitting sensor based on electrochemiluminescence. *ACS Nano*, 14(7), 8716–8723. <https://doi.org/10.1021/acsnano.0c03186>
- [9] Campea, M. A., Majcher, M. J., Lofts, A., & Hoare, T. (2021). A review of design and fabrication methods for nanoparticle network hydrogels for biomedical, environmental, and industrial applications. *Advanced Functional Materials*, 31(33), 2102355. <https://doi.org/10.1002/adfm.202102355>
- [10] Chen et al., (2019). Construction of a flexible electrochemiluminescence platform for sweat detection. *Chemical Science*, 10(25), 6295–6303. <https://doi.org/10.1039/c9sc01937e>
- [11] Song, L., Chen, J., Xu, B. B., & Huang, Y. (2021). Flexible plasmonic biosensors for healthcare monitoring: progress and prospects. *ACS Nano*, 15(12), 18822–18847. <https://doi.org/10.1021/acsnano.1c07176>
- [12] Xu et al., (2019). Smartphone-based battery-free and flexible electrochemical patch for calcium and chloride ions detections in biofluids. *Sensors and Actuators B-chemical*, 297, 126743. <https://doi.org/10.1016/j.snb.2019.126743>
- [13] Pu, Z., Wang, R., Wu, J., Yu, H., Xu, K., & Li, D. (2016). A flexible electrochemical glucose sensor with composite nanostructured surface of the working electrode. *Sensors and Actuators B-chemical*, 230, 801–809. <https://doi.org/10.1016/j.snb.2016.02.115>
- [14] Jeerapan, I., & Poorahong, S. (2020). Review—Flexible and Stretchable Electrochemical Sensing Systems: Materials, energy sources, and Integrations. *Journal of the Electrochemical Society*, 167(3), 037573. <https://doi.org/10.1149/1945-7111/ab7117>
- [15] Fakayode et al., (2023). Fluorescent chemical sensors: applications in analytical, environmental, forensic, pharmaceutical, biological, and biomedical sample measurement, and

- clinical diagnosis. *Applied Spectroscopy Reviews*, 1–89. <https://doi.org/10.1080/05704928.2023.2177666>
- [16] Tokuda et al., (2014). CMOS image sensor-based implantable glucose sensor using glucose-responsive fluorescent hydrogel. *Biomedical Optics Express*, 5(11), 3859. <https://doi.org/10.1364/boe.5.003859>
- [17] Llères, D., Swift, S., & Lamond, A. I. (2007). Detecting Protein-Protein Interactions In Vivo with FRET using Multiphoton Fluorescence Lifetime Imaging Microscopy (FLIM). *Current Protocols in Cytometry*, 42(1). <https://doi.org/10.1002/0471142956.cy1210s42>
- [18] Santos, L et al., (2014). WO3 Nanoparticle-Based Conformable pH Sensor. *ACS Applied Materials & Interfaces*, 6(15), 12226–12234. <https://doi.org/10.1021/am501724h>
- [19] Rahman, T., Cheng, C., Karagoz, B., Renn, M., Schrandt, M., Gellman, A. J., & Panat, R. (2019). High performance flexible temperature sensors via nanoparticle printing. *ACS Applied Nano Materials*, 2(5), 3280–3291. <https://doi.org/10.1021/acsanm.9b00628>
- [20] Gaur, M., Misra, C., Yadav, A. B., Swaroop, S., Maolmhuaidh, F. Ó., Bechelany, M., & Barhoum, A. (2021). Biomedical applications of carbon nanomaterials: fullerenes, quantum dots, nanotubes, nanofibers, and graphene. *Materials*, 14(20), 5978. <https://doi.org/10.3390/ma14205978>
- [21] Single-walled carbon nanotubes: structure, properties, applications, and health & safety. Carbon nanotube supplier – 97% of the global SWCNT market. (n.d.). Retrieved from <https://tuball.com/articles/single-walled-carbon-nanotubes>
- [22] Maduraiveeran, G., Sasidharan, M., & Ganesan, V. (2018). Electrochemical sensor and biosensor platforms based on advanced nanomaterials for biological and biomedical applications. *Biosensors and Bioelectronics*, 103, 113–129. <https://doi.org/10.1016/j.bios.2017.12.031>
- [23] Fritea, L., Banica, F., Costea, T., Moldovan, L., Dobjanschi, L., Muresan, M., & Cavalu, S. (2021). Metal Nanoparticles and Carbon-Based Nanomaterials for Improved Performances of Electrochemical (Bio)Sensors with Biomedical Applications. *Materials*, 14(21), 6319. <https://doi.org/10.3390/ma14216319>
- [24] Carbon nanotubes. (n.d.). Retrieved from <https://www.understandingnano.com/what-are-carbon-nanotubes.html>
- [25] Koutsogiannis, P., Thomou, E., Stamatis, H., Gournis, D., & Rudolf, P. (2020). Advances in fluorescent carbon dots for biomedical applications. *Advances in Physics: X*, 5(1), 1758592. <https://doi.org/10.1080/23746149.2020.1758592>
- [26] Kurian, M., & Paul, A. (2021). Recent trends in the use of green sources for carbon dot synthesis—A short review. *Carbon Trends*, 3, 100032. <https://doi.org/10.1016/j.cartre.2021.100032>
- [27] Nemčková, K., & Labuda, J. (2021). Advanced materials-integrated electrochemical sensors as promising medical diagnostics tools: A review. *Materials Science and Engineering: C*, 120, 111751. <https://doi.org/10.1016/j.msec.2020.111751>
- [28] Ławkowska, K., Pokrywczyńska, M., Koper, K., Kluth, L. A., Drewa, T., & Adamowicz, J. (2021). Application of graphene in tissue engineering of the nervous system. *International Journal of Molecular Sciences*, 23(1), 33. <https://doi.org/10.3390/ijms23010033>
- [29] Bellier, N., Baipaywad, P., Ryu, N., Lee, J. Y., & Park, H. (2022). Recent biomedical advancements in graphene oxide- and reduced graphene oxide-based nanocomposite nanocarriers. *Biomaterials Research*, 26(1). <https://doi.org/10.1186/s40824-022-00313-2>
- [30] Curreri, A. M., Mitragotri, S., & Tanner, E. E. L. (2021). Recent advances in ionic liquids in biomedicine. *Advanced Science*, 8(17), 2004819. <https://doi.org/10.1002/advs.202004819>

- [31] Yang, N., Gong, F., Zhou, Y., Qiao, Y., & Cheng, L. (2022). Liquid metals: Preparation, surface engineering, and biomedical applications. *Coordination Chemistry Reviews*, 471, 214731. <https://doi.org/10.1016/j.ccr.2022.214731>
- [32] Su et al., (2020). Printable, highly sensitive flexible temperature sensors for human body temperature monitoring: a review. *Nanoscale Research Letters*, 15(1). <https://doi.org/10.1186/s11671-020-03428-4>
- [33] Nan et al., (2022). Review of Flexible Wearable Sensor Devices for Biomedical Application. *Micromachines*, 13(9), 1395. <https://doi.org/10.3390/mi13091395>
- [34] Wang, B., Zhang, W., Zhao, F., Yu, W. W., Elezzabi, A. Y., Liu, L., & Li, H. (2022). An overview of recent progress in the development of flexible electrochromic devices. *Nano Materials Science*. <https://doi.org/10.1016/j.nanoms.2022.08.002>
- [35] Hine, P. J., Astruc, A., & Ward, I. M. (2004). Hot compaction of polyethylene naphthalate. *Journal of Applied Polymer Science*, 93(2), 796–802. <https://doi.org/10.1002/app.20517>
- [36] Briand, D., Oprea, A., Courbat, J., & Barsan, N. (2011). Making environmental sensors on plastic foil. *Materials Today*, 14(9), 416–423. [https://doi.org/10.1016/s1369-7021\(11\)70186-9](https://doi.org/10.1016/s1369-7021(11)70186-9)
- [37] Li, Y., Mao, Y., Xiao, C., Xu, X., & Li, X. (2020). Flexible pH sensor based on a conductive PANI membrane for pH monitoring. *RSC Advances*, 10(1), 21–28. <https://doi.org/10.1039/c9ra09188b>
- [38] Chen, Y., Wu, C., Tsai, J., & Wang, G. (2012). Electrochemical impedimetric biosensor based on a nanostructured polycarbonate substrate. *International Journal of Nanomedicine*, 133. <https://doi.org/10.2147/ijn.s27225>
- [39] Wu, W., Zhong, X., Wang, W., Miao, Q., & Zhu, J. (2010). Flexible PDMS-based three-electrode sensor. *Electrochemistry Communications*, 12(11), 1600–1604. <https://doi.org/10.1016/j.elecom.2010.09.005>
- [40] Yan, T., Zhang, G., Chai, H., Qu, L., & Zhang, X. (2021). Flexible biosensors based on colorimetry, fluorescence, and electrochemistry for Point-of-Care testing. *Frontiers in Bioengineering and Biotechnology*, 9. <https://doi.org/10.3389/fbioe.2021.753692>
- [41] Karim, K., Lamaoui, A., & Amine, A. (2023). Paper-based optical sensors paired with smartphones for biomedical analysis. *Journal of Pharmaceutical and Biomedical Analysis*, 225, 115207. <https://doi.org/10.1016/j.jpba.2022.115207>
- [42] Benjamin, S. R., De Lima, F., Nascimento, V. a. D., De Andrade, G. M., & Oriá, R. B. (2023). Advancement in Paper-Based electrochemical biosensing and emerging diagnostic methods. *Biosensors*, 13(7), 689. <https://doi.org/10.3390/bios13070689>
- [43] Arena, A., Donato, N., Saitta, G., Bonavita, A., Rizzo, G., & Neri, G. (2010). Flexible ethanol sensors on glossy paper substrates operating at room temperature. *Sensors and Actuators B-chemical*, 145(1), 488–494. <https://doi.org/10.1016/j.snb.2009.12.053>
- [44] Cho, S., Chang, T., Yu, T., & Lee, C. H. (2022). Smart electronic textiles for wearable sensing and display. *Biosensors*, 12(4), 222. <https://doi.org/10.3390/bios12040222>
- [45] Wang, X., Zhang, M., Zhang, L., Xu, J., Xiao, X., & Zhang, X. (2022). Inkjet-printed flexible sensors: From function materials, manufacture process, and applications perspective. *Materials Today Communications*, 31, 103263. <https://doi.org/10.1016/j.mtcomm.2022.103263>
- [46] Magliulo, M., Mulla, M. Y., Singh, M., Macchia, E., Tiwari, A., Torsi, L., & Manoli, K. (2015). Printable and flexible electronics: from TFTs to bioelectronic devices. *Journal of Materials Chemistry C*, 3(48), 12347–12363. <https://doi.org/10.1039/c5tc02737c>

- [47] Khan, S., Ali, S., & Bermak, A. (2019). Recent developments in printing flexible and wearable sensing electronics for healthcare applications. *Sensors*, *19*(5), 1230. <https://doi.org/10.3390/s19051230>
- [48] Herbert, R., Lim, H., Park, S., Kim, J. H., & Yeo, W. (2021). Recent advances in printing technologies of nanomaterials for implantable wireless systems in health monitoring and diagnosis. *Advanced Healthcare Materials*, *10*(17), 2100158. <https://doi.org/10.1002/adhm.202100158>
- [49] Gonzalez-Macia, L., Morrin, A., Smyth, M. R., & Killard, A. J. (2010). Advanced printing and deposition methodologies for the fabrication of biosensors and biodevices. *Analyst*, *135*(5), 845. <https://doi.org/10.1039/b916888e>
- [50] Cruz, S. M. F., Rocha, L. A., & Viana, J. C. (2018). Printing technologies on flexible substrates for printed electronics. In InTech eBooks. <https://doi.org/10.5772/intechopen.76161>
- [51] Gong, X., Huang, K., Wu, Y., & Zhang, X. (2022). Recent progress on screen-printed flexible sensors for human health monitoring. *Sensors and Actuators A-physical*, *345*, 113821. <https://doi.org/10.1016/j.sna.2022.113821>
- [52] Jeerapan, I., & Khumngern, S. (2023). Printed Devices for wearable biosensors: laboratory to emerging markets. *IEEE Journal on Flexible Electronics*, *1*. <https://doi.org/10.1109/jflex.2023.3272624>
- [53] Dkhar, D. S., Kumari, R., Malode, S. J., Shetti, N. P., & Chandra, P. (2023). Integrated lab-on-a-chip devices: Fabrication methodologies, transduction system for sensing purposes. *Journal of Pharmaceutical and Biomedical Analysis*, *223*, 115120. <https://doi.org/10.1016/j.jpba.2022.115120>
- [54] Zub, K., Hoepfner, S., & Schubert, U. S. (2022). Inkjet printing and 3D printing strategies for biosensing, analytical, and diagnostic applications. *Advanced Materials*, *34*(31), 2105015. <https://doi.org/10.1002/adma.202105015>
- [55] Zhang, X., Pu, Z., Su, X., Li, C., Zheng, H., & Li, D. (2023). Flexible organic field-effect transistors-based biosensors: progress and perspectives. *Analytical and Bioanalytical Chemistry*, *415*(9), 1607–1625. <https://doi.org/10.1007/s00216-023-04553-6>
- [56] Mikolajek, M., Friederich, A., Bauer, W., & Binder, J. R. (2015c). Requirements to ceramic suspensions for inkjet printing. ResearchGate. Retrieved from https://www.researchgate.net/publication/273322282_Requirements_to_Ceramic_Suspensions_for_Inkjet_Printing#fullTextFileContent
- [57] Hussain, A., Abbas, N., & Ali, A. (2022). Inkjet Printing: a viable technology for biosensor fabrication. *Chemosensors*, *10*(3), 103. <https://doi.org/10.3390/chemosensors10030103>
- [58] How does thermal inkjet printing work? (n.d.). InkJet, Inc. Retrieved from <https://www.inkjetinc.com/resources/how-does-thermal-inkjet-printing-work-ij>
- [59] Li, J., Rossignol, F., & Macdonald, J. (2015). Inkjet printing for biosensor fabrication: combining chemistry and technology for advanced manufacturing. *Lab on a Chip*, *15*(12), 2538–2558. <https://doi.org/10.1039/c5lc00235d>
- [60] Phillips, T. (2016). Introduction to industrial inkjet printing — *IMI Europe - high quality inkjet conferences and courses*. IMI Europe. Retrieved from <https://imieurope.com/inkjet-blog/2016/2/8/industrial-inkjet-printing>
- [61] What you should know about inkjet technology - Edge Colours. (2019, February 18). Retrieved from <https://edgecolours.com/what-you-should-know-about-inkjet-technology/>

- [62] Du, X., Wankhede, S. P., Prasad, S., Shehri, A. A., Morse, J., & Lakal, N. (2022). A review of inkjet printing technology for personalized-healthcare wearable devices. *Journal of Materials Chemistry C*, 10(38), 14091–14115. <https://doi.org/10.1039/d2tc02511f>
- [63] Lan, L., Zou, J., Jiang, C., Liu, B., Wang, L., & Peng, J. (2017c). Inkjet printing for electroluminescent devices: emissive materials, film formation, and display prototypes. *Frontiers of Optoelectronics*, 10(4), 329–352. <https://doi.org/10.1007/s12200-017-0765-x>
- [64] Lin, Z., Wu, G., Zhao, L., & Lai, K. W. C. (2019b). Carbon Nanomaterial-Based Biosensors: A Review of Design and Applications. *IEEE Nanotechnology Magazine*, 13(5), 4–14. <https://doi.org/10.1109/mnano.2019.2927774>
- [65] Yang, X., & Cheng, H. (2020). Recent developments of flexible and stretchable electrochemical biosensors. *Micromachines*, 11(3), 243. <https://doi.org/10.3390/mi11030243>
- [66] Simonenko et al., (2022). Printing Technologies as an Emerging approach in Gas Sensors: Survey of literature. *Sensors*, 22(9), 3473. <https://doi.org/10.3390/s22093473>
- [67] ECKART GmbH. (2020, April 16). What is Offset Printing? - Tutorial from ECKART [Video file]. Retrieved from <https://www.youtube.com/watch?v=HuQeBmzpyhU>
- [68] Agarwala, S., Goh, G. L., & Yeong, W. Y. (2017b). Optimizing aerosol jet printing process of silver ink for printed electronics. *IOP Conference Series*, 191, 012027. <https://doi.org/10.1088/1757-899x/191/1/012027>
- [69] Salim, A., & Lim, S. (2019). Recent advances in noninvasive flexible and wearable wireless biosensors. *Biosensors and Bioelectronics*, 141, 111422. <https://doi.org/10.1016/j.bios.2019.111422>
- [70] Patel, S., Park, H., Bonato, P., Chan, L., & Rodgers, M. M. (2012). A review of wearable sensors and systems with application in rehabilitation. *Journal of Neuroengineering and Rehabilitation*, 9(1). <https://doi.org/10.1186/1743-0003-9-21>
- [71] Qiao, L., Benzigar, M. R., Subramony, J. A., Lovell, N. H., & Liu, G. (2020). Advances in sweat wearables: sample extraction, Real-Time biosensing, and flexible platforms. *ACS Applied Materials & Interfaces*, 12(30), 34337–34361. <https://doi.org/10.1021/acsami.0c07614>
- [72] Lou, Z., Wang, L., Jiang, K., Wei, Z., & Shen, G. (2020). Reviews of wearable healthcare systems: Materials, devices and system integration. *Materials Science and Engineering R*, 140, 100523. <https://doi.org/10.1016/j.mser.2019.100523>
- [73] Ray et al., (2019). Bio-Integrated Wearable Systems: A comprehensive review. *Chemical Reviews*, 119(8), 5461–5533. <https://doi.org/10.1021/acs.chemrev.8b00573>
- [74] Nam, D., Min, J., & Park, K. (2021). Next-Generation Wearable Biosensors Developed with Flexible Bio-Chips. *Micromachines*, 12(1), 64. <https://doi.org/10.3390/mi12010064>
- [75] Ersman, et al., (2019). All-printed large-scale integrated circuits based on organic electrochemical transistors. *Nature Communications*, 10(1). <https://doi.org/10.1038/s41467-019-13079-4>
- [76] Yang, Y., & Gao, W. (2019). Wearable and flexible electronics for continuous molecular monitoring. *Chemical Society Reviews*, 48(6), 1465–1491. <https://doi.org/10.1039/c7cs00730b>
- [77] Li, X., Zeng, X., Xia, F., Jin, W., Liu, Y., & Hu, Y. (2020). Recent advances in flexible and stretchable sensing systems: From the perspective of system integration. *ACS Nano*, 14(6), 6449–6469. <https://doi.org/10.1021/acsnano.0c01164>
- [78] Zulqarnain, M., Stanzione, S., Rathinavel, G., Smout, S., Willegems, M., Myny, K., & Cantatore, E. (2020). A flexible ECG patch compatible with NFC RF communication. *Npj Flexible Electronics*, 4(1). <https://doi.org/10.1038/s41528-020-0077-x>

- [79] Park et al., (2023). Fully Screen-Printed PI/PEG blends enabled patternable electrodes for scalable manufacturing of Skin-Conformal, stretchable, wearable electronics. *ACS Applied Materials & Interfaces*, 15(1), 2092–2103. <https://doi.org/10.1021/acsami.2c17653>
- [80] Chen, S., Qi, J., Fan, S., Qiao, Z., Yeo, J. C., & Lim, C. T. (2021). Flexible wearable sensors for cardiovascular health monitoring. *Advanced Healthcare Materials*, 10(17), 2100116. <https://doi.org/10.1002/adhm.202100116>
- [81] Kwak, Y. H., Kim, W., Park, K. B., Kim, K., & Seo, S. (2017). Flexible heartbeat sensor for wearable device. *Biosensors and Bioelectronics*, 94, 250–255. <https://doi.org/10.1016/j.bios.2017.03.016>
- [82] Lee, J. W., Choi, Y. J., Jang, J. H., Yeom, S. H., Lee, W., & Ju, B. K. (2020). High sensitivity flexible paper temperature sensor and body-attachable patch for thermometers. *Sensors and Actuators A-physical*, 313, 112205. <https://doi.org/10.1016/j.sna.2020.112205>
- [83] Zafar, H., Channa, A., Jeoti, V., & Stojanovic, G. (2022). Comprehensive review on wearable Sweat-Glucose sensors for continuous glucose monitoring. *Sensors*, 22(2), 638. <https://doi.org/10.3390/s22020638>
- [84] Zhang et al., (2023). Flexible and wearable biosensors for monitoring health conditions. *Biosensors*, 13(6), 630. <https://doi.org/10.3390/bios13060630>
- [85] Zhang et al., (2022). Wearable biosensors for human fatigue diagnosis: A review. *Bioengineering & Translational Medicine*, 8(1). <https://doi.org/10.1002/btm2.10318>
- [86] Zafar, H., Channa, A., Jeoti, V., & Stojanovic, G. (2022b). Comprehensive review on wearable Sweat-Glucose sensors for continuous glucose monitoring. *Sensors*, 22(2), 638. <https://doi.org/10.3390/s22020638>
- [87] Donati, P., Pomili, T., Boselli, L., & Pompa, P. P. (2020). Colorimetric nanoplasmonics to spot hyperglycemia from saliva. *Frontiers in Bioengineering and Biotechnology*, 8. <https://doi.org/10.3389/fbioe.2020.601216>
- [88] Chen, C., Dong, Z., Shen, J., Chen, H., Zhu, Y., & Zhu, Z. (2018). 2D photonic crystal hydrogel sensor for tear glucose monitoring. *ACS Omega*, 3(3), 3211–3217. <https://doi.org/10.1021/acsomega.7b02046>
- [89] Zhang, Z., Azizi, M., Lee, M., Davidowsky, P., Lawrence, P., & Abbaspourrad, A. (2019). A versatile, cost-effective, and flexible wearable biosensor for in situ and ex situ sweat analysis, and personalized nutrition assessment. *Lab on a Chip*, 19(20), 3448–3460. <https://doi.org/10.1039/c9lc00734b>
- [90] Choi, J., Ghaffari, R., Baker, L. B., & Rogers, J. A. (2018). Skin-interfaced systems for sweat collection and analytics. *Science Advances*, 4(2). <https://doi.org/10.1126/sciadv.aar3921>
- [91] Tang et al., (2021). Wearable sensors and systems for Wound Healing-Related PH and temperature detection. *Micromachines*, 12(4), 430. <https://doi.org/10.3390/mi12040430>
- [92] Hussin, H., Sooin, N., Hatta, S. F. W. M., Rezali, F. a. M., & Wahab, Y. A. (2021). Review—Recent progress in the Diversity of InkJet-Printed Flexible Sensor Structures in Biomedical Engineering Applications. *Journal of the Electrochemical Society*, 168(7), 077508. <https://doi.org/10.1149/1945-7111/ac0e4b>
- [93] Legner, C., Kalwa, U., Patel, V., Chesmore, A., & Pandey, S. (2019). Sweat sensing in the smart wearables era: Towards integrative, multifunctional and body-compliant perspiration analysis. *Sensors and Actuators A-physical*, 296, 200–221. <https://doi.org/10.1016/j.sna.2019.07.020>

- [94] Rodrigues, D. S. S., Barbosa, A. I., Rebelo, R., Kwon, I. K., Reis, R. L., & Correlo, V. M. (2020). Skin-Integrated wearable systems and Implantable biosensors: A Comprehensive review. *Biosensors*, *10*(7), 79. <https://doi.org/10.3390/bios10070079>
- [95] Alberto, J., Leal, C., Fernandes, C. P., Lopes, P. A., Paisana, H., De Almeida, A. T., & Tavakoli, M. (2020). Fully Untethered Battery-free Biomonitoring Electronic Tattoo with Wireless Energy Harvesting. *Scientific Reports*, *10*(1). <https://doi.org/10.1038/s41598-020-62097-6>
- [96] Kim, C. H., Lee, D. H., Youn, J., Lee, H., & Jeong, J. (2021b). Simple and cost-effective microfabrication of flexible and stretchable electronics for wearable multi-functional electrophysiological monitoring. *Scientific Reports*, *11*(1). <https://doi.org/10.1038/s41598-021-94397-w>
- [97] Diamond, D., Coyle, S., Scarmagnani, S., & Hayes, J. F. (2008). Wireless sensor networks and Chemo-/Biosensing. *Chemical Reviews*, *108*(2), 652–679. <https://doi.org/10.1021/cr0681187>
- [98] Applications of polyimides (PI). (n.d.). Retrieved from <https://omnexus.specialchem.com/selection-guide/polyimide-pi-plastic/popular-applications>
- [99] Liang, T., & Yuan, Y. J. (2016). Wearable medical monitoring systems based on wireless networks: A Review. *IEEE Sensors Journal*, *1*. <https://doi.org/10.1109/jsen.2016.2597312>
- [100] Teymourian, H., Mercier, P. P., & Wang, J. (2022). An integrated wearable microneedle array for the continuous monitoring of multiple biomarkers in interstitial fluid. *Nature Biomedical Engineering*, *6*(11), 1214–1224. <https://doi.org/10.1038/s41551-022-00887-1>
- [101] Rao, M., Newe, T., Grout, I., Lewis, & Mathur, A. (2015). FPGA Based Real Time “Secure” Body Temperature Monitoring Suitable for WBSN. *IEEE International Conference on Computer and Information Technology; Ubiquitous Computing and Communications; Dependable, Autonomic and Secure Computing; Pervasive Intelligence and Computing*. <https://doi.org/10.1109/cit/iucc/dasc/picom.2015.22>
- [102] Ghafar-Zadeh, E. (2015). Wireless integrated biosensors for Point-of-Care diagnostic applications. *Sensors*, *15*(2), 3236–3261. <https://doi.org/10.3390/s150203236>
- [103] Rashid, R. A., Arifin, S. H. S., Rahim, M. K. A., Sarijari, M. A., & Mahalin, N. H. (2008). Home healthcare via wireless biomedical sensor network. *IEEE INTERNATIONAL RF AND MICROWAVE CONFERENCE PROCEEDINGS*. <https://doi.org/10.1109/rfm.2008.4897437>
- [104] Nag, A., Mukhopadhyay, S. C., & Kosel, J. (2017). Wearable Flexible Sensors: A review. *IEEE Sensors Journal*, *17*(13), 3949–3960. <https://doi.org/10.1109/jsen.2017.2705700>
- [105] Rahim, M. R. A., Rashid, R. A., Ariffin, S. H. S., Fisal, N., Sarijari, M. A., & Hamid, M. K. A. (2011). Testbed design for Wireless Biomedical Sensor Network (WBSN) application. *International Conference on Computer Applications and Industrial Electronics (ICCAIE) 2011*. <https://doi.org/10.1109/iccaie.2011.6162146>
- [106] Javaid, N., Ahmad, A., Khan, Y., Khan, Z. A., & Alghamdi, T. A. (2014). A relay based routing protocol for wireless In-Body sensor networks. *Wireless Personal Communications*, *80*(3), 1063–1078. <https://doi.org/10.1007/s11277-014-2071-x>
- [107] Phan et al., (2022). A Flexible, Wearable, and Wireless Biosensor Patch with Internet of Medical Things Applications. *Biosensors*, *12*(3), 139. <https://doi.org/10.3390/bios12030139>
- [108] Chen, X., Meng, M. Q., & Ren, H. (2005). Design of Sensor Node Platform for Wireless Biomedical Sensor Networks. *IEEE Engineering in Medicine and Biology 27th Annual Conference*. <https://doi.org/10.1109/iembs.2005.1615510>
- [109] Wang, X., Liu, Z., & Zhang, T. (2017). Flexible sensing electronics for Wearable/Attachable health Monitoring. *Small*, *13*(25), 1602790. <https://doi.org/10.1002/sml.201602790>

- [110] Yang, M., Li, M., Cheng, J., & Wang, H. (2021). A movable type bioelectronics printing technology for modular fabrication of biosensors. *Scientific Reports*, 11(1). <https://doi.org/10.1038/s41598-021-01741-1>
- [111] Christoe, M. J., Han, J., & Kalantar-Zadeh, K. (2019). Telecommunications and data processing in flexible electronic systems. *Advanced Materials and Technologies*, 5(1), 1900733. <https://doi.org/10.1002/admt.201900733>
- [112] Maier, A., Sharp, A., & Vagapov, Y. (2017). Comparative analysis and practical implementation of the ESP32 microcontroller module for the internet of things. *7th IEEE Int. Conference on Internet Technologies and Applications ITA-17, Wrexham, UK*. <https://doi.org/10.1109/itecha.2017.8101926>
- [113] Mostafalu, P., Lenk, W., Dokmeci, M. R., Ziaie, B., Khademhosseini, A., & Sonkusale, S. (2015). Wireless flexible smart bandage for continuous monitoring of wound oxygenation. *IEEE Transactions on Biomedical Circuits and Systems*, 9(5), 670–677. <https://doi.org/10.1109/tbcas.2015.2488582>
- [114] Fu, Y., & Guo, J. (2018). Blood cholesterol monitoring with smartphone as miniaturized electrochemical analyzer for cardiovascular disease prevention. *IEEE Transactions on Biomedical Circuits and Systems*, 12(4), 784–790. <https://doi.org/10.1109/tbcas.2018.2845856>
- [115] Benatti et al., (2015). A versatile embedded platform for EMG acquisition and gesture recognition. *IEEE Transactions on Biomedical Circuits and Systems*, 9(5), 620–630. <https://doi.org/10.1109/tbcas.2015.2476555>
- [116] Park, Y. G., & S, L. (2019). Recent progress in wireless sensors for wearable electronics. *Sensors*, 19(20), 4353. <https://doi.org/10.3390/s19204353>
- [117] Li et al., (2018). Epidermis-Inspired ultrathin 3D cellular sensor array for Self-Powered biomedical monitoring. *ACS Applied Materials & Interfaces*, 10(48), 41070–41075. <https://doi.org/10.1021/acsami.8b14514>
- [118] Yáñez-Sedeño, P., Campuzano, S., & Pingarrón, J. M. (2020). Screen-Printed Electrodes: Promising paper and wearable transducers for (Bio)Sensing. *Biosensors*, 10(7), 76. <https://doi.org/10.3390/bios10070076>
- [119] Zhao, L., Li, H., Meng, J., & Li, Z. (2019). The recent advances in self-powered medical information sensors. *InfoMat*, 2(1), 212–234. <https://doi.org/10.1002/inf2.12064>
- [120] Nasri, F., Moussa, N., & Mtibaa, A. (2014). Intelligent Mobile System for Healthcare Based On WSN and Android. *International Journal of Computer Trends and Technology*, 12(4), 187–192. <https://doi.org/10.14445/22312803/ijctt-v12p137>
- [121] Al-Fuqaha, A., Guizani, M., Mohammadi, M., Aledhari, M., & Ayyash, M. (2015). Internet of Things: A survey on enabling technologies, protocols, and applications. *IEEE Communications Surveys and Tutorials*, 17(4), 2347–2376. <https://doi.org/10.1109/comst.2015.2444095>
- [122] Nasri, F., & Mtibaa, A. (2017). Smart Mobile Healthcare System based on WBSN and 5G. *International Journal of Advanced Computer Science and Applications*, 8(10). <https://doi.org/10.14569/ijacsa.2017.081020>
- [123] Naghdi, T., Ardalan, S., Adib, Z. A., Sharifi, A. R., & Golmohammadi, H. (2023). Moving toward smart biomedical sensing. *Biosensors and Bioelectronics*, 223, 115009. <https://doi.org/10.1016/j.bios.2022.115009>
- [124] Parate, R. K., & Sharma, S. J. (2020). Design of a Client Server Based Body Signal Monitoring System. *International Journal of Engineering Research and Applications*, 10(7). Retrieved from <https://www.ijera.com/papers/vol10no7/Series-7/H1007074649.pdf>

- [125] Lalithadevi, B., & Krishnaveni. (2021). An Internet of Things(IoT) Based Intelligent Framework for Healthcare – A Survey. *3rd International Conference on Signal Processing and Communication (ICPSC)*. <https://doi.org/10.1109/icspc51351.2021.9451739>
- [126] Elankavi, R., Krishnamoorthy, P., Jose, J. J., & Surekha, R. (2022). Smart IoT based Human Well-being Monitoring in Health Care System. *2022 3rd International Conference on Electronics and Sustainable Communication Systems (ICESC)*. <https://doi.org/10.1109/icesc54411.2022.9885413>
- [127] Orpa, T. H., Ahnaf, A., Ovi, T. B., & Rizu, M. I. (2022). An IoT Based Healthcare Solution With ESP32 Using Machine Learning Model. *4th International Conference on Sustainable Technologies for Industry 4.0 (STI)*. <https://doi.org/10.1109/sti56238.2022.10103231>
- [128] OpenSystems Media. (n.d.). How IoT is Transforming the Healthcare Industry - Embedded Computing Design. Retrieved from <https://embeddedcomputing.com/application/healthcare/telehealth-healthcare-iot/how-iot-is-transforming-the-healthcare-industry>
- [129] Kumar, E. M., Zahoor, A., Sruthi, C. S. L., Vaishnavi, K., & Chowdary, V. R. (2023). Smart Wearable Device to Prevent Accidents Caused by Medical Emergencies. *Proceedings of the 7th International Conference on Computing Methodologies and Communication (ICCMC-2023)*. <https://doi.org/10.1109/iccmc56507.2023.10084266>
- [130] Phan et al., (2022). A Flexible, Wearable, and Wireless Biosensor Patch with Internet of Medical Things Applications. *Biosensors*, *12*(3), 139. <https://doi.org/10.3390/bios12030139>
- [131] Abdullah, M. I., Raya, L., Norazman, M. a. A., & Suprihadi, U. (2022). Covid-19 Patient Health Monitoring System Using IoT. *IEEE 13th Control and System Graduate Research Colloquium (ICSGRC)*. <https://doi.org/10.1109/icsgrc55096.2022.9845162>
- [132] Ali, F. I., Ali, T. E., & Al_Dahan, Z. T. (2023). Private Backend Server Software-Based Telehealthcare Tracking and Monitoring System. *International Journal of Online and Biomedical Engineering*, *19*(01), 119–134. <https://doi.org/10.3991/ijoe.v19i01.32433>
- [133] Abilesh, K. S., Naveen, V., Pozhilan, S., Shanmugaraja, P., & Raffik, R. (2023). AI Health – IoT based Smart Medicine Box. *2nd International Conference on Advancements in Electrical, Electronics, Communication, Computing and Automation (ICAECA)*. <https://doi.org/10.1109/ICAECA56562.2023.10200103>
- [134] ESP32-WROOM-32. (2023). Retrieved September 2, 2023, from https://www.espressif.com/sites/default/files/documentation/esp32-wroom-32_datasheet_en.pdf
- [135] Goparaju, S. U. N., Vaddhiparthi, S. S. S., Pradeep, C. H., Vattam, A., & Gangadharan, D. (2021). Design of an IoT System for Machine Learning Calibrated TDS Measurement in Smart Campus. *IEEE 7th World Forum on Internet of Things (WF-IoT)*. <https://doi.org/10.1109/wf-iot51360.2021.9595057>
- [136] Bonek et al., (2020). Development of a Flexible and Wireless ECG Monitoring Device. *IEEE SENSORS*. <https://doi.org/10.1109/sensors47125.2020.9278904>
- [137] ESP32-WROOM-32D. (2023). Retrieved September 2, 2023, from https://www.espressif.com/sites/default/files/documentation/esp32-wroom-32d_esp32-wroom-32u_datasheet_en.pdf
- [138] ESP32-WROOM-32D. (2023). Retrieved September 2, 2023, from https://www.espressif.com/sites/default/files/documentation/esp32-wroom-32d_esp32-wroom-32u_datasheet_en.pdf
- [139] Vilela, D., Romeo, A., & Sanchez, S. (2016). Flexible sensors for biomedical technology. *Lab on a Chip*, *16*(3), 402–408. <https://doi.org/10.1039/c5lc90136g>

- [140] Cui, Z., Poblete, F. R., & Zhu, Y. (2019). Tailoring the Temperature Coefficient of Resistance of Silver Nanowire Nanocomposites and their Application as Stretchable Temperature Sensors. *ACS Applied Materials & Interfaces*, 11(19), 17836–17842. <https://doi.org/10.1021/acsami.9b04045>
- [141] Shin et al., (2019). Sensitive Wearable Temperature Sensor with Seamless Monolithic Integration. *Advanced Materials*, 32(2), 1905527. <https://doi.org/10.1002/adma.201905527>
- [142] Han et al., (2018). Battery-free, wireless sensors for full-body pressure and temperature mapping. *Science Translational Medicine*, 10(435). <https://doi.org/10.1126/scitranslmed.aan4950>
- [143] Liu, R., He, L., Cao, M., Sun, Z., Zhu, R., & Li, Y. (2021). Flexible temperature sensors. *Frontiers in Chemistry*, 9. <https://doi.org/10.3389/fchem.2021.539678>
- [144] Flexible IoT Temperature patch for healthcare Application - Innovation Hub@HK. (n.d.). Retrieved from <https://www.innovationhub.hk/article/flexible-iot-temperature-patch-for-healthcare-application>
- [145] Yun, S., Lee, J. H., Liu, J., & Kim, C. (2019). A flexible wireless sensor patch for Real-Time monitoring of heart rate and body temperature. *IEICE Transactions on Information and Systems*, E102.D(5), 1115–1118. <https://doi.org/10.1587/transinf.2018edl8167>
- [146] Song, C., Zeng, P., Wang, Z., Zhang, H., & Huang, Y. (2018). Wearable continuous body temperature measurement using multiple artificial neural networks. *IEEE Transactions on Industrial Informatics*, 14(10), 4395–4406. <https://doi.org/10.1109/tii.2018.2793905>
- [147] Li, Q., Zhang, L. N., Tao, X., & Ding, X. (2017). Review of flexible temperature sensing networks for wearable Physiological Monitoring. *Advanced Healthcare Materials*, 6(12), 1601371. <https://doi.org/10.1002/adhm.201601371>
- [148] Uth, M., Koch, J., & Sattler, F. A. (2016). Body core Temperature sensing: challenges and new sensor technologies. *Procedia Engineering*, 168, 89–92. <https://doi.org/10.1016/j.proeng.2016.11.154>
- [149] Campbell, I. (2011b). Body temperature and its regulation. *Anaesthesia & Intensive Care Medicine*, 12(6), 240–244. <https://doi.org/10.1016/j.mpaic.2011.03.002>
- [150] How to convert skin temperature to core temperature? (n.d.). Retrieved from <https://biology.stackexchange.com/questions/57211/how-to-convert-skin-temperature-to-core-temperature>
- [151] Huan, J., Bernstein, J. S., Difuntorum, P., Masna, N. V. R., Gravenstein, N., Bhunia, S., & Mandal, S. (2022). A wearable skin temperature monitoring system for early detection of infections. *IEEE Sensors Journal*, 22(2), 1670–1679. <https://doi.org/10.1109/jsen.2021.3131500>
- [152] Lu et al., (2021). Wireless and Flexible Skin Moisture and Temperature Sensor Sheets toward the Study of Thermoregulator Center. *Advanced Healthcare Materials*, 10(17), 2100103. <https://doi.org/10.1002/adhm.202100103>
- [153] Draper, J. W., & Boag, J. W. (1971). The calculation of skin temperature distributions in thermography. *Physics in Medicine and Biology*, 16(2), 201–211. <https://doi.org/10.1088/0031-9155/16/2/301>
- [154] Arens, E., & Zhang, H. (2006). The skin's role in human thermoregulation and comfort. In *Elsevier eBooks* (pp. 560–602). <https://doi.org/10.1533/9781845692261.3.560>
- [155] Park et al., (2021). Highly Sensitive On-Skin Temperature Sensors Based on Biocompatible Hydrogels with Thermoresponsive Transparency and Resistivity. *Advanced Healthcare Materials*, 10(14), 2100469. <https://doi.org/10.1002/adhm.202100469>

- [156] Metzmacher, H., Wölki, D., Schmidt, C., Frisch, J., & Van Treeck, C. (2018). Real-time human skin temperature analysis using thermal image recognition for thermal comfort assessment. *Energy and Buildings*, 158, 1063–1078. <https://doi.org/10.1016/j.enbuild.2017.09.032>
- [157] Li, F., Xue, H., Lin, X., Zhao, H., & Zhang, T. (2022). Wearable Temperature Sensor with High Resolution for Skin Temperature Monitoring. *ACS Applied Materials & Interfaces*, 14(38), 43844–43852. <https://doi.org/10.1021/acsami.2c15687>
- [158] McNeill et al., (2017). Wearable wireless sensor patch for continuous monitoring of skin temperature, pressure, and relative humidity. *IEEE International Symposium on Circuits and Systems (ISCAS)*. <https://doi.org/10.1109/iscas.2017.8050898>
- [159] Jeon, J. H., Lee, H., & Bao, Z. (2012). Flexible wireless temperature sensors based on NI Microparticle-Filled binary polymer composites. *Advanced Materials*, 25(6), 850–855. <https://doi.org/10.1002/adma.201204082>
- [160] Kuzubasoglu, B. A., & Bahadir, S. K. (2020). Flexible temperature sensors: A review. *Sensors and Actuators A-physical*, 315, 112282. <https://doi.org/10.1016/j.sna.2020.112282>
- [161] Storr, W. (2022). Wheatstone Bridge. *Basic Electronics Tutorials*. Retrieved from <https://www.electronics-tutorials.ws/blog/wheatstone-bridge.html>
- [162] Neella, N., Gaddam, V., Nayak, M. M., Dinesh, N. S., & Rajanna, K. (2017). Scalable fabrication of highly sensitive flexible temperature sensors based on silver nanoparticles coated reduced graphene oxide nanocomposite thin films. *Sensors and Actuators A-physical*, 268, 173–182. <https://doi.org/10.1016/j.sna.2017.11.011>
- [163] Staff, E. (2022, July 25). Optimizing thermistor-based temperature sensing systems: Challenges. Embedded.com. Retrieved from <https://www.embedded.com>
- [164] Crosby, P. H. N., & Netravali, A. N. (2022). Green Thermochromic Materials: A Brief Review. *Advanced Sustainable Systems*, 6(9), 2200208. <https://doi.org/10.1002/adsu.202200208>
- [165] Christie, R., Robertson, S., & Taylor, S. (2012). Design concepts for a temperature-sensitive environment using thermochromic colour change. *JAIC - Journal of the International Colour Association*, 1. Retrieved from <http://aic-colour-journal.org/index.php/JAIC/article/view/80>
- [166] Christie, R., Robertson, S., & Taylor, S. (2012). Design concepts for a temperature-sensitive environment using thermochromic colour change. *JAIC - Journal of the International Colour Association*, 1. Retrieved from <http://aic-colour-journal.org/index.php/JAIC/article/view/80>
- [167] Thiagalingam et al., (2005). A thermochromic dispersive electrode can measure the underlying skin temperature and prevent burns during radiofrequency ablation. *Journal of Cardiovascular Electrophysiology*, 16(7), 781–788. <https://doi.org/10.1111/j.1540-8167.2005.40747.x>
- [168] Xu et al., (2021). Multimode Visualization of Electronic Skin from Bioinspired Colorimetric Sensor. *ACS Applied Materials & Interfaces*, 13(25), 30205–30212. <https://doi.org/10.1021/acsami.1c07360>
- [169] Lee et al., (2020). User-Interactive thermotherapeutic electronic skin based on stretchable thermochromic strain sensor. *Advanced Science*, 7(17), 2001184. <https://doi.org/10.1002/advs.202001184>
- [170] Chen et al., (2018). A skin-like stretchable colorimetric temperature sensor. *Science China. Materials*, 61(7), 969–976. <https://doi.org/10.1007/s40843-018-9266-8>
- [171] Thermochromic Screen Printing Ink Black 31°C. (n.d.). Retrieved September 17, 2023, from <https://www.sfxco.uk/collections/products-for-screen-printing/products/thermochromic-screen-printing-ink-black-31-c>

- [172] Thermochromic Screen Printing Ink Black 47°C. (n.d.). Retrieved September 17, 2023, from <https://www.sfxco.uk/collections/products-for-screen-printing/products/thermochromic-screen-printing-ink-black-47-c>
- [173] Temperature responsive Thermochromic ink - Orange to Neon Yellow. (n.d.). Retrieved September 17, 2023, from <https://www.sfxco.uk/collections/products-for-screen-printing/products/thermochromic-acrylic-paint-orange-to-neon-yellow?variant=31581607460948>
- [174] Keithley 2612B - Dual-channel System SourceMeter SMU Instrument (200 V, 10 A Pulse). (n.d.). Retrieved September 17, 2023, from <https://www.tequipment.net/Keithley2612B.html>
- [175] WAINLUX K6. (n.d.). Retrieved September 17, 2023, from <https://www.wainlux.com/product/wainlux-k6/>
- [176] NovaCentrix. (n.d.). HPR-059 Carbon Black Ink - NovaCentrix. Retrieved September 18, 2023, from <https://www.novacentrix.com/product/hpr-059-carbon-black/>
- [177] NovaCentrix. (n.d.). HPS-FG77 Silver Nanoflake Ink - NovaCentrix. Retrieved September 18, 2023, from <https://www.novacentrix.com/product/hps-fg77-silver-nanoflake/>
- [178] Polyethylene terephthalate (PET) - Polymers - Research materials - Goodfellow. (n.d.). Retrieved September 18, 2023, from <https://www.goodfellow.com/information/larger-quantities/513/536/polymers/polyethylene-terephthalate-pet>
- [179] Kapton® HN Film 0.125mm thick 610mm coil W. (n.d.). Retrieved September 18, 2023, from <https://www.goodfellow.com/p/im30-fm-000150/kapton-hn-film>
- [180] NÜVE – Dry Heat Sterilizers / Ovens FN 400/500. (n.d.). Retrieved September 18, 2023, from <https://nuve.com.tr/en/products/dry-heat-sterilizers-ovens>
- [181] Ever Bright HK - S-200HF Pneumatic flat screen printer. (n.d.). Retrieved September 18, 2023, from http://hk.everbgt.com/EN/product_detail.php?lv1=2&parentid=&pdcatid=19&pdid=112
- [182] Shenzhen GVDA Technology Co., Ltd. (2022, December 25). The difference between internal heating soldering station and external heating soldering station - Knowledge. GVDA. Retrieved September 18, 2023, from <https://www.gvda-instrument.com>
- [183] UTi260B Heavy Duty Thermal Camera. (n.d.). Retrieved September 18, 2023, from <https://thermal.uni-trend.com/product/uti260b/>
- [184] FLIR SC655 Infrared Camera | Thermal Imagers | Instrumart. (n.d.). Retrieved September 18, 2023, from <https://www.instrumart.com/products/37221/flir-sc655-infrared-camera>
- [185] MX51 Microscopes - Olympus Semiconductor & Flat Panel Display Inspection Solution. (n.d.). Retrieved September 19, 2023, from <https://www.olympus-ims.com/en/microscope/mx51/>
- [186] Temperature Coefficient of Resistance - formula & solved problems. Electrical Volt. Retrieved September 19, 2023, from <https://www.electricalvolt.com/2019/08/temperature-coefficient-of-resistance/>
- [187] ImageJ. Wikipedia. Retrieved September 19, 2023 from <https://en.wikipedia.org/wiki/ImageJ>
- [188] OriginLab - Origin and OriginPro - data analysis and graphing software. (n.d.). Retrieved September 19, 2023, from <https://www.originlab.com/>
- [189] WIFI Bluetooth ESP32-WROOM-32D - HiTechChain. Retrieved September 19, 2023, from <https://hitechchain.se/en/iot/wifi-bluetooth-esp32-wroom-32d-utvecklingskort>
- [190] Thermistor NTC 10K 3950 - Epoxy w/Wire. (n.d.). Retrieved September 19, 2023, from <https://grobotronics.com/thermistor-ntc-10k-3950-epoxy-w-wire.html?sl=en>
- [191] Metal Film Resistors 10K Ohm. (n.d.). Retrieved September 19, 2023, from <https://www.amazon.de/-/en/Metal-Resistors-0-125W-Tolerances-Ribbon/dp/B085MGHFND>

- [192] 3.3K ohm 0.25W Metal Film Resistor 1%, 3K3, MFR, 0.25 watts, Fixed resistor, Color Code Resistor. (n.d.). Retrieved September 19, 2023, from https://projectpoint.in/index.php?route=product/product&product_id=499262327445
- [193] 6.8K 0.25W Metal Film Resistor (6.8K 1/4W MFR Resistor) - SRK ELECTRONICS. Retrieved September 19, 2023, from <https://www.srkelectronics.in/product/6-8k-0-25w-metal-film-resistor-6-8k-1-4w-mfr-resistor/>
- [194] Breadboard 830 tie point (Classic). (n.d.). Retrieved September 19, 2023, from <https://grobotronics.com/breadboard-830-tie-point-classic.html?sl=en>
- [195] Jumper Wires 15cm male to male - Pack of 10. (n.d.). Retrieved September 19, 2023, from <https://grobotronics.com/jumper-wires-15cm-male-to-male-pack-of-10.html>
- [196] Vis, P. J. (n.d.). Voltage Divider Circuit Calculator - For NTC Thermistor. Retrieved September 19, 2023, from <https://www.petervis.com/electronics%20guides/calculators/thermistor/thermistor.html>
- [197] Thorat, S. (2020, May 19). Thermistor | Types, Diagram, Working, Advantages, Application. Retrieved September 19, 2023, from <https://learnmech.com/what-is-thermistor-types-of-thermistor-advantages-and-disadvantages/>
- [198] Teja, R. (2021). Wheatstone Bridge | Working, Examples, applications. ElectronicsHub. Retrieved September 19, 2023 from <https://www.electronicshub.org/wheatstone-bridge/>
- [199] NTC Thermistors - Temperature Measurement with A Wheatstone Bridge | Ametherm. (2023, March 13). Retrieved September 19, 2023 from <https://www.ametherm.com/thermistor/ntc-thermistors-temperature-measurement-with-wheatstone-bridge>
- [200] Kuphaldt, T. R. (2021). Temperature coefficient of resistance. *Physics of Conductors and Insulators / Electronics Textbook*. Retrieved September 19, 2023 from <https://www.allaboutcircuits.com/textbook/direct-current/chpt-12/temperature-coefficient-resistance/>
- [201] Engineers, L. M. (2023, April 26). ESP32 Basics: Analog-to-Digital Converter (ADC). Retrieved September 19, 2023 from <https://lastminuteengineers.com/esp32-basics-adc/>
- [202] Adafruit (n.d.). 10K Precision Epoxy Thermistor. Retrieved September 19, 2023 from <https://www.adafruit.com/product/372>
- [203] Jang, J., Hyun, B. G., Ji, S., Cho, E., An, B. W., Cheong, W. H., & Park, J. U. (2017). Rapid production of large-area, transparent and stretchable electrodes using metal nanofibers as wirelessly operated wearable heaters. *Npg Asia Materials*, 9(9), e432. <https://doi.org/10.1038/am.2017.172>
- [204] Santos, S., (2019). ESP32 Access Point (AP) for web Server | Random nerd tutorials. *Random Nerd Tutorials*. Retrieved September 20, 2023, from <https://randomnerdtutorials.com/esp32-access-point-ap-web-server/>
- [205] Santos, S., (2023b). ESP32 Useful Wi-Fi Library Functions (Arduino IDE) | Random Nerd Tutorials. *Random Nerd Tutorials*. Retrieved September 20, 2023, from <https://randomnerdtutorials.com/esp32-useful-wi-fi-functions-arduino/>
- [206] What is User Experience (UX) Design? (2023b). The Interaction Design Foundation. Retrieved September 20, 2023, from <https://www.interaction-design.org/literature/topics/ux-design>
- [207] Santos, S., (2021). ESP32 BLE Server and Client (Bluetooth Low Energy) | Random Nerd tutorials. *Random Nerd Tutorials*. Retrieved September 20, 2023, from <https://randomnerdtutorials.com/esp32-ble-server-client/>
- [208] Custer, C. (2023, June 29). What is a UUID, and what is it used for? Cockroach Labs. Retrieved September 20, 2023, from <https://www.cockroachlabs.com>

- [209] Lesson 2 – BLE profiles, services, characteristics, device roles and network topology. (2020, December 31). Retrieved September 20, 2023, from <https://embeddedcentric.com/lesson-2-ble-profiles-services-characteristics-device-roles-and-network-topology/>
- [210] Introduction · React native. (2023, September 14). Retrieved September 20, 2023, from <https://reactnative.dev/docs/getting-started>
- [211] Reference: Expo SDK. (n.d.). Retrieved September 20, 2023, from <https://docs.expo.dev/versions/latest/>
- [212] Base64 - MDN Web Docs Glossary: Definitions of Web-related terms | MDN. (2023, August 30). Retrieved September 20, 2023, from <https://developer.mozilla.org/en-US/docs/Glossary/Base64>
- [213] Triggs, R. (2023). Android app permissions explained and how to use them. *Android Authority*. Retrieved September 20, 2023, from <https://www.androidauthority.com/app-permissions-886758/>